

PhD Thesis

Finite-element-based unit cell models for simulating vertically perforated clay block masonry and their application to optimize clay block products

submitted in satisfaction of the requirements for the degree
Doctor of Science in Civil Engineering
of the TU Wien, Faculty of Civil and Environmental Engineering

Dissertation

Finite-Elemente-basierte Einheitszellen-Modelle zur Simulation von Hochlochziegelmauerwerk und deren Anwendung zur Optimierung von Ziegelprodukten

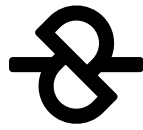
ausgeführt zum Zwecke der Erlangung des akademischen Grads
Doktor der technischen Wissenschaften
eingereicht an der TU Wien, Fakultät für Bau- und Umweltingenieurwesen

Dipl.-Ing. **Raphael Reismüller** BSc

Matr.Nr.: 01228814

- Supervisor:** Univ.-Prof. Dipl.-Ing. Dr.techn. **Josef Füssl**
Institute for Mechanics of Materials and Structures
Research Unit for Structural Simulation and Timber Engineering
TU Wien
Karlsplatz 13/202, 1040 Vienna, Austria
- Reviewer:** Prof. **Gabriele Milani**
Department of Architecture, Built Environment and Construction Engineering
Technical University in Milan
Piazza Leonardo da Vinci 32, 20133 Milan, Italy
- Reviewer:** Assistant Prof. **Rita Esposito**
Department of Materials, Mechanics, Management & Design
Delft University of Technology
Building 23, Stevinweg 1, 2628 CN Delft, The Netherlands

Vienna, October 2023



Acknowledgements

Standing here, at the end of this exciting journey, I feel the deepest gratitude towards all the people, who helped me along the way. Without the help of these people, I would not have been able to finish this thesis.

First and foremost, I would like to express my deepest gratitude to my supervisor Josef Füssl for his support and guidance throughout the last years. I am very grateful for the freedom he gave me to pursue my own ideas and for the many fruitful discussions we had. Next, I am extremely thankful to the examiners of my thesis, Prof. Gabriele Milani and Prof. Rita Esposito, for their time and effort in reviewing my work. Special thanks should also go to my colleagues Markus Königsberger, Markus Lukacevic, and Sebastian Pech, for their contributions to the research presented in this thesis. The collaboration with them was a great pleasure and their invaluable advice clearly increased the quality of my scientific work. Most of the research within this thesis was conducted in the context of the research project *Innovative Brick 2* in collaboration with our industry partner *Wienerberger*. I would like to thank the project partners, especially Andreas Jäger, for the great cooperation and the many interesting and helpful discussions.

It was always a great pleasure working in such a kind and fruitful atmosphere, as it is present at the Institute for Mechanics of Materials and Structures (IMWS). Thus, I would like to thank the head of the institute Christian Hellmich, for providing this great environment. I am also very grateful to everyone at the institute, who made my work life easier. In this regard, many thanks to Gabriele Ostrowski, Martina Pöll, and Astrid Schuh, for their administrative work and also to David Kaufmann and Jan Vales, for their IT assistance. Thanks should also go to all my colleagues at the institute, for the great time we had together during meetings, lunch breaks, coffee breaks, christmas parties, etc.

Besides the people directly involved in this thesis, there are also those, who helped laying the foundation of my work. In this regard, I would like to thank Christian Schranz for the guidance and support he provided me from day one at the TU Wien. I am extremely grateful for the invaluable opportunities he provided, which eventually led to this thesis. For the biggest part of this foundation, I am deeply indebted to my parents. Thank you for your never-ending support, your encouragement, and the opportunity to pursue my educational path until the studies at the TU Wien.

Finally, I would like to express my deepest gratitude to my wife Pia for her unconditional support and endless patience throughout the last years and my daughters Marisol and Luna for the joy they bring to my life.

Abstract

Being one of the oldest building materials in human history, clay block masonry remains widely used in modern construction. Over time, modern clay blocks have evolved to be more lightweight and offer better thermal insulation properties. As a result, vertical perforations were introduced to the blocks. Due to this intricate block geometry, the brittle and orthotropic behavior of fired clay, and the interaction between blocks through mortar or glued joints, describing the behavior of masonry through numerical models is a major challenge. Consequently, current clay block products and masonry design rules are largely based on empirical studies. Hence, this thesis presents finite-element-based unit cell models for simulating the complex behavior of clay block masonry structures and their potential application in optimizing clay block products.

Since lateral tensile stresses in the transversal webs are the main reason for the failure of vertically perforated clay block masonry under dominant vertical compression, reinforced bed joints are a promising approach to increase the compressive strength, without changing the block geometry. Using the eXtended Finite Element Method to model the fracture of fired clay and a multiscale homogenization approach to incorporate the effect of the reinforcement on the mortar joint, the impact of reinforced bed joints on the compressive strength of clay block masonry is investigated. The results indicate that the 5 %-quantile of the compressive strength can be increased by up to 33 %, with reinforced bed joints.

Among all the experiments required to obtain a specific level of material certification, fire tests are the most expensive and time-consuming. For this reason, a numerical model for predicting the fire resistance of clay block masonry has been developed. The aim is to provide a small-sized, yet detailed model, which is capable of predicting the performance of a masonry wall in a fire test and offering insights into the involved failure mechanisms. A novel energy-based spalling criterion allows for decoupling the spalling of the longitudinal webs from the vertical loading. Thus, a two-dimensional temperature-displacement finite element model is adequate, which reduces the computational effort significantly. The model is validated using novel experimental data.

As structural engineers increasingly rely on modern FE software for the design of entire structures, an understanding of the effective masonry strengths under various loading states becomes essential. Although failure surfaces for masonry can be found in the literature, the calibration of the necessary parameters often requires experiments with complex loading conditions. Hence, the unit cell model for the vertical compressive strength is extended by a failure model for the mortar joints and validated using experimental data from the literature. Applying this model to a simplified geometry, the peak stress states of masonry under 150 different loading conditions are investigated. In doing so, seven different failure mechanisms are identified and assigned to regions with similar loading conditions. Furthermore, the numerically obtained peak stress states are used to calibrate failure surfaces from the literature: the failure surface formulated by Ganz (1985) and the Rankine–Hill failure surface proposed by Lourenço (1996). Both failure surfaces show good agreement with the numerically obtained results. Nevertheless, qualitative differences compared to the Rankine–Hill failure surface under governing vertical tension and governing vertical compression are observed. Finally, a concept for calibrating the parameters of the Rankine–Hill surface is presented, using the developed numerical model as a substitute for experiments.

Kurzfassung

Als einer der ältesten Baustoffe in der Geschichte der Menschheit wird Ziegelmauerwerk auch heute noch häufig verwendet. Im Laufe der Zeit wurden die Ziegel für moderne Ansprüche optimiert. Vertikale Löcher verbessern die Wärmedämmeigenschaften und reduzieren das Gewicht der Ziegel. Diese komplexe Ziegelgeometrie, das spröde und orthotrope Verhalten von gebranntem Ton sowie die Wechselwirkung zwischen Ziegel und Mörtel machen die numerische Modellierung von Ziegelmauerwerk zu einer großen Herausforderung. Deshalb beruhen die verfügbaren Ziegelprodukte und die Bemessungsregeln für Mauerwerk hauptsächlich auf empirischen Studien. In dieser Arbeit werden daher Finite-Elemente-basierte Einheitszellenmodelle zur Modellierung des komplexen Verhaltens von Hochlochziegelmauerwerk vorgestellt und zur Optimierung von Ziegelprodukten angewandt.

Da horizontale Zugspannungen in den Querstegen die Hauptursache für das Versagen von Hochlochziegelmauerwerk unter Vertikaldruck sind, stellen bewehrte Lagerfugen einen vielversprechenden Ansatz zur Erhöhung der Druckfestigkeit dar, ohne die Geometrie der Ziegel zu verändern. Unter Verwendung von XFEM zur Modellierung des Ziegelversagens und eines Mehrskalen-Homogenisierungsansatzes zur Berücksichtigung der Bewehrung in der Mörtelfuge wird die Auswirkung von verstärkten Lagerfugen auf die Druckfestigkeit untersucht. Die Ergebnisse zeigen, dass das 5 %-Quantil der Druckfestigkeit durch bewehrte Lagerfugen um bis zu 33 % gesteigert werden kann.

Von allen Versuchen, die zur Erlangung einer Materialzertifizierung erforderlich sind, sind Brandversuche die teuersten und zeitaufwändigsten. Daher wird ein numerisches Modell zur Vorhersage der Feuerbeständigkeit von Ziegelmauerwerk entwickelt. Ein neuartiges energiebasiertes Abplatzkriterium erlaubt es, das Abplatzen der Längsstege von der vertikalen Belastung zu entkoppeln. Damit ist ein zweidimensionales FE-Modell ausreichend, was den Rechenaufwand erheblich reduziert, aber dennoch einen detaillierten Einblick in die Versagensmechanismen ermöglicht. Das Modell wird anhand neuer experimenteller Daten validiert.

Da Bauingenieure bei der Bemessung ganzer Bauwerke auf moderne FE-Software angewiesen sind, ist die Kenntnis von effektiven Mauerwerksfestigkeiten unter verschiedenen Belastungszuständen von großer Bedeutung. In der Literatur sind zwar Versagensflächen für Mauerwerk verfügbar, jedoch erfordert die Kalibrierung der notwendigen Parameter oft Experimente mit komplexen Randbedingungen. Daher wird das bereits entwickelte Einheitszellenmodell durch ein Versagensmodell für die Mörtelfuge erweitert und mit experimentellen Daten aus der Literatur validiert. Anhand einer vereinfachten Geometrie werden die Grenzspannungszustände von Mauerwerk unter 150 verschiedenen Lastfällen untersucht. Dabei werden sieben verschiedene Versagensmechanismen identifiziert und Regionen mit ähnlichen Belastungszuständen zugeordnet. Die numerisch ermittelten Grenzspannungszustände ermöglichen die Kalibrierung zweier Versagensflächen aus der Literatur: jene nach Ganz (1985) und die Rankine-Hill-Versagensfläche nach Lourenço (1996). Beide Versagensflächen stimmen gut mit den numerisch ermittelten Ergebnissen überein. Dennoch sind qualitative Unterschiede im Vergleich zur Rankine-Hill-Fläche bei überwiegend vertikalem Zug und überwiegend vertikalem Druck zu beobachten. Abschließend wird ein Konzept zur Kalibrierung der Parameter der Rankine-Hill-Fläche mithilfe des numerischen Modells vorgestellt.

Contents

Introduction	13
Motivation	13
Research Objectives and Outline of the Thesis	15
Contributions by the author	17
1 Impact of bed joint reinforcement on the compressive strength	19
1.1 Introduction	20
1.2 Modeling strategies	22
1.2.1 Unit cell with periodic boundary conditions	23
1.2.2 Brittle failure of fired clay	26
1.2.3 Mortar bed joint	30
1.2.4 Surface interaction between brick and mortar	32
1.2.5 Stochastic allocation of material strengths to the webs	32
1.2.6 Validating the strategies	34
1.3 Compressive strength increase of vertically perforated clay block masonry	39
1.3.1 Unit cell	39
1.3.2 Brick	40
1.3.3 Mortar	41
1.3.4 Numerical approaches	41
1.4 Results and discussion	43
1.4.1 Fixed strength simulation	43
1.4.2 Random strength simulation	44
1.4.3 Feasible volume fraction	46
1.5 Conclusion	47
2 Finite-element model for vertically perforated clay block masonry in fire tests	49
2.1 Introduction	50
2.2 Fire experiments on vertically perforated clay block masonry	53
2.2.1 Test setup	53
2.2.2 Test results: temperature evolutions and spalling times	54
2.3 Numerical modeling	56
2.3.1 Sequential spalling and associated modeling phases	56
2.3.2 Decoupling of fire loading from vertical loading and corresponding unit-cell models	57
2.3.3 Two-dimensional transient thermal finite-element model	58
2.3.4 Two-dimensional mechanical finite-element model	64
2.3.5 Three-dimensional mechanical finite-element model	70

2.4	Model results, validation, and discussion	72
2.4.1	Evolution of temperature fields	72
2.4.2	Evolution of stress fields and sequential spalling	75
2.4.3	Stresses due to vertical loading and ultimate failure of the wall	77
2.5	Conclusion	79
3	Unit cell model for predicting the failure stress state under arbitrary in-plane loads	81
3.1	Introduction	82
3.2	Modeling Strategies	84
3.2.1	Utilizing the periodicity of masonry – Unit cell concept	84
3.2.2	Failure mechanisms implemented in the finite element model	87
3.2.3	Failure Criterion	90
3.3	Experiments and Simulations	91
3.3.1	Experiments used for Validation	91
3.3.2	Simulation Program	92
3.4	Results and Discussion	99
3.5	Conclusion and Outlook	106
3.6	Appendix A: Calibration of the Failure Surface according to Ganz	108
3.7	Appendix B: Calibration of the Rankine-Hill Surface	109
3.8	Appendix C: Orthotropic Hoffman criterion	111
4	Developing failure surfaces using a validated numerical unit cell model	113
4.1	Introduction	114
4.2	Failure Surfaces for Vertically Perforated Clay Block Masonry	117
4.2.1	Failure surface according to Ganz	117
4.2.2	Rankine–Hill failure surface according to Lourenço	118
4.3	Numerical Model and Simulation Program	120
4.3.1	Simplified Geometry	120
4.3.2	Unit Cell Concept	120
4.3.3	FE Model and Mesh	121
4.3.4	Material Properties	122
4.3.5	Load Application and Sampling Procedure	123
4.3.6	Computational Aspects	125
4.3.7	Postprocessing	126
4.4	Results and Discussion	127
4.4.1	Numerically obtained failure surface	127
4.4.2	Comparison to available failure surfaces	130
4.4.3	Application to real block designs	133
4.4.4	Concept for deriving a numerically calibrated failure surface	135
4.5	Conclusion and Outlook	137
4.6	Appendix A: Failure Criteria according to Ganz	139
4.6.1	Block Failure	139
4.6.2	Mortar Joint Failure	139
4.7	Appendix B: Rankine–Hill Surface	140

Conclusion and Perspectives	141
Main Findings	141
Perspectives and Future Research	143
Publications	157
Books	157
Journal Articles	157
Conference Proceedings	158
Conference Presentations	158
Master's Thesis (own and supervised)	158
Curriculum Vitae	159

Introduction

Motivation

Clay block masonry is one of the oldest building materials in human history. The first known fired clay bricks probably date back to 3000 BC. Since then, clay block masonry has been used in many different cultures and has been continuously developed. However, the main concept stayed essentially the same: clay blocks are stacked on top of each other and connected with mortar. The simplicity of this concept is one of the main reasons for the widespread use of masonry. Additionally, the raw material is available almost everywhere in the world and the basic production of the blocks is not overly complicated. For modern high-quality products, on the other hand, a great deal of material and process experience is required.

One of the most important developments for meeting today's requirements for energy-efficient buildings was the development of vertically perforated clay blocks. These blocks have a complex geometry with slender webs and vertical perforations, leading to low thermal conductivity and low weight. In combination with thin layer mortar or polyurethane adhesive, vertically perforated clay blocks allow for fast and easy construction of load-bearing and non-load-bearing walls. Thus, vertically perforated clay block masonry is a highly appreciated building material in many countries, especially in Europe.

However, the upcoming of steel and concrete construction in the 20th century led to a decline in the use of masonry. Especially in industrialized countries, steel and concrete construction became the preferred building method for larger buildings. Nevertheless, vertically perforated clay block masonry is still the most used building material for single-family houses and smaller residential buildings, for its good thermal insulation properties and a pleasant indoor climate. Yet, the limited knowledge of the complex material behavior, and the lack of simple design methods, may reduce the use of masonry also in this area. Thus, there is a need to improve the understanding of the material behavior and to develop simple design methods for masonry.

Clay block masonry consists of different materials, which all influence the material behavior in different ways. The raw material for the clay blocks is natural clay, which has a unique mineralogical composition, depending on the local clay reservoir. This natural material is then mixed with different pore-forming additives and burned at high temperatures, leading to a complex pore space. Before the firing process, the raw material is extruded, leading to its unique block geometry with vertical perforations. This extrusion process causes orthotropic material properties. Another level of complexity is introduced, when the blocks are composed to a masonry wall in combination with a joint material, such as cement mortar or polyurethane adhesive. Additionally, while the horizontal bed joints are in general always filled with mortar, there are different types of head joints, which lead to a strongly different load-bearing behavior, especially under horizontal and shear loading. Each of these components contributes to the complex material behavior of a vertically perforated clay block wall.

Notably, the variation of some parameters affects different macroscopic material properties contrarily. For example, increasing the size of the vertical perforations improves the thermal insulation properties,

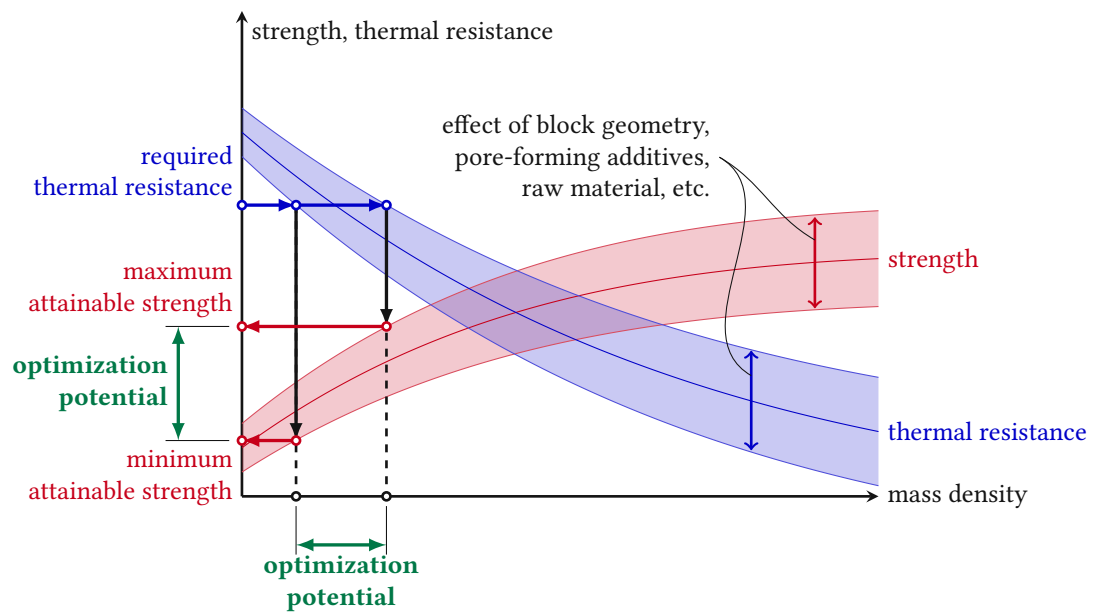


Fig. 1: Optimization potential of vertically perforated clay block masonry. Starting with a requirement for the thermal resistance, a minimum and a maximum attainable strength can be identified, considering the block geometry, the pore-forming additives, and the raw material. The optimization potential is the difference between the maximum and the minimum attainable strength. The same procedure can be applied for a strength requirement.

but reduces the compressive strength. Therefore, optimizing vertically perforated clay block masonry is always a trade-off between different material properties. The goal and boundaries of the optimization problem have to be chosen wisely, considering the desired application area of the product (see Fig. 1).

Currently used clay block products are the result of decades of development involving mostly empirical testing and rules of thumb. Remarkably, for modifying the block geometry, the optimization potential for the thermal properties and the vertical compressive strength is already exhausted, as Bruggi and Taliercio [18] showed using topology optimization. The larger optimization potential for the vertical compressive strength and the thermal properties lies in the optimization of the clay material itself, as Buchner et al. [19–23] showed with their multi-scale homogenization model. Additionally, new ways of optimizing the material properties are sought after, such as the use of bed joint reinforcement. However, there is still a lot of expensive testing involved, since there are currently no simple and scientifically sound numerical models for predicting the macroscopic material behavior of vertically perforated clay block masonry. Thus, clay block manufacturers and researchers would benefit from new numerical models.

Typically, three different experiments are performed for characterizing the material behavior of a specific vertically perforated clay block: uniaxial compressive tests on single blocks and uniaxial compressive tests on wall specimens according to EN 1052-1 [43], and shear tests on specimens consisting of two or three blocks according to EN 1052-3 [44]. While these tests consider the most relevant load cases, i. e. vertical compression and shear loading, no information on the horizontal and vertical tensile strength, and the horizontal compressive strength is gathered. However, these material properties can be crucial for the design of masonry structures under certain loading conditions. Kiefer et al. [76] already showed, that the vertical compressive strength of vertically perforated clay block masonry can

be predicted with a unit cell finite element model. Thus, their model can be used as a substitute for the vertical compressive tests on wall specimens. Finding a sound numerical model for predicting the other material properties would allow for reducing the number of experiments needed for characterizing the material behavior of a specific vertically perforated clay block.

Another issue leading to the preference for concrete and steel is the low priority given to masonry in civil engineering curricula. The reason for that is not only the complexity of masonry as a material but also the structural composition of masonry buildings. While steel and concrete buildings consist mostly of beams, slabs, and columns, masonry buildings consist of walls, which are more difficult to analyze. Considering a typical civil engineering curriculum, the students learn how to analyze beams, slabs, and columns in the first semesters. The load bearing behavior of walls is harder to grasp, which is why it is often postponed to later semesters and kept short. Therefore, the knowledge of masonry is often limited to the basics, which in turn makes civil engineers reluctant to calculate masonry. This also has an impact on masonry research, which is why there are significantly fewer publications on masonry than on steel and concrete.

As a result, macroscopic failure surfaces for masonry are not well developed, although they are essential for the design of entire masonry structures with FE software. Since FE software is nowadays an essential part of a structural engineer's modeling process, including failure surfaces in FE software would probably compensate for the lack of knowledge of masonry in civil engineering curricula. Notably, it is not the lack of failure surfaces, that is the problem, but the difficult calibration process. For example, the Rankine–Hill failure surface proposed by Lourenço [86] is well-suited for the implementation into FE software. However, the calibration process requires numerous tests on wall specimens with complex loading states. Therefore, a scientifically sound numerical model for predicting the macroscopic material behavior of vertically perforated clay block masonry would be a valuable tool for substituting the experiments needed for calibrating the failure surface.

Last but not least, as a major problem of our society, the climate change is also a concern for the construction industry. Thus, the production of building materials is also under scrutiny. In recent years, reducing CO₂ emissions has become a major goal for many companies. Clay block masonry is a sustainable building material, since masonry buildings have a large life span, and clay blocks are mostly made of natural raw materials which constitute 74 % of the earth's crust [33]. Nevertheless, the production of clay blocks is energy intensive and the production process is not optimized yet. Additionally, extensive testing is also environmentally unfriendly, since it requires a lot of material and energy. Therefore, it is desirable to reduce the number of experiments and replace them with numerical simulations, where possible.

This Ph.D. thesis is intended to contribute to developing new design methods for vertically perforated clay block masonry by using numerical simulations. Thus, we developed unit cell finite element models for vertically perforated clay block masonry, which allow for predicting the mechanical and thermal behavior of the material under different loading conditions. Using these models, the number of experiments needed for optimizing the material can be reduced and the understanding of the material behavior can be improved.

Research Objectives and Outline of the Thesis

This thesis consists of four publications in peer-reviewed scientific journals. Publication 4 is currently under review. For the sake of consistency, some phrases and symbols have been changed compared to

the original publications, without changing the scientific content. The main research objectives of these publications are summarized below.

In **Publication 1** we investigated the influence of bed joint reinforcement on the vertical compressive strength of vertically perforated clay block masonry. For this purpose, we used the numerical unit cell model proposed by Kiefer et al. [76] and extended it to consider bed joint reinforcement. This was achieved by introducing a multi-scale homogenization procedure, which allows for computing the effective elastic properties of the reinforced bed joint. By varying the reinforcement ratio, we wanted to quantify the influence of bed joint reinforcement on the compressive strength of vertically perforated clay block masonry. By comparing the considered reinforcement ratios with the reinforcement ratios achieved with commercial glass fiber products, we wanted to assess the applicability of the proposed model for the design of bed joint reinforcement in vertically perforated clay block masonry. Additionally, we investigated the effect of material strength fluctuations on the vertical compressive masonry strength by introducing a stochastic FE approach. Thereby, we randomly allocated material strengths to the transversal webs of each block and simulated ten different models with varying reinforcement ratios.

Publication 2 deals with the numerical simulation of a fire test on vertically perforated clay block masonry. The main research objective was to find an efficient FE-based procedure to predict the performance of a masonry wall in a fire test, as a substitute for expensive experiments. Thereby, we used a 2D transient thermal FE model to model the heat transfer through the wall and a 2D mechanical FE model with periodic boundary conditions to model the mechanical response. Since the performance of a masonry wall in a fire situation is strongly influenced by spalling of the longitudinal webs, we used a stepwise approach, to account for the material degradation due to spalling. To identify the exact moments of spalling, we proposed an energy-based criterion, which is based on the assumption, that the overall strain energy in the first longitudinal web decreases abruptly when spalling occurs. The proposed criterion was validated by comparing the predicted spalling moments with the results of a fire test on vertically perforated clay block masonry.

Publication 3 concerns the extension of the unit cell FE model used in Publication 1 for arbitrary in-plane loading states. For this purpose, we introduced a cohesive behavior interaction criterion for considering joint failure. Using a two-condition failure criterion, the model allows for computing the peak stress state for a given loading path. We validated the proposed model using seven uniaxial compressive tests with inclined bed joints from the literature. Subsequently, we simulated additional loading states and compared the numerically obtained peak stress states to the Rankine–Hill failure surface. In doing so, the model could serve as a basis for the numerical calibration of macroscopic failure surfaces for vertically perforated clay block masonry.

In **Publication 4** we used the FE model developed in Publication 3 to provide a concept for numerically obtaining macroscopic failure surfaces for vertically perforated clay block masonry. Thereby, we simulated 150 different loading states and obtained the peak stress state and the governing failure mechanism of each simulation. Additionally, we considered three different head joint types, to identify how these types affect the obtained peak stresses. Using that many different loading states, we needed to define a simplified block geometry, to keep the computation time at a reasonable level. Subsequently, we compared the numerically obtained peak stresses with two failure surfaces from literature, to pinpoint similarities and differences. Considering the Rankine–Hill failure surface, we also investigated different calibration approaches, to identify the most suitable one. To verify the results obtained with the simplified model, we performed additional simulations using two real block geometries. Taking the

identified similarities and differences into account we proposed a concept for numerically calibrating the Rankine–Hill failure surface for vertically perforated clay block masonry.

Contributions by the author

The author’s contributions to the publications are as follows:

- **Publication 1**, *A finite-element-based approach to quantify the impact of bed joint reinforcement on the compressive strength of vertically perforated clay block masonry*: The author developed the proposed numerical model, performed all simulations, and prepared most of the manuscript.
- **Publication 2**, *The performance of vertically perforated clay block masonry in fire tests predicted by a finite-element model including an energy-based criterion to identify spalling*: The author developed the proposed model, performed all simulations, and prepared most of the manuscript.
- **Publication 3**, *A numerical unit cell model for predicting the failure stress state of vertically perforated clay block masonry under arbitrary in-plane loads*: The author developed the proposed model, performed all simulations, and prepared most of the manuscript.
- **Publication 4**, *Developing failure surfaces for vertically perforated clay block masonry using a validated numerical unit cell model*: The author developed the proposed model, performed all simulations, and prepared most of the manuscript.

I would like to acknowledge that my last name has changed from Suda to Reismüller in 2021 since I took my wife’s last name when we got married. The earlier work, including the first publication within this thesis, was published under the name Suda, while subsequent contributions have been made under the name Reismüller.

Publication 1

A finite-element-based approach to quantify the impact of bed joint reinforcement on the compressive strength of vertically perforated clay block masonry.

Authors Raphael Suda¹, Thomas Kiefer, Christian Schranz, Josef Füssl
Published in *Engineering Structures*, 239 (2021) 112277
DOI <https://doi.org/10.1016/j.engstruct.2021.112277>

Abstract

Since lateral tensile stresses trigger failure of vertically perforated clay block masonry under vertical loading, reinforcement of the bed joints introduces a new way to improve the vertical resistance of masonry. The aim of this work is to estimate the feasible increase of the vertical compressive strength by means of the eXtended Finite Element Method (XFEM). Using a unit cell approach and a stochastic strength distribution, the increase of the masonry strength's 5 %-quantile could be predicted with 33 %. Hence, this work constitutes the vast potential of fiber-reinforced bed joints in improving the vertical compressive strength of clay block masonry.

¹My last name has changed from Suda to Reismüller in 2021 since I took my wife's last name when we got married.

1.1 Introduction

Being one of the oldest building materials in human history, brick masonry has been used widely, especially in Central Europe. Despite its excellent properties (such as durability, sound protection, energy efficiency, and superior indoor climate), masonry lost its dominating role in the building industry, due to the rise of steel and reinforced concrete in the second half of the twentieth century. While innovative research in concrete and steel constructions encouraged the wide usage of these materials, big innovations in optimizing the load-bearing capabilities of newly built block masonry have not been found. Developments such as the use of polyurethane-based glue in the bed joints simplify the construction process, however, the strength of masonry structures is not enhanced, if not even reduced. However, the activity in masonry research has increased again in this field of interest, especially because of the rapid development of computational mechanical methods (see e. g. [4, 9, 58, 61, 84, 86, 93, 94, 102, 109, 135]).

Recently, Kiefer et al. [76] proposed a numerical simulation tool to derive the compressive strength of masonry made of vertically perforated clay blocks, as they are widely used for residential low-rise buildings in central Europe. The usage of such kinds of blocks, laid in thin-bed mortar without mortared head joints, results in numerous advantages, for instance, shorter building periods, higher accuracy of construction, and improved masonry properties regarding thermal insulation. However, using this construction technique does not allow for a continuous mortar layer between the blocks, resulting in vertically connected chambers. Especially with installations in the façade and subsequently occurring air circulation, this causes severe problems concerning the airtightness of the building shell. This airtightness is demanded by standards to prevent problems, such as arising mold (e. g. DIN 4108-1 [35]). To encounter this problem, bed joints are occasionally reinforced with fibers, leading to a continuous mortar layer. In the investigated block masonry, failure under vertical compressive loading is triggered by transverse tensile stresses and subsequent occurring cracks. Yet, the fiber reinforcement within the mortar layer increases its stiffness, thereby reducing the tensile stresses in the transversal webs of the block. Since the potential for optimization in changing the block geometry is rather exhausted (see e. g. [18, 27, 107, 141]), reinforcement of the bed joints introduces a new way to improve not only the ductility and horizontal strength (as e.g. Sadek and Lissel [132] already showed) but also the vertical compressive strength of masonry (as e.g. Jasiński and Drobiec [73] suspected for solid autoclaved aerated concrete masonry).

Thus, the main aim of this work is to assess the feasible compressive strength increase due to fiber reinforcement of the bed joints, by extending the unit cell approach proposed by Kiefer et al. [76], which uses the *eXtended Finite Element Method (XFEM)* combined with the *Virtual Crack Closure Technique (VCCT)* to model the brittle fracture of brick. Other popular modeling approaches are *smearred damage models* like regularized damage models or phase field models (see e. g. [38, 90, 97, 114]). While the XFEM introduces discrete cracks in the finite element model, smeared damage approaches are able to model smeared fracture zones by including damage variables in the constitutive model. Especially when facing problems like hard-to-predict initial crack locations, uniting cracks, or dynamic crack growth, classic XFEM poses hard-to-overcome problems. Although different approaches for improving the traditional XFEM tackle these shortcomings (see e. g. [36, 150, 153]), smeared damage models stay superior in the aforementioned cases. Since the location of cracks could be predicted easily and uniting cracks were not relevant to the problem, using a stable, reliably validated, and already available numerical model seemed to be sufficient for reaching this goal.

Building on this model, the outline of the paper can be summarized as follows: First of all, the reinforced mortar joints were introduced by homogenizing the overall stiffness based on a multi-scale material model. Secondly, this modeling strategy was validated by means of compression tests on solid brick pillars, conducted by Trinko et al. [144]. Considering these adaptations, a relation between the amount of reinforcement and the overall strength increase could be developed. Additionally, ten different models with stochastically allocated strength values were generated and numerically evaluated with and without reinforcement. In that way, the effect of strength fluctuations within the clay block could be investigated. These fluctuations are often caused by micro-cracks or material inhomogeneities, originating from the production process.

Finally, a reasonable estimate for the vertical compressive strength increase of clay block masonry due to fiber-reinforced bed joints should be provided. Section 1.2 contains an overview of the applied modeling strategies as well as the validation of these, while Section 1.3 provides a detailed description of the numerical model. Afterwards, the results are explained and discussed in Section 1.4, followed by final conclusions to the work in Section 1.5.

1.2 Modeling strategies

In the development of new block geometries, manufacturers conduct compressive tests on two different specimen types: single blocks and standardized wall specimens according to EN 1052-1:1998 [43]. The standardized wall specimen is two block lengths wide, five block heights high, and includes mortar joints, thereby reproducing the load transfer mechanisms inside a masonry wall. Due to the difference of these specimens, the obtained compressive strength is significantly smaller when testing a wall specimen than in the single block experiment. This difference originates in the distinct failure mechanisms of both tests.

In the single-block experiment, the block's top and bottom surfaces are fully in contact with the steel plates of the testing machine. Therefore, the applied vertical forces induce approximately constant vertical compressive stresses over the block's cross-section (see Fig. 1.1a). Additionally, the friction between the machinery and the specimen disables the lateral deformation of the block's top and bottom faces, leading to lateral compressive stresses close to the top and bottom faces. Conversely, in block masonry under axial compression, as it is represented by the wall specimen, the vertical compressive stresses vary over the block's cross-section. While the vertical stresses are approximately constant at half the height of each block, transversal webs not standing on top of each other cannot underlie vertical stresses on the top and bottom faces (see Fig. 1.1b). Hence, the forces have to be redistributed to the load-transferring longitudinal webs, yielding tensile stresses on the surface, similar to a plate under vertical loading supported in both lower corners (see Fig. 1.1c).

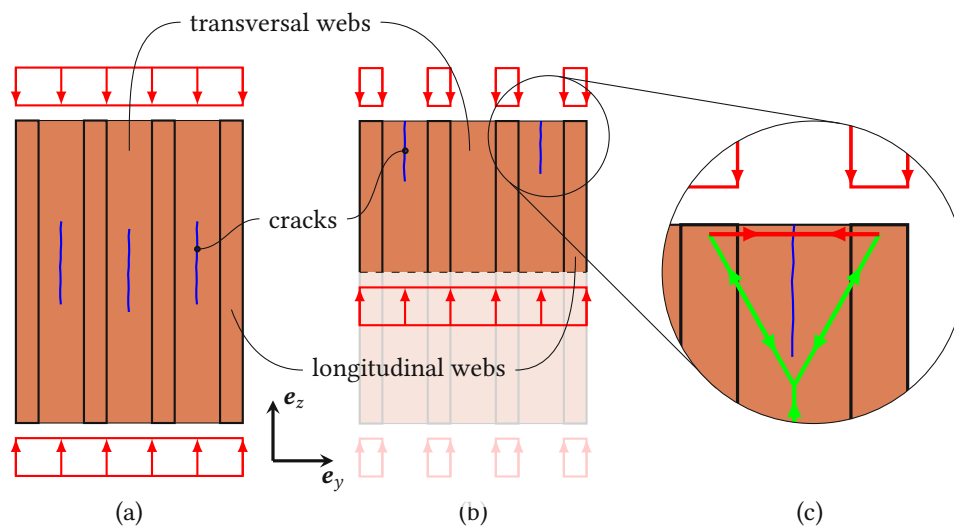


Fig. 1.1: Differences in load transfer of (a) single block specimen and (b) wall specimen. The truss system in (c) visualizes the load transfer from transversal webs to longitudinal webs (green – compressive force, red – tensile force). The vector e_y is normal to the wall surface.

There is no way to reliably predict the compressive strength of masonry solely on the single block strength; thus, it is important to consider both block and mortar in the numerical simulation tool. Since the numerical simulation of the whole standardized wall specimen is rather time-consuming, Kiefer et al. [76] suggested the usage of a unit cell approach with periodic boundary conditions. This approach enables the simulation of an infinitely large masonry wall, represented through a sufficiently large, characteristic part of the wall. Hence, it was possible to simulate a uniaxial macroscopic stress state,

as can be expected in the middle of the wall specimen, with a model, which was 80 % smaller than the real specimen. In combination with Hoffman's orthotropic damage criterion [67] and discrete crack simulation by means of the eXtended Finite Element Method (XFEM), they were able to efficiently predict the vertical compressive strength of different block geometries.

1.2.1 Unit cell with periodic boundary conditions

A masonry wall is here considered a two-dimensionally periodic structure; bricks (or blocks) and mortar form a constantly repeating pattern. To reduce the computational expense of the numerical simulation, it seems obvious to make use of this structural property. Doing so, it is sufficient to define the mechanical properties solely on a small part of the structure, the so-called *repeating unit cell*, with periodic boundary conditions.

The periodicity of masonry with a lateral block offset of half the block length (see Fig. 1.2) can be defined by a basis of two linearly independent vectors \mathbf{v}_1 and \mathbf{v}_2 , with the following characteristics: Any point \mathbf{x}_b within the structure can be reached by translating a starting point \mathbf{x}_a along a vector $m_1 \cdot \mathbf{v}_1 + m_2 \cdot \mathbf{v}_2$ ($m_1, m_2 \in \mathbb{Z}$). Points \mathbf{x}_a and \mathbf{x}_b , which are associated in that manner, have the same mechanical properties. The smallest possible unit cell, without considering line or point symmetries, would be the parallelogram spanned by the two vectors \mathbf{v}_1 and \mathbf{v}_2 . However, for easily applying the periodic boundary conditions on the FE mesh, it is better to have a cuboid unit cell. Therefore, the extracted section in Fig. 1.3 was chosen as unit cell. The vectors \mathbf{c}_x and \mathbf{c}_z describe the unit cell periodicity in directions \mathbf{e}_x and \mathbf{e}_z , respectively.

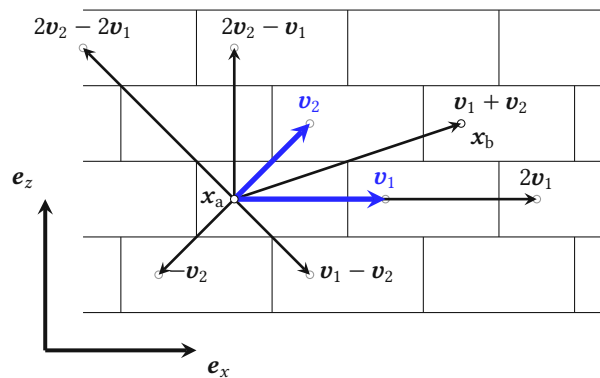


Fig. 1.2: Two-dimensional periodicity of a common bonding pattern

Hence, the masonry wall consists of a periodic concatenation of unit cells. Both in undeformed and deformed state, these unit cells have to form a geometrically compatible structure. To satisfy this condition, periodic boundary conditions were formed and applied to the unit cell. These special boundary conditions ensure that two neighboring faces (thus, opposing faces of a unit cell) deform in the same manner: every point \mathbf{s}_k on the unit cell's face has a corresponding point $\mathbf{s}_k + \mathbf{c}_k$ on the opposing face.

Michel et al. [96] split the strain field $\boldsymbol{\varepsilon}(\mathbf{x})$ in a constant part $\langle \boldsymbol{\varepsilon} \rangle$ and a locally fluctuating part $\boldsymbol{\varepsilon}'(\mathbf{x})$:

$$\boldsymbol{\varepsilon}(\mathbf{x}) = \langle \boldsymbol{\varepsilon} \rangle + \boldsymbol{\varepsilon}'(\mathbf{x}), \quad (1.1)$$

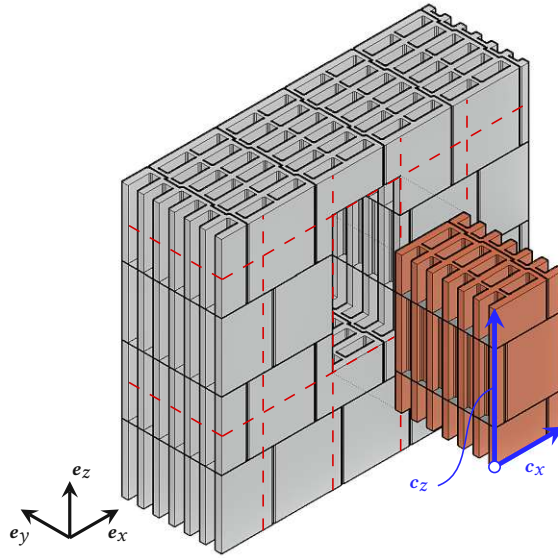


Fig. 1.3: Chosen unit cell

where \mathbf{x} marks a point within the unit cell. The constant part of the strain field is defined as mean value over the volume V :

$$\langle \boldsymbol{\varepsilon} \rangle = \frac{1}{|V|} \int_V \boldsymbol{\varepsilon}(\mathbf{x}) d\mathbf{x}. \quad (1.2)$$

Following Eqs. (1.1) and (1.2), the local fluctuations have to vanish on average. Integrating Eq. (1.1) yields to the deformation field $\mathbf{u}(\mathbf{x})$:

$$\mathbf{u}(\mathbf{x}) = \langle \boldsymbol{\varepsilon} \rangle \cdot \mathbf{x} + \mathbf{u}'(\mathbf{x}). \quad (1.3)$$

Each repetition of the unit cell contributes the same deformation $\Delta \mathbf{u}$ to the overall deformation. This deformation can be calculated for each pair of corresponding points, by means of Eq. (1.3):

$$\Delta \mathbf{u}_k = \mathbf{u}(\mathbf{s}_k + \mathbf{c}_k) - \mathbf{u}(\mathbf{s}_k) = \langle \boldsymbol{\varepsilon} \rangle \cdot \mathbf{c}_k. \quad (1.4)$$

Since $\langle \boldsymbol{\varepsilon} \rangle$ and \mathbf{c}_k are constant within the unit cell, the deformation difference of two in direction k opposing faces, $\Delta \mathbf{u}_k$, has to be constant too. This property enables the definition of so-called primary vertices; the deformation of those primary vertices defines the deformation state on the boundary of the unit cell.

Fig. 1.4a shows a reasonable name convention for cuboid unit cells, proposed by Böhm [13]. Hereby, faces are labeled N , S , E , W , T , and B (*North*, *South*, *East*, *West*, *Top*, and *Bottom*, respectively), while names of edges and vertices consist of the labels of the intersecting faces (eg. SE for an edge and SWB for a vertex).

The chosen unit cell is periodic in x - and z -direction, the y -axis is rectangular to the wall surface. Therefore, the faces *East* and *West* are coupled, as well as *Top* and *Bottom*, while *South* and *North* may deform freely. Although this paper only considers strictly vertical loading, the following periodic boundary conditions include the implementation of more general deformation states. Considering the

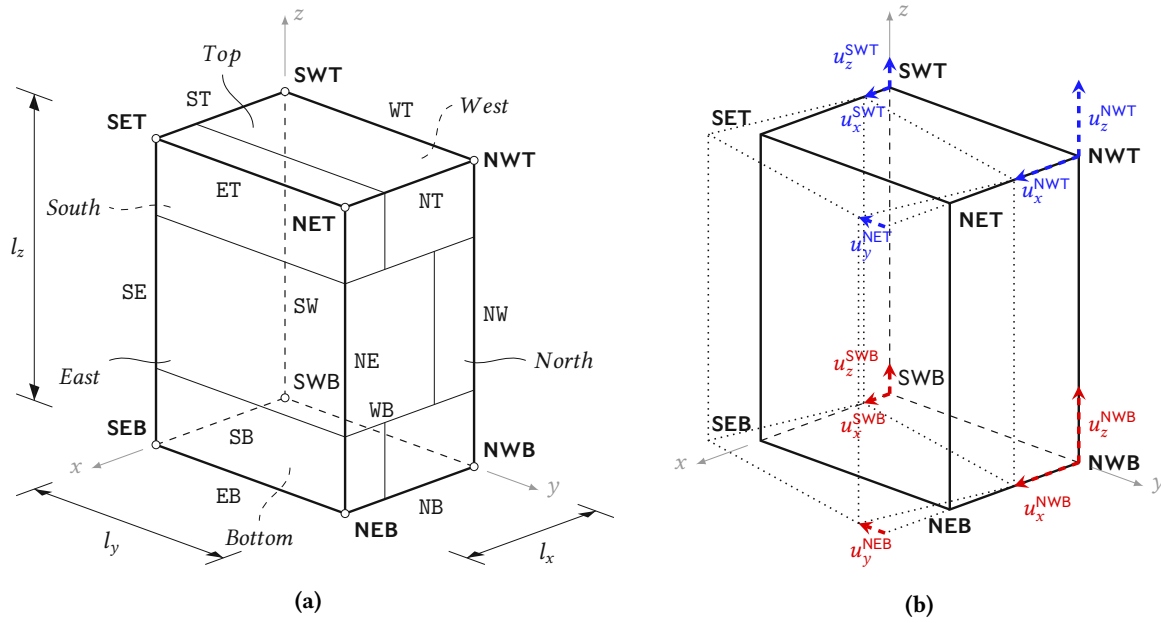


Fig. 1.4: (a) Name convention for the faces, edges, and vertices of a three-dimensional cuboid unit cell and (b) Translation and rotation of face *West* due to displacements of primary nodes.

translation of the edges *WB* and *WT*, the displacements in x - and z -direction are the following on each point on face *Bottom* (see Fig. 1.4b):

$$\begin{pmatrix} u_x^B(y) \\ u_z^B(y) \end{pmatrix} = \begin{pmatrix} u_x^{\text{SWB}} \\ u_z^{\text{SWB}} \end{pmatrix} + \frac{y}{l_y} \cdot \begin{pmatrix} u_x^{\text{NWB}} - u_x^{\text{SWB}} \\ u_z^{\text{NWB}} - u_z^{\text{SWB}} \end{pmatrix}. \quad (1.5)$$

The same relation applies on face *Top*:

$$\begin{pmatrix} u_x^T(y) \\ u_z^T(y) \end{pmatrix} = \begin{pmatrix} u_x^{\text{SWT}} \\ u_z^{\text{SWT}} \end{pmatrix} + \frac{y}{l_y} \cdot \begin{pmatrix} u_x^{\text{NWT}} - u_x^{\text{SWT}} \\ u_z^{\text{NWT}} - u_z^{\text{SWT}} \end{pmatrix}. \quad (1.6)$$

Since u_x^{SWB} and u_x^{NWB} are not necessarily equal, rotations may occur, which result in displacements along the y -axis, u_y (see Fig. 1.4b):

$$u_y^B(x) = u_y^{\text{SWB}} - \frac{x}{l_y} \cdot (u_x^{\text{NWB}} - u_x^{\text{SWB}}) \quad \text{and} \quad (1.7)$$

$$u_y^T(x) = u_y^{\text{SWT}} - \frac{x}{l_y} \cdot (u_x^{\text{NWT}} - u_x^{\text{SWT}}). \quad (1.8)$$

Joining Eqs. (1.5) to (1.8) results in the coupling of the faces *Top* and *Bottom*:

$$\Delta \mathbf{u}_z = \begin{pmatrix} u_x^T(x, y) - u_x^B(x, y) \\ u_y^T(x, y) - u_y^B(x, y) \\ u_z^T(x, y) - u_z^B(x, y) \end{pmatrix} = \begin{pmatrix} u_x^{\text{SWT}} - u_x^{\text{SWB}} \\ u_y^{\text{SWT}} - u_y^{\text{SWB}} \\ u_z^{\text{SWT}} - u_z^{\text{SWB}} \end{pmatrix} + \begin{pmatrix} \frac{y}{l_y} \cdot ((u_x^{\text{NWT}} - u_x^{\text{SWT}}) - (u_x^{\text{NWB}} - u_x^{\text{SWB}})) \\ -\frac{x}{l_y} \cdot ((u_x^{\text{NWT}} - u_x^{\text{SWT}}) - (u_x^{\text{NWB}} - u_x^{\text{SWB}})) \\ \frac{y}{l_y} \cdot ((u_z^{\text{NWT}} - u_z^{\text{SWT}}) - (u_z^{\text{NWB}} - u_z^{\text{SWB}})) \end{pmatrix}. \quad (1.9)$$

Formulating the deformations for the edges WB and EB in an analogous manner results in the coupling of the faces *East* and *West*:

$$\Delta \mathbf{u}_x = \begin{pmatrix} u_x^E(y, z) - u_x^W(y, z) \\ u_y^E(y, z) - u_y^W(y, z) \\ u_z^E(y, z) - u_z^W(y, z) \end{pmatrix} = \begin{pmatrix} u_x^{\text{SEB}} - u_x^{\text{SWB}} \\ u_y^{\text{SEB}} - u_y^{\text{SWB}} \\ u_z^{\text{SEB}} - u_z^{\text{SWB}} \end{pmatrix} + \begin{pmatrix} \frac{y}{l_y} \cdot ((u_x^{\text{NEB}} - u_x^{\text{SEB}}) - (u_x^{\text{NWB}} - u_x^{\text{SWB}})) \\ -\frac{z}{l_z} \cdot ((u_z^{\text{NEB}} - u_z^{\text{SEB}}) - (u_z^{\text{NWB}} - u_z^{\text{SWB}})) \\ \frac{y}{l_y} \cdot ((u_z^{\text{NEB}} - u_z^{\text{SEB}}) - (u_z^{\text{NWB}} - u_z^{\text{SWB}})) \end{pmatrix}. \quad (1.10)$$

The linear equations (1.9) and (1.10) were applied to each pair of corresponding nodes to ensure the geometrical compatibility of the unit cell in any loading scenario. Both free surfaces *Top* and *Bottom* may deform freely; thus, the stresses on those surfaces have to equal zero. Hence, merely the deformations of six out of eight vertices are needed to fully define the boundary conditions. Therefore, these vertices, SWT, NWT, SWB, NWB, SEB, and NEB, are designated primary nodes. To simulate a specific loading scenario, deformations were applied on the primary nodes, following Eq. (1.4). A pure vertical loading is applied by specifying the constant strain in *z*-direction, $\langle \varepsilon_{zz} \rangle$, to nonzero, while setting each other constant strain component to zero:

$$\Delta \mathbf{u}_x = \langle \boldsymbol{\varepsilon} \rangle \cdot \mathbf{c}_x = \begin{pmatrix} 0 \\ 0 \\ 0 \end{pmatrix}, \quad \Delta \mathbf{u}_z = \langle \boldsymbol{\varepsilon} \rangle \cdot \mathbf{c}_z = \begin{pmatrix} 0 \\ 0 \\ \langle \varepsilon_{zz} \rangle \cdot l_z \end{pmatrix}. \quad (1.11)$$

Excluding rigid body translations and rotations, the periodic boundary conditions (Eqs. (1.9) and (1.10)) only fulfill these constraints by setting the vertical displacements of the vertices NWT and SWT to $\langle \varepsilon_{zz} \rangle \cdot l_z$ and the remaining displacements to zero (see Fig. 1.5).

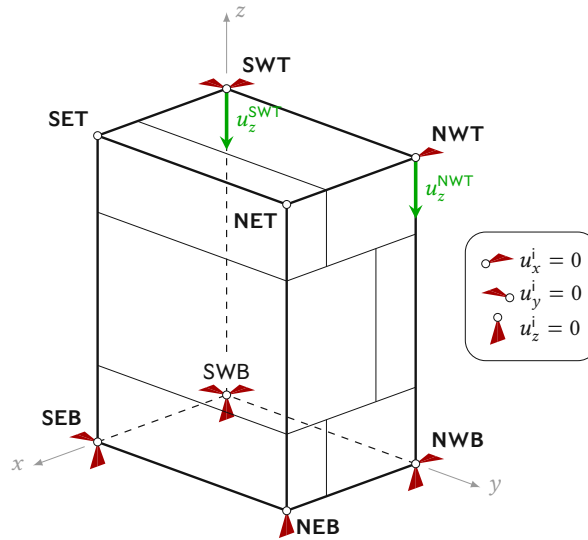


Fig. 1.5: Applied deformations on the unit cell

1.2.2 Brittle failure of fired clay

Extruded bricks show a distinct orthotropic material behavior, caused by the production process. When the raw mixture is being extruded, the flat clay minerals align parallel to the extrusion direction, as Bourret et al. [17] showed. The highest stiffness and strength values are oriented in the extrusion

direction, while the values in the perpendicular direction may be significantly smaller. This orthotropy especially occurs in vertically perforated clay blocks with thin webs. Fig. 1.6 shows the varying local coordinate systems over the block's cross-section. While the local Z -axis is always parallel to the global z -axis (the extrusion direction), the orientation of the L - and T -axis depends on the location within the block geometry. The L -axis (longitudinal) is parallel to the longer side of each part; the T -axis (transversal) is rectangular to the L -axis. Capital letters are used for the local coordinates (L , T , Z), whereas lower case letters indicate global coordinates (x , y , z). Two different types of webs may be distinguished due to the geometry of the vertical perforations: *longitudinal webs* are aligned lengthwise with the wall, *transversal webs* are oriented rectangular to the wall surface.

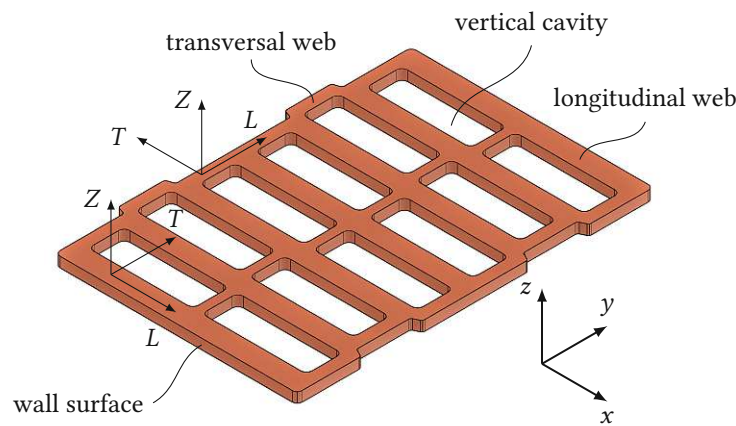


Fig. 1.6: Parts of a vertically perforated clay block and local coordinates for describing the material properties

Cracking processes are a central matter in the failure of brittle materials like fired clay. Those cracks are always attended with high gradients in the stress field near the crack tip. Thus, the mesh would have to be refined around the crack tip. Consequently, the mesh has to be continually updated when simulating propagating cracks. The eXtended Finite Element Method (XFEM), introduced by Belytschko and Black [7], allows the modeling of discrete propagating cracks without remeshing. Based on the partition of unity finite element method of Melenk and Babuška [92], the elements are being subdivided into parts, on which different shape functions are applied. This partition enables the local enrichment of the nodal degrees of freedom with special displacement functions:

$$\mathbf{u}(\mathbf{x}) \approx \sum_i^{NN} N_i(\mathbf{x}) \cdot \left[u_i + H_i(\mathbf{x}) \cdot a_i + \sum_j G_j(\mathbf{x}) \cdot b_{ij} \right], \quad (1.12)$$

where N_i are the used nodal shape functions, u_i the nodal displacements, H_i the nodal enrichment functions, G_j the crack tip functions, and a_i as well as b_{ij} the additional degrees of freedom for totally and partly cracked elements. While the first term in square brackets of Eq. (1.12) describes the approximation of the displacement field for the uncracked regions, the second and third part apply for fully and partly cracked elements, respectively. The numerical simulation tool was modeled in the commercial FE software *Abaqus*, in which the crack tip functions are not considered. Since these functions depict the large stress gradients near the crack tip, the used approach is more sensitive to the chosen mesh. Being fully aware of this fact, the chosen meshes were sufficiently refined where needed.

For describing the location and geometry of cracks, the so-called level-set method is applied [59, 99]. The two level-set functions $\phi(\mathbf{x})$ and $\psi(\mathbf{x})$ are able to describe the location of a crack, relative to a given position \mathbf{x} . The function $\phi(\mathbf{x})$ specifies the orthogonal distance of the point \mathbf{x} to the crack surface, while $\psi(\mathbf{x})$ denotes the distance to the crack tip. With these two functions, the crack geometry may be described, whereas

$$\phi(\mathbf{x}) = 0, \psi(\mathbf{x}) < 0 \quad \text{defines the crack surface,} \quad (1.13)$$

$$\phi(\mathbf{x}) = 0, \psi(\mathbf{x}) = 0 \quad \text{defines the crack tip, and} \quad (1.14)$$

$$\psi(\mathbf{x}) > 0 \quad \text{is not located on the crack at all.} \quad (1.15)$$

Abaqus uses the modified Heaviside function $H(x)$ [99] as the nodal enrichment function:

$$H_i(\mathbf{x}) = H(\phi(\mathbf{x})) = \begin{cases} -1 & \text{for } \phi(\mathbf{x}) < 0 \\ +1 & \text{for } \phi(\mathbf{x}) \geq 0 \end{cases}. \quad (1.16)$$

The level-set for the crack surface, $\phi(\mathbf{x})$, is directly used as the argument for the enrichment function.

Two different components are necessary for the modeling of propagating cracks with the FEM:

1. a **damage initiation criterion** $f(\sigma)$ to indicate failure within an element, and
2. a **damage evolution criterion** to define the ductility and therefore the propagation rate of the crack.

When the damage initiation criterion indicates failure, the affected element is being partitioned along a plane surface, given by the maximum plain stress, but **not yet** split. Those partitions stay bonded until the damage evolution criterion is fulfilled. Within the present work, a combination of Hoffman's orthotropic failure criterion [67] with the Virtual Crack Closure Technique (VCCT) was used.

1.2.2.1 Crack initiation with the orthotropic Hoffman criterion

Graubner and Richter [58] studied different failure criteria for the numerical simulation of brick and found the Hoffman criterion [67] to be suitable for modeling brick failure. The criterion uses each component of the stress tensor σ and is capable of indicating failure under tensile as well as combined stress states. Triaxial compression failure cannot be depicted with the Hoffman criterion. Since the main reason for failure are tensile stresses in the transversal webs, this lack of coverage is acceptable for the present work. Anyhow, Kiefer et al. [76] have shown that even a simple principal stress criterion yields reasonable results, which confirms the assumption of lateral tensile stresses governing the failure mechanism.

Mathematically, Hoffman's failure criterion reads as follows:

$$\begin{aligned} f(\sigma) = & C_1 \cdot (\sigma_{TT} - \sigma_{ZZ})^2 + C_2 \cdot (\sigma_{ZZ} - \sigma_{LL})^2 \\ & + C_3 \cdot (\sigma_{LL} - \sigma_{TT})^2 \\ & + C_4 \cdot \sigma_{LL} + C_5 \cdot \sigma_{TT} + C_6 \cdot \sigma_{ZZ} \\ & + C_7 \cdot (\sigma_{LT})^2 + C_8 \cdot (\sigma_{TZ})^2 + C_9 \cdot (\sigma_{LZ})^2, \end{aligned} \quad (1.17)$$

with the components of the stress tensor, σ_{ij} , and the constant parameters C_1 to C_9 depending on the materials tensile, compressive, and shear strengths, $\sigma_{t,i}$, $\sigma_{c,i}$, and $\sigma_{s,ij}$, respectively:

$$C_1 = \frac{1}{2} \left[(\sigma_{t,T} \cdot \sigma_{c,T})^{-1} + (\sigma_{t,Z} \cdot \sigma_{c,Z})^{-1} - (\sigma_{t,L} \cdot \sigma_{c,L})^{-1} \right], \quad (1.18)$$

C_2 and C_3 by permutation of indices L, T, Z ,

$$C_4 = (\sigma_{t,L})^{-1} - (\sigma_{c,L})^{-1}, \quad (1.19)$$

C_5 and C_6 by permutation of indices L, T, Z ,

$$C_7 = (\sigma_{s,TZ})^{-2}, \quad (1.20)$$

C_8 and C_9 by permutation of indices L, T, Z .

While tensile and compressive strengths are available from experiments (see Section 1.3.2), the shear strengths could only be estimated. Graubner and Richter [58] obtained reasonable results by assuming the shear strengths between the mean value of the corresponding tensile strengths and half of the mean value of the corresponding compressive strengths:

$$\tau_{ij,\min} = \frac{\sigma_{t,i} + \sigma_{t,j}}{2}, \quad \tau_{ij,\max} = \frac{\sigma_{c,i} + \sigma_{c,j}}{4}. \quad (1.21)$$

In the present work, the shear strengths were specified as mean value of those boundaries.

1.2.2.2 Crack propagation with the Virtual Crack Closure Technique

The brittle material behavior of fired clay can be described accurately by means of linear elastic fracture mechanics, which forms the basis for the application of the Virtual Crack Closure Technique. The main assumption of this technique is the following: The released strain energy due to the opening of a crack is equal to the energy, required for closing the same crack. Based on this assumption, the energy release rate G is calculated and compared with the critical energy release rate G_c , which is a material property. As soon as the energy release rate exceeds the critical value, the crack extends. In the present work, the crack propagation criterion was defined to consider all three failure modes by means of a power law (as it is implemented in *Abaqus*):

$$f = \frac{G}{G_c} = \left(\frac{G_I}{G_{I,c}} \right)^a + \left(\frac{G_{II}}{G_{II,c}} \right)^b + \left(\frac{G_{III}}{G_{III,c}} \right)^c = 1. \quad (1.22)$$

Hereby, the energy release rate is calculated and compared to the critical energy release rate for each failure mode separately. Additionally, the superscripts a , b , and c affect the interaction between the failure modes.

Kiefer et al. [76] assigned 0.025 J/mm^2 to the critical energy release rate for mode-I failure, $G_{I,c}$. These values were chosen after Eis and Vassilev [41], who did three-point bending tests on different brick specimens and back-calculated the fracture energy via a genetic algorithm proposed by Hannawald [63]. Bocca et al. [12] determined similar fracture energy values from three-point bending tests and achieved good results recalculating the experiments with a cohesive crack model considering linear elastic fracture mechanics. While critical energy release rates for mode-I failure are already scarce in the literature, data for mode II and mode III are even harder to find. However, since Kiefer et al. showed that the tensile stresses govern failure of vertically perforated clay block masonry, mode I is

the decisive failure mode. Therefore, the values $G_{II,c}$ and $G_{III,c}$ have to be distinctly higher, for example $G_{II,c}/G_{I,c} = G_{III,c}/G_{I,c} = 10$, as proposed by Kiefer et al. Considering this ratio, $G_{II,c}$ and $G_{III,c}$ were set to 0.25 J/mm^2 , assuming linear interaction the coefficients a , b , and c were all set to 1.

1.2.3 Mortar bed joint

The considered vertically perforated clay blocks are usually used with thin bed mortar as bed joints. In general, those mortars consist of cement, chalk, and sand or quartz sand powder. Thin bed mortar behaves similarly to concrete without reinforcement: strengths and Young's modulus are isotropic, the mortar basically deforms linear elastic and fails brittle under tensile stresses without distinct plastic behavior. While the compressive strength of different thin-bed mortars is fairly high, the tensile stresses stay rather low in comparison.

Due to the hydraulic solidification of cement mortar, the material properties strongly depend on the amount of available water. For complete hydration of the mortar, a water-cement ratio around 0.4 is ideal – the weight of available water should be 0.4 times the cement's weight. Since fired clay tends to absorb significant amounts of the water bound to the mortar, manufacturers adjust their mortars to their range of products; in the mixing instruction a water amount is specified, which takes the absorption behavior of the fired clay into account. The compressive strength obtained from experiments on mortar specimens is therefore smaller than the compressive strength of the same mortar as part of the masonry.

Within this work, the mortar material behavior was considered linear elastic and isotropic. Mortar failure was assumed to be insignificant for the vertical compressive strength of the numerical model. This assumption is based on the following reasons:

- The (already high) compressive strength obtained from tests on mortar cubes increases further in the masonry due to the absorption behavior of the fired clay.
- In those regions of the reinforced mortar joint, that are not located on top of a web, tensile stresses occur. Additionally, shrinkage yields small cracks. Those regions are therefore considered as cracked within the model; accordingly, solely the stiffness of the glass fiber mesh is considered there (see Section 1.3.3).

1.2.3.1 Reinforced mortar with homogenized stiffness

To encounter the aforementioned problems regarding airtightness using vertically perforated clay block masonry, a glass fiber mesh is occasionally embedded in the mortar bed joints. Failure of the masonry is induced by lateral tensile stresses in the webs due to transversal webs being not on top of each other. The fiber mesh within the mortar joint increases its overall stiffness, thereby reducing the tensile stresses in the transversal webs of the block. Glass fibers have a rather high Young's modulus and tensile strength, compared to common mortars (see Table 1.1).

Tab. 1.1: Glass fiber properties compared to thin bed mortar [52, 68]

	glass fiber	mortar
Young's modulus E	80 000 MPa	5000 MPa
Tensile strength σ_t	2000 MPa	7.7 MPa

The mesh was assumed to be fully embedded in mortar, lying midmost in the bed joint (see Fig. 1.7). Discretely modeling each glass fiber would be inefficient; not only the modeling of every single fiber would have been time-consuming (especially when modeling different ratios of reinforcement!), but the computational expense would also increase heavily. Instead, the reinforced Mortar joint was considered as a homogenized layer within the model; the homogenized material parameters were obtained from a multiscale model. Therefore, only the materials' stiffness tensors \mathbb{C}_i , the volume fractions of the components on the entire layer, f_i , and information about the fiber's orientation were needed.

The homogenization was conducted on a representative part of the layer, the so-called *representative volume element* (RVE, see Fig. 1.7). For reasonably defining an RVE, the *separation of scales* must be fulfilled:

$$d \stackrel{\sim 1.5-3}{\ll} l \stackrel{\sim 5-10}{\ll} \mathcal{L}, \quad (1.23)$$

meaning that the characteristic length of the RVE, l , has to be at least one and a half to three times bigger than the characteristic size of the inhomogeneities, d , [40, 122] and at least five to ten times smaller than the characteristic length scale of the loading, \mathcal{L} [77]. With this requirement fulfilled, the strains and stresses on the macroscale (on the edges of the RVE), $\boldsymbol{\varepsilon}^M$ and $\boldsymbol{\sigma}^M$, respectively, may be calculated from the stresses and strains on the microscale, $\boldsymbol{\varepsilon}^\mu$ and $\boldsymbol{\sigma}^\mu$, in the following way:

$$\boldsymbol{\varepsilon}^M = \langle \boldsymbol{\varepsilon}^\mu(\mathbf{x}^\mu) \rangle, \quad \boldsymbol{\sigma}^M = \langle \boldsymbol{\sigma}^\mu(\mathbf{x}^\mu) \rangle, \quad (1.24)$$

where $\langle \cdot \rangle$ is defined as the average over the RVE's volume, similar to the definition in Eq. (1.2).

The microstructure consists of different regions with quasi-homogeneous properties – the so-called material phases. In this case, the material phases are mortar and glass fibers. Each of those phases r occupies a volume V_r^μ , and therefore has a volume fraction f_r^μ on the entire volume V_{RVE} :

$$f_r^\mu = \frac{V_r^\mu}{V_{\text{RVE}}}, \quad \sum_{r=1}^{N_r} f_r^\mu = 1, \quad (1.25)$$

where N_r is the total number of material phases. With these volume fractions defined, the homogenization scheme in Eq. (1.24) simplifies to the following discrete scheme:

$$\boldsymbol{\varepsilon}^M = \sum_{r=1}^{N_r} f_r^\mu \cdot \boldsymbol{\varepsilon}_r^\mu(\mathbf{x}^\mu), \quad \boldsymbol{\sigma}^M = \sum_{r=1}^{N_r} f_r^\mu \cdot \boldsymbol{\sigma}_r^\mu(\mathbf{x}^\mu) \quad (1.26)$$

The homogenized stiffness tensor \mathbb{C}^M is then calculated as follows:

$$\mathbb{C}^M = \sum_{r=1}^{N_r} f_r^\mu \cdot \mathbb{C}_r^\mu : \mathbb{A}_r^\mu, \quad (1.27)$$

with each phase's stiffness tensor \mathbb{C}_r^μ and concentration tensor \mathbb{A}_r^μ .

Eshelby [49] and Laws [81] provided an approach to calculate these concentration tensors, which only requires the knowledge of the inclusions' shape additionally to the phases' stiffness tensors. The glass fibers were considered as cylindrical inclusions in two orthogonal directions (see Fig. 1.7); the Mori-Tanaka-scheme [103] was used for solving the homogenization problem.

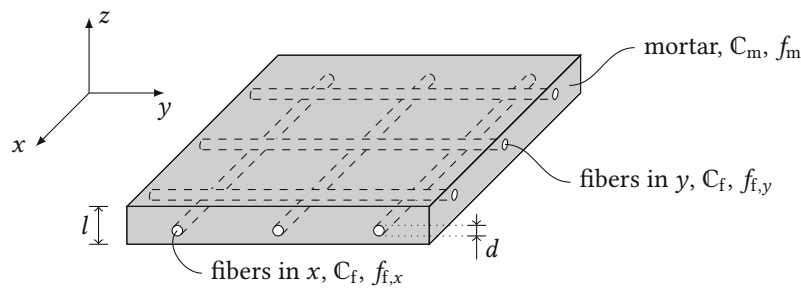


Fig. 1.7: Representative volume element (RVE)

1.2.4 Surface interaction between brick and mortar

The contact properties between brick and mortar play a major role in the interaction of both materials. Hereby, the shear strength τ_u depends on the present axial (compressive) stress in the joint. Van der Pluijm [145] proposes a relation, based on Coulomb's friction law:

$$\tau_u = c_0 - \tan(\varphi) \cdot \sigma_n, \quad (1.28)$$

with the shear bond strength c_0 , the angle of internal friction φ , and the axial compressive strength σ_n . As long as the shear stresses on the interface remain sufficiently small, the bonding of brick and mortar stays intact. Hence, the interface is modeled as being tied. To check out the validity of this clearly strong simplification, the shear stresses on the interface were monitored throughout the simulations.

1.2.5 Stochastic allocation of material strengths to the webs

Calculations with homogeneous material properties showed that without reinforcement the first crack was critical for the failure. When exceeding a certain amount of reinforcement, additional cracks may be formed before reaching the peak stress (see Section 1.4.1). Considering that fired clay is a rather inhomogeneous material – the production process causes microcracks to occur –, the weakest web of the block should be the one triggering failure. Let's assume, that this weakest web has a significantly smaller strength than each other web. Now, if failure of the reinforced masonry requires the formation of a second crack, the strength increase due to the stiffer bed joint should be even higher than in the first case. Therefore, a stochastic approach was chosen to capture these effects within the model.

Inhomogeneities in the single block are common, affecting the material's strength. On the one hand, the used clay is a natural resource; thus, inclusions may occur in the mixture. On the other hand, the mechanical impact on the blocks during the production process as well as the firing process accompanied by material shrinkage induce microcracks.

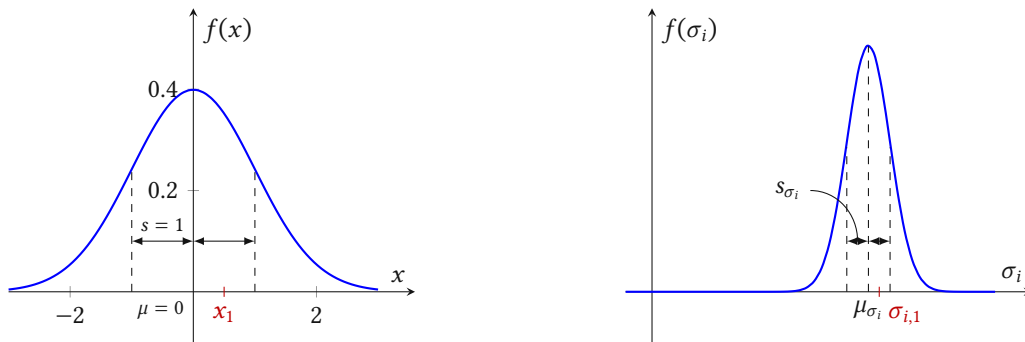
Structural inhomogeneities, like microcracks, are the main reason for the fluctuation of the obtained strengths. Each block in the numerical model was subdivided into longitudinal webs and transversal webs. Since cracks-inducing failure only occurs in the transversal webs, solely the differences between these webs were considered. Thereby, a random strength was allocated to each transversal web, while assuming that each web separately has a homogeneous strength.

Kiefer et al. [76] obtained tensile and compressive strengths from experiments in longitudinal, transversal, and extrusion directions. Therefore, mean values μ and standard deviations s are available, assuming that the strength values are distributed normally. For each transversal web, a value x was randomly

generated from a standard normal distribution (see Fig. 1.8a) with the function `randn()` in the programming language *Julia* [10]. The probability density function of the standard normal distribution ensures the random values are around the mean value of 0. Consider x as kind of a strength modification parameter: If x is lower than 0, the strength is less than the mean value; if x is greater than 0, conversely. This parameter was then used to calculate the tensile and compressive stresses for each direction L , T , and Z :

$$\sigma_i = \mu_{\sigma_i} - x \cdot s_{\sigma_i}, \quad (1.29)$$

with the mean value μ_{σ_i} and standard deviation s_{σ_i} of the treated strength σ_i (see Fig. 1.8b). The obtained values were further used to calculate the shear strengths according to Eq. (1.21).



(a) The value x_1 is randomly picked from a standard normal distribution. (b) With a given mean value μ_{σ_i} and standard deviation s_{σ_i} the randomly picked strength $\sigma_{i,1}$ can be calculated.

Fig. 1.8: Standard normal distribution (a) and normal distribution of material strength σ_i (b).

During cracking processes in a system, energy is released. Since the damage evolution depends on the critical energy release rate, the strength fluctuation due to existing microcracks has to be considered. The entirely undamaged material with a failure stress $\sigma_{f,\max}$ has a critical energy release rate $G_{c,\max}$. At the mean failure stress μ_{σ_f} , the critical energy release rate results in μ_{G_c} , which is defined by the values $G_{c,I}$ to $G_{c,III}$ for each failure mode in Section 1.2.2.2. Since the production-related damage and, therefore, the failure stress σ_f varies with each transversal web, the related critical energy release rate G_c^* has to deviate from the mean value by ΔG :

$$G_c^* = \mu_{G_c} - \Delta G. \quad (1.30)$$

Note, that the difference ΔG may be negative in the case of a web, being stronger than the average. Griffith [60] proposed a way to calculate the critical stress as follows:

$$\sigma_f = \sqrt{\frac{G_c \cdot E}{\pi \cdot a}}, \quad (1.31)$$

with the material's Young's modulus E and the crack length a . Comparing the deviating failure stress σ_f^* to the mean failure stress μ_{σ_f} in terms of Griffith's formulation yields to an equation for the adapted critical energy release rate G_c^* (see Fig. 1.9):

$$\frac{\mu_{\sigma_f}}{\sigma_f^*} = \sqrt{\frac{\mu_{G_c}}{G_c^*}} \quad \rightarrow \quad G_c^* = \mu_{G_c} \cdot \frac{\sigma_f^{*2}}{\mu_{\sigma_f}^2}. \quad (1.32)$$

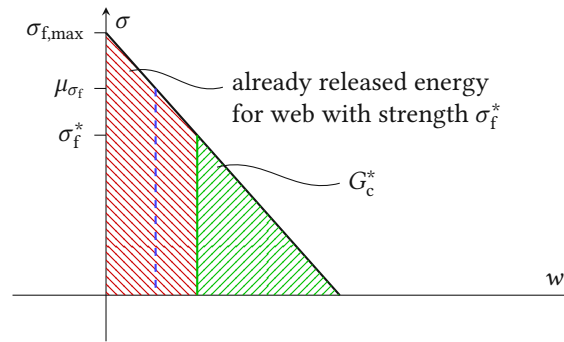


Fig. 1.9: The critical energy release rate is reduced due to production-related damage.

1.2.6 Validating the strategies

Trinko et al. [144] investigated the effect of fiber-reinforced bed joints on the vertical compressive strength of brick masonry in experiments on solid brick pillars (see Fig. 1.10). Therefore, he tested three pillars without reinforcement and another three pillars, reinforced with a glass fiber mesh, as it is typically used for plastering facades. He considered pillars with a square cross-section and eight layers, consisting of Austrian standard-sized bricks reduced to 40 % of their original size. Hence, the pillars were 10 cm wide and 22.2 cm high, with a 2 mm mortar joint between each layer of bricks. Those masonry specimens were modeled with the previously described simulation strategies (Sections 1.2.1 and 1.2.5) in order to verify the proposed numerical model, which was then used to estimate the effect of a reinforced mortar bed joint on the compressive strength of vertically perforated clay blocks. Kiefer et al. [76] already validated the model for the compressive strength of unreinforced clay block masonry by an extensive set of experiments. Therefore, the focus lies in the validation of the modeling strategies considering the bed joint reinforcement.

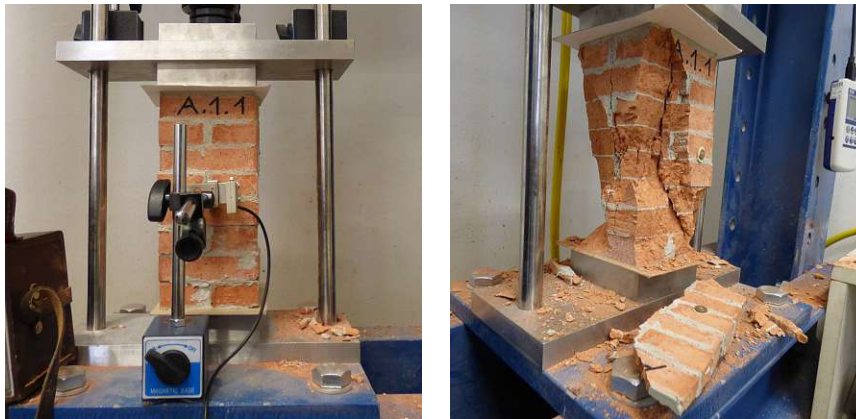


Fig. 1.10: Solid brick pillar without reinforcement, before and after the experiment [144]

1.2.6.1 Material parameters

Trinko et al. [144] experimentally obtained most of the material parameters in Tables 1.2 to 1.4 for the used brick and mortar, missing values were predicted by applying ratios between values obtained in literature.

Tab. 1.2: Orthotropic elastic properties for solid bricks [144]

Young's modulus (MPa)			Poisson's ratio			Shear modulus (MPa)		
E_{LL}	E_{TT}	E_{ZZ}	ν_{TZ}	ν_{ZL}	ν_{LT}	G_{TZ}	G_{ZL}	G_{LT}
9951 (±898.6)	8670 (±471.7)	13 500	0.1	0.1	0.1	3774 (±261.2)	3725 (±232.3)	2700

Values in parenthesis represent standard deviations.

Tab. 1.3: Orthotropic material strengths for solid bricks [144]

Compressive strength (MPa)			Tensile strength (MPa)			Shear strength (MPa)		
$\sigma_{c,L}$	$\sigma_{c,T}$	$\sigma_{c,Z}$	$\sigma_{t,L}$	$\sigma_{t,T}$	$\sigma_{t,Z}$	$\sigma_{s,TZ}$	$\sigma_{s,ZL}$	$\sigma_{s,LT}$
16.42 (±1.62)	13.69 (±2.56)	21.38 (±2.79)	8.04 ^a	6.87 ^a	9.12 ^a	8.38 ^b	9.02 ^b	7.49 ^b

Values in parenthesis represent standard deviations.

^a Scaled based on experiments conducted by Kiefer et al. [76].

^b Mean value of results obtained with Eq. (1.21).

Tab. 1.4: Isotropic elastic properties of the used mortar

Young's modulus	E	8378 MPa (±264.93)
Poisson's ratio	ν	0.223 (±0.00474)

Values in parenthesis are standard deviations.

Brick

Nine independent parameters, eg. three Young's moduli E_i , three Poisson's ratios ν_{ij} , and three shear moduli G_{ij} , are necessary to fully describe the stiffness tensor of an orthotropic material. Measuring the travel time of ultrasonic longitudinal and transverse waves through a solid specimen for each direction L , T , and Z yields six independent components of the stiffness tensor. With the Poisson's ratios of the brick approximated with 0.1 according to the data provided by Hannawald and Brameshuber [64], the Young's moduli and shear moduli could be calculated (see Table 1.2).

To obtain the compressive strengths, Trinko et al. [144] conducted compression tests in each principal material direction. While the tensile strengths were scaled to the compressive strengths with the ratio given by Kiefer et al. [76], the shear strengths were estimated as the mean value of Eq. (1.21). Table 1.3 contains all the strength values used for the model.

Mortar

Measuring the travel time of ultrasonic transverse and longitudinal waves led Trinko et al. [144] to the stiffness properties of mortar. Since the mortar is supposed to be isotropic, the two independent measured values suffice to fully describe the stiffness tensor of the mortar.

Glass fiber mesh and reinforced mortar

Synthetically coated glass fibers form the orthogonally organized mesh, with a mesh width of 4 mm, which was embedded in the bed joint of the pillars. Since the fiber strands consist of numerous fine glass fibers, the cross-section of the strands may vary over the mesh. Therefore, a reliable way to estimate the volume fraction of the glass fibers is found over the areal weight of the mesh. Hence, dividing the areal weight m by the mass density ρ_f times the bed joint thickness d_m times two (for considering only fibers oriented in the same direction), results in the volume fractions in directions x and y , $f_{f,x}$ and $f_{f,y}$, respectively:

$$f_{f,x} = f_{f,y} = \frac{m}{2 \cdot \rho_f \cdot d_m} = \frac{0.0145 \text{ g/cm}^2}{2 \cdot 2.5 \text{ g/cm}^3 \cdot 0.2 \text{ cm}} = 1.45 \%. \quad (1.33)$$

Applying the homogenization scheme presented in Section 1.2.3.1 on the mortar properties in Table 1.4, the glass fiber properties in Table 1.1 and the volume fractions in Eq. (1.33) yields the homogenized stiffness of the reinforced mortar. Thereby, the components C_{xxxx} and C_{yyyy} of the stiffness tensor, which have a strong influence on the lateral stresses triggering failure, increase around 13 %.

1.2.6.2 Experimental results

Trinko et al. [144] obtained failure loads for each specimen and divided them by their cross-section to receive the vertical compressive masonry strengths in Table 1.5. While the mean value of the masonry strength increased by 15.38 % when reinforcing the mortar bed joint, the standard deviation of the results decreased significantly. Additionally, Trinko et al. observed a main difference in the failure mechanism: While the specimens *without reinforcement* failed brittle, immediately after the first crack occurred, the *reinforced* specimens allowed the loading to be increased further, even after the first crack. Hence, the reinforced mortar joints caused a more ductile damage evolution behavior.

Tab. 1.5: Vertical compressive strength of the specimen (MPa) [144]

		Series	
		w/o reinforcement	with reinforcement
Test	I	15.08	15.91
	II	11.96	16.39
	III	14.82	16.00
Mean value		13.95 (± 1.73)	16.10 (± 0.26)
Increase		—	15.38 %

Values in parenthesis represent standard deviations.

1.2.6.3 Numerical results

Both the unreinforced and reinforced specimens were simulated with the modeling strategies above (except the stochastic allocation of strengths), considering the material parameters in Tables 1.2 to 1.4. The representative unit cell consists of two bricks and two bed joints in height (see Fig. 1.11). As the solid brick pillars are more than two times higher than wide, a uniaxial stress state can be expected in the middle of the specimen. Hence, the unit cell approach with periodic boundary conditions, which

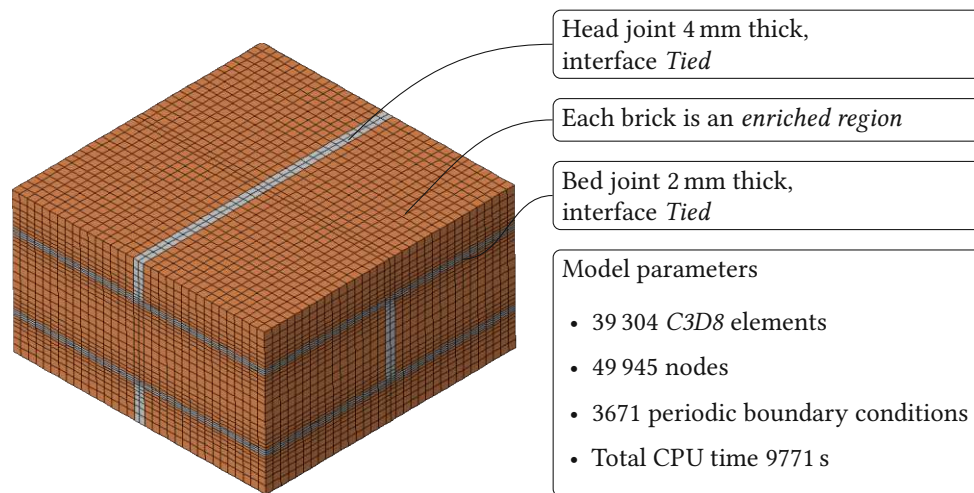


Fig. 1.11: FE mesh of the solid brick model

represents an infinitely large pillar in a uniaxial stress state, is suitable for efficiently modeling the considered problem.

When comparing the obtained masonry strengths to each other, the numerical results fit rather accurately to the experimentally found values (see Fig. 1.12). While the boxes represent the experiments, the crosses mark the numerically obtained strengths. Both models led to results just above the mean value of the experiments and predicted a strength increase of 13.64 % (compared to 15.38 % in the experiments). Since the tensile failure of the mortar head joints was neglected, an overestimation of the peak stress seems reasonable. Modeling the pillars without a mortared head joint at all would lead to a lower bound of the peak stress, as comparative calculations showed.

Additionally, the same mechanism as Trinko et al. observed, occurred: While the unreinforced pillar failed immediately after the formation of the first crack, the reinforced pillar could bear a load increase, even after the first crack occurred (see Fig. 1.13). The experiments showed a distinct nonlinear behavior, due to micro-cracks in both brick and mortar as well as the rupture of the head joints. Since solely

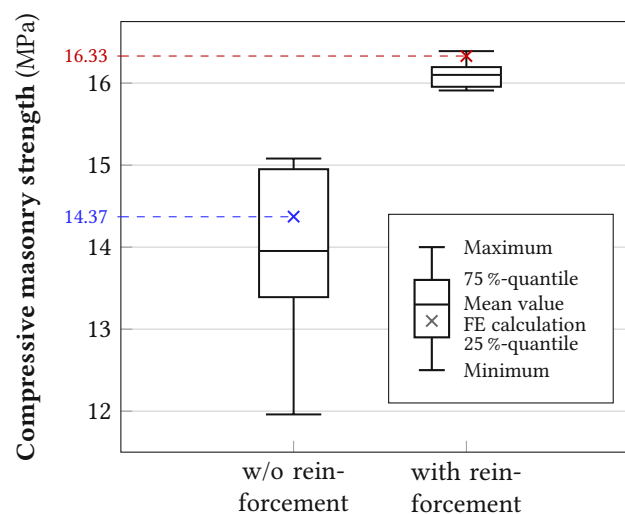


Fig. 1.12: Numerical results compared to the experimental results

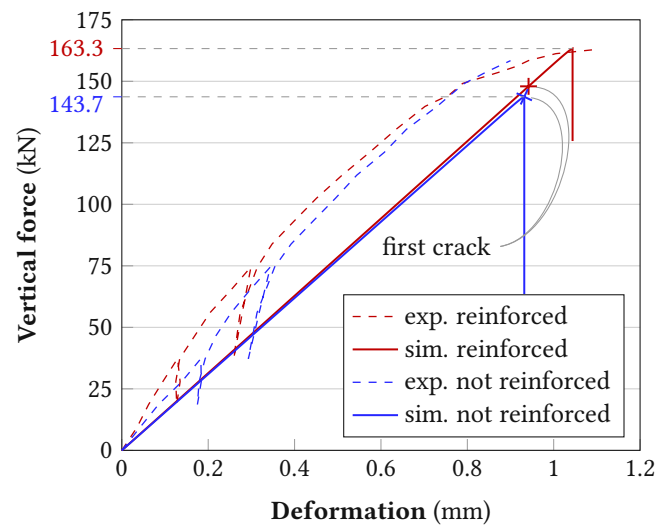


Fig. 1.13: Load-displacement diagram for simulations and experiments (with and without reinforcement)

macro cracks in the brick units were introduced in the model, which is crucial for the magnitude of the peak stress, the numerical simulations followed a linear path until peak stress.

Considering the good agreement of the peak stress values between the simulations and the experiments, the proposed modeling strategies seem to be suitable for application on the block masonry model.

1.3 Compressive strength increase of vertically perforated clay block masonry

In the next step, the validated numerical simulation tool was used to estimate the increase of the vertical compressive strength of vertically perforated clay block masonry due to the use of reinforced bed joints.

1.3.1 Unit cell

The examined block has a height of 249 mm and a length of 248 mm. Choosing the unit cell one block long and two blocks high and considering a 1 mm thick bed joint, as well as a 1 mm wide horizontal gap between the blocks, the total dimensions of the cell add up to 249 mm length and 500 mm height. Hence, the periodicity vectors \mathbf{c}_x and \mathbf{c}_z are:

$$\mathbf{c}_x = \begin{pmatrix} 249 \\ 0 \\ 0 \end{pmatrix} \text{ mm} \quad \text{and} \quad \mathbf{c}_z = \begin{pmatrix} 0 \\ 0 \\ 500 \end{pmatrix} \text{ mm.} \quad (1.34)$$

As a perfect offset of half a block's width is not to be expected on a construction site, the offset was modeled slightly higher, thereby minimizing the contact area. Hence, compressive stresses are directly transferred between the longitudinal webs, but not between the transversal webs. Since the mortar layer over the vertical shafts and transversal webs was supposed to be damaged due to shrinkage-induced cracks, the bed joint was partitioned into two sections (see Fig. 1.14):

- the uncracked mortar layer above the longitudinal webs of the blocks and
- the cracked mortar layer above the vertical shafts and transversal webs of the blocks.

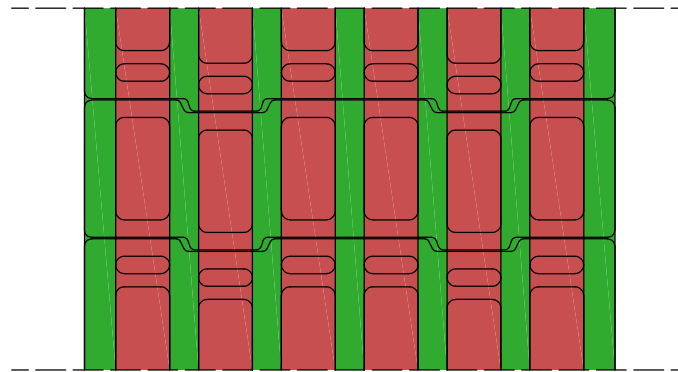


Fig. 1.14: Partitioning of the bed joint in two sections: uncracked (green) and cracked (red). The black lines represent the outline of the blocks directly below and above the bed joint.

While the uncracked section was modeled with the properties of the pure mortar or the homogenized properties of the reinforced mortar, the cracked part was not modeled at all in the unreinforced model. However, the properties of the glass fiber mesh were considered in the model with reinforcement. Fig. 1.15 shows the FE mesh of the modeled unit cell. The transversal webs were defined as *enriched regions*, thus regions where nodal degrees of freedom are enriched. The simulations were run on a high-performance computing cluster, using eight CPU cores in parallel per model. Therefore, the calculations took approximately 4 hours on average.

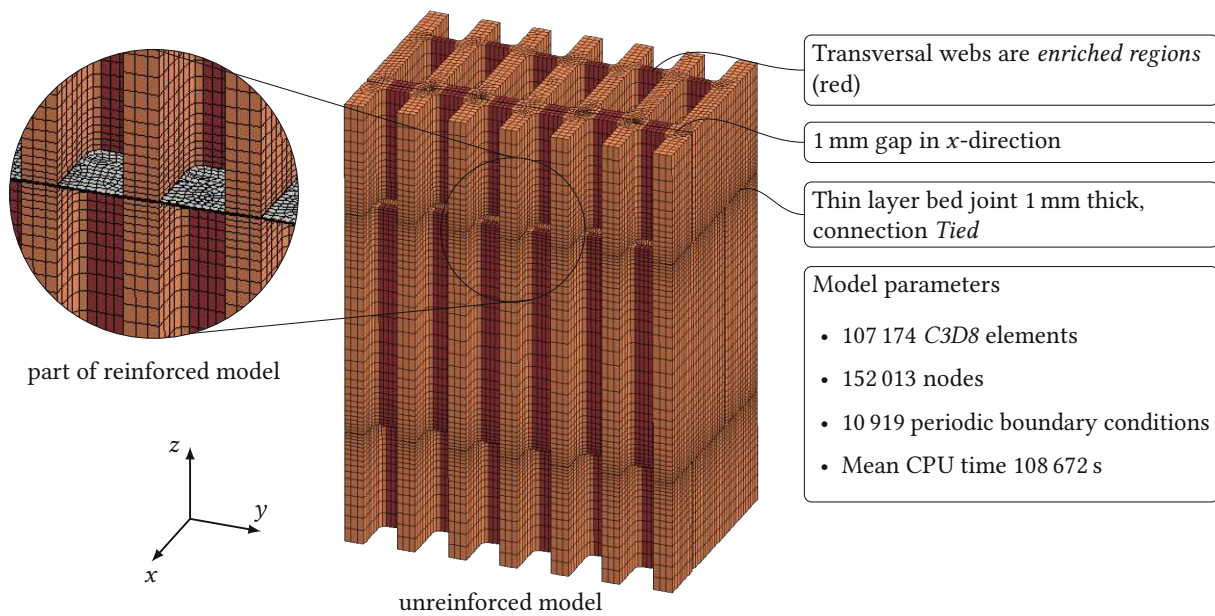


Fig. 1.15: FE mesh of the unreinforced model and part of the reinforced model

1.3.2 Brick

Nine independent parameters, more precisely the Young's moduli E_{LL} , E_{TT} , E_{ZZ} , the Poisson's ratios ν_{LT} , ν_{TZ} , ν_{ZL} , and the shear moduli G_{LT} , G_{TZ} , G_{ZL} , were used to define the stiffness properties of the used clay (see Table 1.6). Kiefer et al. [76] obtained values for E_{ZZ} in experiments on comparable blocks and took them as a basis for calculating the remaining Young's moduli and shear moduli, with the ratios from Bourret et al. [17] as well as Hannawald and Brameshuber [64]. As before, the Poisson's ratios were estimated with the experimentally obtained data from Hannawald and Brameshuber.

For the strength properties Kiefer et al. [76] referred to an extensive series of compressive and bending tensile tests of a comparable block (see Table 1.7). The shear strengths were estimated as the mean values of the results, obtained in Eq. (1.21).

Tab. 1.6: Applied transversally isotropic, elastic properties of the vertically perforated clay blocks [76]

Young's modulus (MPa)			Poisson's ratio			Shear modulus (MPa)		
E_{LL}	E_{TT}	E_{ZZ}	ν_{TZ}	ν_{ZL}	ν_{LT}	G_{TZ}	G_{ZL}	G_{LT}
8738	8738	11 970 (±465)	0.1	0.1	0.1	5509	5509	3972

Values in parenthesis represent the standard deviation.

Tab. 1.7: Applied orthotropic strength properties of the vertically perforated clay blocks [76]

Compressive strength (MPa)			Tensile strength (MPa)			Shear strength (MPa)		
$\sigma_{c,L}$	$\sigma_{c,T}$	$\sigma_{c,Z}$	$\sigma_{t,L}$	$\sigma_{t,T}$	$\sigma_{t,Z}$	$\sigma_{s,TZ}$	$\sigma_{s,ZL}$	$\sigma_{s,LT}$
20.8 ^a	15.0 ^a	21.8 (±1.15)	8.2 ^a	7.0 ^a	9.3 ^a	8.675 ^b	9.7 ^b	8.275 ^b

Values in parenthesis represent the standard deviation.

^a Scaled with ratios, obtained in other experiments (see [76]).

^b Mean value of results obtained with Eq. (1.21).

Tab. 1.8: Applied isotropic, elastic properties of the thin-bed mortar [76]

Young's modulus	E	5000 MPa
Poisson's ratio	ν	0.2

Tab. 1.9: Applied elastic properties of the reinforced mortar joint between the longitudinal webs

Young's modulus (MPa)			Poisson's ratio			Shear modulus (MPa)		
E_{xx}	E_{yy}	E_{zz}	ν_{yz}	ν_{zx}	ν_{xy}	G_{yz}	G_{zx}	G_{xy}
$E_f \cdot f_{f,x}$	$E_f \cdot f_{f,y}$	5000	0.001	0.001	0.001	10	10	10

1.3.3 Mortar

Compressive failure of the mortar bed joint is not considered relevant for the given loading scenario. In the absence of experimental data, Kiefer et al. [76] estimated the elastic properties considering the findings of Vekey [147] as well as Sarhosis and Sheng [134] (see Table 1.8).

While the elastic properties of the uncracked reinforced mortar were homogenized by means of the homogenization scheme presented in Section 1.2.3.1, solely the properties of the fiber mesh were considered in the cracked regions (see Table 1.9). To avoid numerical problems due to changing thickness of the mortar layer, the fiber stiffness was converted to an effective stiffness over the thickness of the mortar layer. Therefore, the lateral Young's moduli were obtained by multiplying the fiber's Young's modulus E_f with the volume fraction in the particular direction, $f_{f,i}$. Since the shear stiffness of the mesh is rather small, compared to the Young's modulus, the shear moduli and Poisson's ratio were set to nearly zero.

1.3.4 Numerical approaches

1.3.4.1 Fixed strength values

For developing a relationship between the volume fraction of the reinforcing mesh and the compressive masonry strength, at first 25 models with different volume fractions were simulated. Hereby, the volume fraction of the glass fibers was increased in steps of 0.25 %, starting at 0 % until reaching 6 %. The allocated strengths for these models were fixed to the mean values, given in Table 1.7.

1.3.4.2 Stochastic allocated strength values

For the stochastic approach, ten models with different strength allocations were randomly generated. Thereby, random strength properties were assigned to each transversal web according to Section 1.2.5. Each model was simulated in three different states: without reinforcement, reinforced with $f_{t,y} = 3\%$, and reinforced with $f_{t,y} = 6\%$. Therefore, 30 models were simulated in total, the results were statistically evaluated afterwards.

1.4 Results and discussion

1.4.1 Fixed strength simulation

Fig. 1.16 shows the developed relationship between the volume fraction of the glass fibers and the compressive masonry strength. While the blue curve denotes the calculated compressive masonry strength, the red dashed curve defines the average compressive stress when the first crack occurred in the model. Thus, the average compressive stress when the first crack occurs increases linearly, which confirms the assumption of decreasing lateral stresses with increasing mortar stiffness. After the first crack occurrence, the models behave differently with varying volume fraction. Until a volume fraction of $f_{t,y} = 1.75\%$, the numerical models failed immediately after the first crack occurred. With higher amounts of reinforcement, the applied load could be increased beyond the first crack loading. Detailed examination of the resulting crack patterns revealed that, with the volume fraction exceeding 2%, the first crack was being held together by the stiffer bed joint. Additionally, the load could be increased, until a second transversal web failed (see Fig. 1.17). Therefore, the reinforced bed joint caused the lateral tensile stresses to distribute more evenly over the block profile.

Comparing the failure mechanisms observed, this is in accordance with Kiefer et al. [76], who showed that the used approach not only serves an accurate prediction of the compressive masonry strength but also allows for identification of the failure mechanism of vertically perforated block masonry: a spalling of the outer longitudinal webs, due to tensile failure of the transversal webs behind.

When a crack forms in the model without reinforcement, the released tensile stresses redistribute mainly to the crack tip, which is why the crack propagates fast. In the reinforced models, the glass fiber mesh takes most of the released stresses; crack propagation is therefore suspended. Nevertheless, the failure mechanism stayed the same.

At the highest modeled volume fraction, the reinforced bed joint enabled a total masonry strength increase of 19.5%.

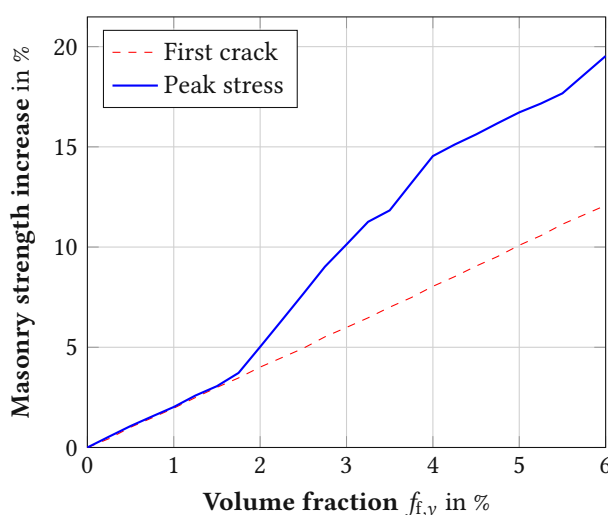


Fig. 1.16: Effect of the glass fiber reinforcement on the vertical compressive masonry strength

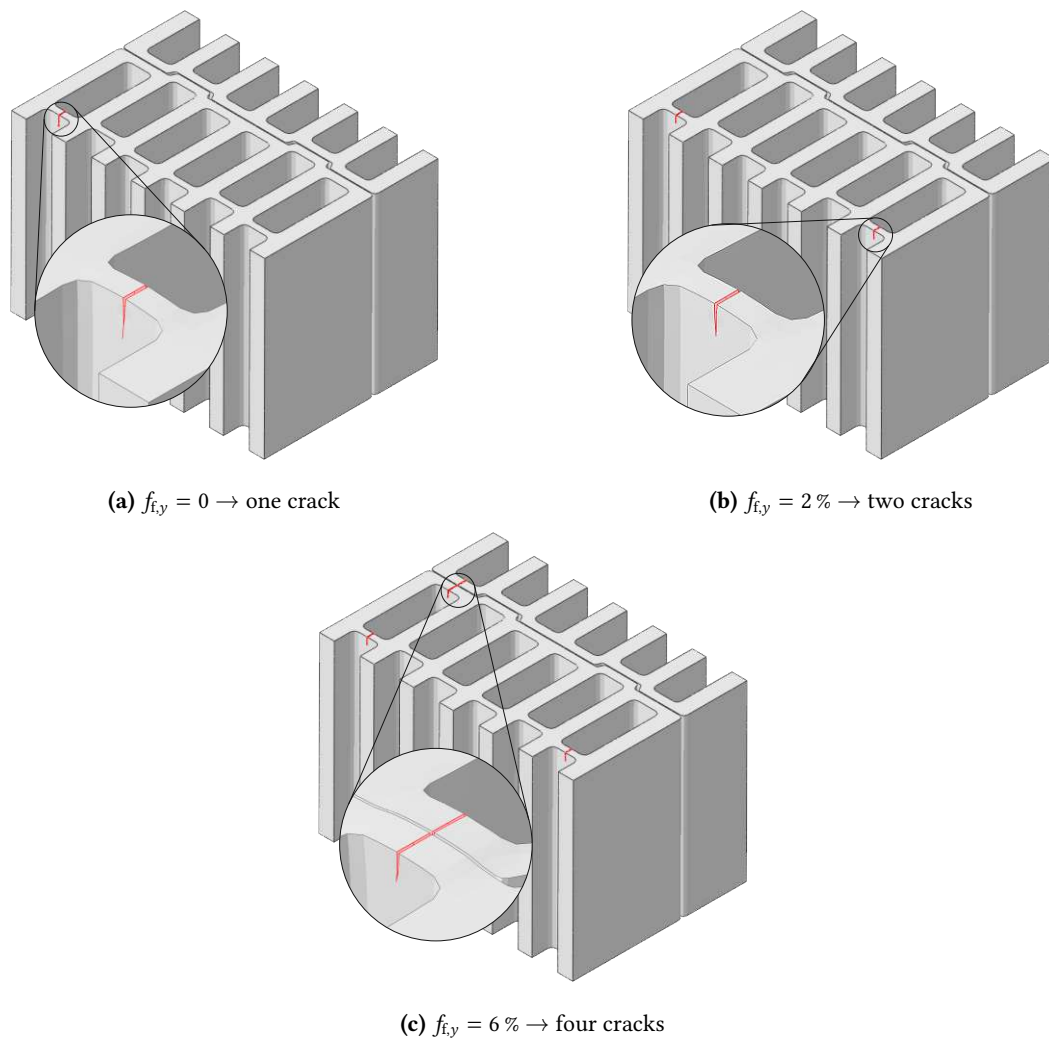


Fig. 1.17: Comparison of the crack pattern at peak stress with different volume fractions $f_{t,y}$. The asymmetric crack pattern originates in asymmetries of the mesh.

1.4.2 Random strength simulation

The location of the first crack could be predicted in the first approach: due to the homogeneous strengths, the web being subject to the greatest tensile stresses is expected to tear apart first. Taking a closer look at the distribution of longitudinal stresses σ_L , the outer webs turn out to be the ones with the highest stresses. Considering the randomly allocated web strengths, such a prediction cannot be made anymore. The results showed that if there was an extremely weak web in the middle of the block, the first crack occurred there (see Fig. 1.18). Interestingly, in cases where the firstly torn web was not one of the outer webs, the loading could be increased after the first crack, even without reinforcement. In each of the ten models, the compressive masonry strength was not reached until at least one of the outer webs contained a crack. Hence, the failure mechanism of the models amounted to the familiar mechanism of vertically perforated block masonry: a spalling of the outer shell.

The randomly generated models consisted of webs with lower strengths than the mean values as well as webs with higher strengths. Therefore, on average the mean clay strength over an individual model amounted to approximately the mean strengths in Table 1.7. However, each of the randomly generated

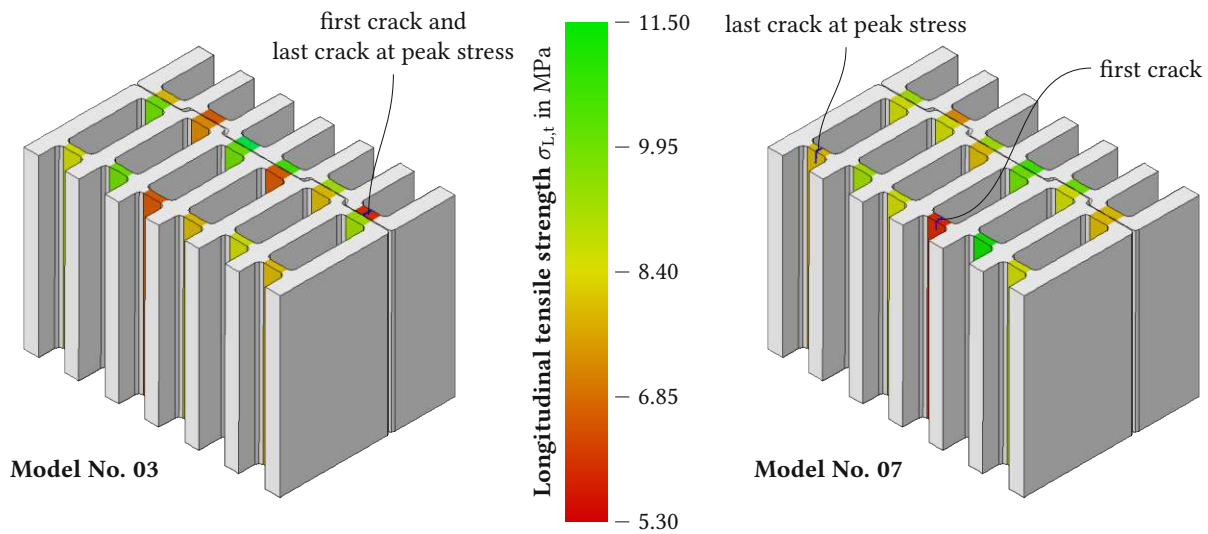


Fig. 1.18: Comparison of the crack pattern at peak stress with different strength allocations on unreinforced models.

models led to a lower compressive masonry strength than with the homogeneously allocated strengths. This illustrates that the webs with strengths below average have a greater effect on the compressive strength than the stronger ones, even though the weakest web alone is not decisive for structural failure.

Fig. 1.19a shows the increase of the compressive masonry strength with the volume fraction. Since the strength increase of each individual model more or less doubled when changing the volume fraction from 3% to 6%, the standard deviation changed in the same manner. The mean value of the strength increase at the highest modeled volume fraction amounted to 28.87%.

Even though the obtained masonry strengths were consistently lower in the randomly generated models, the mean strength increase exceeded the aforementioned by 9%.

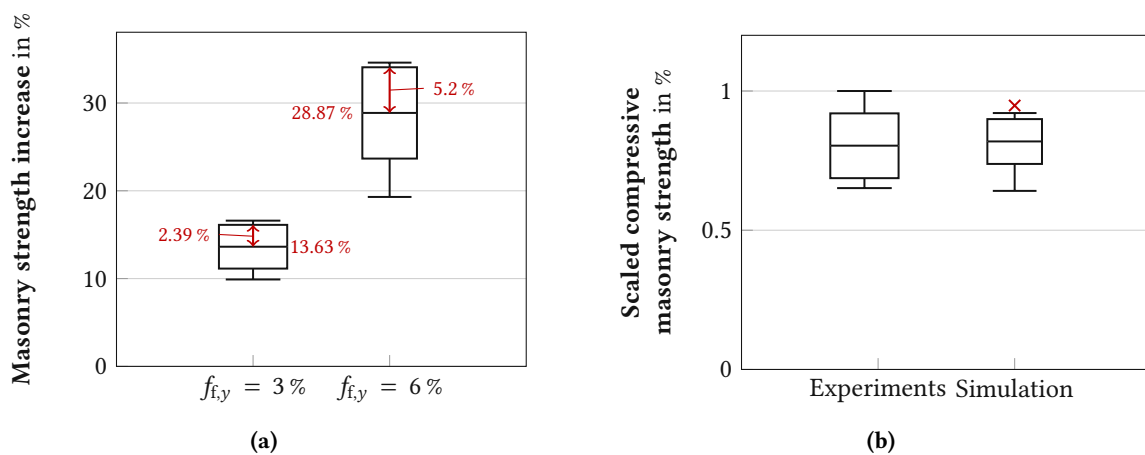


Fig. 1.19: (a) Statistical evaluation of the strength increase and (b) Compressive strengths obtained in experiments on RILEM samples (left box) compared to results using the stochastic simulation approach (right box) and the results according to Kiefer et al. [76] (marked with x). The strength values are scaled to the maximum strength obtained in the experiments.

Fig. 1.19b shows the obtained results with the stochastic simulation approach without reinforcement (right box) in comparison to compressive tests on RILEM samples, using the examined block geometry (left box). While Kiefer et al. [76] accomplished estimating the compressive strength within the fluctuation of the test results (red cross), the stochastic approach reproduces even these fluctuations pretty accurately. The simulated mean value is nearly the same as the mean value obtained in experiments.

1.4.3 Feasible volume fraction

Regarding the maximum feasible volume fraction of reinforcement within the bed joint, one can consider the aforementioned separation of scales (see Eq. (1.23)). Assuming perfectly round fiber strands with a diameter of $1/\alpha$ times the joint thickness, in an orthogonally arranged mesh with a constant mesh width of β times the strand diameter, the volume fraction can be calculated as follows:

$$f_{i,y} = \frac{A_{\text{fiber}}}{A_{\text{joint}}} = \frac{\frac{d^2 \pi}{4} \cdot \frac{l}{a}}{l \cdot h} = \frac{\frac{h^2 \pi}{\alpha^2 \cdot 4} \cdot \frac{l}{\beta \cdot h}}{l \cdot h} = \frac{\pi}{4 \cdot \alpha^2 \cdot \beta}. \quad (1.35)$$

Considering the generally acknowledged values for the separation of scales, α should be at least 1.5 to 3 [40, 122]. Additionally, the mesh width should be great enough, not to separate the mortar joint into two layers. Hence, a mesh width three times greater than the fiber strand diameter seems to be reasonable. Using 2 for α and 3 for β in Eq. (1.35), the maximum volume fraction results in 6.54 %.

Concludingly, the simulated volume fraction of 6 % seems to be reasonably attainable with an embedded glass fiber mesh. Therefore, the 5 %-quantile of the compressive masonry strength could reach an increase of over 33 % (see Table 1.10).

Tab. 1.10: Comparison of the fixed value and random value strength increase

	Volume fraction $f_{i,y}$ (%)		
	0	3.0	6.0
Fixed values			
increase	—	10.1	19.5
Statistically allocated values			
Mean value increase	—	13.63	28.87
5 %-quantile increase	—	15.28	33.81

1.5 Conclusion

Within the present work, a numerical approach for estimating the effect of glass fiber-reinforced bed joints on the vertical compressive strength of vertically perforated clay block masonry was developed. Based on the presented research, the following conclusions could be drawn:

- Glass fiber reinforced bed joints enable a significant increase in the vertical compressive strength of perforated clay block masonry. The compressive masonry strength increase can be split up into two mechanisms:
 - the *first crack occurring at a higher load*, due to the decrease of lateral tensile stresses, and
 - the *onset of cracking arising at a higher load*, as the fiber mesh bridges the open crack.
- The reinforcement within the mortar layer prevents the outer shell from spalling, after the first cracks occur, thereby yielding a more ductile damage behavior.
- Weaker webs within the block affect the vertical compressive strength, which is why the approach from Kiefer et al. [76] tended to overestimate the test results. Nevertheless, considering the fluctuation of test results and the high effort for stochastic calculations, their approach seems to be sufficient to reasonably estimate masonry strengths.

Besides numerous advantages of glass fiber reinforced bed joints (such as the increase of ductility, weather protection during construction, or a continuous mortar layer), the conducted simulations reveal the potential of bed joint reinforcement in raising the compressive masonry strength. While the potential for optimization is exhausted in modifying the block geometry, bed joint reinforcement could be a possible approach for increasing the masonry strength further. Even for already existing block geometries, the approach could enable a significantly higher vertical compressive strength with relatively low effort. Thereby, it is necessary to emphasize that the presented compressive strength increase of vertical perforated clay blocks originates in numerical simulations with complex modeling strategies, which were solely validated by experiments on solid brick masonry pillars. Hence, to check the significance of these results, a series of experiments on vertically perforated clay block masonry is necessary.

By use of the presented unit cell approach, arbitrary loading states on masonry walls can be investigated apart from uniaxial compression. Therefore, the effect of a reinforced bed joint on the load-carrying capacity in shear or bending scenarios could be estimated. For these reasons, the presented approach constitutes a significant contribution to the potential assessment of fiber-reinforced bed joints.

Acknowledgements

The authors gratefully acknowledge the financial support of the Austrian Research Promotion Agency (FFG, project number 865067) and the industry partner Wienerberger for funding the research work within the project “Innovative Brick 2”. Furthermore, the authors acknowledge TU Wien Bibliothek for financial support through its “Open Access Funding Programme”.

Publication 2

The performance of vertically perforated clay block masonry in fire tests predicted by a finite-element model including an energy-based criterion to identify spalling

Authors Raphael Reismüller, Markus Königsberger, Andreas Jäger, Josef Füssl

Published in *Fire Safety Journal*, 135 (2023) 103729

DOI <https://doi.org/10.1016/j.firesaf.2022.103729>

Abstract

Fire tests on masonry are one of the most expensive experiments in developing new vertically perforated clay block geometries. Numerical simulations might be a reasonable substitute for such experiments, leading to a significant cost reduction in the development phase. However, the prediction of such tests with numerical modeling concepts is challenging due to large temperature and stress gradients, highly non-linear material effects, and the complex geometry of the blocks. Herein, we present a finite-element-based concept, including thermal and mechanical simulations, a unit-cell approach, a smeared damage model, and a novel energy-based spalling criterion to describe the structural and material behavior of a masonry wall in a fire experiment. We could predict the obtained spalling times of longitudinal webs and the total endurance of a masonry wall without any empirical fitting parameters in good agreement with experimental data. These results show that we can use our modeling approach for simulating such fire tests, enabling a much cheaper and more efficient development of block geometries.

2.1 Introduction

Fired clay block masonry obtains its strength and stiffness through a controlled firing process of the main constituents: the blocks. Nevertheless, fire poses a crucial impact on the load-carrying capacity of fired clay block masonry. Therefore, elaborate experiments are necessary to predict how resilient a masonry wall is to fire. These large-scale experiments are time-consuming, require special testing equipment, and, therefore, are costly. A review of different testing methods under fire was recently published by Daware and Naser [31].

The rapid advancements in computational methods and the increasing performance of modern computers allow the simulation of complex and highly non-linear problems in a reasonable amount of time. Hence, shifting the current procedure from these elaborate experiments to simulations seems obvious. However, these experiments are compulsory to obtain a certain level of product certification according to EN 13501-2 [45]. Nonetheless, simulations seem to be a reasonable substitute for the experiments when comparing different block designs before bringing the best one to certification.

A growing group of scientists is trying to advance research considering the simulation of masonry under elevated temperatures. Kumar and Srivastava [80] published a comprehensive review of numerical models for structural frames with masonry infills in case of fire. Different approaches for solid block masonry exist using two-dimensional models [105, 124], or three-dimensional models [79, 117].

Another set of publications is dedicated to hollow block masonry made out of concrete or fired clay. Again there are two-dimensional approaches [106] as well as three-dimensional approaches [32, 108, 112, 116]. Especially in Central Europe, vertically perforated clay block masonry is used extensively, particularly in residential buildings. Such vertically perforated clay blocks have a void pattern formed by orthogonally oriented webs. These webs can be divided into two groups according to their orientation: *longitudinal webs* are oriented parallel to the wall surface; *transversal webs* are oriented orthogonal to the wall surface (see Fig. 2.1). To our knowledge, the approach introduced by Nguyen and Meftah [112] is currently the only published model which covers the requirements for this kind of masonry. In a three-dimensional coupled temperature-displacement finite-element analysis, they simulated four full-scale fire experiments with good agreement of the temperatures and displacements. Nguyen and Meftah thoroughly investigated the mechanisms driving the failure of vertically perforated clay block masonry in fire experiments and identified the progressive spalling of the longitudinal webs as the most relevant [111, 113]. This mechanism refers to the detachment of parts of the masonry wall, which leads

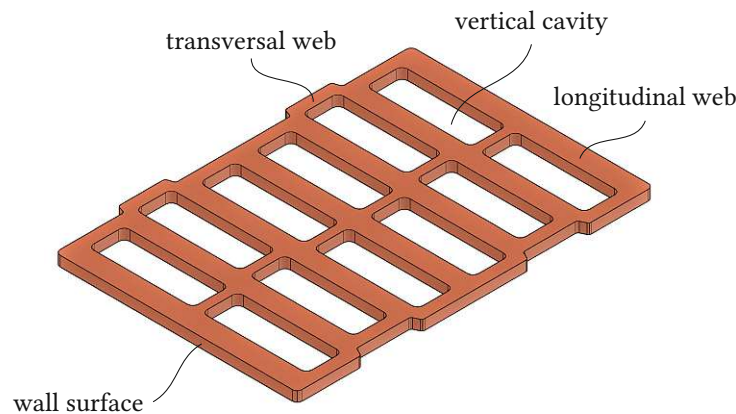


Fig. 2.1: Parts of a vertically perforated clay block.

to a decreasing wall thickness. With vertical loads present, spalling is accompanied by an increasing load eccentricity, which introduces significant bending moments. In their studies, they suggested three mechanisms driving spalling:

- detachment of longitudinal webs due to tensile cracks at the intersection between longitudinal webs and transversal webs,
- buckling of longitudinal webs due to compressive stresses, and
- crushing of longitudinal webs due to a network of compressive cracks.

Therefore, they proposed a spalling criterion based on a maximum stress condition and plate buckling equations and introduced it to their finite-element framework.

Especially the first mechanism, i. e. the interaction between transversal and longitudinal webs, is essential for the mechanical behavior in fire situations for the following reasons: In the case of a fire, the longitudinal web closest to the fire gets heated up. This increase in temperature causes a significant increase in strains. Since the temperature in the second longitudinal web increases delayed to the first one, these two webs show a difference in temperature-induced strains. These strains would not induce any stresses in an internally static determinate system, but this is not the case with a typical block design. Some design features, such as the type of head joint, the masonry bond, and the transversal webs, restrict the thermally-induced strains, inflicting stresses in different regions of the block.

In the case of fire, the mentioned strain difference of the longitudinal webs induces significant stresses in the transversal webs, which will start failing at some point. As soon as a certain amount of transversal webs has failed, the outermost longitudinal web spalls due to the vertical loading [111]. As more and more longitudinal webs fail, the eccentricity of the vertical load increases until the whole wall collapses eventually.

While the model of Nguyen and Meftah [112] can simulate a fire experiment with good results, we wanted to take a more detailed look at the stresses and damage appearing in the blocks, requiring a finer mesh. Especially when comparing different block designs or optimizing a product, these details can be essential. Since Nguyen and Meftah [112] modeled an entire wall specimen, a finer mesh would lead to exploding computation times. Therefore, we used a *unit-cell approach* to model only a small representative part of the specimen with *periodic boundary conditions*. The saved computational expense could be reinvested in more detailed meshing and sophisticated non-linear material models. Unfortunately, the overall deformation of the wall cannot be obtained using this approach. Since the model published by Nguyen and Meftah [112] already does a great job in calculating the deformations, the main aim of our study should be in another field of interest: the estimation of the endurance of load-bearing vertically perforated clay brick masonry in fire situations with a focus on the stress and strain fields, as well as damage in the cross-section.

Thus, the outline of the work can be summarized as follows: First, we created a two-dimensional transient thermal finite-element model to simulate the non-linear heat transfer in a wall made of vertically perforated clay block masonry. Secondly, we defined a novel *energy-based spalling criterion* to predict the failure of the wall in terms of spalling of longitudinal webs. Then we applied the nodal temperatures gained from the thermal model to a two-dimensional mechanical finite-element model. Using *Concrete Damaged Plasticity (CDP)*, a *unit-cell approach* with *periodic boundary conditions*, and the *energy-based spalling criterion*, this model was able to reproduce the behavior of a masonry wall in a standard fire test, without using any empirical fitting parameters. We also used a three-dimensional

mechanical finite-element model to observe the stresses introduced by the vertical loading applied in the experiment. Given the model's high level of detail, the proposed approach provides unique insights into the behavior of fired clay block masonry in fire situations.

Section 2.2 contains a short description of the used experiments. An overview of the applied modeling strategies, the numerical model, and the used material properties is provided in Section 2.3. Afterward, the results are explained and discussed in Section 2.4, followed by conclusions to these results in Section 2.5.

2.2 Fire experiments on vertically perforated clay block masonry

2.2.1 Test setup

The tested masonry wall specimen was seven blocks high and six blocks wide, resulting in an approximately 3.00 m high and 3.00 m wide specimen (see Fig. 2.2a). This specimen was placed in a concrete frame with gaps on the left and right sides; these gaps were then filled with insulation. The blocks were connected by thin-bed mortar in the horizontal joints. The two adjacent blocks were in contact in the vertical joints, but no mortar was used. The blocks themselves had a thickness of 200 mm with the void pattern shown in Fig. 2.2b. While the *unexposed* side was plastered, the *fire-exposed* side was covered with 120 mm expanded polystyrene (EPS) and a 13 mm gypsum plasterboard.

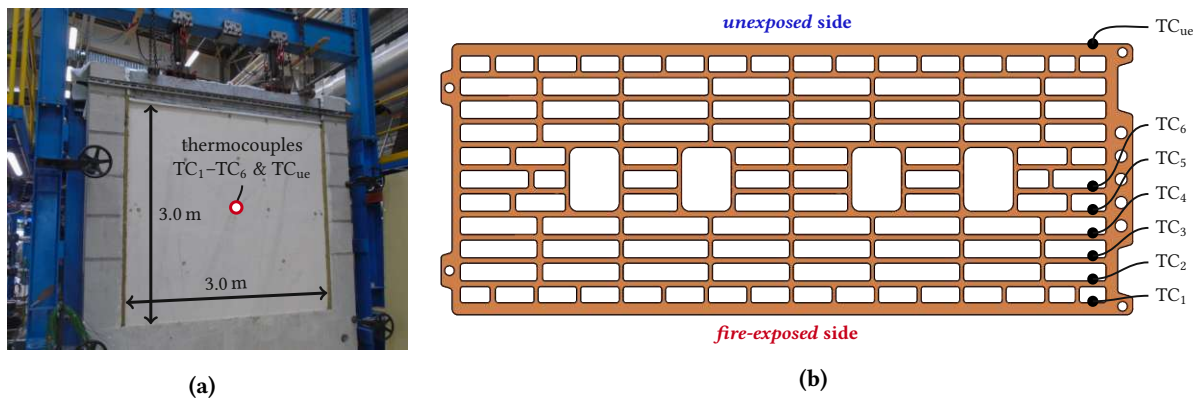


Fig. 2.2: Masonry specimen (a) subjected to vertical compressive load. The Block geometry (b) is composed of many slender webs. The seven thermocouples (TC) relevant for the simulations were sitting in six adjacent cavities and on the *unexposed* side, all located in the center of the wall.

Thermal and mechanical loads were applied, as described next. The wall was subjected to vertical compressive loads amounting to 130 kN/m (load-controlled application using hydraulic presses), which corresponds to approximately 10 % of the compressive masonry strength. This load was applied to a loading bar resting on top of the specimen and kept constant throughout the experiment. An additional construction guided the loading bar to minimize out-of-plane deformations (see Fig. 2.2a). The plasterboard side of the wall faced a furnace in which the temperature was increased according to the temperature curve in EN 13501-2 [45] (similar to the curve in ISO 834-1 [70]) reading as

$$T_{\text{furnace}} = 345 \cdot \log_{10}(8t + 1) + 20, \quad (2.1)$$

with the time t starting at the beginning of the experiment (see also Fig. 2.3).

The temperature was monitored at multiple locations, i. e. the furnace, the cavities, and the unexposed face of the wall. The thermocouples relevant to the simulations were positioned along the thickness direction inside six different adjacent cavities of the block and on the unexposed side, all located in the center of the wall (see points labeled TC₁ to TC₆ as well as TC_{ue} in Fig. 2.2).

2.2.2 Test results: temperature evolutions and spalling times

The moment when the plasterboard fell off and the EPS burned down, i. e. the moment when the blocks were exposed to the thermal load, was considered the actual start of the test for the simulations, indicated by $t = 0$. The times referred to are always shown in relation to the total time, i. e. $\tau = \frac{t}{t_{\max}}$. While the temperature did not increase significantly on the unexposed side of the wall (see thermocouple TC_{ue} in Fig. 2.3), the temperature in the cavities increased in sequential fashion (see Fig. 2.3) due to sequential spalling of the longitudinal webs. After spalling of the first web, a rapid increase of the temperature T_{TC1} in the outermost cavity could be observed, quickly followed by a similarly rapid increase of T_{TC2} . The temperature T_{TC3} increased significantly only after roughly $\tau = 0.116$, the increase for temperature T_{TC4} became significant around $\tau = 0.290$. The temperature in the fifth outermost cavity T_{TC5} increased significantly only after roughly $\tau = 0.362$, but the increase was already less sharp. The temperature T_{TC6} remained below 120 °C, even after $\tau = 1.0$, when the wall finally collapsed.

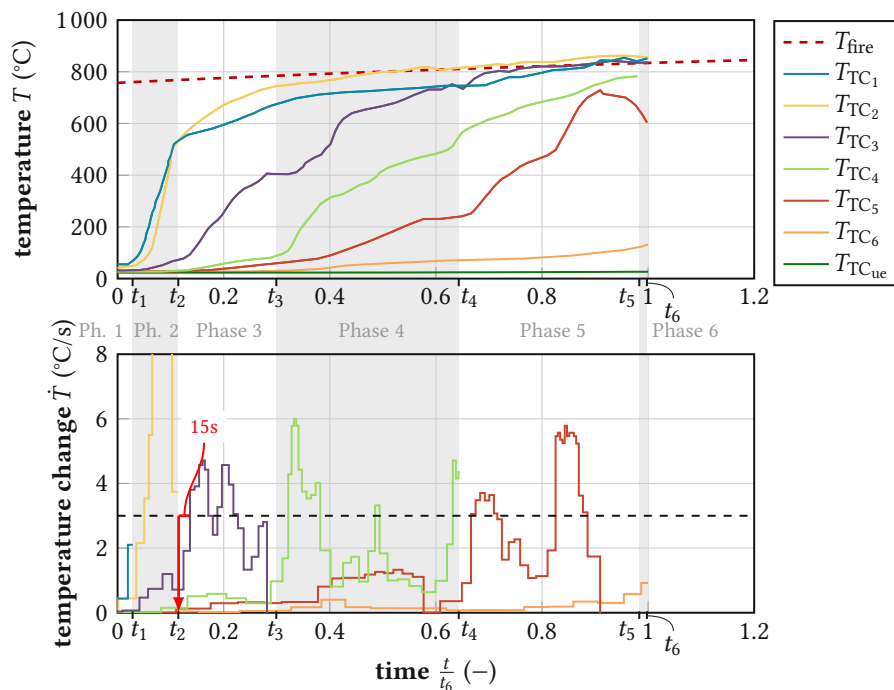


Fig. 2.3: Evolution of cavity temperatures T_i (top) and evolution of temperature change \dot{T}_i (bottom). The spalling times t_i for each phase were estimated 15 s before the temperature change reached 3 °C/s, as shown for t_2 . The respective curves are cut off as soon as a thermocouple is considered exposed to the furnace temperature. The furnace temperature T_{fire} was derived according to EN 13501-2 [45] as well as ISO 834-1 [70].

Deformations towards the furnace could be observed, with a maximum value at approximately $\frac{1}{3}$ of the specimen height. These deformations can be traced back to the material expansion at the fire-exposed side in combination with the boundary conditions and are already well-documented in literature (e. g. Nguyen and Meftah [111], Prakash et al. [124]). According to these publications, the bottom edge can be considered as clamped, which leads to bending moments in the wall. From the center of the wall downward, these bending moments yield vertical compressive stresses on the fire-exposed side, causing the most severe degradation of the blocks at these locations. Therefore, we used the thermocouples located in the center for evaluating the results and validating the numerical model.

As discussed next, we estimated the times when the longitudinal webs spalled in the experiment from the cavity temperature gradients (Fig. 2.3). This spalling time t_i of the longitudinal web i was estimated by the sharp increase of the temperature derivative in the next cavity measured with thermocouple TC_{i+1} . Since the mass of the heated longitudinal web delays the temperature increase in the cavity behind, spalling was considered to occur 15 s before the temperature change reached 3°C/s (the dashed line indicates this threshold in Fig. 2.3). For t_5 , this criterion could not be applied since the temperature change of thermocouple TC_6 stayed below this threshold. Given the increasing gradient of T_{TC_6} at the end of the experiment, t_5 was chosen 10 s before t_6 , where the wall collapsed. The estimated spalling times are summarized in Table 2.1, and they were used to divide the experiment into seven Phases (0 to 6), which are dealt with individually in the following modeling section. Notably, these times were solely used for validating the thermal modeling strategies; in the simulations, an energy-based criterion was used to obtain spalling times from a mechanical finite-element model.

Tab. 2.1: Subdivision of the experiment into seven Phases according to the experimentally observed spalling times.

Phase 0		Start of the experiment, wall loaded with 130 kN/m
_____	$\tau_0 = \frac{t_0}{t_6} = 0.000$	Gypsum plasterboard came down, EPS burned down, block surface exposed to fire
Phase 1		
_____	$\tau_1 = \frac{t_1}{t_6} = 0.028$	First longitudinal web spalled, second web exposed to fire
Phase 2		
_____	$\tau_2 = \frac{t_2}{t_6} = 0.115$	Second longitudinal web spalled, third web exposed to fire
Phase 3		
_____	$\tau_3 = \frac{t_3}{t_6} = 0.300$	Third longitudinal web spalled, fourth web exposed to fire
Phase 4		
_____	$\tau_4 = \frac{t_4}{t_6} = 0.645$	Fourth longitudinal web spalled. fifth web exposed to fire
Phase 5		
_____	$\tau_5 = \frac{t_5}{t_6} = 0.986$	Fifth longitudinal web spalled, sixth web exposed to fire
Phase 6		
_____	$\tau_6 = \frac{t_6}{t_6} = 1.000$	Wall collapsed

2.3 Numerical modeling

2.3.1 Sequential spalling and associated modeling phases

The sequential spalling of the longitudinal webs leads to a geometry change and a corresponding change in the boundary conditions. Hence, the numerical modeling of the fire experiment was divided into seven phases introduced in Table 2.1. Note that the spalling times obtained from the experiment were not used for the numerical model (except for validating the 2D thermal model in Section 2.4.1). Instead, an energy-based spalling criterion was used to obtain a spalling time for each phase of the numerical model. Phase 0 was considered irrelevant for the model since the cavity temperatures remained very low due to the thermal insulation provided by the intact EPS cover (see Section 2.2). As for Phase 1, the initial block geometry was used. In Phase 2, the first longitudinal web and all transversal webs in the first cavity were removed (Fig. 2.4), leading to the exposure of the second longitudinal web to the fire. This strategy was extended to all following phases until Phase 6, where the first five longitudinal webs and the corresponding parts of the transversal webs were removed.

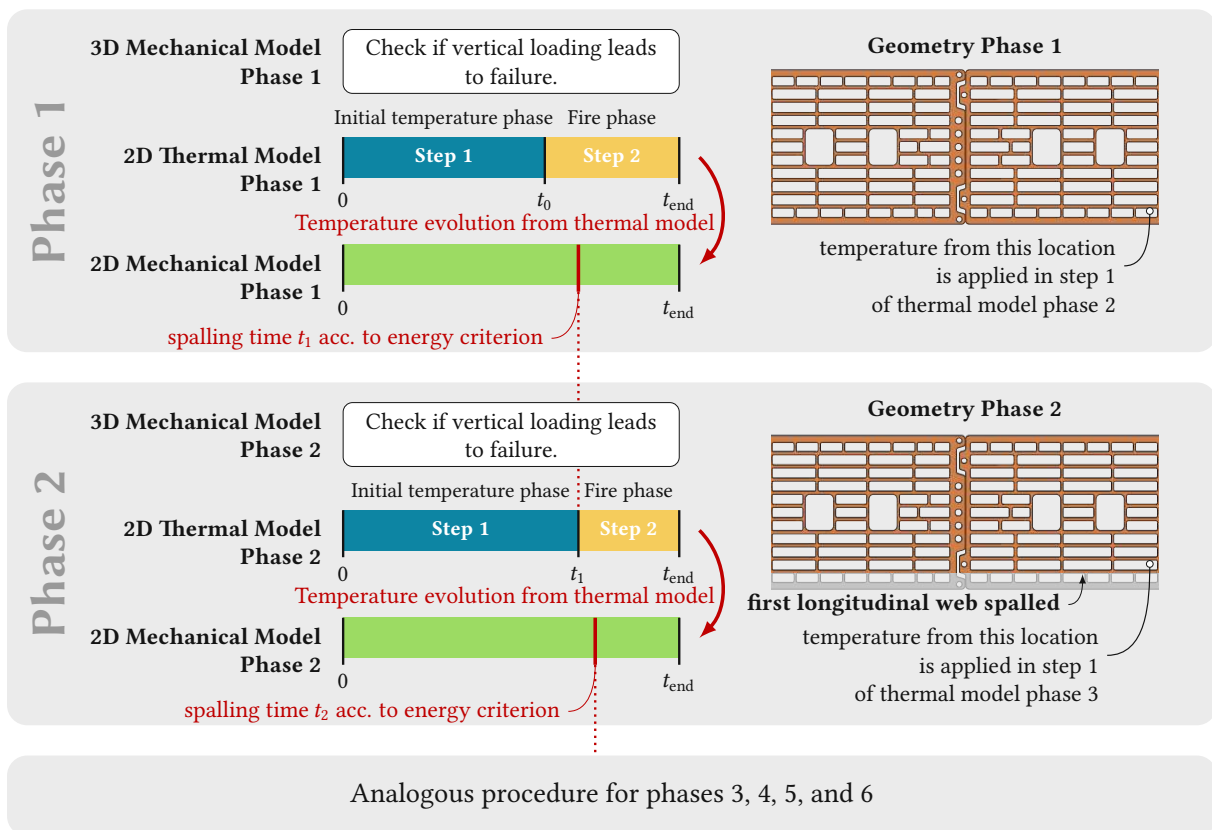


Fig. 2.4: Overview of the sequential procedure for modeling the six-phase fire experiment (Phases 1 to 6, experimental Phase 0 is omitted): Each phase consists of an elastic 3D mechanical model, a two-step 2D thermal, and a 2D mechanical model. The nodal temperatures obtained in the thermal model of Phase i were imposed on the mesh of the corresponding mechanical model of Phase i . The spalling time predicted in the mechanical model of Phase i sets the duration of the steps in the thermal model of the subsequent Phase $i + 1$.

2.3.2 Decoupling of fire loading from vertical loading and corresponding unit-cell models

Previous fire experiments of masonry without vertical loading, see e.g. Nguyen and Meftah [111], indicate no spalling of longitudinal webs and no wall failure until the end of the experiment but significant cracking in transversal webs. In contrast, tests with vertical loading, like the test presented in Section 2.2, show prevalent spalling of longitudinal webs after the cracking of the adjacent transversal webs. Notably, the sequential spalling of the webs introduces an eccentricity of the vertical loading (see Fig. 2.6b), which leads to bending moments in the wall and thus to additional vertical stresses, which eventually lead to the collapse of the whole structure.

For both loaded and unloaded walls, failure of transversal webs due to temperature-induced stresses is crucial and was tackled in the first step, independently from the vertical loading. A two-dimensional finite-element model was used to solve two main problems: (i) to predict the transient temperature field in the brick wall for each phase of the fire test and (ii) to model the cracking of transversal webs due to temperature-induced stresses leading to spalling of the longitudinal webs. Notably, the modeling of the transient temperature field within a single phase is, in good approximation, *independent* of the mechanical solution since the deformations were generally small compared to the size of the structure and since stresses have no effect on the thermal properties of the materials. Therefore, the sub-problems mentioned above could be solved individually: A 2D thermal model was used to obtain the temperature field (Section 2.3.3), which was then applied to a 2D mechanical model (Section 2.3.4) to predict the stress field and eventually the spalling (see Fig. 2.4). The vertical loading and the load eccentricity were then considered separately within a 3D finite-element model (Section 2.3.5). Although three different FE models in each phase are necessary for this approach, the decoupling is still more efficient than a single 3D coupled approach with a similar mesh and material behavior.

A unit-cell approach was adopted to minimize the computational effort. In more detail, the 2D unit-cell exhibits a length of a single brick and contains two halves of the brick connected by a central joint (see Fig. 2.5). The corresponding 3D unit-cell is two blocks high and one block wide (see Fig. 2.6a) and is based on a recently developed FE model for failure of masonry Kiefer et al. [76].

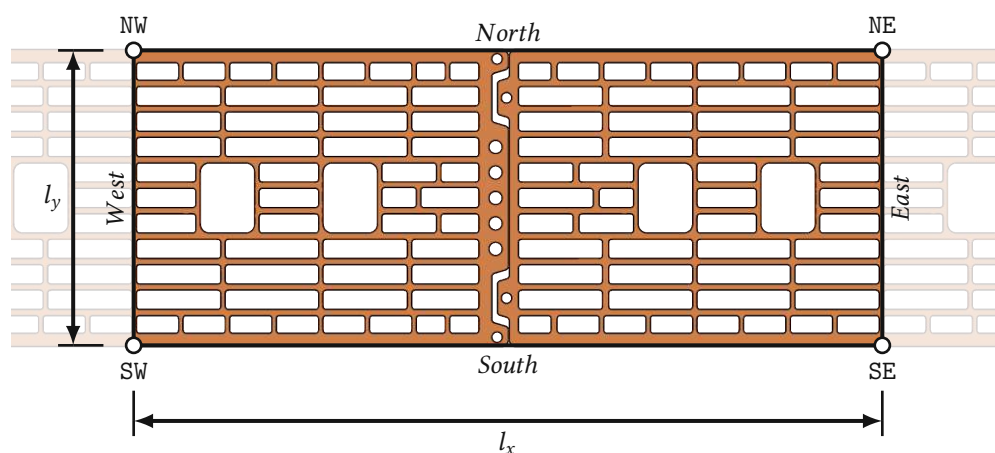


Fig. 2.5: Two-dimensional unit-cell model. The edges of the model were named North, East, South, and West; the Vertices were named after the edges intersecting in the particular vertex.

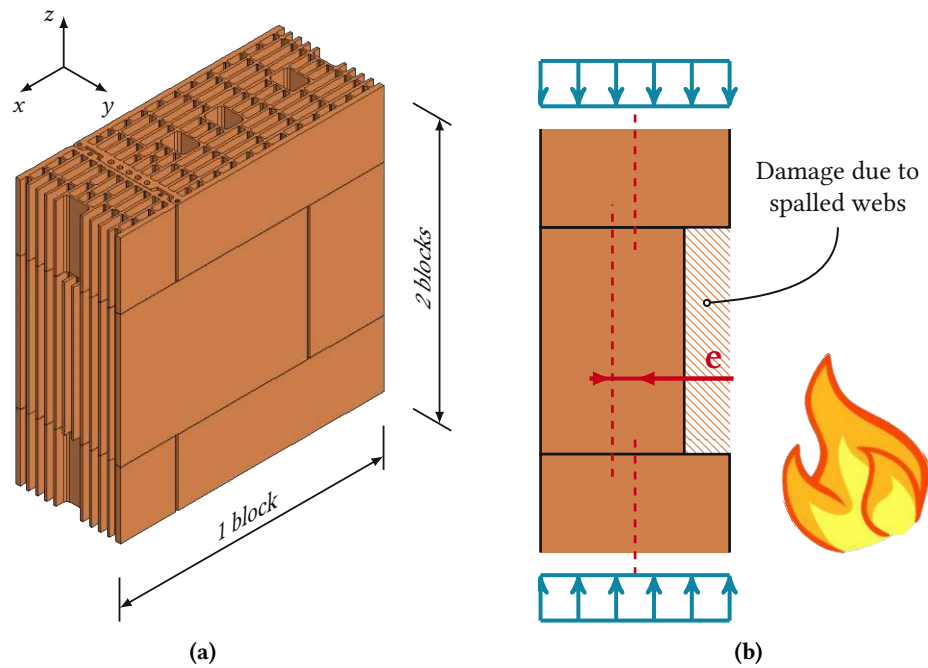


Fig. 2.6: Three-dimensional mechanical finite-element model (a) and load eccentricity (b), which is introduced by the spalling longitudinal webs.

2.3.3 Two-dimensional transient thermal finite-element model

2.3.3.1 Strategy, mesh, and boundary conditions

A two-dimensional transient thermal finite-element simulation was performed in the FE software Abaqus to identify the temperature field over the entire duration of the experiment. Thereby, both the solid clay parts and the air-filled cavities were considered in the model. For the latter, a temperature-dependent effective thermal conductivity was introduced to model convective and radiant heat transfer. Conductive heat transfer can be described by the heat conduction equation, which reads as

$$(\rho \cdot c_p) \cdot \dot{T} - \nabla(\lambda \cdot \nabla T) = 0, \quad (2.2)$$

with the mass density ρ , the heat capacity c_p , the temperature T , and the thermal conductivity tensor λ [8]. In the case of isotropic conductivity, the thermal conductivity tensor is formed by multiplying the thermal conductivity λ with the identity matrix \mathbf{I} .

Each thermal model consists of two loading steps (see Fig. 2.4). In both steps, adiabatic boundary conditions were applied on the East and West side of the model. On the “unexposed” side of the model (North), the temperature was fixed at 21 °C in both steps. To recreate the temperature and heat flux field at the end of the previous Phase $i - 1$ in Phase i , the temperature T_{TCi-1} (see Fig. 2.2) was applied on the *fire-exposed* side of the model (South) in the first step. In the second step, the furnace temperature according to Eq. (2.1) [45, 70] was applied directly on the fire-exposed side of the model. The boundary conditions can be found in Fig. 2.7. The finite-element models consist of 14 676 to 29 183 three-node and four-node linear diffusive heat transfer elements (DC2D3 and DC2D4, respectively), see Fig. 2.7.

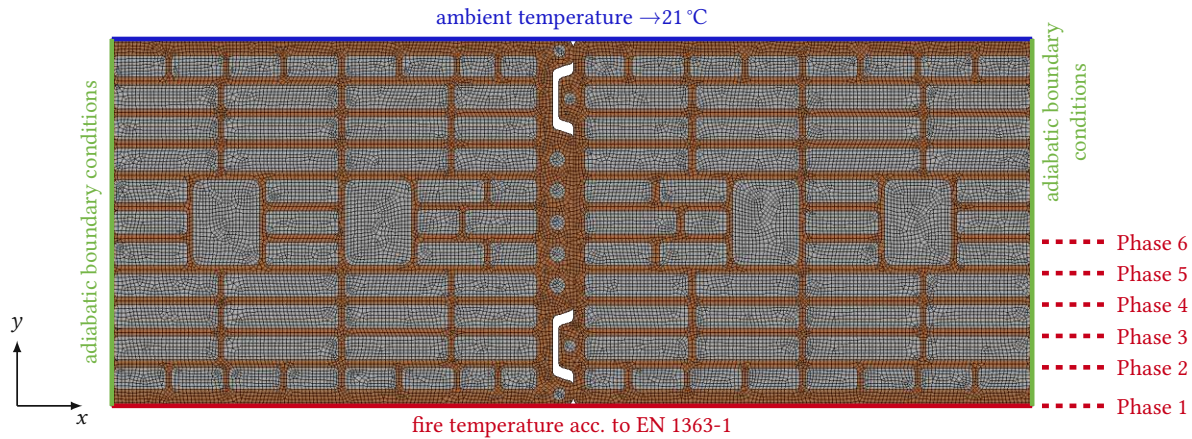


Fig. 2.7: The two-dimensional thermal finite-element model for the first experimental phase (all webs intact) with the imposed boundary conditions. The dashed lines indicate where the geometry was cut for later phases and, therefore, where the fire temperature was applied.

2.3.3.2 Thermal properties of fired clay

The mass density of the fired clay in the experiments was $\rho_c = 1575 \text{ kg/m}^3$ and was considered to be temperature-independent, see also Table 2.2. In contrast to the mass density, the thermal conductivity and specific heat were considered temperature-dependent [1, 113]. At room temperature, they amount to $\lambda_c = 0.42 \text{ W}/(\text{m} \cdot \text{K})$ (calculated according to EN 1745 [46]) and $c_{p,c} = 876 \text{ J}/(\text{kg} \cdot \text{K})$ [112]. From steady-state heat flow experiments on hollow clay blocks, Nguyen et al. [113] estimated a relatively constant thermal conductivity of approximately $300 \text{ }^\circ\text{C}$ followed by a linear decrease to 39 % of the initial value at $800 \text{ }^\circ\text{C}$. However, calculating the thermal conductivity from measurements on the mass density, the specific heat, and the thermal diffusivity, AIT [1] obtained a nearly linear decrease of the thermal conductivity up to $400 \text{ }^\circ\text{C}$. A linear decrease from 21 to $800 \text{ }^\circ\text{C}$ was used for the numerical simulations (see Fig. 2.8a), considering these observations. Notably, running the model with both evolutions suggested in the literature led to nearly identical temperature results.

The specific heat of fired clay increases slightly with increasing temperature [1], whereby a significant peak is considered around $100 \text{ }^\circ\text{C}$ (see Fig. 2.8b). Using this relation, we followed the suggestions in the EN 1996-1-2 [47] standard, and the modeling strategies adopted by Nguyen et al. [113] for clay blocks as well as Prakash et al. [124] for concrete blocks (see Fig. 2.8b). The corresponding increase, $\Delta c_{p,c}^{\text{peak}} = 2825 \text{ J}/(\text{kg} \cdot \text{K})$, results from the evaporation of water bound in the pores of the brick and is obtained from the brick's water content $\omega_c = 1.25 \%$ as [113]:

$$\Delta c_{p,c}^{\text{peak}} = \frac{2 \cdot \omega_c \cdot H_{\text{vap}}}{\Delta T_{\text{peak}}} \quad (2.3)$$

with the latent heat of vaporisation of water, $H_{\text{vap}} = 2260 \text{ kJ/kg}$, and with $\Delta T_{\text{peak}} = 20 \text{ K}$ as the temperature interval for the peak. This way, the heat capacity at $100 \text{ }^\circ\text{C}$ is approximately four times higher than the initial value (see Fig. 2.8b).

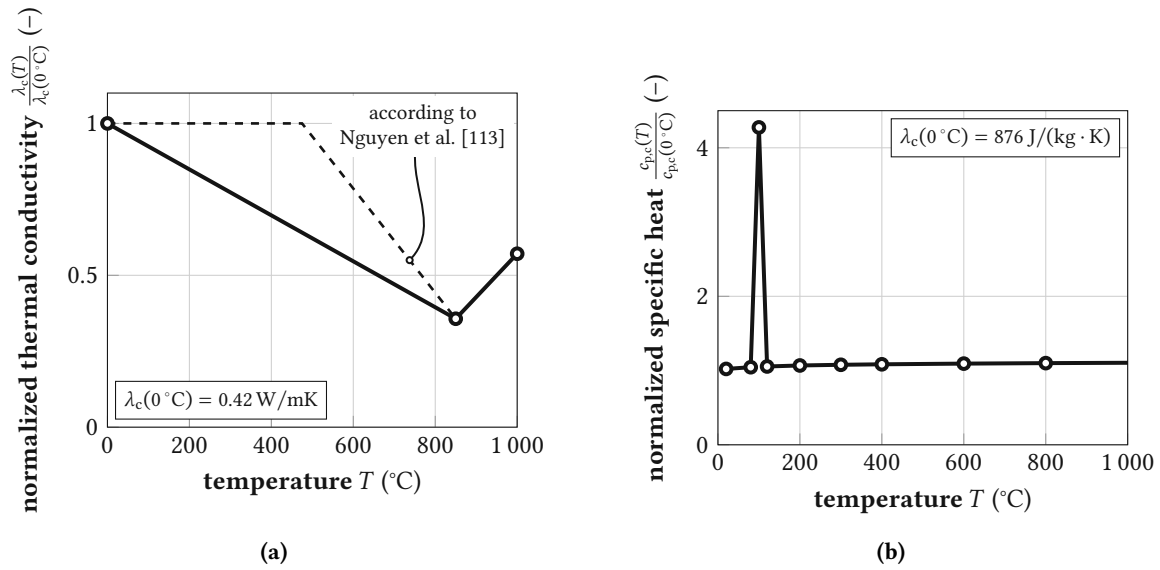


Fig. 2.8: Temperature-dependent thermal properties of fired clay used in the finite-element model: (a) thermal conductivity from a combination of results from [1], and [113], (b) specific heat according to [113].

Tab. 2.2: Thermo-mechanical properties of air, fired clay, and mortar at $T_{\text{ref}} = 21^\circ\text{C}$.

Air		temp.-dep.	Reference
Mass density ρ_a	1.2 kg/m ³	✓	Fig. 2.10e, [146]
Specific heat $c_{p,a}$	1007 J/(kg · K)	✓	Fig. 2.10d, [146]
Thermal cond. λ_a	0.024 W/(m · K)	✓	Fig. 2.10c, [146]
Kin. viscosity ν_a	$1.59 \times 10^{-5} \text{ m}^2/\text{s}$	✓	Fig. 2.10a, [146]
Dyn. viscosity η_a	$1.82 \times 10^{-5} \text{ kg}/(\text{m} \cdot \text{s})$	✓	Fig. 2.10b, [146]
Fired clay		temp.-dep.	Reference
Mass density ρ_c	1575 kg/m ³	×	-
Specific heat $c_{p,c}$	876 J/(kg · K)	✓	Fig. 2.8b, [113]
Thermal cond. λ_c	0.42 W/(m · K)	✓	Fig. 2.8a, [1, 113]
Emissivity ε_c	0.9	×	[82, 112]
CTE $\alpha_{T,c}$	$8 \times 10^{-6} \text{ T}^{-1}$	✓	Fig. 2.15b, [6]
Young's mod. E_c	10 220 MPa	✓	Fig. 2.15a, [76, 113]
Poisson's ratio ν_c	0.2	×	[76]
Tensile strength $\sigma_{f,t,c}$	7.5 MPa	×	Fig. 2.13a, [76, 145]
Comp. strength $\sigma_{f,c,c}$	27.6 MPa	×	Fig. 2.13b, [76]
Mortar		temp. -dep.	Reference
Young's mod. E_m	5000 MPa	×	[76]
Poisson's ratio ν_m	0.1	×	[76]

2.3.3.3 Heat transfer in the cavities – Conduction, convection, and radiation

Heat transfer is driven by three mechanisms: *conduction*, *convection*, and *radiation*. While conduction dominates in solids, convection and radiation are decisive in gases.

Neither convective nor radiant heat transfer in the air cavities was modeled directly. Instead, we considered convection and radiation through an effective conductivity, $\lambda_{\text{eff,rad}}$ and $\lambda_{\text{eff,conv}}$ respectively, as this is often done when calculating the thermal resistance of ventilated air-spaces behind façades [125]. Adding these quantities to the thermal conductivity λ_a leads to an overall effective conductivity λ_{eff} ,

$$\lambda_{\text{eff}} = \lambda_a + \lambda_{\text{eff,rad}} + \lambda_{\text{eff,conv}}, \quad (2.4)$$

which was used in Abaqus within a purely conductive transient heat transfer simulation based on Eq. (2.2). This strategy comes with an inaccuracy compared to the “real” problem. However, we also wanted the same model to be fit for simulating clay block masonry with insulation-filled cavities. In a comparative analysis, the temperature distributions only varied by a maximum of 20 °C

The effective radiant heat transfer is dealt with first. Since the heat flow in the given problem is nearly one-dimensional (i. e. in y -direction), only the surfaces parallel to the wall were considered when calculating the effective conductivity. Radiation of transversal webs was neglected (see Fig. 2.9). The radiant heat flow q_{rad} between two surfaces, which dimensions are significantly larger than their distance, follows from the Stefan-Boltzmann law as (Willems [152, p. 25])

$$q_{\text{rad}} = \frac{\sigma}{\frac{1}{\varepsilon_1} + \frac{1}{\varepsilon_2} - 1} \cdot (T_1^4 - T_2^4). \quad (2.5)$$

Hereby, σ is the Stefan-Boltzmann constant ($5.67 \times 10^{-8} \text{ W}/(\text{m}^2\text{K}^4)$), ε_i is the emissivity of surface i , and T_i is the surface temperature of surface i . The surfaces are denoted 1 and 2, as shown in Fig. 2.9. The

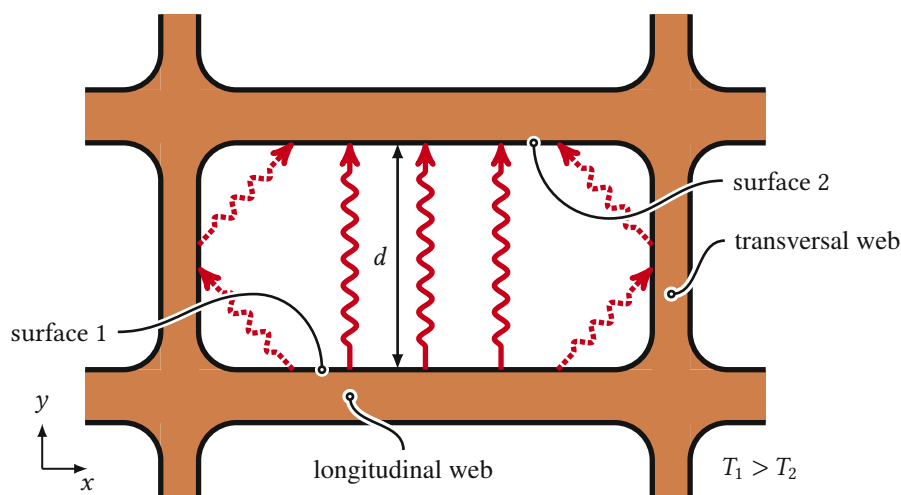


Fig. 2.9: Horizontal section of vertically perforated brick: Governing paths of radiant heat transfer. The thermal interaction of the transversal webs due to radiation (dashed paths) was neglected.

emissivity was set to 0.9 for both surfaces [82, 112]. The corresponding one-dimensional conductive heat flow within the air void follows from Fourier's law of heat conduction in the form

$$q_{\text{eff,rad}} = \frac{\lambda_{\text{eff,rad}}}{d} \cdot (T_1 - T_2), \quad (2.6)$$

where $\lambda_{\text{eff,rad}}$ is the effective radiant thermal conductivity and d is the layer's thickness. Equating Eqs. (2.5) and (2.6) allows for the determination of the sought effective conductivity of the voids, reading as

$$\lambda_{\text{eff,rad}} = \frac{\sigma \cdot d}{\frac{1}{\varepsilon_1} + \frac{1}{\varepsilon_2} - 1} \cdot \frac{T_1^4 - T_2^4}{T_1 - T_2}. \quad (2.7)$$

Convective heat flow depends on the thermal conductivity of the gas, λ_a , and the so-called Nusselt number Nu , which describes the ratio of the amount of heat transported in a flowing medium, compared to a static one:

$$\lambda_{\text{eff,conv}} = Nu \cdot \lambda_a. \quad (2.8)$$

For calculating the Nusselt number, the cavities were considered as vertical shafts, which are heated from one side. The VDI Heat Atlas pp. 681–682 [146], provides the following equation for this case:

$$Nu = \left(\left(0.08333 \cdot Ra \cdot \frac{d}{H} \right)^{-\frac{3}{2}} + \left(0.61 \cdot \left(Ra \cdot \frac{d}{H} \right)^{\frac{1}{4}} \right)^{-\frac{3}{2}} \right)^{-\frac{2}{3}}. \quad (2.9)$$

Hereby, d and H are the cavity's thickness and height, respectively. The Rayleigh number Ra is defined by

$$Ra = \frac{g \cdot (T_1 - T_m) \cdot d^3}{T_m \cdot \nu_a^2} \cdot Pr \quad \text{with the Prandtl number } Pr = \frac{\eta_a \cdot c_{p,a}}{\lambda_a}, \quad (2.10)$$

with the gravitational constant g (9.81 m/s²), the mean temperature of the air in the cavity, T_m , and the distance between the cavity surfaces, d . ν_a , η_a , $c_{p,a}$, and λ_a are the kinematic viscosity, the dynamic viscosity, the heat capacity, and the thermal conductivity of air, respectively. The aforementioned properties were obtained for temperatures from 0 °C to 1000 °C according to the VDI Heat Atlas pp. 302–393 [146] (see Fig. 2.10 and Table 2.2).

For calculating the effective thermal conductivity according to Eqs. (2.4), (2.7) and (2.10), the cavities were sorted into four groups, considering their thickness d (6 mm, 8 mm, 14 mm, and 38 mm). The height of the cavities amounts to $H = 3.0$ m, assuming that they form a connected shaft from the bottom to the top of the wall. Fig. 2.11a shows the calculated effective thermal conductivity for the cavity groups. Since the heat transfer at higher temperatures is governed by radiation and the distance of the surfaces has nearly no impact on the radiant heat transfer, the effective conductivity increases significantly with increasing thickness (e. g. Group 2, which contains the cavities in the middle with the largest thickness). For the smaller cavities, which are outnumbering the larger ones, the effective thermal conductivity λ_{eff} exceeds the value of fired clay around 200 °C–300 °C.

The temperature-dependent mass density of air, ρ_a was also taken from the VDI Heat Atlas pp. 302–393 [146]. A significant decrease in mass density with increasing temperature can be observed (see Fig. 2.10e).

Since the effective conductivity depends on the surface temperatures in the cavities, and these surface temperatures, in turn, depend on the effective conductivity, an iteration process seems to be necessary.

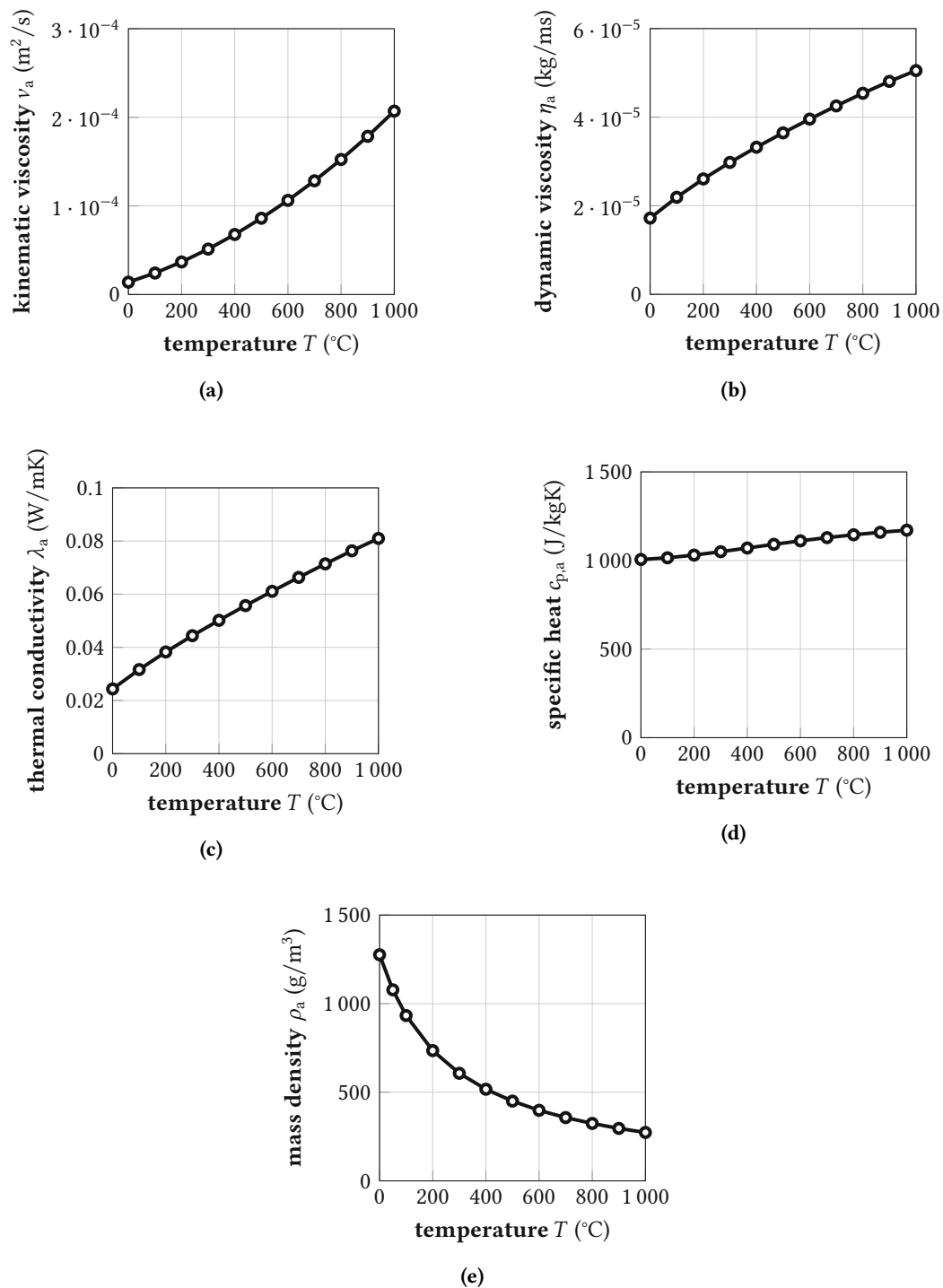


Fig. 2.10: Temperature-dependent thermal properties of air used in the finite-element model: (a) kinematic viscosity ν_a , (b) dynamic viscosity η_a , (c) thermal conductivity λ_a , (d) specific heat $c_{p,a}$, and (e) mass density ρ_a [146].

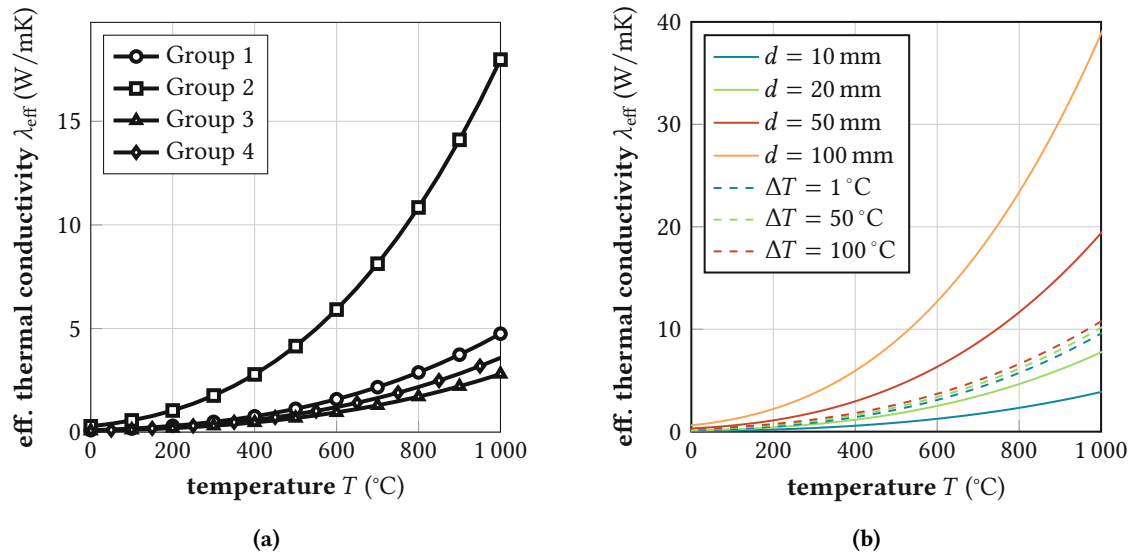


Fig. 2.11: (a) Effective thermal conductivity of the cavities, λ_{eff} , subdivided into four groups, depending on the cavity thickness: 14 mm (Group 1), 38 mm (Group 2), 6 mm (Group 3), and 8 mm (Group 4). The values were derived using Eqs. (2.4) and (2.10). (b) Case study for estimating the impact of temperature difference $\Delta T = T_1 - T_2$ (with $d = 25$ mm) and distance between the cavity surfaces d (with $\Delta T = 10^\circ\text{C}$) on the effective thermal conductivity λ_{eff} of the cavities.

However, evaluating Eqs. (2.8) and (2.10) for different temperature differences and different cavity sizes showed that the influence of the temperature difference between the surfaces is insignificant. In contrast, the distance between the surfaces has a significant impact (see Fig. 2.11b). Hence, the heat transfer was calculated without iteration using a fixed temperature difference of 50°C .

2.3.4 Two-dimensional mechanical finite-element model

2.3.4.1 Strategy, mesh, and boundary conditions

By analogy to the thermal model discussed before, geometrically identical two-dimensional mechanical finite-element models (see Fig. 2.12) were created for each of the experimental phases (see Fig. 2.4). These models were used to evaluate the stress fields resulting from the temperature fields calculated with the thermal model and to predict the sequential spalling of the longitudinal webs. The models consist of 3885 to 6336 three-node and four-node linear plane stress elements (CPS3 and CPS4, respectively). A plane stress model with vanishing vertical stresses $\sigma_{zz} = 0$ was considered since the dead weight was neglected, and the vertical load was only considered in the three-dimensional model. In contrast to the thermal models, elements in the cavities were not needed, and the mesh was only refined in the first two longitudinal webs to shorten computation times.

Periodic boundary conditions (PBC) were considered to couple the displacements on the West and East boundary of the unit-cell (see Fig. 2.5). In contrast, North and South boundaries may deform freely. This way, a periodic (in longitudinal x direction) structure is modeled, which is comparable to the tested wall, given that the wall length is more than one order of magnitude larger than the wall thickness.

The linear equations, which couple the displacements of the East and West, were derived as described next. The displacements u_x and u_y of each point on the East boundary can then be defined by the

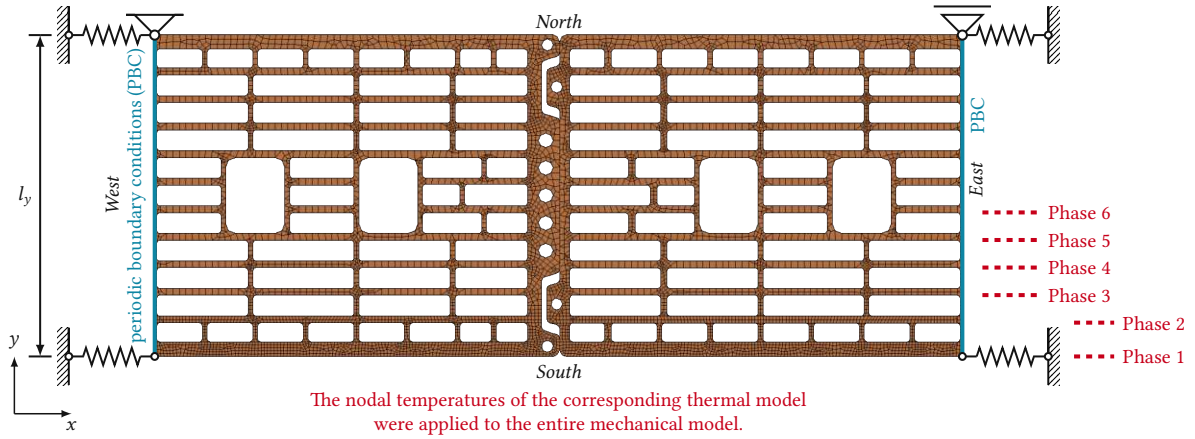


Fig. 2.12: The two-dimensional mechanical finite-element model for the first experimental phase (all webs intact) with the imposed boundary conditions. The dashed lines indicate where the geometry was cut for later phases and, therefore, where the fire temperature was applied.

displacements of the *vertex nodes* on this boundary (NE, SE, NW or SW, see Fig. 2.5), the length of the model in y -direction, l_y , and the location of the point:

$$\begin{pmatrix} u_x^E(y) \\ u_y^E(y) \end{pmatrix} = \begin{pmatrix} u_x^{SE} \\ u_y^{SE} \end{pmatrix} + \frac{y}{l_y} \cdot \begin{pmatrix} u_x^{NE} - u_x^{SE} \\ u_y^{NE} - u_y^{SE} \end{pmatrix}. \quad (2.11)$$

The same relation applies on the West boundary:

$$\begin{pmatrix} u_x^W(y) \\ u_y^W(y) \end{pmatrix} = \begin{pmatrix} u_x^{SW} \\ u_y^{SW} \end{pmatrix} + \frac{y}{l_y} \cdot \begin{pmatrix} u_x^{NW} - u_x^{SW} \\ u_y^{NW} - u_y^{SW} \end{pmatrix}. \quad (2.12)$$

Forming the difference of Eqs. (2.11) and (2.12) results in the coupling of the edges East and West:

$$\begin{pmatrix} \Delta u_x \\ \Delta u_y \end{pmatrix} = \begin{pmatrix} u_x^E(y) - u_x^W(y) \\ u_y^E(y) - u_y^W(y) \end{pmatrix} = \frac{l_y - y}{l_y} \cdot \begin{pmatrix} u_x^{SE} - u_x^{SW} \\ u_y^{SE} - u_y^{SW} \end{pmatrix} + \frac{y}{l_y} \cdot \begin{pmatrix} u_x^{NE} - u_x^{NW} \\ u_y^{NE} - u_y^{NW} \end{pmatrix}. \quad (2.13)$$

The linear equation (2.13) was applied to each pair of corresponding nodes to ensure the geometrical compatibility of the unit-cell. For applying the PBCs to the model, we developed the free-to-use module *AbaqusUnitCell2D* [126] for the scientific programming language *Julia* (see Bezanson et al. [10]), which works for Abaqus input files. Notably, a 3D counterpart of these equations can be found in Suda et al. [142].

Additionally, springs were introduced at the four vertices (labeled NW, NE, SW, SE in Fig. 2.12) to consider the stiffening effect, which originates in the offset of the upper and lower block layer. This offset leads to a reduction of the horizontal in-plane deformations (x -direction). The spring stiffness (300 N/m) was chosen in such a way that the estimated spalling time for Modeling Phase 1 corresponded with the experimental observations. For the subsequent phases, this value was not changed. Apart from the kinematic boundary conditions, the temperature field of the associated thermal model was applied to the whole mechanical model. The boundary conditions can be found in Fig. 2.12.

2.3.4.2 Constitutive behavior adopted for numerical simulations

The stresses are coupled to the temperatures in the constitutive law (see Mang and Hofstetter [88])

$$\sigma_{ij} = \frac{E}{1+\nu} \cdot \left(\varepsilon_{ij} + \frac{\nu}{1-2\nu} \cdot \varepsilon_{kk} \cdot \delta_{ij} \right) - \frac{E}{1-2\nu} \cdot \alpha_T \cdot (T - T_0) \cdot \delta_{ij} \quad (2.14)$$

with the nine independent components of the stress tensor, σ_{ij} , the material's Young's modulus, Poisson's ratio, and thermal expansion coefficient, E , ν , and α_T respectively, the nine independent components of the strain tensor, ε_{ij} , the Kronecker delta δ_{ij} , and the current temperature T as well as the initial temperature T_0 . Eq. (2.14) only describes the linear elastic constitutive law; material non-linearities were considered by implementing *Concrete Damaged Plasticity (CDP)*.

CDP is a plasticity-based smeared-damage model developed for concrete, suitable for use with quasi-brittle materials. Iuorio and Dauda [71] as well as Silva et al. [140] already successfully applied CDP for fired clay. The model considers two main failure mechanisms: cracking under tensile and crushing under compressive stresses. Two hardening variables control the evolution of the yield surface for tension and compression separately, $\tilde{\varepsilon}_t^{\text{pl}}$ and $\tilde{\varepsilon}_c^{\text{pl}}$ respectively. Therefore, it is possible to define different softening behavior for the tensile and compressive regimes. The yield function implemented in Abaqus (see Dassault Systèmes [29]) is a function proposed by Lubliner et al. [87] with adaptations made by Lee and Fenves [83]:

$$F = \frac{1}{1-\alpha} (\bar{q} - 3\alpha \cdot \bar{p} + \beta (\tilde{\varepsilon}^{\text{pl}}) \cdot \langle \hat{\sigma}_{\text{max}} \rangle - \gamma \cdot \langle -\hat{\sigma}_{\text{max}} \rangle) - \bar{\sigma}_c(\tilde{\varepsilon}_c^{\text{pl}}) = 0, \quad (2.15)$$

with the hydrostatic pressure stress \bar{p} , the Mises equivalent stress \bar{q} , and the maximum principal effective stress $\hat{\sigma}_{\text{max}}$. These stress values are derived from the effective stress tensor $\bar{\sigma}$:

$$\bar{\sigma} = \mathbf{D}_0^{\text{el}} \cdot (\boldsymbol{\varepsilon} - \boldsymbol{\varepsilon}^{\text{pl}}), \quad (2.16)$$

with the initial, undamaged elasticity tensor \mathbf{D}_0^{el} , and the total as well as the plastic strain tensor, $\boldsymbol{\varepsilon}$ and $\boldsymbol{\varepsilon}^{\text{pl}}$ respectively. This total strain tensor includes elastic and plastic strains but not temperature-induced strains. The three variables α , β , and γ are derived from the input parameters as follows:

$$\alpha = \frac{\sigma_{b0}/\sigma_{c0} - 1}{2 \cdot \sigma_{b0}/\sigma_{c0} - 1}, \quad \beta = \frac{\bar{\sigma}_c \left(\tilde{\varepsilon}_t^{\text{pl}} \right)}{\bar{\sigma}_t \left(\tilde{\varepsilon}_t^{\text{pl}} \right)} \cdot (1 - \alpha) - (1 + \alpha), \quad \text{and} \quad \gamma = \frac{3 \cdot (1 - K_c)}{2 \cdot K_c - 1}. \quad (2.17)$$

The parameter K_c controls the shape of the meridional plane of the yield surface and was set to $K_c = 2/3$ to approximate the yield surface of Mohr-Coulomb's criterion [29]. The dilation angle ψ amounts to 5° . The remaining input parameters, namely the ratio of initial equibiaxial compressive yield stress to initial uniaxial compressive yield stress, σ_{b0}/σ_{c0} , the "eccentricity" of the flow potential, ϵ , and the viscosity parameter, μ , take the values 1.16, 0.1, and 0, respectively, according to Silva et al. [140].

The tensile softening for the CDP, $\bar{\sigma}_t(\tilde{\varepsilon}_t^{\text{pl}})$, was defined according to Van der Pluijm [145], who used a relation proposed by Hordijk and Reinhardt [69] for concrete (see Fig. 2.13a). The peak stress amounts to $\sigma_{f,t,c} = 7.5$ MPa, which is the materials tensile strength discussed in Section 2.3.4.4. The plastic strain value at reaching the minimal stress was chosen in a way that the mode-I-fracture energy in the simulation would fit commonly accepted values for fired clay (0.05 J/mm², see e. g. [12, 41, 63]).

Since tensile stresses are the most crucial for the failure of vertically perforated fired clay blocks (see Kiefer et al. [76] and Suda et al. [142], as well as Nguyen and Meftah [111, 112]), the main focus was the correct depiction of the tensile softening. Thus, for the compressive softening, $\bar{\sigma}_c(\bar{\epsilon}_c^{pl})$, consideration of a bilinear stress-strain relation with plateau stress $\sigma_{f,c,c} = 27.6$ MPa was sufficient (see Fig. 2.13b and Table 2.2). The compressive and tensile strengths used for CDP are discussed in more detail in Section 2.3.4.4.

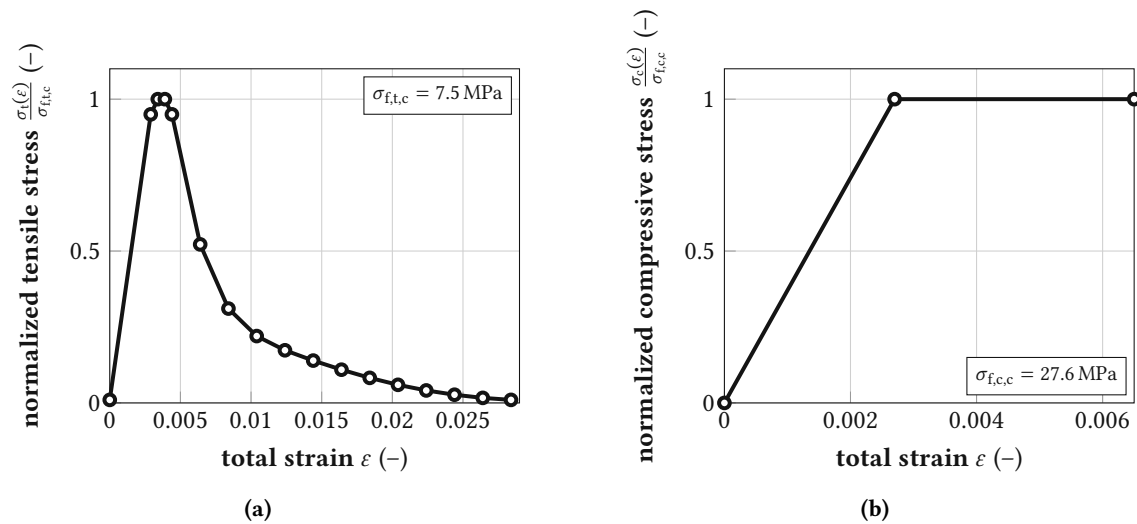


Fig. 2.13: Adopted softening behavior for fired clay in the tensile regime (a) [145], [69] and compressive regime (b).

2.3.4.3 Energy-based spalling criterion and failure of the wall

To complete the modeling of temperature-induced *sequential* failure of the longitudinal webs in the brick wall, as observed experimentally, a criterion for spalling of the longitudinal web closest to the furnace, as well as a criterion for overall wall failure, were required. For the spalling criterion, we recall that failure of the connection between the transversal and the longitudinal webs triggers spalling (see Nguyen and Meftah [111] as well as Nguyen and Meftah [112]). An elastic approach, where the stresses in these connections are observed, is inadequate since the first cracks in the plastic simulations led to a redistribution of stresses and not yet to wall collapse. Therefore, we needed a criterion that is able to find the critical point where a redistribution of the stresses yields spalling of the longitudinal web exposed to fire. Given the smeared damage approach in the framework of the adopted CDP (see Section 2.3.4.2), the model can predict damage localization accompanied by dissipative plastic deformations. We expect energy to dissipate progressively during the simulations following the progressive increase of temperature-induced stresses. After some time, we expect the damage to yield an abrupt increase in plastic deformations and thus dissipated energy, particularly in the connection of transversal and longitudinal webs, accompanied by a drop in elastically stored energy (strain energy). These energy changes indicate internal load redistribution, and we assume that spalling is occurring at this point in the experiment. After a spalling event, the model geometry is changed accordingly, and the next modeling phase is entered. The flowchart in Fig. 2.14 qualitatively shows the implementation of our energy-based spalling criterion.

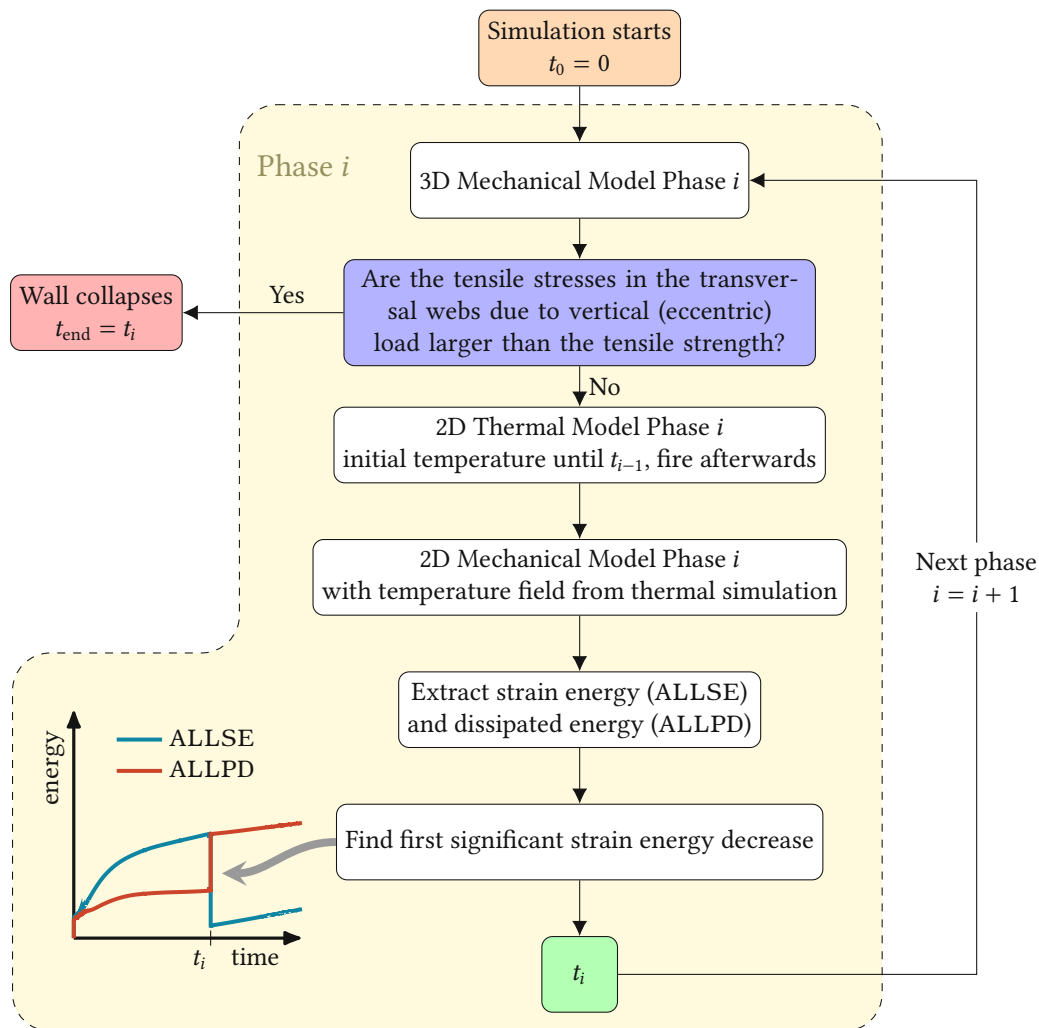


Fig. 2.14: Flow chart for the entire simulation process explaining the spalling and failure criterion. Spalling of a longitudinal web was predicted considering the evolution of the strain energy and the dissipated energy due to plastic deformations in the 2D mechanical simulation. The obtained spalling time was then used for the 2D thermal simulation of the subsequent Phase. The 3D mechanical simulations were used to identify the failure of the wall.

The overall failure of the wall was found considering the elastic 3D mechanical simulations. In each phase, the tensile stresses in the transversal webs (see also Fig. 2.20) were compared to the material's tensile strength. When these stresses exceeded the tensile strength, we considered the last obtained spalling time t_i as the total time at wall failure t_{end} (see Fig. 2.14).

2.3.4.4 Mechanical properties of fired clay

While EN 1996-1-2 [47] suggests a linear decreasing Young's modulus with increasing temperature, experimental observations show a slightly different behavior (e. g. Nguyen et al. [113]). Nguyen et al. suggest a decrease to approximately 70 % of the initial value between 21 °C and 100 °C, while staying nearly constant at higher temperatures (see Fig. 2.15a). Between 800 °C and 1000 °C Young's modulus decreases again to 15 % of its initial value. This behavior was implemented in the finite-element simulations.

Fired clay in extruded clay blocks shows a significant orthotropic behavior originating in the extrusion process [17]. Extensive information on the orthotropic microstructure of fired clay and the corresponding mechanical modeling can be found in the research of Kariem et al. [74, 75] and Buchner et al. [19, 21]. The plate-like shape of the webs causes the clay minerals to be oriented parallel to the web's surface. Therefore, Young's modulus parallel to the web's surface is approximately 100 %–200 % larger than orthogonal to it, depending on the composition of the clay material [20]. Unfortunately, using CDP as plasticity law does not allow anisotropic material stiffness. Since the web length is by 5 to 18 times larger than their thickness, the occurring in-plane stresses are significantly larger than the out-of-plane stresses. Hence, the larger in-plane value of Young's modulus was used, which amounts to $E_c = 13\,500\text{ MPa}$ at $T_{\text{ref}} = 21\text{ }^\circ\text{C}$.

The coefficient of thermal expansion (CTE) of the clay mixture was determined in a dilatometric analysis. It amounts to $\alpha_{T,c} = 8 \times 10^{-6}\text{ T}^{-1}$ at $T_{\text{ref}} = 21\text{ }^\circ\text{C}$ and is nearly constant until approximately $400\text{ }^\circ\text{C}$; then it starts to increase sharply, with a peak around $575\text{ }^\circ\text{C}$. This sharp increase occurs due to the conversion of quartz from α -quartz to β -quartz (see e. g. Müller et al. [104]). The phenomenon is called *quartz inversion*, and the increase can reach up to 100 %, depending on the amount of quartz in the clay. After the quartz inversion, the CTE decreases again, being lower than before in general (see e. g. [6]). For the simulations, the CTE at $575\text{ }^\circ\text{C}$ was chosen to be 70 % higher than the initial value and nearly 50 % lower than the initial value at higher temperatures (see Fig. 2.15b).

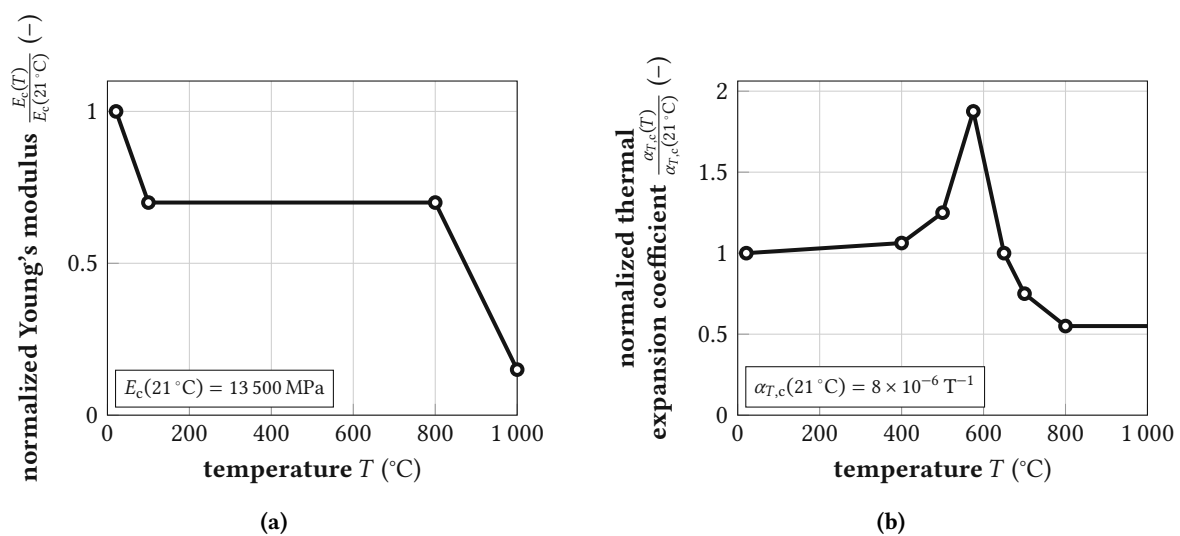


Fig. 2.15: Mechanical properties of fired clay used in the finite-element model. Young's modulus [112] (a) and the thermal expansion coefficient (b) were considered temperature-dependent.

Like the stiffness, the tensile and compressive strengths of extruded fired clay are orthotropic, with the largest strengths observed in the extrusion direction [76]. The strengths normal to this direction depend primarily on the orientation of a specific web. In general, the in-plane strengths are larger than the out-of-plane strengths. Again, the strengths had to be defined as isotropic with CDP as plasticity behavior. The larger in-plane strengths, $\sigma_{f,t,c} = 7.5\text{ MPa}$ and $\sigma_{f,c,c} = 27.6\text{ MPa}$, were chosen as tensile and compressive strength for the finite-element simulations, given the same reasoning as for Young's modulus. The material strengths were identified in compressive and three-point bending tests and were assumed to be temperature-independent in the simulations, although a temperature-dependancy can be observed in fired clay. In literature, we found two different contrary evolutions of the material

strengths: EN 1996-1-2 [47] describes a linearly decreasing strength with increasing temperature. In contrast, Nguyen and Meftah [112] used an increasing strength with temperature, which they obtained from experiments on different fired clay blocks. A currently running research project revealed a similar trend as Nguyen and Meftah used, corroborating this evolution. Additionally, the decreasing strength evolution is not suggested anymore in the new draft of EN 1996-1-2 in 2022. Therefore, we assume the suggested relation from Nguyen and Meftah to be appropriate.

The temperature-strength-relation Nguyen and Meftah [112] used shows a 10 % increase until 400 °C. Only above 400 °C the strength increases more rapidly up to 74 % of its initial value at 21 °C. The largest stresses leading to spalling occurred in the transversal webs behind the longitudinal web exposed to fire. The nodal temperatures in these regions were always below 500 °C (see also Fig. 2.16 and supplementary material¹). Therefore, the strength increase can be expected to be around 10 %. This inaccuracy was acceptable in our study, considering the strength variations of fired clay due to defects and the heterogeneous nature of fired clay. Therefore, the simplification of the strength evolution as temperature-independent seems to be appropriate in this case. Thermal creep effects were not considered, given the brittle material behavior and the short duration until failure occurs.

2.3.4.5 Numerical aspects

The rapidly increasing temperatures combined with the very brittle material behavior led to a numerical problem of high complexity. Therefore, the *Step stabilization* in Abaqus was used to overcome numerical instabilities. This stabilization method introduces an artificial damping factor, which is used to calculate nodal damping forces for nodes with spontaneously rising nodal velocities (see also Dassault Systèmes [29]).

2.3.5 Three-dimensional mechanical finite-element model

A three-dimensional model was used to model the stress field due to the vertical loading and to identify the overall failure of the wall. This model is based on the research of Kiefer et al. [76]. In contrast to the two-dimensional models, the mortar joints were also considered. Since the thickness of the thin-bed mortar joint was less than 1 % of the block height, a simplified micro-modeling approach was considered, i. e. mortar was modeled as a 2D cohesive surface connecting the bricks rather than a 3D region (see Lourenço [86]). The models consist of 272 686 to 433 524 eight-node linear brick elements (C3D8). Analogous to the 2D model, a unit-cell concept with periodic boundary conditions was adopted to minimize the numerical expenses while maintaining a detailed geometry. With a height of two blocks and a width of one block, the chosen unit-cell is the smallest possible unit-cell without considering point and line symmetries (see Fig. 2.6a).

In the three-dimensional formulation of the periodic boundary conditions, not only the East and West surfaces of the continuum are coupled, but also the top and bottom surfaces. Further details on the implementation of the periodic boundary conditions can be found in Kiefer et al. [76] as well as Suda et al. [142].

The vertical loading of the wall was introduced as vertical stress $\sigma_{zz}(y)$ on the top and bottom surface of the unit-cell. Notably, the progressive spalling of the longitudinal webs leads to a progressively increasing load eccentricity e (see Fig. 2.6b), yielding a linear stress distribution in the thickness direction

¹The supplementary material can be found in the online version of the published article, which is available under <https://doi.org/10.1016/j.firesaf.2022.103729>.

of the wall, with larger vertical compression on the unexposed side and smaller vertical compression on the fire-exposed side. Thus, these phase-specific vertical stresses $\sigma_{zz}(y)$ read as

$$\sigma_{zz}(y) = \frac{N}{A} + \frac{N \cdot e}{I_x} \cdot y, \quad (2.18)$$

with the constant vertical load, N , the net cross-sectional area A , the moment of inertia I_x , and the coordinate in thickness direction y , which is related to the phase-specific center of mass of the cross-section.

The elastic properties of fired clay are described in Section 2.3.4.2, the elastic properties of mortar were overtaken from previous studies [76, 142], considering findings from Domone and Illston [39] as well as Sarhosis and Sheng [134]. This way, the orthogonal and tangential interface stiffness for the cohesive surface properties amount to $K_{nn} = 5000 \text{ N/mm}$ and $K_{ss} = K_{tt} = 2083 \text{ N/mm}$, respectively. Mortar failure was not considered relevant.

2.4 Model results, validation, and discussion

2.4.1 Evolution of temperature fields

Fig. 2.16a shows the distribution of nodal temperatures in Phase 4 as a qualitative example for all the modeling phases. Similar graphs for the other five modeling phases are given in the supplementary material². The temperature is around 850 °C at the fire-exposed surface and decreases significantly to approximately 530 °C on the opposite surface of the first longitudinal web. Interestingly, the surface temperature of the second longitudinal web is higher at the center of the cavities compared to the regions close to transversal webs, demonstrating that the heat transfer resistance through the cavity is smaller than the one through the fired clay. Already in the third longitudinal web, the temperature stayed nearly constant. In the cavities, the temperature decrease is less significant, suggesting a smaller heat transfer resistance there. The wavy appearance of the temperature distribution underlines this suggestion since the higher temperatures advanced slightly further through the wall directly behind the air-filled cavities. At the moment of spalling, the large temperature on the South side of the model did only advance to the second row of cavities. The nodal temperature stayed near the initial value of 21 °C from the third longitudinal web upwards.

The simulated temperatures were compared to the experimentally measured temperatures inside the cavities to validate the thermal model (see Fig. 2.17). Notably, the spalling times required for differentiating the six phases were not yet calculated from the mechanical simulations but approximated from the experimental values, as described in Section 2.2. In general, the thermal simulations agree well with the experiments. The model underestimates the cavity temperature at the beginning of each phase but slightly overestimates it afterward. Notably, the model also nicely predicts the slowdown of the temperature increase related to the evaporation of pore water observed in almost all phases at around 100 °C. In the sixth cavity, the temperature increase in the simulations is significantly larger than in the experiment. One possible reason for that can be found in the fourth longitudinal web. The spalling of the fourth web was approximated using the temperature increase in the fifth cavity. However, spalling is not the only possible reason for a temperature increase. The fourth web could have been cracked open at another wall location. Then the temperature in the cavity behind might already increase, although the web is still intact. Since the temperature trend differs significantly from the other curves, the thermocouples might also have been corrupted. Either way, the temperatures in the sixth cavity were not that important for the simulation since the last phase of the experiment did not last very long.

The good agreement of simulated and measured temperature evolutions during Phases 1 to 5 underlines the validity of the chosen temperature model and motivates the discussion of the heat transfer mechanism. At the beginning of the simulation, the maximum heat flux could be observed in the transversal webs, while the heat flux in the cavities was low in comparison (see Fig. 2.18a). Around 250 °C, the distribution started to shift, and in the end, nearly all the heat was transferred through the cavities (see Fig. 2.18b). This observation suggests the following conclusion: While the cavities are essential for the high thermal resistance of the block at ambient temperatures, the drastically increasing part of radiant heat transfer in the cavities at higher temperatures has a negative impact on the insulation condition (I according to the classification standard EN 13501-2 [45]).

²The supplementary material can be found in the online version of the published article, which is available under <https://doi.org/10.1016/j.firesaf.2022.103729>.

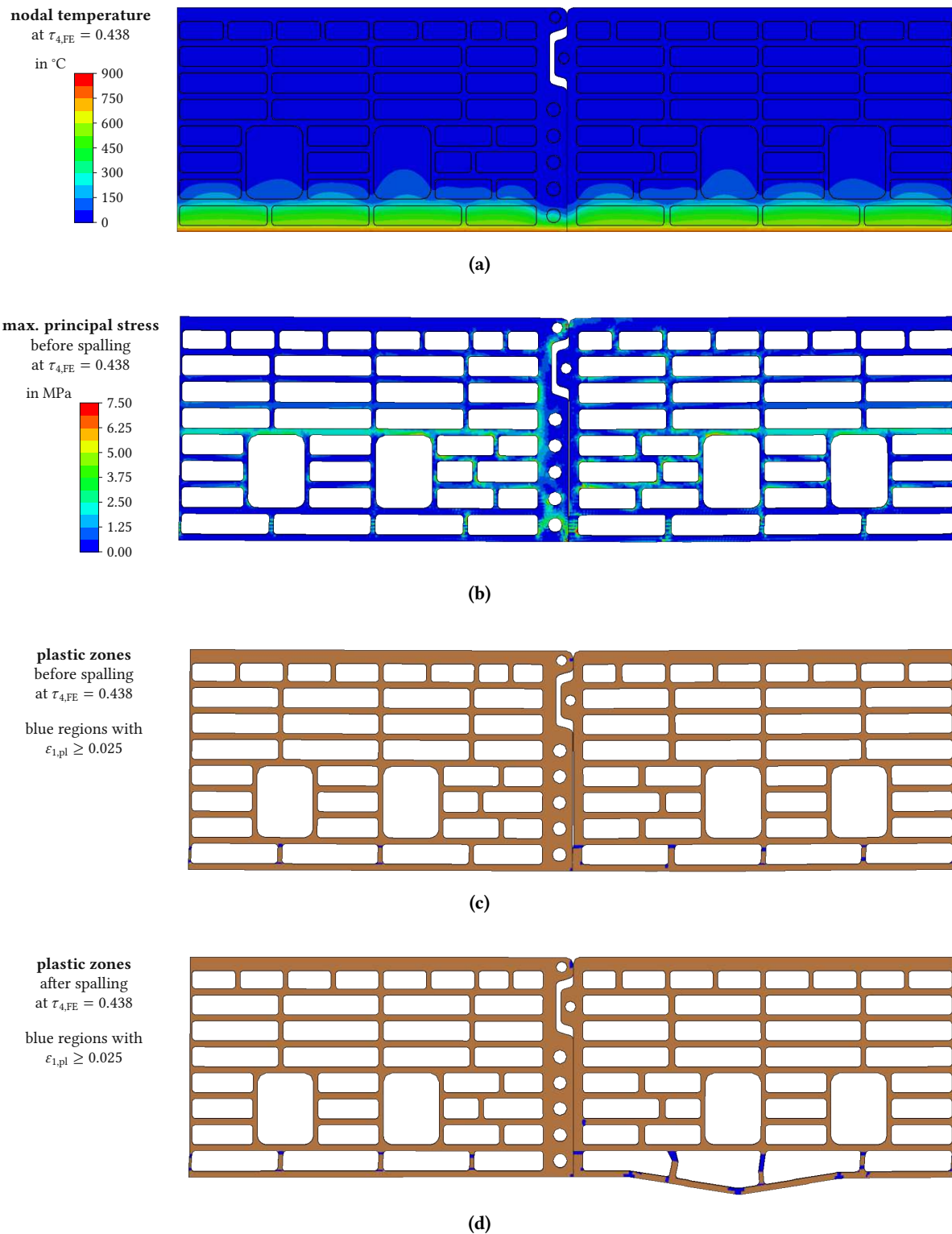


Fig. 2.16: Nodal temperature (a) and maximum principal stresses (b) in Phase 4 right before estimated spalling time $\tau_{4,FE} = 0.438$. Plastic zones indicated by the maximum principal plastic strain $\epsilon_{1,pl} \geq 0.025$ (blue regions) right before (c) and after (d) this spalling time. Similar graphics for the other five modeling phases are provided in the supplementary material.

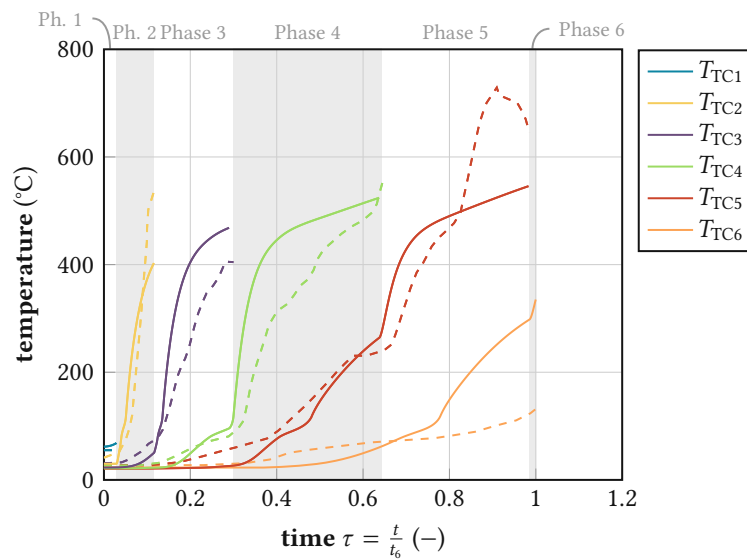


Fig. 2.17: Comparison of measured (dashed lines) and predicted (solid lines) evolution of cavity temperatures.

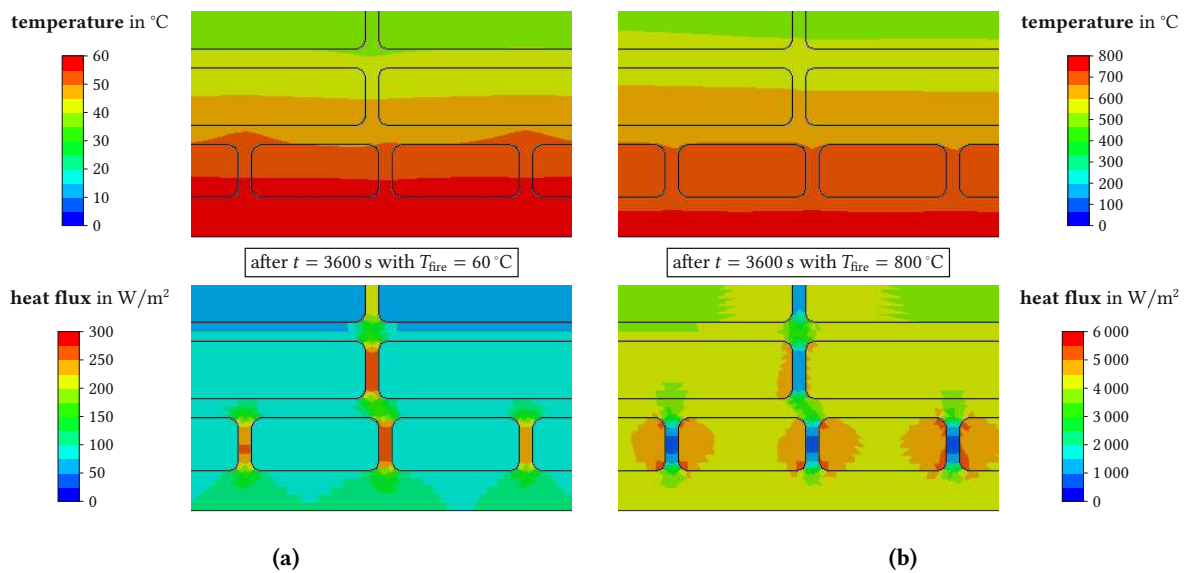


Fig. 2.18: Detail of temperature (top) and heat flux (bottom) in the first three longitudinal webs at (a) $t = 3600$ s with firing temperature (at the bottom surface) of 60 °C, showing that heat is transferred preferably through transversal webs, and (b) $t = 3600$ s with firing temperature 800 °C, showing that heat is transferred preferably through cavities.

2.4.2 Evolution of stress fields and sequential spalling

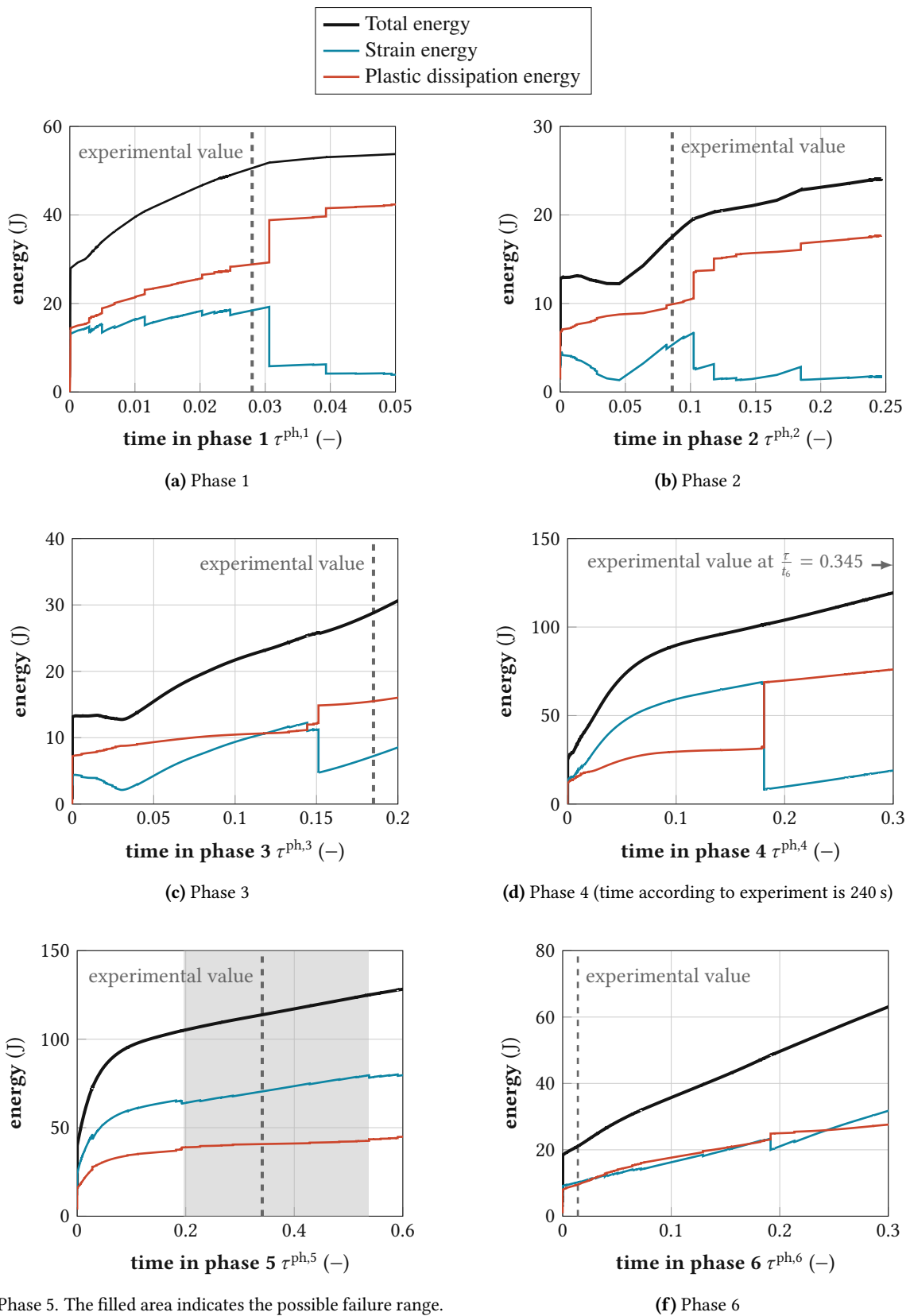
Fig. 2.16b shows the distribution of the maximum principal stresses in Phase 4 as a qualitative example for all the modeling phases. The most significant tensile stresses occur in the connection between the transversal and longitudinal webs (red areas). Since the outermost longitudinal web expands towards the head joint, the transversal webs closest to the head joint are the most critical. In Phase 4, the fifth longitudinal web shows tensile stresses, which are increasing to the middle of the block. In the earlier phases, such tensile stresses occur in the second longitudinal web; see the supplementary material³ for corresponding graphs. Due to the large cavities in the middle of the block, these tensile stresses are redistributed to the first longitudinal web behind these large cavities. Compressive stresses occur in the outermost longitudinal web, counteracting these tensile stresses. Note that these compressive stresses cannot be seen in Fig. 2.16b, due to the choice of the shown variable.

Besides the negative impact on the insulation condition, the decrease in effective thermal resistance at higher temperatures (shown in Fig. 2.18) also has a positive effect on the performance of the wall in the fire experiment: Large temperature gradients are the reason for large stresses in the block, which lead to failure of the webs (this affects the parameters R and E in the classification standard EN 13501-2 [45]). A loss in the overall thermal resistance yields a faster decrease of these temperature gradients and, therefore, smaller stresses.

Next, the identification of the spalling times is discussed. The plastic deformations mainly occur in the connection between the transversal and longitudinal webs. Nevertheless, the plastic dissipated energy in these regions dominates the dissipated energy of the whole model. Thus, the evolution of the total energy, strain energy, and dissipated energy of the whole 2D model are plotted in Fig. 2.19 for each of the six model phases. Notably, the time values $\tau^{\text{ph},i}$ on the horizontal axis are related to the start of the corresponding phase rather than the failure of the insulation, as the total time τ is. Interestingly, the total energy curves of Phases 1, 4, and 5 increase concavely, which are the models where the first longitudinal webs are continuous and in contact in the head joint (see the block geometry depicted in Fig. 2.2). In both phases, where the outermost webs are not in contact at the head joint (Phases 2 and 3), the strain energy decreases before it increases concavely. After some time, the dissipated energy increases abruptly (revealed by the jump of the red line in Fig. 2.19) while the strain energy decreases in the same way, at least for Phases 1 to 4. This time was considered the model-predicted spalling time. The deformations and plastic strains in the model changed at these moments (e. g. Figs. 2.16c and 2.16d for Phase 4): While just a few transversal webs between the two longitudinal partitions closest to the fire showed plastic zones before the derived time, each transversal web in this row showed significant plastic strains afterward. Additionally, the longitudinal web closest to the fire buckled, as already demonstrated by Nguyen and Meftah [111]. Most notably, the experimentally measured spalling time for Phases 1 to 4 is remarkably close to the predicted counterpart (see Fig. 2.19), which corroborates the two-dimensional mechanical model and its underlying assumptions.

While the plastic zones in Phases 1 to 4 concentrate in the outermost transversal webs, they are much more evenly distributed over the wall thickness in Phases 5 and 6. This observation can be traced back to the large holes in the middle of the brick (see Fig. 2.2). The web structure is less rigid than in the phases before due to the non-continuous longitudinal webs six and seven and the offset transversal webs. Thus, temperature-induced deformations are less hindered, leading, in turn, to smaller stresses and a less brittle behavior without pronounced jumps in the evolution of the cumulative dissipated

³The supplementary material can be found in the online version of the published article, which is available <https://doi.org/10.1016/j.firesaf.2022.103729>.



(e) Phase 5. The filled area indicates the possible failure range.

(f) Phase 6

Fig. 2.19: Whole model energy values

energy. Nevertheless, in Phase 5, two small jumps could be observed (see Fig. 2.19e). The range between the corresponding time instants ($\tau^{\text{ph},5} = 0.196$ and $\tau^{\text{ph},5} = 0.587$) was considered as a possible interval where the longitudinal web spalled. This interval nicely bounds the experimentally determined spalling time amounting to 0.341. In Phase 6, a small dissipation burst occurs at $\tau^{\text{ph},6} = 0.188$, but this time instant is already well after the experimentally determined collapse of the wall. This way, we expect the stresses due to the already significant eccentric vertical loading to be critical, as analyzed next.

2.4.3 Stresses due to vertical loading and ultimate failure of the wall

Tensile stresses in the transversal webs lead to the failure of vertically perforated clay block masonry under vertical compression (see Suda et al. [142]). Since the study focuses on the spalling of the outermost longitudinal webs, the maximum tensile stresses in the transversal webs right behind the first longitudinal web are the most interesting to observe (see Fig. 2.20). These stresses are large in the bed joints and rapidly decrease when going vertically to the middle of the block. In the first five phases, the stresses are below the tensile strength (see Table 2.3). Therefore, the vertical loading alone would not lead to the failure of the wall in these phases. However, the tensile stress in Phase 5 is only insignificantly below the tensile strength. From Phase 5 to Phase 6, the maximum tensile stress more than doubles and is well above the tensile strength. The underlying reason for this increase is the outermost longitudinal web being non-continuous in Phase 6. Therefore, we consider that the wall collapses at the end of Phase 5 when the fifth longitudinal web spalls. The observations in the experiment support this modeling result since the wall endured only a few seconds after Phase 6 was reached.

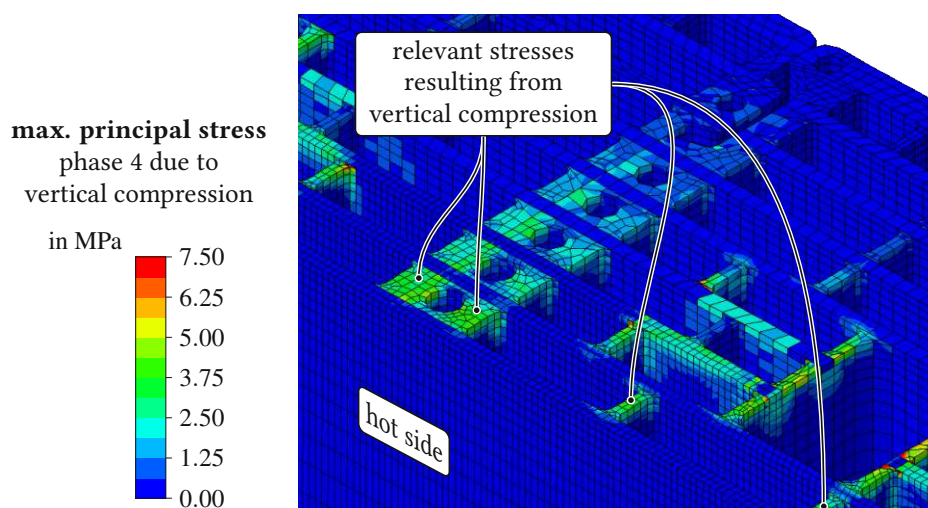


Fig. 2.20: Maximum principal stresses in the transversal webs of the three-dimensional mechanical model in Phase 4 due to vertical loading.

Tab. 2.3: Ratio of the largest tensile stresses to the material's tensile strength in the outermost transversal webs of the corresponding model phase.

Phase 1	Phase 2	Phase 3	Phase 4	Phase 5	Phase 6
21.3 %	37.6 %	49.2 %	73.6 %	95.3 %	199.7 %

Finally, the time until collapse predicted by the model is compared to the experimentally measured collapse time. Fig. 2.21 shows the overall time of the simulations compared to the experiment. Given the predicted spalling range in Phase 5 (Fig. 2.19e), two bounds were predicted for the total time until collapse, see Fig. 2.21. The experimentally measured collapse time nicely falls in between these two bounds. It is reasonable to be closer to the upper bound because of the implemented unit-cell concept: The same failure state is assumed over the whole width of the wall since the unit-cell is repeated periodically. The specimen in the experiment started to fail in the center of the wall, while other regions stayed intact. Therefore, a shorter overall time in the simulations seems reasonable.

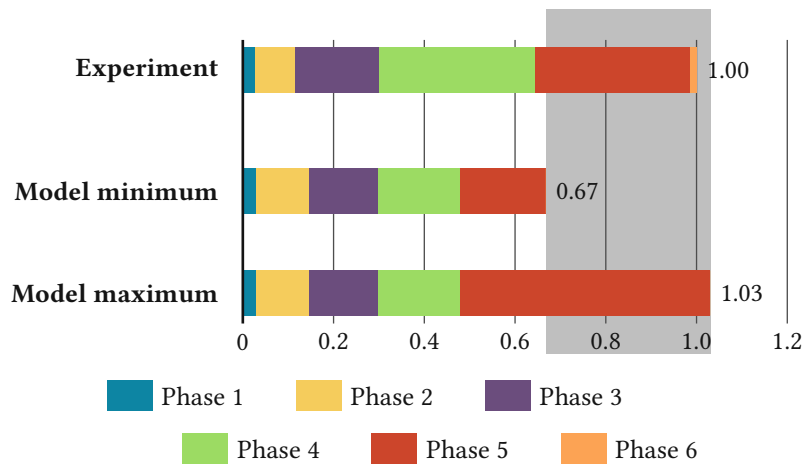


Fig. 2.21: Comparison of model-predicted and experimentally determined time until the collapse of the wall, subdivided into the six phases corresponding to the sequential spalling of the outermost webs; the gray area in the background marks the interval spanned by the two limit cases predicted by the model.

2.5 Conclusion

Within this work, a coupled temperature-displacement finite-element model for assessing the performance of vertically perforated clay block masonry in a firing test was presented and compared to novel experimental data. Using an energy-based spalling criterion combined with a unit-cell approach allowed for modeling only a small region and, thus, saved numerical expenses. Hence, non-linear and temperature-dependent material behavior and fine meshing could be used, enabling detailed insights into the distribution and evolution of stresses, strains, and local damage zones. Since the model only considers a small region of the whole wall, no information about the overall deformation could be gained, such as obtained in e. g. Nguyen and Meftah [112]. Nevertheless, the presented approach contributes to a better understanding of the complex mechanisms involved in the behavior of vertically perforated clay block masonry in fire situations.

The simulation was split into six sequential phases with slightly different geometry, considering spalling of the longitudinal webs as the critical mechanism for failure. Spalling of the webs could be decoupled from the vertical loading; thus, a two-dimensional modeling approach was sufficient for simulating the firing test. Nonetheless, purely elastic three-dimensional mechanical models helped interpret the results from the two-dimensional models and depict the failure of the entire wall.

The temperatures simulated with the proposed two-dimensional thermal model show good agreement with the experiments, even after spalling of the longitudinal webs. Additionally, the thermal simulations revealed a redistribution of the heat flow from the transversal webs to the air-filled cavities at higher temperatures. This change in heat transfer is driven by the increasing impact of radiation and convection at higher temperatures. Therewith, a positive and negative effect of the air-filled cavities on the performance in the firing test could be derived.

A novel energy-based spalling criterion was presented for predicting the longitudinal webs' spalling. By identifying a qualitative decrease in strain energy (and vice versa, an increase of dissipated energy), this criterion allowed the depiction of spalling for each phase.

Thus, considering the temperatures of the two-dimensional thermal models, the energy evolution of the two-dimensional mechanical models, and the maximum principal stresses of the three-dimensional mechanical models for each phase, we were able to predict the performance of a vertically perforated clay block wall in a firing test. The simulated performance showed good agreement with experimental measurements, notably without any empirical fitting parameters.

In general, finding an optimum for vertically perforated clay blocks is a hard-to-achieve goal since there are masses of existing product designs and infinite possible new configurations. Performing a parameter study for a specific design seems to be a more reasonable approach. Hence, utilizing the available computational methods by extending the block design experience by numerical approaches like the presented model could help to improve the block design process.

Acknowledgements

The authors gratefully acknowledge the support of the industry partner Wienerberger to the research work within the project “Innovative Brick 2”. Furthermore, the authors acknowledge TU Wien Bibliothek for financial support through its “Open Access Funding Programme”. Funding: The Austrian Research Promotion Agency supported this work [grant number 865067].

Publication 3

A numerical unit cell model for predicting the failure stress state of vertically perforated clay block masonry under arbitrary in-plane loads

Authors Raphael Reismüller, Markus Lukacevic, Sebastian Pech, Andreas Jäger, Josef Füssl

Published in *Engineering Structures*, 293 (2023) 116557

DOI <https://doi.org/10.1016/j.engstruct.2023.116557>

Abstract

As vertically perforated clay block masonry advances into more demanding building categories, knowledge of the effective masonry strength under different loading states becomes crucial. However, experimentally identifying macroscopic failure surfaces for such masonry requires a massive effort. In this study, we propose a FEM-based simulation concept to predict failure stress states of masonry under arbitrary in-plane loading. The proposed concept is validated using seven experiments from the literature. Subsequently, subjecting the validated model to various load cases allows for deriving a failure surface comparable to the Rankine-Hill surface. Thus, by applying the presented concept, we can effectively generate macroscopic failure surfaces for any perforated clay block design.

3.1 Introduction

Being one of the oldest materials in human history, clay block masonry remains a popular material for its low thermal conductivity, durability, fire resistance, and ease of construction, particularly in residential and low-rise buildings. In recent years, the construction industry has increasingly focused on reducing its carbon footprint, which has highlighted the challenge of reducing CO₂ emissions in the fabrication process of fired clay blocks. Therefore, new ways to optimize the production process and the products themselves are being considered [19–21, 23].

Moreover, although masonry offers numerous benefits, it has recently fallen behind other traditional materials, such as steel and concrete, when it comes to the accessibility and simplicity of structural analysis using finite element (FE) software. This is partly due to the challenge of acquiring effective strength parameters under different loading conditions for the great variety of modern masonry products. As an increasing number of structural engineers depend on the conveniences provided by modern FE software, it is crucial to develop new methods for obtaining these strength parameters to calibrate effective failure surfaces.

Although there are several approaches for defining failure surfaces for masonry, only a few of them apply to vertically perforated clay block masonry. One of these surfaces was proposed by Ganz [54], who analytically defined twelve failure criteria (see Appendix A). Thereby, he considered different failure mechanisms typically occurring in masonry structures and derived criteria from the geometry of the blocks and the material properties. Another approach is the Rankine-Hill surface developed by Lourenço [86], which is one of the most widely used approaches for simulating the behavior of masonry structures under different loading conditions (refer to [24, 28, 56, 57, 98, 110, 115, 129]). The Rankine-Hill surface consists of two parts: a Hill-type criterion for compressive failure and a Rankine-type criterion for shear and tensile failure (see Appendix B). Both criteria were developed to qualitatively model the experimentally observed failure behavior of a masonry wall without considering specific failure mechanisms.

To calibrate such failure surfaces, macroscopic experiments that characterize the material's behavior under different loading conditions are required. This is already a complex task for a few selected loading states. In addition, the product palette of masonry is becoming increasingly diverse, thus, making an experimental identification of the failure surfaces impossible. One solution to this challenge is the use of reliable numerical models to simulate the needed macroscopic experiments for the calibration of the surfaces. Such accurate simulations of the masonry's behavior under different loading conditions provide a more efficient and cost-effective alternative to conducting physical experiments.

Using computational methods for predicting the behavior of masonry is getting more and more attention [16, 53, 84, 135, 136, 138, 142, 154]. Recently, Kiefer et al. [76] proposed an FE-based approach to predict the compressive strength of vertically perforated clay block masonry. Using the eXtended Finite Element Method (XFEM) [7] and the orthotropic Hoffman criterion [67] in combination with a unit cell approach and periodic boundary conditions, they were able to accurately predict the vertical compressive strength of eight different block designs. In this study, we enhance this numerical model by adding additional failure mechanisms to depict the failure under arbitrary in-plane loading scenarios.

For validation of the numerical model, a set of experiments is necessary. Recently, Bitterli and Salmanpour [11, 133] published a suitable experimental study for vertically perforated clay block masonry, in which they did seven compressive tests on wall specimens with inclined bed joints. Although the specimens were loaded uniaxially, changing the incline angle from 0°–90° in steps of 15° led to different combinations of compressive and shear stresses orthogonal to the joint system. In these experiments,

they identified the key failure mechanisms under combined compressive and shear loads and a relation between the bed joint incline and the obtainable peak stress. Thus, we used these experiments for the validation of the presented numerical model.

The outline of the work is as follows: First, we enhanced the numerical model developed by Kiefer et al. [76] by introducing a failure criterion for the mortar joints. For this, we back-calculated the damage properties of the mortar joints by simulating shear tests on masonry triplets [11, 133]. Secondly, we validated the model by simulating the experiments conducted by Bitterli and Salmanpour [11, 133] using the FE software Abaqus. The numerically obtained failure stress states matched the experimental results and the key failure mechanisms could be replicated in our simulations. After proving the validity of the model, we simulated additional loading combinations on the same model to calibrate the failure surfaces following Ganz [54] and Lourenço [86]. The obtained failure surfaces showed good agreement with the simulations used for validation. Therefore, the model has the potential to substitute experiments for calibrating failure surfaces.

Section 3.2 contains an overview of the applied modeling strategies and the numerical model. The application of these modeling strategies for simulating the verification experiments is provided in Section 3.3. Afterward, the results are explained and discussed in Section 3.4, followed by conclusions in Section 3.5.

3.2 Modeling Strategies

While *solid* clay block masonry was already used 5000 years ago, *vertically perforated* clay blocks are nowadays commonly used in Central Europe because of their improved properties and material efficiency. A pattern of vertical cavities is introduced to the solid clay block, which creates a network of slender, plate-like webs. These webs are mostly orthogonal and can be categorized by their orientation (see also Fig. 3.1):

- Longitudinal webs are oriented parallel to the wall surface (x - z -plane),
- Transversal webs are oriented perpendicular to the wall surface (y - z -plane).

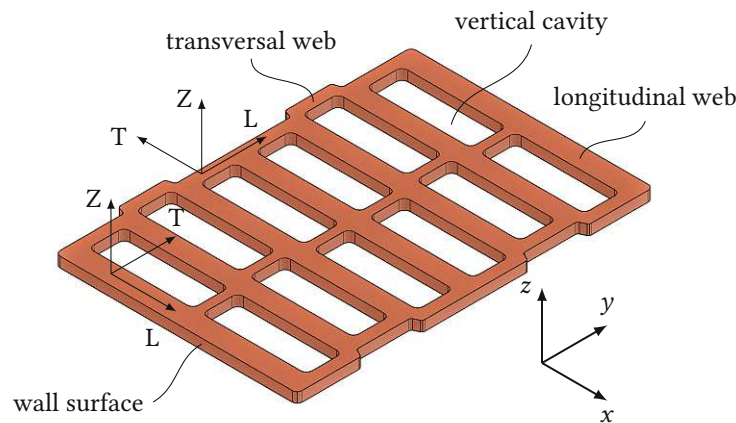


Fig. 3.1: Parts of a vertically perforated clay block and material orientation represented by the L-T-Z coordinate system (from [127]). While the Z-axis coincides with the z-axis, the L- and T-axis follow the orientation of the webs.

In general, masonry is constructed by putting prefabricated blocks together in a regular pattern, joined by an adhesive material between these blocks, to ensure a sufficient tensile and shear strength of the resulting structure. Traditionally, mortar was used for this purpose. Nowadays, other materials like polyurethane glue simplify the production process. Horizontal joints are referred to as *bed joints*, vertical ones as *head joints*. In terms of strength, these joints are a structural weakness; however, they are necessary for the structure's ductility, required to withstand cyclic shear loads e.g., during earthquakes.

3.2.1 Utilizing the periodicity of masonry – Unit cell concept

Since vertically perforated clay block masonry is commonly built up in a periodic pattern, the use of a unit cell approach with periodic boundary conditions is possible. Hence, a unit cell concept was implemented, which was proposed by Kiefer et al. [76] and applied with minor adaptations in [142]. Using this concept we can approximate the response of the entire specimen by modeling only a small part of the structure, the so-called *repeating unit cell*. Hence, the computation times can be kept short, although complex non-linear material models are used.

3.2.1.1 Defining a repeating unit cell

For simplifying the definition of the periodic boundary conditions within the FEM framework, a cuboid unit cell was chosen. The smallest cuboid unit cell found in a masonry wall with an offset of half a

block's width is two blocks high and one block wide (see Fig. 3.2). The following convention was used for referring to the surfaces, edges, and vertices of the unit cell [14]:

- Surfaces are denoted *North, South, East, West, Top, and Bottom*.
- The names of the edges and vertices consist of the first letters of the intersecting surfaces (e. g. NW and SWB).

The unit cell consists of six parts, which are segments of two full clay blocks. The dimensions of each part P1 to P6 are shown in Fig. 3.2b. For modeling the mortar joints we decided to use a simplified micro-modeling approach [86]. Therefore, we modeled the blocks in full detail, while reducing the mortar joints to 2D interfaces between those blocks. When reducing the mortar joints to interfaces, the total dimensions of the unit cell can be kept constant by evenly distributing the thickness of each joint to the dimensions of the adjacent blocks [86]. Since increasing the web thickness would have a significant effect on the structural behavior, the thickness of the head joint was evenly distributed to the length of each cavity. The interaction properties for considering the mortar joints (see Section 3.2.2.2) were imposed on each surface in contact with another surface.

3.2.1.2 Periodic Boundary Conditions and Homogenization

The repeating unit cell is two-dimensionally periodic, i. e., in x - and z -direction, using the same coordinate system as shown in Fig. 3.1. The vectors c_x and c_z describe this periodicity and contain essentially the dimension of the unit cell in the given direction. To ensure geometric compatibility between the neighboring instances of the unit cell in the deformed state, periodic boundary conditions were applied on the periodic surfaces. These periodic boundary conditions are linear equations, which couple the displacements of each pair of corresponding points on opposing surfaces to the displacements of the

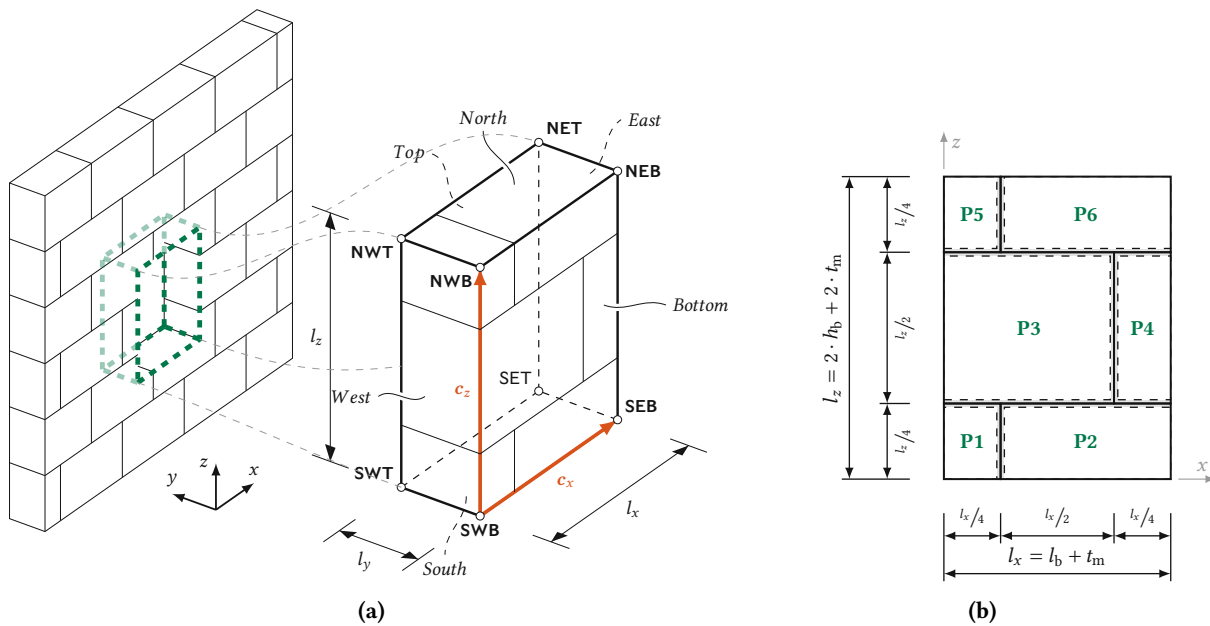


Fig. 3.2: Composition and geometry of the chosen repeating unit cell as part of the entire structure (a) and dimensions of the six fired clay parts (b). The naming convention in (a) is based on the suggestions from Böhm [14].

primary nodes of the unit cell. Hence, the displacement of a point *A* on surface *South* is coupled to the displacement of the opposing point *B* on surface *North* and the displacements of the primary nodes. The same applies to each point on surface *East* and the opposing point on surface *West*. In contrast, the surfaces *Top* and *Bottom* may deform freely. A more detailed explanation of the implementation of the periodic boundary conditions is given in Suda et al. [142].

Using periodic boundary conditions, the deformation difference $\Delta \mathbf{u}$ between two surfaces is constant [96]. Hence, for prescribing a deformation-controlled loading on the repeating unit cell, this deformation difference has to be defined for only two pairs of nodes per periodicity direction: the primary nodes (e. g., SWB-NWB and SWT-NWT in *z*-direction). By systematically controlling these deformation differences, we can impose effective in-plane strain states on the unit cell (see Table 3.1). Thus, we can simulate arbitrary macroscopic in-plane strain states $\bar{\boldsymbol{\varepsilon}}$ by combining the load cases in Table 3.1. These macroscopic strains applied to the FE model enable the identification of strains $\boldsymbol{\varepsilon}$ on microscale. These micro strains lead to stresses $\boldsymbol{\sigma}$ on the microscale, which we homogenize to macroscopic stresses $\bar{\boldsymbol{\sigma}}$.

The deformation difference $\Delta \mathbf{u}_i$ is related to the macroscopic strain state $\bar{\boldsymbol{\varepsilon}}$ through the periodicity vector \mathbf{c}_i :

$$\Delta \mathbf{u}_x = \bar{\boldsymbol{\varepsilon}} \cdot \mathbf{c}_x = \begin{pmatrix} \bar{\varepsilon}_{xx} \cdot l_x \\ \bar{\varepsilon}_{xy} \cdot l_x \\ \bar{\varepsilon}_{xz} \cdot l_x \end{pmatrix} \quad \text{and} \quad \Delta \mathbf{u}_z = \bar{\boldsymbol{\varepsilon}} \cdot \mathbf{c}_z = \begin{pmatrix} \bar{\varepsilon}_{xz} \cdot l_z \\ \bar{\varepsilon}_{yz} \cdot l_z \\ \bar{\varepsilon}_{zz} \cdot l_z \end{pmatrix}, \quad (3.1)$$

with the dimensions of the repeating unit cell in *x*- and *z*-direction, l_x and l_z , respectively. Prescribing zero displacements at primary nodes SWB and SWT allows us to fully prescribe the calculated deformation difference at the opposing node, which leads to the relations in Table 3.1.

Tab. 3.1: Primary node displacements for imposing effective strain states.

	strain state	primary node displacement
LC1	$\begin{bmatrix} \bar{\varepsilon}_{xx} & 0 \\ 0 & 0 \end{bmatrix}$	<i>Horizontal uniaxial strain</i> $u_x^{\text{SEB}} = \bar{\varepsilon}_{xx} \cdot l_x, \quad u_x^{\text{SET}} = \bar{\varepsilon}_{xx} \cdot l_x$
LC2	$\begin{bmatrix} 0 & 0 \\ 0 & \bar{\varepsilon}_{zz} \end{bmatrix}$	<i>Vertical uniaxial strain</i> $u_z^{\text{NWB}} = \bar{\varepsilon}_{zz} \cdot l_z, \quad u_z^{\text{NWT}} = \bar{\varepsilon}_{zz} \cdot l_z$
LC3	$\begin{bmatrix} 0 & \bar{\varepsilon}_{xz} \\ \bar{\varepsilon}_{xz} & 0 \end{bmatrix}$	<i>Pure shear strain</i> $u_z^{\text{SEB}} = \bar{\varepsilon}_{xz} \cdot l_x, \quad u_z^{\text{SET}} = \bar{\varepsilon}_{xz} \cdot l_x$ $u_x^{\text{NWB}} = \bar{\varepsilon}_{xz} \cdot l_z, \quad u_x^{\text{NWT}} = \bar{\varepsilon}_{xz} \cdot l_z$

The following primary node displacements were imposed in each case: $u_x^{\text{SWB}} = u_y^{\text{SWB}} = u_z^{\text{SWB}} = 0, u_x^{\text{SWT}} = u_z^{\text{SWT}} = 0, u_y^{\text{SEB}} = 0, \text{ and } u_y^{\text{NWB}} = 0$

3.2.1.3 Stress homogenization

The macroscopic stress state is the main result we wanted to obtain from the simulations. In each point on the surface of the unit cell, multiplying the macroscopic stress tensor $\bar{\boldsymbol{\sigma}}$ with the surface normal vector $\mathbf{n}(\mathbf{x})$ leads to the traction stress vector $\mathbf{t}(\mathbf{x})$. Since the macroscopic stresses are considered constant over the repeating unit cell, these traction stresses are also constant for points with the same surface normal

vector. Integrating the macroscopic traction stresses \mathbf{t} over one surface \mathcal{S} of the repeating unit cell leads to the total amount of forces acting on this surface:

$$\mathbf{F}^i = \int_{\mathcal{S}} \bar{\boldsymbol{\sigma}} \cdot \mathbf{n}_i \, dS = \bar{\boldsymbol{\sigma}} \cdot \mathbf{n}_i \cdot A_i. \quad (3.2)$$

Since the displacements are only prescribed at the primary nodes, the traction forces for a surface are essentially the sum of reaction forces occurring at the primary nodes located on this surface. Evaluating Eq. (3.2) for surfaces *East* with \mathbf{n} pointing in positive x -direction, and *North* with \mathbf{n} pointing in positive z -direction leads to the following relations:

$$\mathbf{F}^E = \mathbf{F}^{\text{SEB}} + \mathbf{F}^{\text{SET}} = \begin{pmatrix} \bar{\sigma}_{xx} \\ \bar{\sigma}_{xy} \\ \bar{\sigma}_{xz} \end{pmatrix} \cdot A_E \quad \text{and} \quad \mathbf{F}^N = \mathbf{F}^{\text{NWB}} + \mathbf{F}^{\text{NWT}} = \begin{pmatrix} \bar{\sigma}_{xz} \\ \bar{\sigma}_{yz} \\ \bar{\sigma}_{zz} \end{pmatrix} \cdot A_N. \quad (3.3)$$

Hence, the macroscopic stress tensor can be obtained from the reaction forces at the primary nodes as

$$\bar{\boldsymbol{\sigma}} = \begin{bmatrix} \frac{F_x^{\text{SEB}} + F_x^{\text{SET}}}{A_E} & \frac{F_z^{\text{SEB}} + F_z^{\text{SET}}}{A_E} \\ \frac{F_x^{\text{NWB}} + F_x^{\text{NWT}}}{A_N} & \frac{F_z^{\text{NWB}} + F_z^{\text{NWT}}}{A_N} \end{bmatrix}. \quad (3.4)$$

It is important to note that the unit cell concept and the homogenization procedure require a homogeneous stress state across the unit cell's dimensions. Consequently, the applicability of these methods is primarily limited to larger masonry walls where this condition can be met. Conversely, when dealing with smaller structures, it is advisable to consider a more detailed micro-modeling approach.

3.2.2 Failure mechanisms implemented in the finite element model

Both clay block failure and joint failure are relevant for the structural collapse of vertically perforated clay block masonry under in-plane loading. The clay blocks mostly fail due to tensile cracks in the transversal or longitudinal webs [76, 85, 142]. For the mortar joints, shear failure or tensile failure (or a combination of both) can be relevant, depending on the stress component perpendicular to the joint [25]. Based on these observations, the following failure mechanisms were implemented in the numerical model.

3.2.2.1 Brittle failure of fired clay

For the brittle failure of the fired-clay blocks a combination of the XFEM [7], the orthotropic Hoffman criterion [67], and the Virtual Crack Closure Technique (VCCT) [130, 131] was used. This strategy was proposed by Kiefer et al. [76] and was successfully applied in another study [142]. The XFEM approach uses special displacement functions at so-called *enriched nodes*, which allow the modeling of discrete propagating cracks without re-meshing. For initiating such cracks, the orthotropic Hoffman criterion is used, which takes into account the material's tensile, compressive, and shear strengths (see Appendix C). Using this formulation, the failure criterion cannot capture triaxial compressive failure. Since the webs can be considered plate-like structures, which are not loaded perpendicular to their surface, the stress state in the webs is nearly plane. Therefore, triaxial compressive failure is not relevant in this case. After a crack is initiated, a *crack evolution criterion*, in our case the VCCT, depicts the onset of the

crack. Details on the implementation of XFEM and VCCT in Abaqus can be found in the Abaqus Online Documentation [30].

Considering orthotropic material behavior is essential for vertically perforated clay blocks, due to the orthotropic nature of extruded fired clay [17, 23, 51]. This orthotropy originates in the manufacturing process, where the raw material is extruded and cut into blocks. During the extrusion process, the flat clay minerals align parallel to the surface of the given part [17], leading to a locally changing coordinate system (L-T-Z) on the material level (see Fig. 3.1). Hence, the stiffness in T-direction is approximately 37%–60% of the stiffness in Z-direction (see Buchner et al. [20]). Since the stiffness in L-direction is only insignificantly below the stiffness in Z-direction, considering the material as transversally isotropic is a reasonable approximation, as Buchner et al. [20] showed. Thus, the material's stiffness and strength were considered transversally isotropic in this work (see Tables 3.3 and 3.4).

The application of the VCCT is based on linear elastic fracture mechanics, which allows a good approximation of the brittle failure of fired clay. The main assumption of the VCCT is that the strain energy released when opening a crack is equal to the strain energy needed to close the same crack [78]. Based on this assumption, the energy release rate G is calculated and compared to a critical value G_c . In the numerical model, a power law was used to consider all three failure modes:

$$f = \frac{G}{G_c} = \left(\frac{G_I}{G_{I,c}} \right)^a + \left(\frac{G_{II}}{G_{II,c}} \right)^b + \left(\frac{G_{III}}{G_{III,c}} \right)^c = 1. \quad (3.5)$$

Considering the findings of Bocca et al. [12], Hannawald [63], as well as Eis and Vassilev [41], lower and upper limits for the mode-I fracture energy are $G_{I,c}^{\min} = 0.01 \text{ J/mm}^2$ and $G_{I,c}^{\max} = 0.05 \text{ J/mm}^2$. Since mode-I failure is governing, the fracture energies for modes II and III were chosen 20 times larger, following Kiefer et al. [76]. The superscripts a , b , and c were all set to 1.

3.2.2.2 Failure of the mortar joints

The shear behavior of mortar joints was thoroughly analyzed by Van der Pluijm [145]. He not only published comprehensive testing data on the strengths but also on the post-peak behavior including fracture energy values. According to Van der Pluijm [145] the shear strength $\tau_{m,f}$ of a mortar joint follows a Mohr-Coloumb law:

$$\tau_{m,f} = \tau_{m,ini} - \mu_m \cdot \sigma_{\perp}, \quad (3.6)$$

with the initial shear strength $\tau_{m,ini}$, the frictional parameter μ_m , and the stress component perpendicular to the joint, σ_{\perp} . Hence, the shear strength increases with increasing compressive stresses perpendicular to the joint and decreases vice versa. With increasing tensile stresses the shear strength eventually reaches zero.

In displacement-controlled shear tests Van der Pluijm [145] observed a damage evolution, which can be sufficiently described by an exponential relation. Furthermore, the remaining shear strength decreases until it reaches a constant residual strength value depending on the stress perpendicular to the joint.

We modeled the joints as interfaces using a surface-to-surface contact formulation [15, 143]. For recreating the joint behavior we deployed a *cohesive behavior* approach in combination with frictional properties, a quadratic stress interaction damage criterion, and exponential damage evolution. A similar approach has been previously used by Bolhassani et al. [15] as well as Thamboo and Dhanasekar [143] for concrete block masonry. In line with Bolhassani et al., we combined the failure mechanisms of both

the mortar and the interface into a single interface criterion. Consequently, the calibrated interface damage properties reproduce the decisive failure mechanism. Conversely, Thamboo and Dhanasekar modeled the mortar joints as three-dimensional continua, employing Concrete Damaged Plasticity for modeling mortar failure and the cohesive approach solely for considering interface failure. We opted for the simplified micro-modeling approach for several reasons. Notably, modeling a typical thin-layer mortar joint with a 1 mm thickness would necessitate an exceedingly fine mesh to maintain viable element aspect ratios. Additionally, this approach also allows for modeling modern joints bonded with polyurethane adhesives with minor adaptations.

The stiffness of the mortar joint is defined through the parameters K_{nn} , K_{ss} , and K_{tt} . These stiffness parameters control the relationship between the traction stresses t_i and the separations δ_i between the surfaces as

$$t_i = K_{ii}\delta_i, \quad \forall i \in \{n, s, t\}. \quad (3.7)$$

Thereby, n , s , and t define an orthogonal coordinate system with n pointing perpendicular to the joint. Thus, the s - t plane is parallel to the joint. Considering isotropic material behavior, the stiffness parameters were derived from the Young's modulus E_m and the shear modulus G_m by multiplication with the joint thickness t_m :

$$K_{nn} = E_m \cdot t_m, \quad \text{and} \quad K_{ss} = K_{tt} = G_m \cdot t_m = \frac{E_m}{2 \cdot (1 + \nu_m)} \cdot t_m. \quad (3.8)$$

Notably, Eq. (3.7) only holds for positive contact clearance (see also the definition in the Abaqus Documentation [30]). For negative clearance (i. e. mortar deformations under compressive stresses) a tabular pressure-overclosure formulation was defined (see Fig. 3.3). Until reaching the compressive strength, tabular definition delivers the same pressure values as with the stiffness parameter K_{nn} . At the compressive strength of the mortar, a plateau is modeled. Since compressive mortar failure was only relevant in some small regions of the model for a limited number of cases, this simplified approach was sufficient to consider non-linear mortar behavior under compressive loads. An insignificant contact pressure at zero overclosure was implemented to overcome numerical problems when initiating contact.

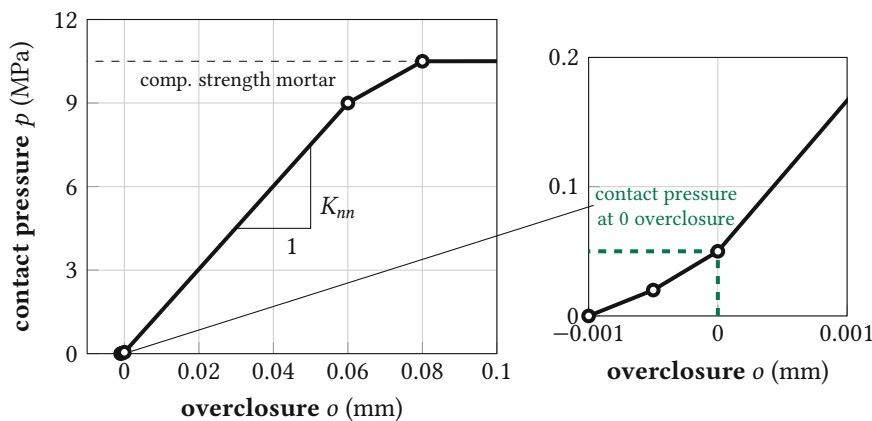


Fig. 3.3: Tabular pressure-overclosure formulation used for modeling the mortar joints in the simulations. A small artificial contact pressure at zero overclosure was implemented to overcome numerical problems when initiating contact.

Within the framework of cohesive behavior, the following quadratic stress interaction was used as a damage criterion:

$$\left(\frac{\langle t_n \rangle}{t_{f,n}}\right)^2 + \left(\frac{t_s}{t_{f,s}}\right)^2 + \left(\frac{t_t}{t_{f,t}}\right)^2 = 1, \quad (3.9)$$

with the traction stresses t_i and the traction strengths $t_{f,i}$. In compression, only the interaction of the shear stresses is considered since $\langle t_n \rangle$ is zero for negative tractions t_n . For implementing a similar relation as depicted by Van der Pluijm [145], we used an additional frictional parameter. With this frictional parameter the shear strengths in Eq. (3.9) are calculated using a Mohr-Coloumb relation and the contact pressure, leading to the following equation:

$$\left(\frac{\langle t_n \rangle}{t_{f,o}}\right)^2 + \left(\frac{t_s}{t_{f,o} - \mu_m \cdot t_n}\right)^2 + \left(\frac{t_t}{t_{f,t} - \mu_m \cdot t_n}\right)^2 = 1, \quad (3.10)$$

which is simplified to

$$\left(\frac{\langle \sigma_{\perp} \rangle}{\sigma_{f,\perp}}\right)^2 + \frac{\tau^2}{(\tau_{m,ini} - \mu_m \cdot \sigma_{\perp})^2} = 1, \quad (3.11)$$

with equal shear strengths $t_s^0 = t_t^0 = \tau_{ini}$ and the total shear stress $\tau^2 = t_s^2 + t_t^2$. Additionally, the traction in n -direction, t_n , and the corresponding strength $t_{f,n}$ were replaced by the stress component perpendicular to the joint, σ_{\perp} , and the tensile strength $\sigma_{f,\perp}$. The material parameters used in the simulations, i. e. peak strengths $\tau_{m,ini}$ and $\sigma_{f,\perp}$ as well as the friction coefficient μ_m , were back-calculated from shear tests and can be found in Section 3.3.

The exponential post-peak behavior observed by Van der Pluijm [145] was modeled by using a displacement-type exponential damage evolution within the cohesive-behavior property (see [30]). Here, two input parameters are necessary: the maximum displacement δ_m^{\max} at which the strength reaches its minimum and an exponential parameter α . The maximum displacement was chosen with $\delta_m^{\max} = 0.15$ mm leading to a fracture energy of 0.088 J/mm², matching the findings by Van der Pluijm [145]. The exponential parameter was set to $\alpha = 5$.

3.2.3 Failure Criterion

For identifying peak stresses for an arbitrary macroscopic strain state a two-condition failure criterion was used. At the macroscopic scale, the stress state before the first significant decrease of a stress component was considered as macroscopic peak stress state $\bar{\sigma}^f$. This criterion was relevant, especially for joint failure, which occurs much more ductile than block failure. Furthermore, a second criterion considering the first crack within the blocks was defined to capture block failure. This was necessary, since some of the simulations, where block failure was relevant, did not produce a significant drop in stresses. Instead, these simulations aborted when the first crack opened. Considering the findings of Kiefer et al. [76] and Suda et al. [142], this is a good approximation, since there, the first crack also occurred just before the peak stress was reached.

3.3 Experiments and Simulations

3.3.1 Experiments used for Validation

For validating the numerical model we used an experimental study conducted by Bitterli and Salmanpour [11, 133] (see Fig. 3.4). In the study, they did uniaxial compression tests on seven masonry specimens with inclined bed joints to investigate the behavior of vertically perforated block masonry under combined compressive and shear loads. The specimens were 1.20 m high and 1.20 m long (see Fig. 3.5a); the bed joint incline was varied from 0° (vertical compression) to 90° (horizontal compression) in increments of 15° . Within this study Bitterli and Salmanpour obtained material strength and stiffness parameters depending on the bed joint incline and also described the changes in failure mechanisms. Each experiment is referred to by the angle of incline and a preceding “E”, i. e., “E75” refers to the experiment with 75° incline.

Additionally, Bitterli and Salmanpour [11, 133] conducted three shear tests on masonry triplets according to EN 1052-3 [44]. These tests were performed with three different levels of pre-compression. Hence, assuming the joint behavior follows a Mohr-Coulomb law, the initial shear strength $\tau_{m,ini}$ and the friction parameter μ_m could be obtained from the results.

Typical vertically perforated clay blocks (*Swissmodul B15/19*) from a Swiss manufacturer were used for the experiments (see Fig. 3.5b). These blocks were 290 mm long, 190 mm high, and 150 mm wide, with a void ratio of 42 %. In compressive tests according to EN 772-1 [48], they obtained a compressive block strength of $f_b = 26.3$ MPa. The mortar used (“Weber mur 920 M15”) is a ready-mixed general-purpose cement mortar. In flexural and compressive tests according to EN 1015-11 [42], Salmanpour [133] obtained a compressive strength of $f_m = 10.5$ MPa and a flexural strength of $f_{mq} = 2.8$ MPa.

Each specimen was loaded cyclically with displacement-controlled loading phases and force-controlled unloading phases until the peak stress was reached. The loads were introduced by hydraulic jacks and

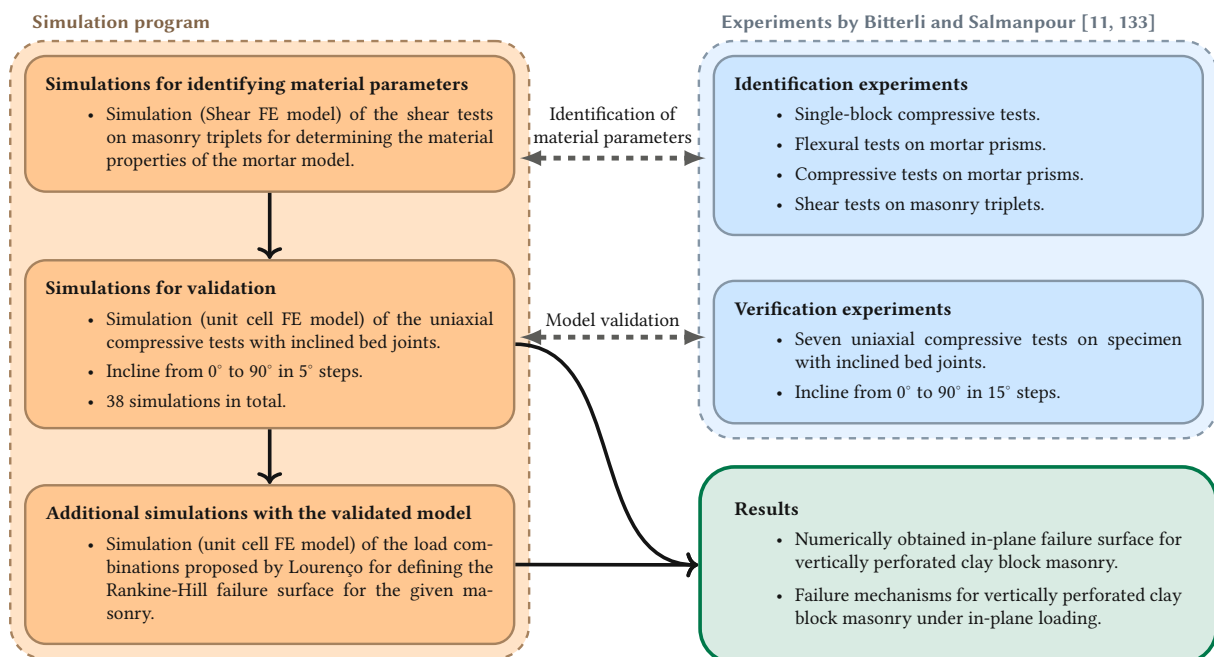


Fig. 3.4: Overview of the modeling procedure.

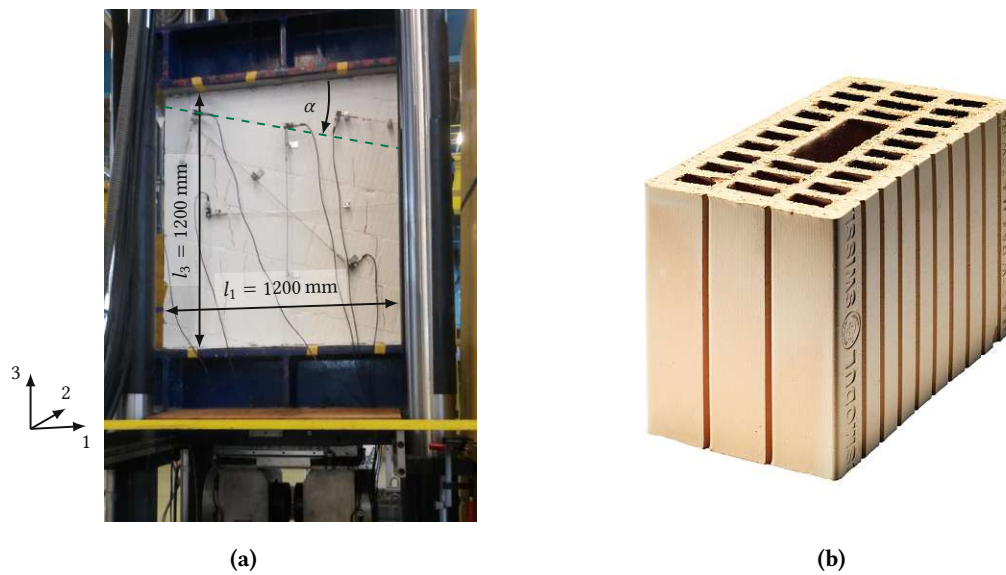


Fig. 3.5: Experiments conducted by Bitterli and Salmanpour [11, 133]: (a) experimental setup for E15 and (b) used clay block *Swissmodul B15/19* (Image from [156]).

distributed by two large spreader beams at the top and bottom of the specimen. Gypsum layers were placed between the spreader beams and the specimen to compensate for surface irregularities. On one surface of the specimen, digital image correlation (DIC) was used for obtaining strain information. On the opposite surface, the deformations were captured by five linear variable differential transformers (LVDTs). The forces used to calculate the resulting stresses were obtained from the testing machine.

The peak stresses obtained by Bitterli and Salmanpour [11, 133] are plotted against the bed joint incline in Fig. 3.6. The vertical compressive strength f_{mz} (E00) was 5.35 MPa. With increasing incline, the compressive strength decreased drastically to 25 % of f_{mz} at E45, whereafter it stayed nearly constant until E75. For E90 the compressive strength increased again to 38 % of the vertical compressive strength. Hence, the largest peak stresses were obtained with predominant compressive loading perpendicular to the bed joint, while the smallest values were observed when the shear stresses reach their maximum.

Besides the peak stresses Bitterli and Salmanpour [11, 133] also analyzed the crack patterns, failure mechanisms and stress-strain-relations. According to their observations, the behavior changed significantly with the bed joint incline. Specimens E00 and E15 failed very brittle, due to cracks in the transversal webs, leading to spalling of the outermost longitudinal webs. The stress-strain relation in z -direction was linear almost until collapse (see Fig. 3.14). Specimen E30 showed both cracks in the blocks and the joints and the failure was more ductile. In experiments E45, E60, and E75, joint failure was triggering collapse, as gliding planes in the bed joints started to form. The failure occurred even more ductile than for E30 and after the peak stress was reached, large strain values could be observed before collapse (see Fig. 3.14). Specimen E90 again failed brittly, showing tensile cracks in the transversal webs.

3.3.2 Simulation Program

For validating the numerical model described in Section 3.2 we modeled each of the experimental setups described above. While Bitterli and Salmanpour [11, 133] investigated the influence of the bed joint incline in increments of 15° , we did simulations in increments of 5° (see Fig. 3.4). Additionally, we defined

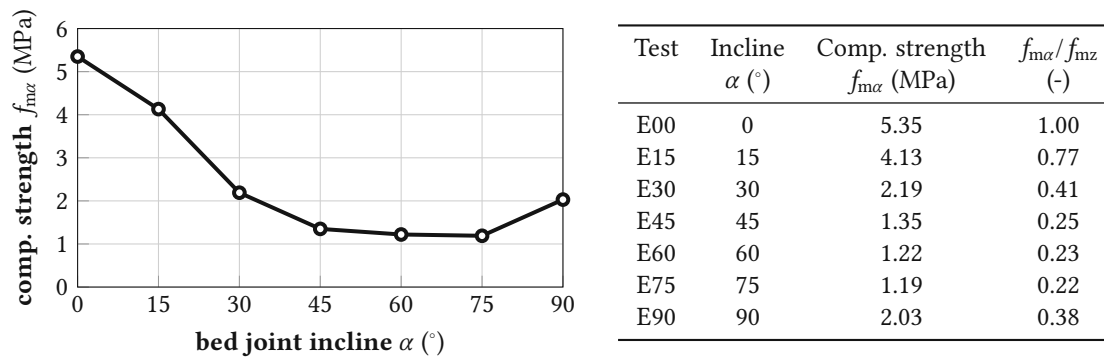


Fig. 3.6: Experimentally obtained peak stresses with varying bed joint incline taken from Bitterli and Salmanpour [11, 133].

upper and lower bounds for the material properties (see Section 3.3.2.3). Hence, a total of 38 simulations were performed in the FE software Abaqus. Similar to the naming convention of the experiments, we refer to the simulations with a prefix “S” to the incline angle. Additionally, “-max” or “-min” is appended to clarify, if the upper or lower bounds of the material properties were used. We derived the geometry, boundary conditions, and material properties for the numerical models from the experimental study, as shown next.

3.3.2.1 Geometry and Mesh

The geometric definition of the FE model follows the unit-cell concept described in Section 3.2.1. Hence, a cuboid part, which is two blocks high and one block wide, was extracted from the specimen (see Fig. 3.7). The FE model consists of six block parts, with an offset of half a block width. These parts are connected with the previously described interface properties in the head joints and the bed joints (see Fig. 3.7). Notably, in the bed joints the transversal webs are mostly not on top of each other due to the horizontal offset. Thus, the surfaces are only connected, where webs were directly on top of each other, leading to a total contact ratio of 64 % in the bed joints. In contrast, the surfaces in the head joints are fully in contact.

The model consists of 107 326 linear eight-node brick elements (C3D8) and 146 646 nodes. In the framework of the XFEM, cracks were allowed to form anywhere in the model, with one restriction: no crack was allowed to initiate within a radius of 20 mm from an existing crack tip.

3.3.2.2 Boundary Conditions

Although each simulation has a different bed joint incline, the geometry and the mesh remain constant for each simulation. Instead of changing the geometry, the boundary conditions were adapted to obtain the desired macroscopic stress state. Therefore, the loading had to be rotated and split up into its components parallel and perpendicular to the bed joints.

We defined two coordinate systems to distinguish between two levels of observation: the *global coordinates* 1-2-3, which follow the orthogonal boundaries of the specimen, and the *local coordinates* x - y - z , which follow the orthogonal system of mortar joints and are already shown in Figs. 3.1 and 3.2 (see Fig. 3.8). In the global coordinate system, the 3-direction is parallel to the uniaxial loading direction (vertical). The plane spanned by the 1- and 3-axis is parallel to the wall’s surface. Hence, the 2-axis

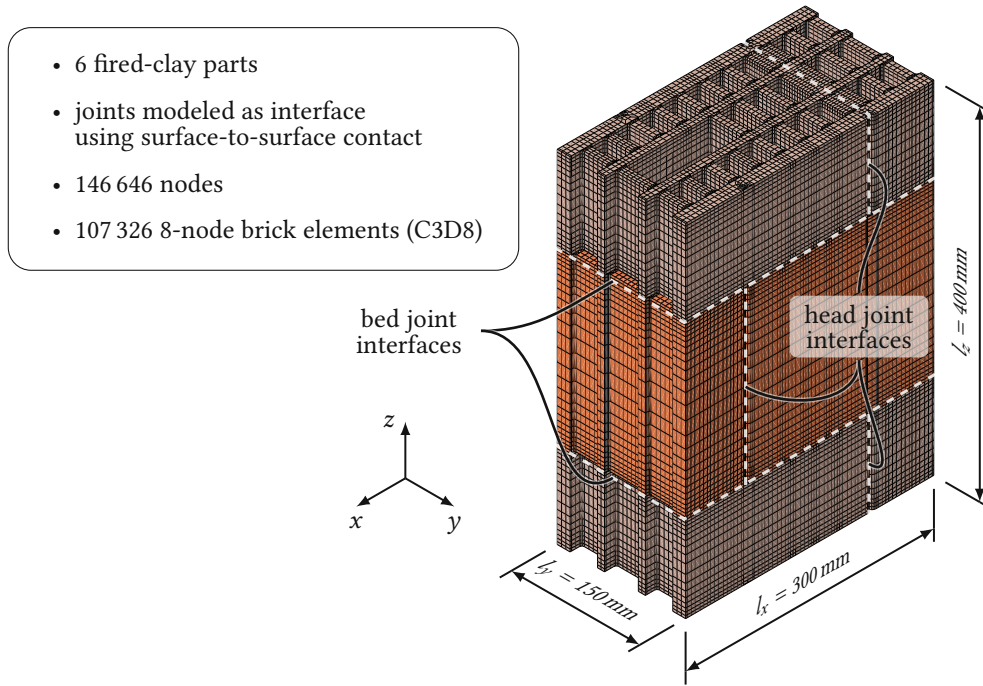


Fig. 3.7: Unit cell finite element model used for the validation simulations (see also Fig. 3.4). The middle layer is colored differently to emphasize the different block layers with mortar interfaces in between.

is perpendicular to this surface. While the global coordinate system is similar in each specimen, the local coordinate system depends on the bed joint incline. It is obtained by rotating the global coordinate system around the 2-axis by the bed joint incline, leading to the x -axis being parallel to the bed joints, the z -axis being parallel to the head joints, and the y -axis coinciding with the 2-axis.

Considering the experimental setup, in the global coordinate system a uniaxial stress state can be assumed in the middle of the specimen. This stress state was rotated by the angle of incline to obtain the equivalent macroscopic stress state in local coordinates:

$$\bar{\sigma}_{\text{local}} = \mathbf{R}(\alpha) \cdot \bar{\sigma}_{\text{global}} \cdot \mathbf{R}^T(\alpha) = \begin{bmatrix} \cos(\alpha) & -\sin(\alpha) \\ \sin(\alpha) & \cos(\alpha) \end{bmatrix} \cdot \begin{bmatrix} 0 & 0 \\ 0 & \bar{\sigma}_{33} \end{bmatrix} \cdot \begin{bmatrix} \cos(\alpha) & \sin(\alpha) \\ -\sin(\alpha) & \cos(\alpha) \end{bmatrix}, \quad (3.12)$$

with the rotation matrix \mathbf{R} .

Knowing the desired local macroscopic stress state, the related local macroscopic strain tensor $\bar{\epsilon}_{\text{local}}$ was calculated according to Hooke's law as

$$\bar{\epsilon}_{\text{local}} = \bar{\mathbf{C}}_{\text{local}}^{-1} : \bar{\sigma}_{\text{local}}, \quad (3.13)$$

with the local macroscopic stiffness tensor $\bar{\mathbf{C}}_{\text{local}}$. This stiffness tensor was found by a numerical stiffness homogenization procedure, utilizing the unit cell approach. The five necessary components of the stiffness tensor could be derived by deliberately eliminating strain components in Hooke's law. Hence,

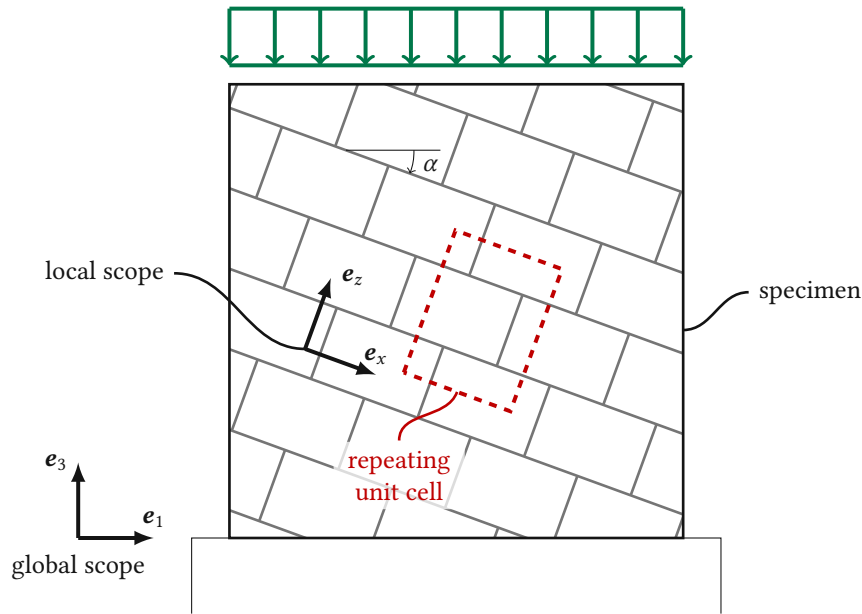


Fig. 3.8: Definition of the local and global coordinate system. Rotating the global coordinate system around the y -axis by the angle of incline α leads to the local coordinate system. The dashed line marks the boundaries of the repeating unit cell, which was used for defining the FE model in Fig. 3.7.

simulating the three strain states LC1–LC3 in Table 3.1 was sufficient for deriving the local macroscopic stiffness tensor as

$$\bar{\mathbf{C}}_{\text{local}} = \begin{bmatrix} \frac{\bar{\sigma}_{xx}^{\text{LC1}}}{\bar{\epsilon}_{xx}^{\text{LC1}}} & \frac{\bar{\sigma}_{xx}^{\text{LC2}}}{\bar{\epsilon}_{xx}^{\text{LC2}}} & 0 \\ \frac{\bar{\sigma}_{zz}^{\text{LC1}}}{\bar{\epsilon}_{xx}^{\text{LC1}}} & \frac{\bar{\sigma}_{zz}^{\text{LC2}}}{\bar{\epsilon}_{xx}^{\text{LC2}}} & 0 \\ 0 & 0 & \frac{\bar{\sigma}_{xz}^{\text{LC3}}}{\bar{\epsilon}_{xz}^{\text{LC3}}} \end{bmatrix}. \quad (3.14)$$

After calculating the local macroscopic strain components with Eq. (3.13), the primary node displacements for each simulation could be derived by a linear combination of the three cases in Table 3.1. Table 3.2 gives an overview of the calculated components for the seven experiments conducted by Bitterli and Salmanpour [11, 133].

Tab. 3.2: Prescribed stresses and strains for the simulated experiments.

ID	α	$\bar{\sigma}_{xx}$	$\bar{\sigma}_{zz}$	$\bar{\sigma}_{xz}$	$\bar{\epsilon}_{xx}$	$\bar{\epsilon}_{zz}$	$\bar{\epsilon}_{xz}$
S00	0°	0.00 MPa	−10.00 MPa	0.00 MPa	0.14×10^{-3}	-1.69×10^{-3}	0.00
S15	15°	−0.67 MPa	−9.33 MPa	−2.50 MPa	-0.07×10^{-3}	-1.57×10^{-3}	-0.83×10^{-3}
S30	30°	−2.50 MPa	−7.50 MPa	−4.33 MPa	-0.63×10^{-3}	-1.23×10^{-3}	-1.45×10^{-3}
S45	45°	−5.00 MPa	−5.00 MPa	−5.00 MPa	-1.40×10^{-3}	-0.78×10^{-3}	-1.67×10^{-3}
S60	60°	−7.50 MPa	−2.50 MPa	−4.33 MPa	-2.17×10^{-3}	-0.32×10^{-3}	-1.45×10^{-3}
S75	75°	−9.33 MPa	−0.67 MPa	−2.50 MPa	-2.74×10^{-3}	0.02×10^{-3}	-0.83×10^{-3}
S90	90°	−10.00 MPa	0.00 MPa	0.00 MPa	-2.94×10^{-3}	0.14×10^{-3}	0.00

3.3.2.3 Material parameters

Fired Clay Blocks

For defining the orthotropic stiffness behavior, we used nine independent parameters, given in the material orientation L-T-Z: the Young's moduli E_{LL} , E_{TT} , E_{ZZ} , the Poisson's ratios ν_{TZ} , ν_{LZ} , ν_{LT} , and the shear moduli G_{TZ} , G_{LZ} , G_{LT} (see Table 3.3). The Young's modulus in Z-direction, E_{ZZ} , could be back-calculated from single-block experiments. With this value as a basis, the other Young's moduli, as well as the shear moduli, were scaled by the ratios obtained from Buchner et al. [20], considering transversally isotropic material behavior. The Poisson's ratios were estimated with the experimentally obtained data from Hannawald [63]. Note, that the parameters refer to the local L-T-Z coordinate system shown in Fig. 3.1.

The nine strength parameters for defining the Hoffman criterion, the compressive strengths $\sigma_{c,L}$, $\sigma_{c,T}$, $\sigma_{c,Z}$, the tensile strengths $\sigma_{t,L}$, $\sigma_{t,T}$, $\sigma_{t,Z}$, and the shear strengths $\sigma_{s,L}$, $\sigma_{s,T}$, $\sigma_{s,Z}$, were found similar to the stiffness parameters. Salmanpour [133] obtained the compressive strength in Z-direction from compressive tests on single blocks according to EN 772-1 [48]. Using this parameter as a basis, the other compressive strengths, as well as the tensile strengths were scaled according to typical ratios for fired clay provided by Kiefer et al. [76] (see Table 3.4). Considering the standard deviation of the compressive strength in Z-direction [133], minimum and maximum values were defined. For estimating each shear strength τ_{ij} an upper and lower bound was found from the corresponding tensile strengths, $\sigma_{t,i}$ and $\sigma_{t,j}$, and compressive strengths $\sigma_{c,i}$ and $\sigma_{c,j}$ [142] as

$$\tau_{ij,\min} = \frac{\sigma_{t,i} + \sigma_{t,j}}{2} \text{ and } \tau_{ij,\max} = \frac{\sigma_{c,i} + \sigma_{c,j}}{4}. \quad (3.15)$$

The mean value of these bound values was used as shear strength for the simulations.

Mortar Joints

From experiments on mortar prisms according to EN 1015-11 [42], Salmanpour [133] obtained the compressive strength $f_m = 10.5$ MPa and flexural strength $f_{mq} = 2.8$ MPa. Additionally, he found the Young's modulus of the mortar, $E_m = 6600$ MPa, in non-destructive compression tests. Hence, the stiffness parameters for the cohesive behavior approach were calculated as $K_{nm} = 660$ N/mm, and $K_{ss} = K_{tt} = 275$ MPa, using Eq. (3.8) with a joint thickness $t = 10$ mm and Poisson's ratio $\nu = 0.2$. Additionally, the pressure-overclosure formulation in Fig. 3.3 was calibrated with the Young's modulus and compressive strength.

The strength parameters for the cohesive surfaces, the initial shear strength $\tau_{m,\text{ini}}$ and the tensile strength $\sigma_{f,\perp}$, and the friction parameter μ_m , were back-calculated from shear tests on masonry triplets (see Fig. 3.9b) [11, 133] with an additional FE model, as discussed next. Considering the symmetry plane in the middle of the triplet, the model consisted of one full clay block, one half clay block, and two steel

Tab. 3.3: Transversally isotropic stiffness used for fired clay and interface stiffness used for mortar.

Fired Clay					Mortar Joints	
$E_{LL} = E_{ZZ}$	E_{TT}	$\nu_{TZ} = \nu_{LZ} = \nu_{LT}$	$G_{TZ} = G_{LT}$	G_{TZ}	K_{nm}	$K_{ss} = K_{tt}$
13 500 MPa	8738 MPa	0.2	3500 MPa	5500 MPa	660 N/mm	275 N/mm

Tab. 3.4: Transversally isotropic strength parameters for fired clay in MPa.

	Tension			Compression			Shear		
	$\sigma_{t,L}$	$\sigma_{t,T}$	$\sigma_{t,Z}$	$\sigma_{c,L}$	$\sigma_{c,T}$	$\sigma_{c,Z}$	$\sigma_{s,TZ}$	$\sigma_{s,LZ}$	$\sigma_{s,LT}$
% of $\sigma_{c,Z}$	29.0	20.0	29.0	100.0	77.0	100.0 ^a	34.4 ^b	39.5 ^b	34.4 ^b
min in (MPa)	7.009	4.834	7.009	24.17	18.61	24.17	8.308	9.547	8.308
max in (MPa)	8.245	5.686	8.245	28.43	21.89	28.43	9.773	11.23	9.773

^a Reference value experimentally obtained by Salmanpour [133]. ^b Calculated according to Eq. (3.15).

plates (see Fig. 3.9a). The lower steel plate was fixed in x -, y - and z -direction along a line parallel to the y -axis, allowing rotations around this direction. Additionally, a displacement symmetry condition was applied to the surface in the middle block, acting as a symmetry plane. The loads were applied in the following two steps: In the first step, we applied a pressure perpendicular to the bed joint (z -direction). In the second step, we fixed this pressure and applied a displacement in x -direction to the upper steel plate, eventually leading to a peak shear stress of the joint under the given pressure in z -direction.

Following this procedure we created four models with different pressure in z -direction, i. e. 0.0 MPa, 0.2 MPa, 0.6 MPa, as well as 1.0 MPa, and optimized the parameters of the interface damage criterion (Section 3.2.2.2) to obtain peak shear stresses in good agreement with the experiments performed by Bitterli and Salmanpour [11, 133]. Hence, these parameters were chosen with $\mu_m = 0.3$, $\sigma_{f,\perp} = 0.3$ MPa and $\tau_{m,ini} = 1.4$ MPa, leading to the results in Fig. 3.9c.

Salmanpour [133] also provided a standard deviation of 13.2 % for the flexural strength. This value was used to define lower and upper bound values for the strength parameters similar to the fired clay blocks (see Table 3.4) considering a normal distribution.

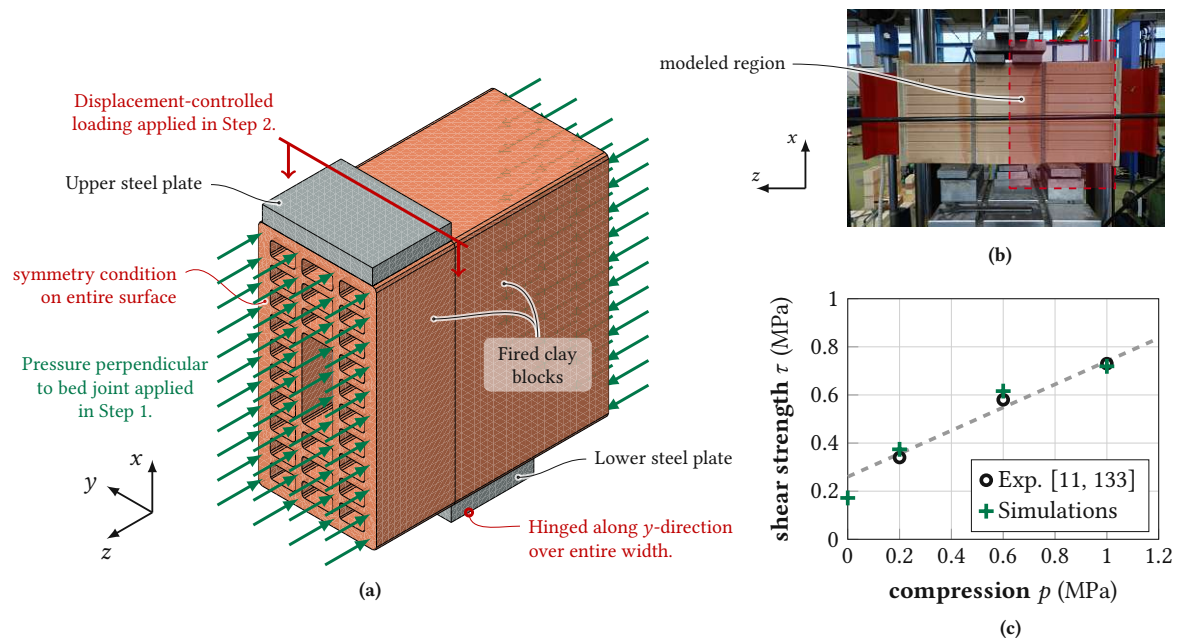


Fig. 3.9: The strength parameters for the mortar joints were derived by simulating shear tests on masonry triplets [11, 133]. (a) Finite element model, (b) experimental setup (from [11, 133]), and (c) comparison of numerically and experimentally obtained results.

3.3.2.4 Computational aspects

For overcoming numerical problems related to the initiation of contact between two surfaces, an additional step was introduced at the beginning of the calculation. In this step, the displacements of each primary node were set to zero. Due to the chosen pressure-overclosure formulation with an insignificant compressive contact stress at zero distance between the surfaces, contact could be ensured in each relevant point, before the displacement-controlled loading was applied in the following step.

The simulations were performed on a high-performance computing cluster with 168 CPUs in total. Using eight CPU cores in parallel, one simulation took approximately 700 minutes on average to finish.

3.4 Results and Discussion

Using the presented numerical approach we were able to identify not only the peak stresses but also the relations between the loading direction and occurring stresses, as well as three key mechanisms leading to failure (see Figs. 3.10 to 3.12 and Table 3.5). We begin by describing these results and comparing them to the experimental observations from Bitterli and Salmanpour [11, 133].

A vertical compressive load leads to vertical compressive stresses in the longitudinal webs, compressive stresses perpendicular to the bed joint, and tensile horizontal stresses in the transversal webs. The reason for these horizontal stresses, which are critical for failure, lies in the structural composition of the blocks and was described in [142]: Due to the offset of the blocks, some of the transversal webs are positioned not directly on top of each other. Therefore, the vertical compressive stresses are redistributed to the longitudinal webs, leading to tensile stresses in the transversal webs. Thus, under mainly vertical compressive loading (S00, S15, and S30), tensile cracks in the transversal webs led to failure (mechanism I, see Fig. 3.10a). Failure in the corresponding experiments (E00, E15, and E30) was governed by vertical cracks beginning in the head joints and spalling of the outermost longitudinal webs (see Fig. 3.10b). The observed spalling can be traced back to the tensile cracks mentioned above, as Kiefer et al. [76] stated.

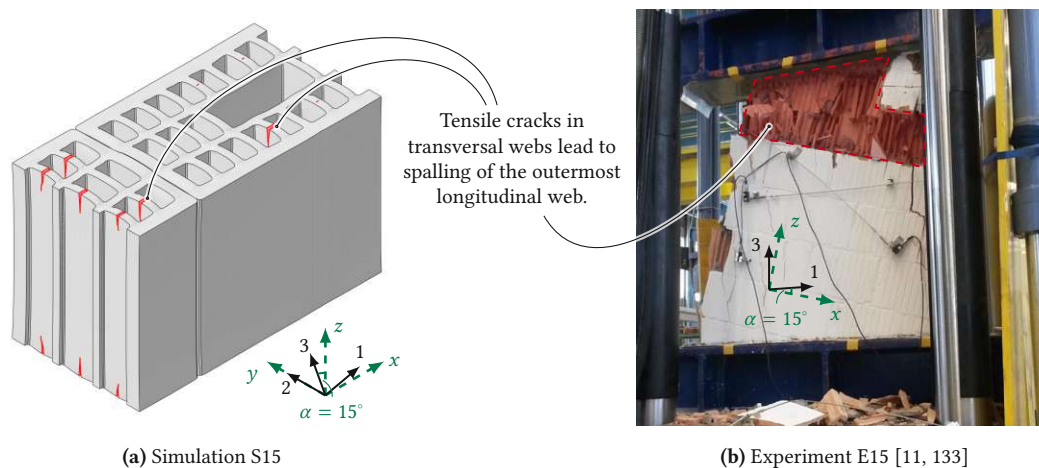


Fig. 3.10: Failure mechanism I – Failure under vertical compressive loading was governed by tensile cracks in the transversal webs and subsequent spalling of the outermost longitudinal webs.

Shear loads lead to shear stresses in the joints as well as the longitudinal webs. Due to the inhomogeneous nature of a masonry wall, shear loads additionally lead to a rotation of the blocks within the wall, introducing bending moments in the joints [101]. These bending moments induce stresses perpendicular to the joints, i. e., tension on one side of the block and compression on the other side, leading again to horizontal stresses in the transversal webs, as described above. In combination with large vertical compressive loads, the stresses perpendicular to the bed joint are entirely compressive. In contrast, for smaller vertical compressive loads tensile stresses perpendicular to the bed joints may be crucial for joint failure. Additionally, the shear strength of the mortar increases with compressive stresses perpendicular to the joint. Hence, for shear loads, the failure mechanism strongly depends on the load magnitude in the local z -direction.

With increasing shear and decreasing vertical compressive stresses (S30, S45, S60, and S75), shear failure of the bed joints was the governing failure mechanism, manifesting in a sliding deformation along

the bed joint (mechanism II, see Fig. 3.11a). The same mechanism could be observed in the corresponding experiments (see Fig. 3.11b). S75 showed a slightly different mechanism from the other simulations: Due to the small amount of vertical compressive stresses, tensile stresses introduced damage to the mortar joints. This damage led to a reduced contact area between the blocks, which again triggered shear failure of the joints. Hence, with larger vertical compressive forces, pure shear failure occurred, while with lower vertical compressive forces a combination of tensile and shear failure was relevant.

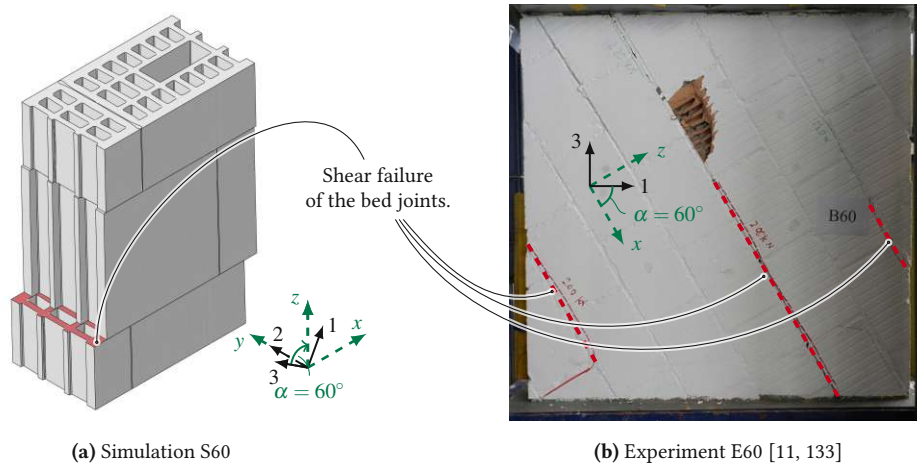


Fig. 3.11: Failure mechanism II – Failure under shear loads was governed by shear failure of the mortar joints. The dashed red lines in (b) mark the regions, where shear failure occurred in the experiments.

Horizontal compressive loads are mostly transferred via horizontal compressive stresses in the longitudinal webs and horizontal compressive stresses in the head joints. These compressive stresses lead to deformations in the mortar head joint in local x -direction, which are larger at the outermost longitudinal webs. This deformation difference between the outermost longitudinal webs and their direct neighbors introduces bending moments in the connecting transversal webs, leading to critical tensile stresses in the connection between transversal and longitudinal webs. Thus, under horizontal compressive loading (S90) tensile cracks in the connection between transversal and longitudinal webs led to failure (mechanism III, see Fig. 3.12a). Again, in the corresponding Experiment (E90) spalling of the outermost longitudinal web was observed in some areas, indicating detachment of these webs. On the left and right sides of the specimen, cracks could be found in similar locations as the simulation predicted (see Fig. 3.12b).

Next, we are going to compare the numerically obtained peak stresses with the experimental results. Therefore, we rotated the evaluated peak stress state $\bar{\sigma}_{\text{local}}^{f,\alpha}$ from the local scope back to the global scope with Eq. (3.12) and the negative value of bed joint incline α . While, theoretically, only the stress component $\bar{\sigma}_{33}^{f,\alpha}$ should be non-zero after rotation, the non-linearities in the calculations led to other components also being non-zero. Nevertheless, these components were significantly smaller than the desired macroscopic global stress in the 3-direction. Hence, for each simulation the component $\bar{\sigma}_{33}^{f,\alpha}$ is compared to the corresponding experimentally obtained peak stress ($f_{m\alpha}$ in Fig. 3.6) in Fig. 3.13 and Table 3.5.

While each green circle in Fig. 3.13 denotes the peak stress of one experiment, the grey area represents the range between the upper and lower boundary of the numerically obtained results. Hence, four out

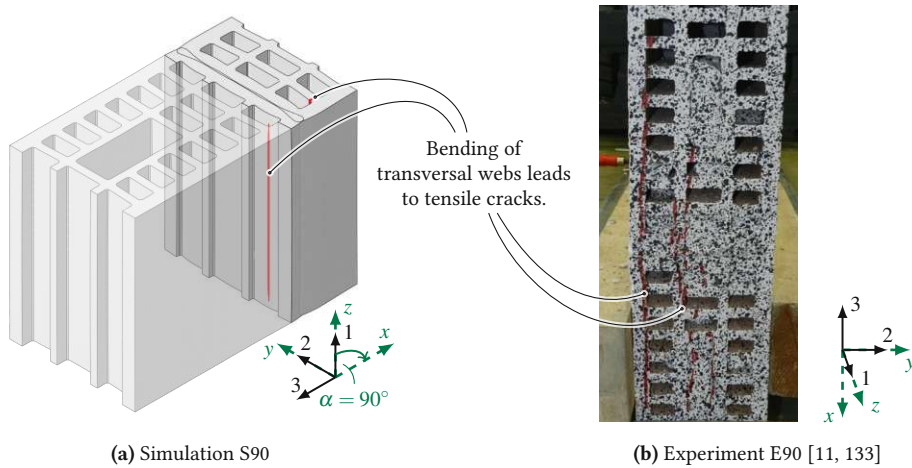


Fig. 3.12: Failure mechanism III – Failure under horizontal compressive loads was governed by tensile cracks in the connection between transversal and longitudinal webs. The image in (b) shows the side view of the specimen. The red lines mark where cracks occurred.

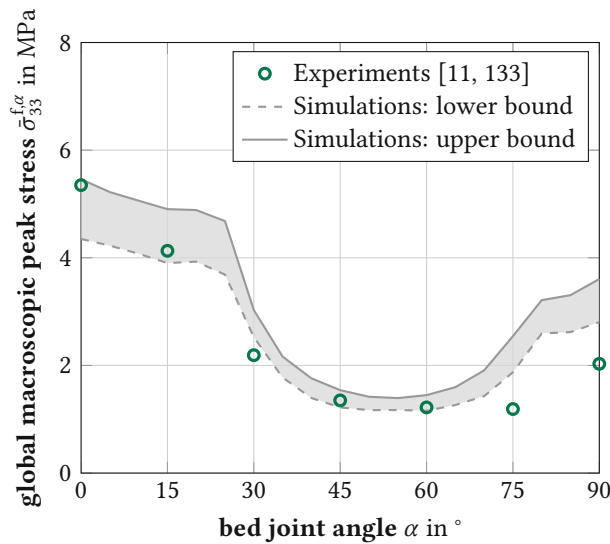


Fig. 3.13: Comparison of numerically and experimentally obtained peak stresses. We obtained the lower and upper bounds of the simulations by using the minimum and maximum material properties defined in Sections 3.2.2.1 and 3.3.2.3

of seven experimentally obtained peak stresses (E00, E15, E45, and E60) are within the upper and lower bounds of the simulation results. E30 delivers a peak stress 13 % below S30-min, which is still acceptably close to the simulation results.

The simulations exhibit the most significant deviations from the experimental results at S75 and S90, with discrepancies of 57 % and 38 %. One possible explanation for this variation is the drying stage that freshly extruded blocks undergo before firing. During this drying process, the intersections between the webs require more time to dry due to the reduced ratio of surface area to clay mass. Consequently, the difference in material shrinkage increases the likelihood of microstructural defects in these intersections [5], which we did not account for in our analysis.

Tab. 3.5: Comparison of numerically and experimentally obtained global macroscopic peak stresses $\bar{\sigma}_{33}^{f,\alpha}$ and observed failure mechanisms.

	Simulations			Experiments [11, 133]		
	peak stress (MPa)		failure mechanism	peak stress (MPa)	failure mechanism	
	min	max				
S00	4.35	5.46	I	E00	5.35	I
S15	3.90	4.90	I	E15	4.13	I
S30	2.53	3.03	I, II	E30	2.19	I, II
S45	1.22	1.54	II	E45	1.35	II
S60	1.16	1.45	II	E60	1.22	II
S75	1.87	2.54	II	E75	1.19	II
S90	2.81	3.61	III	E90	2.03	III

I ... Tensile cracks in the transversal webs leading to spalling of outermost longitudinal webs (Fig. 3.10).

II ... Shear failure of the bed joints (Fig. 3.11).

III ... Tensile cracks in the transversal webs due to bending of these webs (Fig. 3.12).

However, this deviation leads to a less distinct material anisotropy in the simulations compared to the experimentally obtained peak stresses. This anisotropy can be captured by the ratio of the horizontal compressive masonry strength to the vertical counterpart, $f_{m,x}/f_{m,z}$, which is 0.661 in the simulations and 0.379 in the experiments. For different types of vertically perforated block masonry, this value ranges approximately from 0.25 up to 0.63, depending on the amount and position of cavities in the block design [86]. Thus, the model underestimates the material anisotropy for this case and would benefit from implementing the discussed strength reduction due to the drying process.

Overall, the numerically obtained peak stresses follow a similar trend as the experimental results. Notably, the lowest peak stress for shear failure occurs at around $\alpha = 60^\circ$, although the largest shear stress component occurs at $\alpha = 45^\circ$ (see also Table 3.2). The reason for that is the dependency of the shear strength on the compressive stresses perpendicular to the bed joints: While the amount of shear loads is decreasing from S45 to S60, the vertical compressive stresses are also decreasing, leading to a smaller shear strength.

Last but not least, we compare the numerically obtained stress-strain relations ($\bar{\sigma}_{33}-\bar{\epsilon}_{33}$) with the experimental results (see Fig. 3.14). Thereby, we focus on the results of the three simulations S15, S60, and S90, each representative of one failure mechanism.

Simulation S15 behaved linearly until the peak stress was reached, followed by an abrupt drop in stresses. The corresponding experiment E15 showed a lower stiffness than the simulation in the beginning, with a gradually increasing gradient afterward. After the gradient increased to a constant value, the experimentally obtained curve is almost parallel to the numerically obtained curve. Hence, the effective vertical stiffness of the unit cell is comparable to the real stiffness properties.

Simulation S60 behaved nearly linear until the peak stress, showing a minor decrease of the gradient starting at 60 % of the peak stress. The stress decrease after the peak stress was reached is less abrupt than at S15. After a 13.5 % decrease the stress increased again linearly, because of the frictional properties of the interface and the still increasing stress perpendicular to the bed joint. Compared to the corresponding experiment E60, the simulation behaved slightly softer before the peak stress was reached and less ductile afterward.

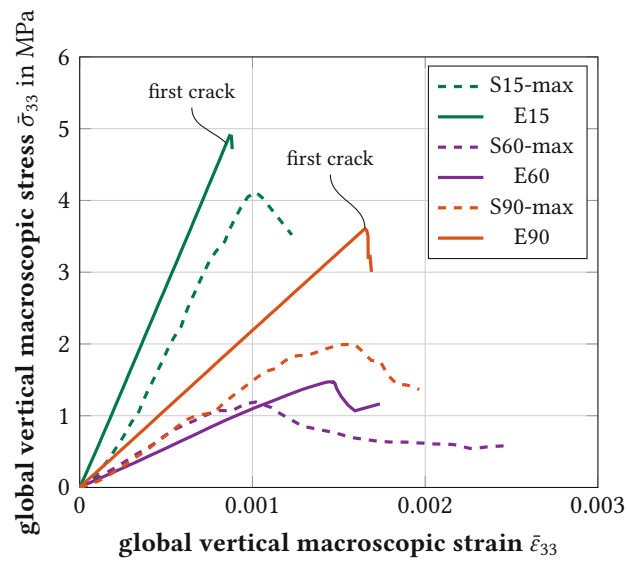


Fig. 3.14: Numerically obtained stress-strain relations (solid lines) compared to the experimental results (dashed lines) for $\alpha \in [15^\circ, 60^\circ, 90^\circ]$. The upper bound of the simulation results was used (max).

Simulation S90 behaved linearly until the peak stress was reached, followed by an abrupt drop in stresses, similar to simulation S15. The corresponding experiment E90 showed an approximately 23% lower stiffness than the simulation and significantly more ductile post-peak behavior.

Notably, our simulations showed markedly fewer pre-peak nonlinearities compared to the experimental results. The root of this discrepancy lies in the inherent nature of the unit cell approach. In an experimental setting, if damage occurs at one point, the load can be redistributed to the intact portions of the specimen. However, due to the periodic boundary conditions of the unit cell approach, any failure-inducing mechanism is subsequently repeated, which contrasts with the resilience observed in real-world experiments.

Motivated by the good agreement of the failure mechanisms and the peak stresses with the experimental results, we simulated additional loading combinations to obtain enough results for fitting a Rankine-Hill surface. Lourenço [86] proposed seven loading combinations for easily defining the failure surface. Two of these loading combinations, horizontal and vertical uniaxial compression (S90 and S00, respectively), are already included in the simulations presented above. Applying the remaining five loading combinations on the numerical model and evaluating the peak stresses with the same failure criterion as above, led to the parameters for the Rankine-Hill surface displayed in Fig. 3.15 (see also Appendix B). The coefficient of determination of the surface compared to the simulations is 0.76. Comparing the peak stresses obtained from simulations S00–S90 to the corresponding load combinations on the Rankine-Hill surface, a good agreement can also be seen (Fig. 3.16a, green circles). Notably, the first significant decrease of the peak stress occurs earlier and the plateau at a larger joint incline is also reached earlier. Hence, the smallest peak stress occurs around $\alpha = 50^\circ$ instead of $\alpha = 60^\circ$.

While each simulation in the compression regime failed in one of the previously discussed failure mechanisms (i. e., I, II, and III), two simulations in the tensile regime showed another mechanism: tensile failure perpendicular to the joints. Since none of the experiments conducted by Bitterli and

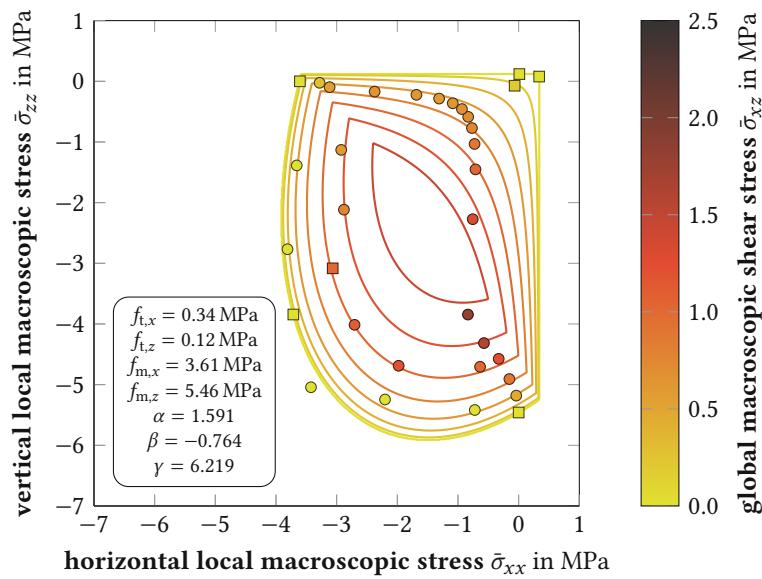


Fig. 3.15: Local macroscopic peak stress states for 34 simulations with different in-plane loading (circles ● and squares ■) compared to a Rankine-Hill surface gained from simulating seven load combinations (squares ■) proposed by Lourenço [86] (see Appendix B). The upper material limits (max) were used. The stresses are given in local coordinates x - y - z .

Salmanpour [11, 133] showed a comparable loading or failure mechanism, we were not able to validate these two results. However, these simulations only have a minor impact on the overall fit of the surface.

The Rankine-Hill surface is capable of qualitatively capturing the failure envelope of masonry in general [86]. Therefore, the good agreement with the simulations underlines the validity of the obtained peak stresses with different loading combinations.

In addition to the fitted Rankine-Hill surface, Fig. 3.16 contains further failure surfaces (Fig. 3.16a) and experiments (Fig. 3.16b) from literature, compared to the simulation results. Another failure surface beside the Rankine-Hill surface, which is applicable for vertically perforated clay block masonry, is the surface developed by Ganz [54]. He analytically defined each part of the failure envelope as a function of geometry and material properties. Calibrated with the block geometry and simulation results (see Appendix A), the failure surface according to Ganz [54] is also similar to the simulation results (Fig. 3.16a, orange crosses). Additionally, we approximated the envelope for shear failure of the bed joint as a function of the incline angle α and the results of the shear tests on masonry triplets ($\tau_{m,ini}$ and μ_m). Therefore, we calculated the macroscopic shear stress from the incline angle α and compared it to the shear strength, obtained from the shear test results using a Mohr-Coloumb criterion, leading to the following relation for calculating the peak stress:

$$\bar{\sigma}_{33}^{f,\alpha} = \frac{2 \cdot \tau_{m,ini} \cdot \sin(\alpha) \cdot \cos(\alpha)}{1 - \sin^4(\alpha) + 2 \cdot \mu_m \cdot \cos^3(\alpha) \cdot \sin(\alpha) + \cos^4(\alpha)}. \quad (3.16)$$

Notably, each of the curves in Fig. 3.16a has the same overall shape, where the first part before the sudden drop is governed by block failure, the second part from the drop to reaching the plateau is governed by shear failure, and the third part is again governed by block failure.

The simulation results are compared with three sets of experimental data in Fig. 3.16b. To facilitate a better comparison, the values of each series were normalized by their global peak stress at $\alpha = 0^\circ$. Dialer

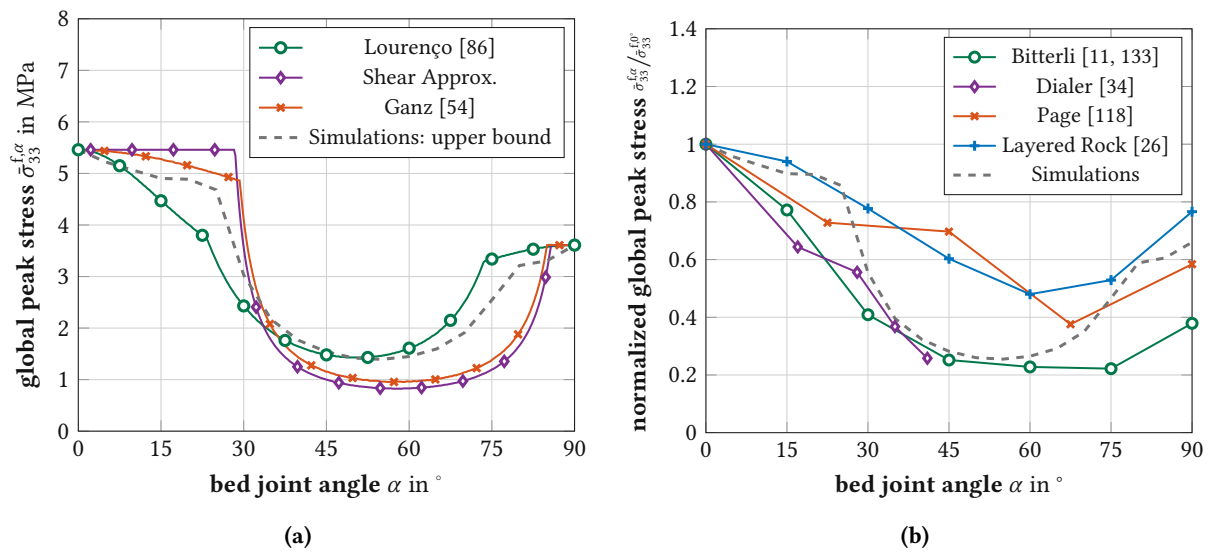


Fig. 3.16: Comparison of the numerically obtained peak stresses with other findings: (a) failure surfaces for the upper bound of material properties, (b) normalized experimental data [11, 26, 34, 118, 133].

[34] and Page [118] performed uniaxial and biaxial tests on solid clay block masonry with different angles of bed joint incline. Additionally, we found a similar relation for experiments on layered rock [26]. Although the curves are quite different, they all share the same overall trend: a decreasing peak stress with increasing bed joint incline, with a minimum between 45° and 75°, followed by an increasing peak stress.

3.5 Conclusion and Outlook

This work describes the development of a numerical model for computing the peak stress of vertically perforated clay block masonry under arbitrary in-plane loads. The previously published model [76, 142] was extended by introducing a realistic material model for the mortar joints. These modeling strategies were combined to simulate a series of experiments with different combinations of biaxial compressive loading and shear loading [133]. The obtained peak stresses were mostly in good agreement with the experimental results. Solely under horizontal compression, the model yielded larger peak stresses, resulting in a less distinct anisotropy, compared to the experiments. Additionally, the three main failure mechanisms observed in the experiments could be realistically replicated with the numerical model. While the failure mechanisms under vertical compression and shear were already published in the literature (e. g. [76, 118, 142, 145]), for the first time the failure under horizontal compressive loading could be linked to deformation differences in the head joint.

After the validation, a Rankine-Hill surface for the given clay block masonry could be fitted by simulating the seven load combinations proposed by Lourenço [86]. This surface nicely matched the numerically obtained peak stresses with the loading combinations investigated by Bitterli and Salmanpour [11, 133]. Additionally, the failure surface proposed by Ganz [54], a criterion for shear failure derived from the mortar parameters, and various experimental series showed qualitatively similar behavior to the numerical results, showcasing their validity.

Thus, the model can be used to generate failure surfaces for different masonry products to be used as a macroscopic failure criterion within FE software. Another application is a parameter study on different geometrical features or material properties, to find the most significant parameters for increasing the macroscopic strength under given boundary conditions. This helps to gain a deeper understanding of the behavior of clay block masonry under in-plane loading.

Although the presented FE model provided valuable insights, the model would benefit from further improvements to better capture the anisotropic behavior. One potential enhancement lies in incorporating reduced strengths in the connection between longitudinal and transversal webs. This adjustment is particularly relevant as mechanical defects are prone to occur in these regions during the drying process. Future research should focus on refining the FE model to effectively account for these localized effects and improve the overall predictive capabilities in this context.

For future studies, another interesting modification of the model would be the adoption of the phase field method (refer e. g. to Miehe et al. [97]) as an alternative to XFEM. In contrast to XFEM, the phase field method offers notable advantages by utilizing a diffusive representation of cracks instead of introducing sharp discontinuities. This approach is known to be very stable, even for complex crack topologies, as e. g. Pech et al. showed for complex wood structures with anisotropic material behavior [120, 121].

Overall, the presented model exhibits great potential for optimizing existing products or developing new block designs, making it a valuable tool for enhancing structural performance in the field of clay block masonry.

Acknowledgements

The authors gratefully acknowledge the financial support of the Austrian Research Promotion Agency (FFG, project number 865067) and the industry partner Wienerberger for funding the research work within the project “Innovative Brick 2”. Furthermore, the authors acknowledge TU Wien Bibliothek for financial support through its Open Access Funding Programme.

3.6 Appendix A: Calibration of the Failure Surface according to Ganz

Ganz [54] proposed a failure surface for masonry with tensile strength, consisting of the following 12 failure criteria:

$$\Phi_{1a} = \bar{\sigma}_{xz}^2 - (\omega_m \cdot f_{m,x} - \bar{\sigma}_{xx}) (2\omega_m \cdot f_{m,z} - \bar{\sigma}_{zz}) \leq 0. \quad (3.17)$$

$$\Phi_{1b} = (1 + \omega_m)^2 \cdot \bar{\sigma}_{xz}^2 + [\omega_m \cdot (\bar{\sigma}_{zz} + f_{m,z}) - \bar{\sigma}_{xx}] [\bar{\sigma}_{zz} + f_{m,z} - f_{m,x} - \omega_m \cdot (\bar{\sigma}_{xx} + f_{m,x})] \leq 0. \quad (3.18)$$

$$\Phi_{1c} = (1 + \omega_m)^2 \cdot \bar{\sigma}_{xz}^2 + [\omega_m \cdot (\bar{\sigma}_{zz} - 2\omega_m \cdot f_{m,z} + f_{m,x} \cdot (1 + \omega_m)) - \bar{\sigma}_{xx}] \cdot [\bar{\sigma}_{zz} - 2\omega_m \cdot f_{m,z} - \omega_m \cdot f_{m,x}] \leq 0. \quad (3.19)$$

$$\Phi_2 = \bar{\sigma}_{xz}^2 - (\bar{\sigma}_{xx} + f_{m,x}) \cdot (\bar{\sigma}_{zz} + f_{m,z}) \leq 0. \quad (3.20)$$

$$\Phi_{3ab} = \bar{\sigma}_{xz}^2 + \bar{\sigma}_{xx} \cdot (\bar{\sigma}_{xx} + f_{m,x}) \leq 0. \quad (3.21)$$

$$\Phi_{3c} = \bar{\sigma}_{xz}^2 + \bar{\sigma}_{xx} \cdot (\bar{\sigma}_{xx} - \omega_m \cdot f_{m,x}) \leq 0. \quad (3.22)$$

$$\Phi_{3d} = 4\omega_m \cdot \bar{\sigma}_{xz}^2 - [\omega_m \cdot f_{m,x} - \bar{\sigma}_{xx} \cdot (1 - \omega_m)]^2 \leq 0. \quad (3.23)$$

$$\Phi_{4a} = \bar{\sigma}_{xz}^2 - (c - \bar{\sigma}_{zz} \cdot \tan(\varphi))^2 \leq 0. \quad (3.24)$$

$$\Phi_{4b} = \bar{\sigma}_{xz}^2 + (\bar{\sigma}_{zz} - f_{t,z} + R_b)^2 - R_b^2 \leq 0. \quad (3.25)$$

$$\Phi_{4c} = \bar{\sigma}_{xz}^2 + \left[\bar{\sigma}_{zz} - f'_{t,z} \cdot \left(\frac{\bar{\sigma}_{xx}}{\mu \cdot f_{m,x}} + 1 \right) + R_c \right]^2 - R_c^2 \leq 0. \quad (3.26)$$

$$\Phi_{4d} = \bar{\sigma}_{xz}^2 \cdot \left(1 + \frac{2 \cdot a_L}{a_S} \cdot \tan(\varphi) \right)^2 - \left(\bar{\sigma}_{zz} \cdot \tan(\varphi) + \bar{\sigma}_{xx} \cdot \frac{2 \cdot a_L}{a_S} - c \right)^2 \leq 0. \quad (3.27)$$

$$\Phi_{4e} = \left(|\bar{\sigma}_{xz}| + \frac{2a_L}{a_S} \cdot \bar{\sigma}_{xx} \right)^2 + \left(\bar{\sigma}_{zz} + |\bar{\sigma}_{xz}| \cdot \frac{2a_L}{a_S} - f_{t,z} + R_b \right)^2 - R_b^2 \leq 0. \quad (3.28)$$

$$R_b = c \cdot \tan\left(\frac{\pi}{4} + \frac{\varphi}{2}\right) - f_{t,z} \cdot \frac{\sin(\varphi)}{1 - \sin(\varphi)} \quad (3.29)$$

$$R_c = c \cdot \tan\left(\frac{\pi}{4} + \frac{\varphi}{2}\right) - f'_{t,z} \cdot \left(\frac{\bar{\sigma}_{xx}}{\mu \cdot f_{m,x}} + 1 \right) \cdot \frac{\sin(\varphi)}{1 - \sin(\varphi)} \quad (3.30)$$

Thereby, $\bar{\sigma}_{xx}$, $\bar{\sigma}_{zz}$, and $\bar{\sigma}_{xz}$ are the in-plane components of the local macroscopic stress tensor. Note, that the indices are different than in the original publication. While Ganz [54] refers to the vertical direction with x and the horizontal direction with y , we use x for the horizontal direction and z for the vertical direction, which is consistent with the local coordinate system used within this work.

For calibration of the surface, 10 parameters are needed, i. e. the uniaxial compressive masonry strengths, $f_{m,x}$ and $f_{m,z}$, the ratio of the tensile strengths to their compressive counterparts, ω_m , the vertical uniaxial tensile masonry strength $f_{t,z}$, the distance of the bed joints, a_L , the distance of the head joints, a_S , the cohesion shear stress and the frictional angle of the joints, c and φ , the tensile strength of the joints, $f'_{t,x}$, and an additional parameter μ . For a detailed description of these properties, we refer to the original publication [54]. We derived the strength parameters from the simulation results as $f_{m,x} = 3.61$ MPa, $f_{m,z} = 5.54$ MPa, $f_{t,z} = 0.12$ MPa, $f'_{t,z} = 0.12$ MPa, and $\omega_m = 0.94$. Furthermore, we gained $a_L = 200$ mm and $a_S = 300$ mm from the block geometry, $c = 0.26$ MPa and $\varphi = 0.48$ from the simulation of the shear tests, and set the additional parameter to $\mu = 1$.

3.7 Appendix B: Calibration of the Rankine-Hill Surface

The Rankine-Hill surface consists of two failure criteria: a Rankine-type criterion and a Hill-type criterion. The Rankine-type surface is defined in the following manner:

$$f_1 = \frac{(\bar{\sigma}_{xx} - f_{t,x}) + (\bar{\sigma}_{zz} - f_{t,z})}{2} + \sqrt{\left(\frac{(\bar{\sigma}_{xx} - f_{t,x}) - (\bar{\sigma}_{zz} - f_{t,z})}{2}\right)^2 + \alpha \bar{\sigma}_{xz}^2} = 0, \quad (3.31)$$

with the parameter α , which defines the size of the attainable shear strength for the Rankine-type surface, the uniaxial tensile strengths $f_{t,x}$ and $f_{t,z}$, and the in-plane components of the local macroscopic stress tensor, $\bar{\sigma}_{xx}$, $\bar{\sigma}_{zz}$, and $\bar{\sigma}_{xz}$.

The Hill-type surface forms a rotated centered ellipsoid, which reads as

$$f_2 = A \cdot \bar{\sigma}_{xx}^2 + B \cdot \bar{\sigma}_{xx} \cdot \bar{\sigma}_{zz} + C \cdot \bar{\sigma}_{zz}^2 + D \cdot \bar{\sigma}_{xz}^2 - 1 = 0. \quad (3.32)$$

The four parameters A , B , C , and D can be derived from the material's tensile strengths, $f_{t,x}$ and $f_{t,z}$, and compressive strengths, $f_{m,x}$ and $f_{m,z}$, in the following way:

$$A = \frac{1}{(f_{m,x})^2}, \quad B = \frac{\beta}{f_{m,x} \cdot f_{m,z}}, \quad C = \frac{1}{(f_{m,z})^2}, \quad \text{and} \quad D = \frac{\gamma}{f_{m,x} \cdot f_{m,z}}, \quad (3.33)$$

with the parameter β , which defines the interaction of axial stresses $\bar{\sigma}_{xx}$ and $\bar{\sigma}_{zz}$ in the compressive regime, and the parameter γ , which defines the size of the attainable shear strength for the Hill-type surface.

Thus, seven parameters are needed to fully calibrate the Rankine-Hill surface, i. e. the uniaxial strengths $f_{t,x}$, $f_{t,z}$, $f_{m,x}$, and $f_{m,z}$, as well as the parameters α , β , and γ . While we obtained the uniaxial strengths from applying the corresponding uniaxial loading to the FE model, we derived the remaining parameters from simulating three additional loading combinations proposed by Lourenço [86] (see Fig. 3.17) using the following equations:

$$\alpha = \frac{1}{9} \cdot \left(1 + 4 \frac{f_{t,x}}{f_\alpha}\right) \cdot \left(1 + 4 \frac{f_{t,z}}{f_\alpha}\right), \quad (3.34)$$

$$\beta = \left[\frac{1}{f_\beta^2} - \frac{1}{f_{m,x}^2} - \frac{1}{f_{m,z}^2} \right] \cdot f_{m,x} f_{m,z}, \quad \text{and} \quad (3.35)$$

$$\gamma = \left[\frac{16}{f_\gamma} - 9 \cdot \left(\frac{1}{f_{m,x}^2} + \frac{\beta}{f_{m,x} \cdot f_{m,z}} + \frac{1}{f_{m,z}^2} \right) \right]. \quad (3.36)$$

Hence, we obtained the following parameters for the Rankine-Hill surface: $f_{t,x} = 0.34$ MPa, $f_{t,z} = 0.12$ MPa, $f_{m,x} = 3.61$ MPa, $f_{m,z} = 5.46$ MPa, $\alpha = 1.591$, $\beta = -0.764$, and $\gamma = 6.219$.

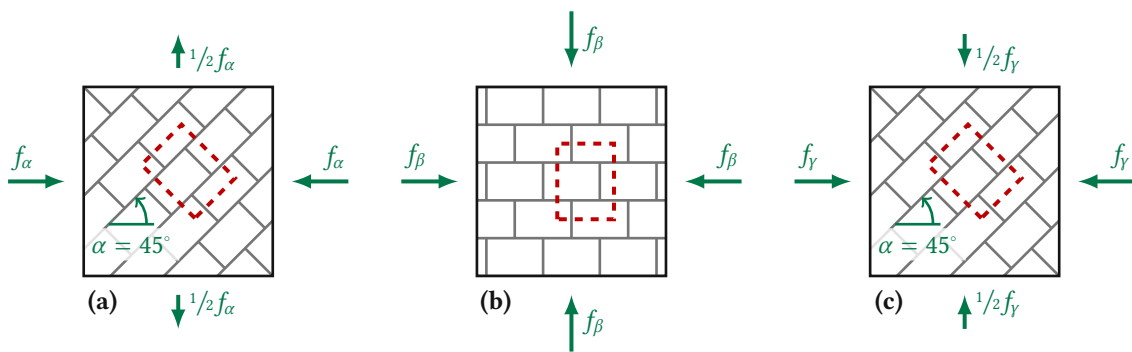


Fig. 3.17: Additional loading combinations proposed by Lourenço [86]. The dashed line marks the boundaries of the repeating unit cell, which was used for defining the FE model in Fig. 3.7.

3.8 Appendix C: Orthotropic Hoffman criterion

The Hoffman criterion uses all six independent components of the stress tensor and is defined as follows:

$$\begin{aligned}
 f(\boldsymbol{\sigma}) = & C_1 \cdot (\sigma_{TT} - \sigma_{ZZ})^2 + C_2 \cdot (\sigma_{ZZ} - \sigma_{LL})^2 + C_3 \cdot (\sigma_{LL} - \sigma_{TT})^2 \\
 & + C_4 \cdot \sigma_{LL} + C_5 \cdot \sigma_{TT} + C_6 \cdot \sigma_{ZZ} \\
 & + C_7 \cdot (\sigma_{LT})^2 + C_8 \cdot (\sigma_{TZ})^2 + C_9 \cdot (\sigma_{LZ})^2,
 \end{aligned} \tag{3.37}$$

Hereby, σ_{ij} are the components of the stress tensor given in the material orientation L-T-Z (shown in Fig. 3.1), and C_1 to C_9 are constants, which are derived from the material's tensile, compressive, and shear strengths, $\sigma_{t,i}$, $\sigma_{c,i}$, and $\sigma_{s,ij}$, respectively:

$$C_1 = \frac{1}{2} \left[(\sigma_{t,T} \cdot \sigma_{c,T})^{-1} + (\sigma_{t,Z} \cdot \sigma_{c,Z})^{-1} - (\sigma_{t,L} \cdot \sigma_{c,L})^{-1} \right], \tag{3.38}$$

C_2 and C_3 by permutation of indices L, T, Z,

$$C_4 = (\sigma_{t,L})^{-1} - (\sigma_{c,L})^{-1}, \tag{3.39}$$

C_5 and C_6 by permutation of indices L, T, Z,

$$C_7 = (\sigma_{s,TZ})^{-2}, \tag{3.40}$$

C_8 and C_9 by permutation of indices L, T, Z..

The Hoffman criterion was implemented using a user subroutine, which can be found in the supplementary material¹.

¹The supplementary material can be found in the online version of the published article, which is available under <https://doi.org/10.1016/j.engstruct.2023.116557>.

Publication 4

Developing failure surfaces for vertically perforated clay block masonry using a validated numerical unit cell model

Authors Raphael Reismüller, Markus Lukacevic, Sebastian Pech, Andreas Jäger, Josef Füssl
Submitted to Structures

Abstract

Finite element software is nowadays an essential part of a structural engineer's modeling process. The simulations range from trivial linear elastic models to highly non-linear ones, accounting for contact, plasticity, viscoelasticity, or fracture. Though fired clay blocks are an excellent and widely used building material, little effort has been made to extend available failure surfaces simulating vertically perforated clay block masonry in modern FE Software. Therefore, developing reliable and efficient ways to predict the effective strength of vertically perforated clay block masonry subjected to different loading states is critical. In this study, we propose a numerical concept for developing failure surfaces for vertically perforated clay block masonry under in-plane loading. Using a previously validated unit cell FE model, we derived the peak stresses from 471 simulations. Subsequently, we compared these results with two failure surfaces from the literature and identified qualitative differences. Taking these differences into account, we propose a concept for numerically calibrating the parameters of the Rankine–Hill failure surface proposed by Lourenço (1996).

4.1 Introduction

Clay block masonry is one of the oldest building materials in human history and has been used for many centuries. Especially in Central Europe, it is still a popular building material for its low thermal conductivity, durability, fire resistance, and ease of construction. Additionally, mainly abundant natural materials are used for the production of clay blocks, which makes them a sustainable building material [123]. Today, mostly vertically perforated clay blocks are used for structural clay block masonry. A typical vertically perforated clay block design consists of a network of slender, plate-like webs, which are mostly oriented orthogonal to each other (see Fig. 4.1). These webs can be categorized by their orientation: *longitudinal webs* are oriented parallel to the wall surface and *transversal webs* are oriented perpendicular to the wall surface.

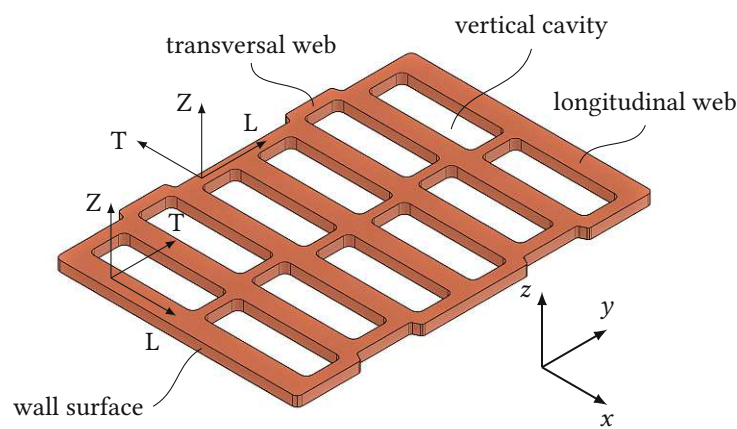


Fig. 4.1: Parts of a vertically perforated clay block and material orientation represented by the L-T-Z coordinate system (from [127]).

In the last decades, masonry has fallen behind other building materials like concrete or steel. This has several reasons: (i) Fired clay fails very brittle and the material properties show large fluctuations since the raw material is a natural product and the production process is not fully controllable. Additionally, the combination of clay blocks and mortar results in a heterogeneous material system, which requires sophisticated homogenization strategies for macroscale simulations. (ii) Block designs, joint types, and bond types are extremely diverse, which makes it difficult to find a general approach for the calculation of clay block masonry. (iii) The maximum strength properties of vertically perforated clay block masonry are typically smaller than those of concrete and steel. Hence, the use of vertically perforated clay block masonry is out of question for high-rise buildings. (iv) The structural system of clay block masonry is very different from the structural systems of other building materials. While steel and concrete structures, can be deconstructed into beams, pillars, and trusses, clay block masonry structures typically consist of plates. A structure's behavior consisting of many plates is harder to grasp than the behavior of beam-and-pillar structures. Thus, although used for so long, masonry has nowadays a subordinate role when thinking of larger buildings.

Modern FE software is massively simplifying the calculation of complex buildings and a rapidly growing number of structural engineers rely on numerical simulations in the design process. In these numerical simulations, the structural components are considered homogeneous continua with effective material properties. Therefore, reliable macroscopic failure surfaces are necessary for assessing the load-bearing capacity of a structure. While failure criteria for concrete and steel are well established in

FE software, this is not the case for masonry. Thus, the implementation of a reliable failure surface for masonry is necessary to keep up with other building materials.

In the last five decades, many studies on different macroscopic material models for masonry were published [2, 34, 50, 54, 62, 65, 66, 86, 89, 100, 118, 137, 139, 148, 149, 155]. Two of these models stand out for their unique prediction qualities and their applicability for vertically perforated clay block masonry: the multi-surface criterion developed by Ganz [54] and the Rankine–Hill surface proposed by Lourenço [86]. Especially the Rankine–Hill surface is well suited for implementation in FE software and some developers already implemented it into their software (e. g. [37]) Thus, the problem is not the lack of failure surfaces, but the calibration of these surfaces for a specific masonry product.

Typically, three different experimental series are carried out for deriving the strength parameters of a masonry product: uniaxial vertical compression tests on single blocks [95], uniaxial vertical compression tests on larger wall specimens [95], and shear tests on specimens consisting of two or three blocks [44]. Since the failure mechanism of a single block under compression is very different from the failure mechanism of a wall specimen under vertical compression [128, 142], the strength parameters from single block tests cannot be used for calibrating macroscopic material properties. Hence, only two different experimental series are generally available for calibrating a macroscopic failure surface without doing any additional tests, whereas Lourenço suggests at least seven experiments on wall specimens (refer to Section 4.2.2). Additionally, uniaxial tensile tests on wall specimens are typically not carried out, since these tests are difficult to perform (see e. g. Ganz and Thürlimann [55]) and the tensile strength is very low compared to the compressive strength [119]. Therefore, the tensile strength of masonry is often neglected, which is a very critical assumption, since it can be crucial under shear loading e. g. in earthquake regions.

Using computational methods for predicting the behavior of masonry is getting more and more attention [16, 53, 84, 135, 136, 138, 142, 154]. Since the computational effort is much lower than for experimental tests, numerical simulations are a good alternative for calibrating a macroscopic failure surface. Thus, we developed and validated a numerical model for the simulation of vertically perforated clay block masonry under arbitrary in-plane loading [128]. Using a unit cell model with periodic boundary conditions (PBC) in combination with the eXtended Finite Element Method (XFEM) [7] and the orthotropic Hoffman criterion [67] we were able to replicate the failure mechanisms of seven experiments on vertically perforated clay block walls [11, 133].

The main aim of the present work is to qualitatively analyze the failure surface of vertically perforated clay block masonry for a simplified block design, using the previously validated model. In doing so, we compare the numerical results to existing failure surfaces to work out similarities, emphasize differences, and provide a concept for using our numerical approach to generate a failure surface for any vertically perforated clay block design.

First, we developed a simplified block design, which is still able to replicate the typical failure mechanisms of vertically perforated clay block masonry. Then, we defined the interface parameters for three typical head joint types: mortared joints, frictional contact, and no contact. Next, we randomly generated 150 different loading combinations using Latin Hypercube Sampling (LHS) [91] and simulated them for each head joint type, using the previously validated numerical model. From each of these simulations, we obtained a peak stress state and a governing failure mechanism. Combining this data, we were able to derive a failure surface for each head joint type and define regions with similar failure mechanisms. Afterwards, we compared the results to the failure surfaces proposed by Ganz [54] and Lourenço [86]. By doing so, we were able to pinpoint differences between the failure surfaces and

the numerical results. For assessing these differences, we next applied the approach to two real block designs. Finally, we gathered the obtained insights to provide a concept for generating a failure surface for any vertically perforated clay block design using our numerical model.

In Section 4.2, we provide a brief summary of the two most common failure surfaces for fired clay block masonry. Section 4.3 contains an overview of the applied modeling strategies and the numerical model. Afterward, we explain and discuss the results in Section 4.4, followed by our conclusions in Section 4.5.

4.2 Failure Surfaces for Vertically Perforated Clay Block Masonry

As stated in the introduction, for the simulation of entire masonry buildings in FE software we need the homogenized elastic properties of masonry and a homogenized failure surface. We refer to the homogenized properties of the wall as *macroscopic* properties. In this manner, we distinguish between two scales of observation: the *macroscale* and the *microscale*. On the microscale both the clay blocks and the mortar joints are considered separately, while on the macroscale, the masonry wall is considered as a homogeneous continuum (see Fig. 4.2). Within this work we focus on the in-plane behavior of masonry, assuming a plane stress state, and considering only axial and shear loading as a simplification.

Macroscopic in-plane failure surfaces describe failure under a given stress state $\bar{\sigma}_{xx}$, $\bar{\sigma}_{zz}$, and $\bar{\sigma}_{xz}$. We define the x -axis as horizontal, the z -axis as vertical, and the y -axis as perpendicular to the wall surface (see Fig. 4.1 and Fig. 4.2).

While the failure surface of Ganz [54] consists of twelve criteria (shown in Appendix A), derived from different failure mechanisms observed in block masonry, the Rankine–Hill surface [86] has only two criteria (shown in Appendix B), which do not depict any failure mechanisms, but they qualitatively describe the overall shape of the in-plane failure envelope. To carve out similarities and differences between these models, they are briefly summarized in the following sections.

4.2.1 Failure surface according to Ganz

Ganz [54] examined three different cases: masonry without tensile strength, reinforced masonry, and masonry with tensile strength. For transferring shear loads under low vertical compression the tensile

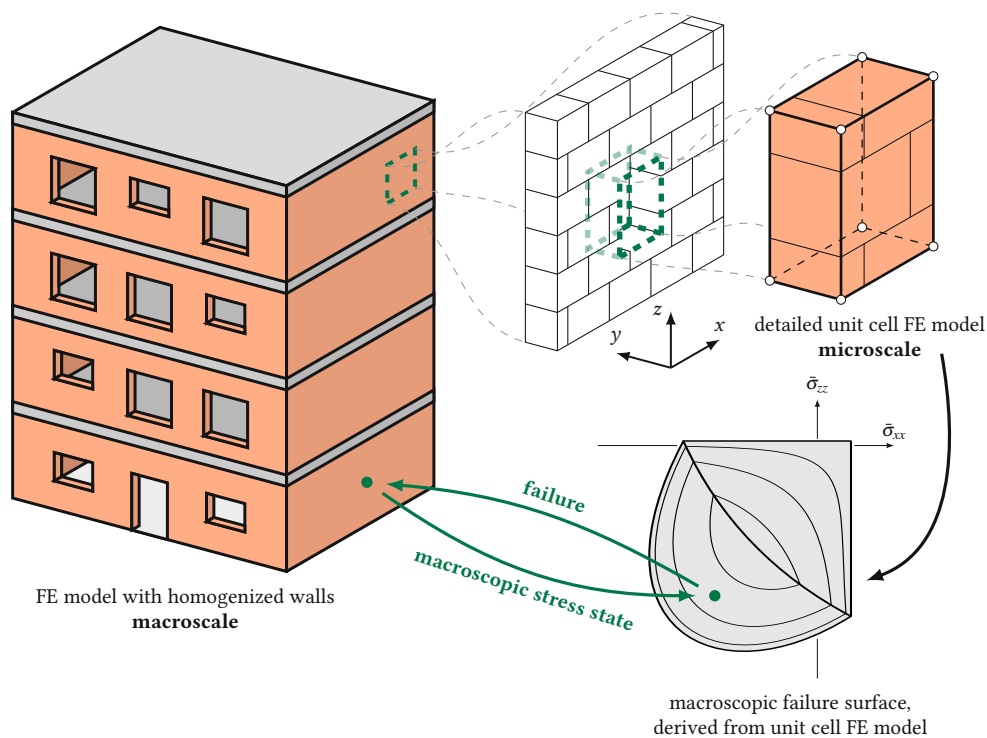


Fig. 4.2: Micro-to-macro homogenization

strength of the mortar joints is crucial. Thus, to utilize the whole potential of the material and to compete with modern building materials, we focused on masonry with tensile strength.

Based on mechanical considerations and typical failure mechanisms, Ganz [54] formulated a macroscopic failure surface from a combination of microscopic material parameters and geometric parameters as well as macroscopic material strengths. Considering both block failure and joint failure, Ganz [54] derived twelve failure criteria, resulting in a complex failure surface with many intersections (see Fig. 4.3a). The failure surface is uniquely capable of predicting the governing failure mechanism for different in-plane stress states, however, the post-peak behavior is not accounted for.

For calibrating the failure surface, the following ten parameters are necessary: the horizontal compressive masonry strength $f_{m,x}$, the vertical compressive masonry strength $f_{m,z}$, the vertical tensile masonry strength $f_{t,z}$, the ratio of the fired clay's tensile strength to its compressive strength ω_m , the tensile mortar strength $f'_{t,z}$, a parameter μ for defining the horizontal uniaxial compressive strength considering joint failure, the joint's cohesion stress c , the joint's angle of friction φ , the head joint distance a_s , and the bed joint distance a_L . For a detailed description of the parameters, we refer to the original publication [54]. The definition of the failure surface can be found in Appendix A.

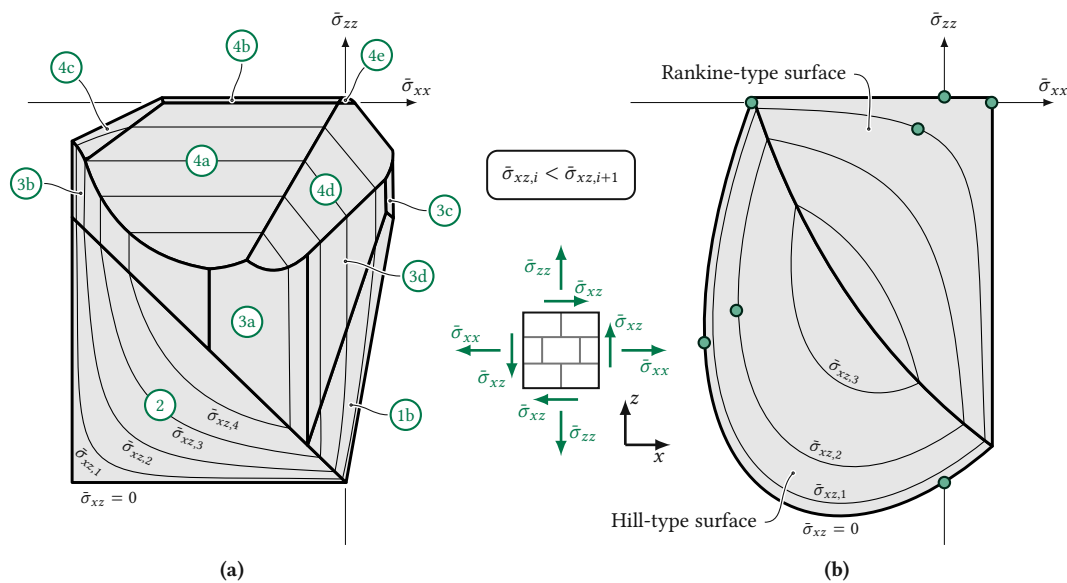


Fig. 4.3: Most commonly used macroscopic in-plane failure surfaces for masonry: (a) Failure Surface proposed by Ganz [54] and (b) Rankine–Hill surface proposed by Lourenço [86]. The numbers in (a) refer to the failure criteria in Appendix A.

4.2.2 Rankine–Hill failure surface according to Lourenço

The anisotropic Rankine–Hill failure surface, proposed by Lourenço [86], consists of two different yield surfaces: a Rankine-type yield surface for tensile failure and a Hill-type yield surface for compressive failure (see Fig. 4.3b). Instead of deriving failure criteria from failure mechanisms as Ganz [54] did, Lourenço [86] defined phenomenological surfaces for the in-plane failure envelope of masonry. Thus, the model is not capable of distinguishing different failure mechanisms. However, it is much easier to implement into FE software and can account for post-peak behavior. Thereby, an exponential softening is used for the Rankine-type surface and a combination of a parabolic hardening with an exponential

softening for the Hill-type surface, which was experimentally shown by Van der Pluijm [145] for tension and, e. g., Jafari et al. [72] for compression.

In this work, we only focused on computing the peak stress. Thus, while Lourenço often refers to the equivalent compressive yield stress $\bar{\sigma}_{c,i}(\kappa_c)$ and the equivalent tensile yield stresses $\bar{\sigma}_{t,i}(\kappa_t)$, depending on the compressive and tensile softening parameters κ_c and κ_t , we substitute these terms with the corresponding material strengths $f_{m,i}$ and $f_{t,i}$, considering the softening parameters to be $\kappa_c = 0$ and $\kappa_t = 0$. The definition of the Rankine–Hill surface can be found in Appendix B.

The Rankine–Hill surface is calibrated for a specific masonry by the following seven parameters: (i) the horizontal tensile masonry strength $f_{t,x}$, (ii) the vertical tensile masonry strength $f_{t,z}$, (iii) the horizontal compressive masonry strength $f_{m,x}$, (iv) the vertical compressive masonry strength $f_{m,z}$, (v) a parameter α for defining the shear strength amount under small axial compressive stresses, (vi) a parameter β for defining the biaxial compressive strength, and (vii) a parameter γ for defining the shear strength amount under large axial compressive stresses. Lourenço [86] suggests an ideal set of seven different loading states (see Fig. 4.4) to obtain the parameter values by a least squares regression. Additional loading states improve the quality of the fit, especially in regions of transitions between failure mechanisms.

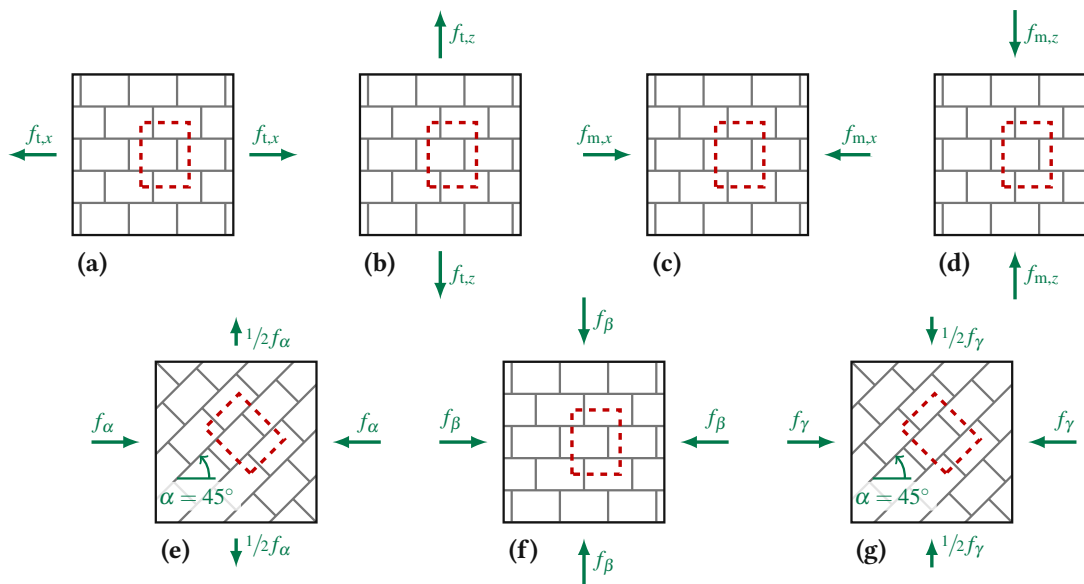


Fig. 4.4: Loading states proposed by Lourenço [86]. The red dashed line represents the outline of the chosen repeating unit cell described in Section 4.3.2.

4.3 Numerical Model and Simulation Program

This study mainly focuses on an FE simulation-based characterization of a macroscopic in-plane failure surface for clay block masonry, which also captures the occurring failure mechanisms. This process requires simulating a vast amount of different model configurations. Thus, we designed a simplified but computationally efficient FE model, which can still realistically predict the failure mechanisms and the ultimate strength of clay block masonry. We derived our numerical model from Kiefer et al. [76] and Suda et al. [142] and extended it to account for joint failure. We already used and validated the model for different in-plane loading combinations in [128]. Using a unit cell approach with PBCs and a simplified block geometry allowed us to use computationally demanding non-linear models like XFEM for modeling cracks in the fired clay and a cohesive interface damage model for considering joint failure. In the following sections, these modeling strategies are explained in detail, beginning with the geometric definition of the FE model, followed by a discussion of the chosen material behavior and simulation techniques.

4.3.1 Simplified Geometry

Since detailed and sophisticated modeling techniques result in long simulation times (for real block geometries approximately 24 hours per simulation with 8 CPUs), we developed a simplified geometry, which is still able to reproduce the typical failure mechanisms of vertically perforated clay blocks. The simplified block geometry consists of two longitudinal as well as two transversal webs (see Figure 4.5) and has a void ratio of 35 %. Each block is 93 mm long, 75 mm wide, and 100 mm high. Using this design, the simulation times could be reduced to approximately one-tenth of the larger simulations.

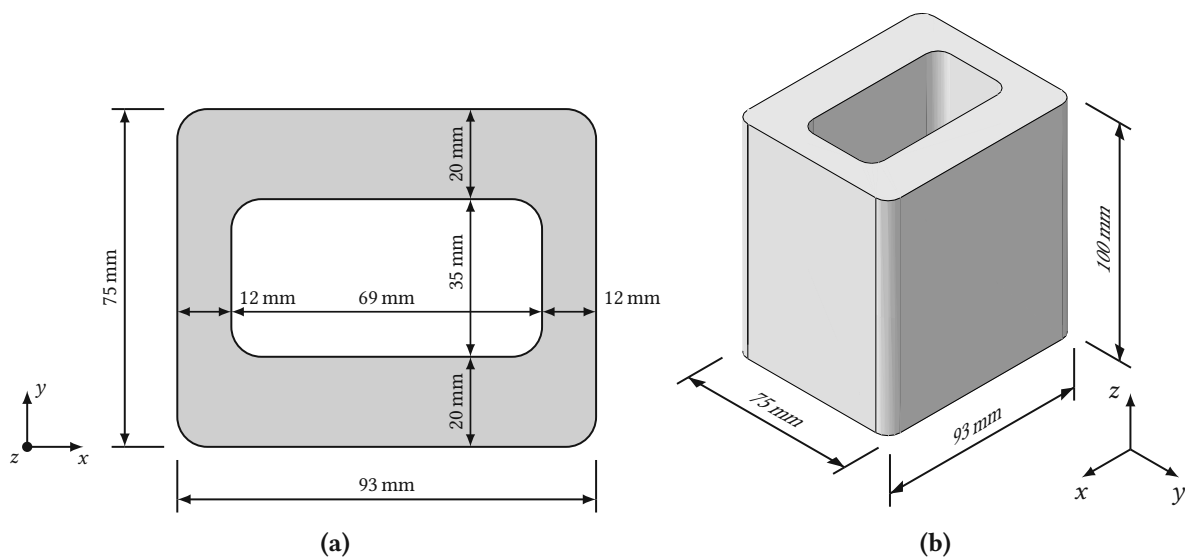


Fig. 4.5: Simplified geometry of a vertically perforated clay block.

4.3.2 Unit Cell Concept

The unit cell concept utilizes repeating patterns in structures, the so-called *repeating unit cell*. In masonry with a regular running bond, the smallest possible repeating unit cell, without considering symmetric

properties, is two blocks high and one block wide with two-dimensional periodicity in x - and z -direction (see Fig. 4.6a). We refer to the surfaces of the repeating unit cell as *North*, *South*, *East*, *West*, *Top*, and *Bottom*, and to the eight vertices according to the surfaces intersecting in this corner (e. g., NWB or SET).

In combination with PBCs, the repeating unit cell behaves as if it was part of an infinitely large wall. Thus, the unit cell concept drastically reduces the numerical effort, compared to simulating a larger structure. The PBCs are linear equations, which couple the displacements of each node on a periodic surface to the displacements of a corresponding node on the opposing surface (i. e., surfaces *East–West* and *North–South*), and to the displacements of the primary nodes located in the corners of the repeating unit cell. These equations are shown in detail in [142].

Since each node pair is coupled to the deformation difference of the primary nodes, we can impose different macroscopic strain states by simply imposing displacements on the primary nodes. We derived these primary node displacements by superposition of the three load cases in Table 4.1.

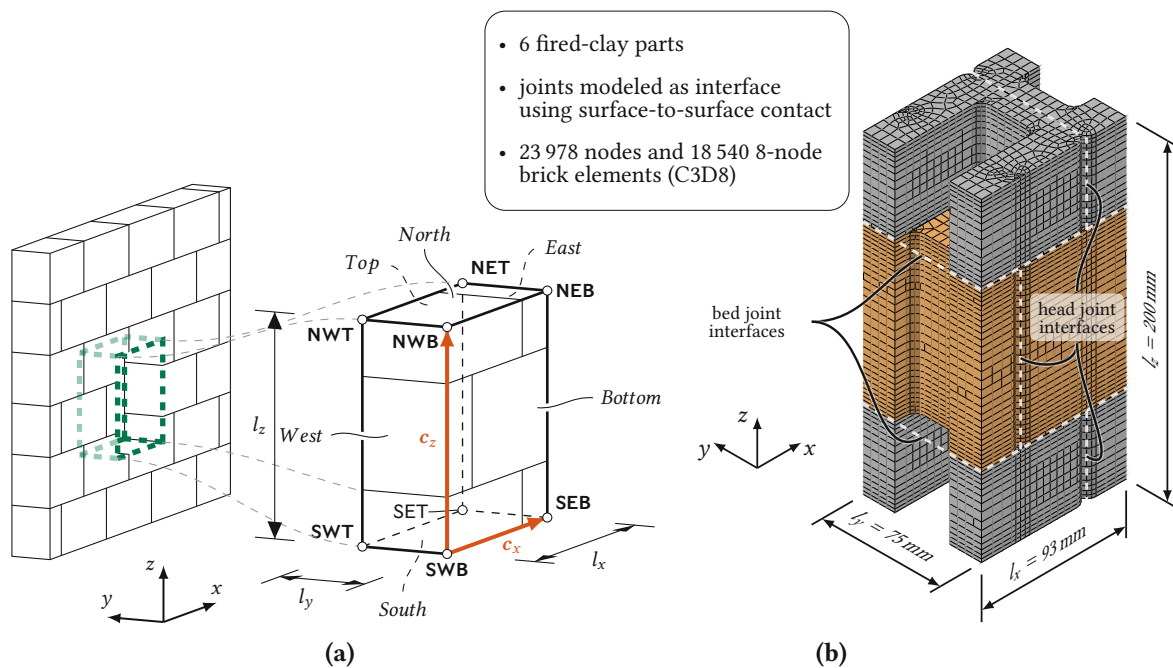


Fig. 4.6: Composition and geometry of the chosen repeating unit cell as part of the entire structure (a) and the FE model (b). The naming convention in (a) is based on the suggestions from Böhmer [14].

4.3.3 FE Model and Mesh

Now that we have defined the geometric boundary conditions, we will move on to the modeling in the FE program Abaqus. We used a simplified micro-modeling approach, meaning, that the blocks are modeled in full detail, while the joints are reduced to an interface with no thickness [86]. Thus, the FE model only consists of six fired clay parts, which are connected by interface couplings in the head joint and the bed joint. We distributed the thickness of the mortar joints to the adjacent blocks to maintain the overall dimensions of the repeating unit cell. The mesh consists of 23 978 nodes and 18 540 C3D8

Tab. 4.1: Primary node displacements for imposing effective macroscopic strain states (from Reismüller et al. [128]).

	strain state	primary node displacement
LC1	$\begin{bmatrix} \bar{\epsilon}_{xx} & 0 \\ 0 & 0 \end{bmatrix}$	<i>Horizontal uniaxial strain</i> $u_x^{\text{SEB}} = \bar{\epsilon}_{xx} \cdot l_x, \quad u_x^{\text{SET}} = \bar{\epsilon}_{xx} \cdot l_x$
LC2	$\begin{bmatrix} 0 & 0 \\ 0 & \bar{\epsilon}_{zz} \end{bmatrix}$	<i>Vertical uniaxial strain</i> $u_z^{\text{NWB}} = \bar{\epsilon}_{zz} \cdot l_z, \quad u_z^{\text{NWT}} = \bar{\epsilon}_{zz} \cdot l_z$
LC3	$\begin{bmatrix} 0 & \bar{\epsilon}_{xz} \\ \bar{\epsilon}_{xz} & 0 \end{bmatrix}$	<i>Pure shear strain</i> $u_z^{\text{SEB}} = \bar{\epsilon}_{xz} \cdot l_x, \quad u_z^{\text{SET}} = \bar{\epsilon}_{xz} \cdot l_x$ $u_x^{\text{NWB}} = \bar{\epsilon}_{xz} \cdot l_z, \quad u_x^{\text{NWT}} = \bar{\epsilon}_{xz} \cdot l_z$

The following primary node displacements were imposed in each case: $u_x^{\text{SWB}} = u_y^{\text{SWB}} = u_z^{\text{SWB}} = 0, \quad u_x^{\text{SWT}} = u_z^{\text{SWT}} = 0, \quad u_y^{\text{SEB}} = 0, \quad u_y^{\text{NWB}} = 0$

elements and is shown in Fig. 4.6a. We derived the displacement boundary conditions for each loading combination from the equations in Table 4.1.

4.3.4 Material Properties

We next discuss the material models used for the fired clay and mortar joints, based on the two governing failure mechanisms in masonry: block failure and joint failure.

Block failure is typically governed by tensile cracks. We discretely modeled these cracks using XFEM, with a linear elastic material behavior for the solid. The orthotropic material strength of extruded fired clay was accounted for by using the orthotropic Hoffman criterion [67] for crack initiation. The onset of a crack was controlled by the Virtual Crack Closure Technique (VCCT). Considering the findings of Bocca et al. [12], Eis and Vassilev [41], and Hannawald [63], we chose the mode-I fracture energy as $G_{\text{Ic}}^{\text{max}} = 0.025 \text{ J/mm}^2$. Following Kiefer et al. [76], we defined the fracture energy for modes II and III as 20 times larger. In the framework of XFEM, cracks were allowed to form anywhere in the model, with one restriction: no crack was allowed to initiate within a radius of 20 mm from an existing crack tip.

We used both transversally isotropic stiffness behavior (see Table 4.2) and transversally isotropic strengths (see Table 4.3), which is a good approximation of the orthotropic behavior of extruded fired clay according to Buchner et al. [23]. We derived the stiffness parameters and the material strengths from Kiefer et al. [76] and Suda et al. [142] considering this transversal isotropy. Thereby, the material direction follows the locally varying L - T - Z coordinate system shown in Fig. 4.1.

Joint failure manifests either in tensile or shear failure of the mortar, or tensile or shear failure of the interface [145]. Since we reduced the mortar joints to an interface with no thickness, both failure mechanisms were considered in one criterion. Thus, the weaker link (either the interface or the mortar

Tab. 4.2: Transversally isotropic stiffness parameters for fired clay.

Fired Clay				
$E_{\text{LL}} = E_{\text{ZZ}}$	E_{TT}	$\nu_{\text{TZ}} = \nu_{\text{LZ}} = \nu_{\text{LT}}$	$G_{\text{TZ}} = G_{\text{LT}}$	G_{TZ}
13 500 MPa	8738 MPa	0.2	3500 MPa	5500 MPa

Tab. 4.3: Transversally isotropic strength parameters for fired clay in MPa.

Tension			Compression			Shear		
$\sigma_{t,L}$	$\sigma_{t,T}$	$\sigma_{t,Z}$	$\sigma_{c,L}$	$\sigma_{c,T}$	$\sigma_{c,Z}$	$\sigma_{s,TZ}$	$\sigma_{s,LZ}$	$\sigma_{s,LT}$
7.009	4.834	7.009	24.17	18.61	24.17	8.308	9.547	8.308

itself) is relevant for failure. For modeling the interface behavior, we used cohesive behavior combined with a quadratic stress interaction criterion for identifying failure

$$\left(\frac{\langle\sigma_{\perp}\rangle}{\sigma_{f,\perp}}\right)^2 + \left(\frac{\tau}{\tau_{m,ini} - \mu_m \cdot \sigma_{\perp}}\right)^2 = 1, \quad (4.1)$$

with the stress component perpendicular to the joint σ_{\perp} , the shear stress τ , the tensile strength perpendicular to the joint $\sigma_{f,\perp}$, the initial value of the shear strength $\tau_{m,ini}$, and the friction coefficient μ_m . Note, that the stress component perpendicular to the joint is nested within Macauley brackets (i. e., $\langle\cdot\rangle$); thus, only tensile stresses are considered. Using cohesive behavior for interfaces in Abaqus results in a linear traction-separation law in tension, but a hard contact in compression (see the Abaqus documentation [29]). Since the mortar joints also show compressive deformations in reality, we used an additional tabular pressure-overclosure definition from Reismüller et al. [128]. Using this definition, the coupled interfaces can overlap, while linearly building up pressure, accounting for the stiffness of the mortar. Additionally, we allowed for a small compressive stress at zero overclosure to overcome numerical instabilities at the beginning of the simulations.

The softening behavior of the joint was modeled exponentially on a displacement basis with a maximum displacement $u_{pl} = 0.15$ mm and an exponent $a = 5$ (for the equations refer to the Abaqus documentation [29]). We considered the mortar to be isotropic and used the material properties from a previous study [128], where we derived the material properties by simulating shear tests on masonry triplets (see Table 4.4).

While we considered one type of bed joint, i. e., a 1 mm thick mortar layer, we wanted to compare three common types of head joints: a mortared head joint (HJM), frictional contact (HJC) in the head joint, and no contact in the head joint (HJG). For considering these three types, we altered the interface properties of the head joint. Table 4.5 shows the interface properties for each specific joint type.

Tab. 4.4: Stiffness and damage properties for the mortar interface.

Interface stiffness		Damage properties		
K_m	$K_{ss} = K_{tt}$	$\sigma_{f,\perp}$	$\tau_{m,ini}$	μ_m
5000 N/mm	2083 N/mm	0.3 MPa	1.4 MPa	0.3

4.3.5 Load Application and Sampling Procedure

As discussed in Section 4.3.2, we can simulate arbitrary macroscopic in-plane *strain* states via imposing displacements at the primary nodes of the repeating unit cell. However, for deriving a failure surface, we require macroscopic *stress* states. Thus, we used the unit cell concept to calculate the macroscopic stiffness tensor of the repeating unit cell [3] and derived the macroscopic strains from the macroscopic stresses via Hooke's law.

Tab. 4.5: Head joint interface properties used for each joint type.

	HJM Mortar	HJC Contact	HJG Gap
Cohesive Behavior	✓	–	–
Friction	✓	✓	–
Interface Damage	✓	–	–
Pressure-Overclosure	✓	–	–

For numerically deriving a failure surface, a representative set of loading states needs to be considered. This failure surface characterizes the material failure due to interacting axial stresses $\bar{\sigma}_{xx}$ and $\bar{\sigma}_{zz}$ and the shear stress $\bar{\sigma}_{xz}$. Expressing this loading state in spherical coordinates, by two angles, $\bar{\varphi}$ and $\bar{\theta}$, and the stress resultant $\bar{\sigma}_r$ (see Figure 4.7a), the load level can be easily controlled for a fixed loading direction. The stresses can be transformed into cartesian coordinates in the following way:

$$\bar{\sigma}_{xx} = \bar{\sigma}_r \cdot \cos \bar{\varphi} \cdot \cos \bar{\theta}, \quad (4.2)$$

$$\bar{\sigma}_{zz} = \bar{\sigma}_r \cdot \sin \bar{\varphi} \cdot \cos \bar{\theta} \quad \text{and} \quad (4.3)$$

$$\bar{\sigma}_{xz} = \bar{\sigma}_r \cdot \sin \bar{\theta}. \quad (4.4)$$

The three variables $\bar{\varphi}$, $\bar{\theta}$, and $\bar{\sigma}_r$ define the sampling domain for deriving the failure surface. By an adaptive load incrementation in the FE simulation, a given orientation ($\bar{\varphi}$, $\bar{\theta}$) is assessed for material failure for all stress resultants. Therefore, we considered only the two angles in the sampling procedure.

The next step was to define a sampling range. While reasonable values for $\bar{\varphi}$ reach from 0 to 2π , $\bar{\theta}$ was sampled from 0 to $\pi/2$, describing a hemisphere. To ensure an even distribution of the samples over this domain, LHS [91] was used for choosing a reasonable set of loading paths. For n samples, the sample domain is evenly divided into n columns and n rows. The samples are randomly placed inside this domain, such that there is exactly one sample in each column and row, leading to a set of samples, which is evenly distributed over the given domain.

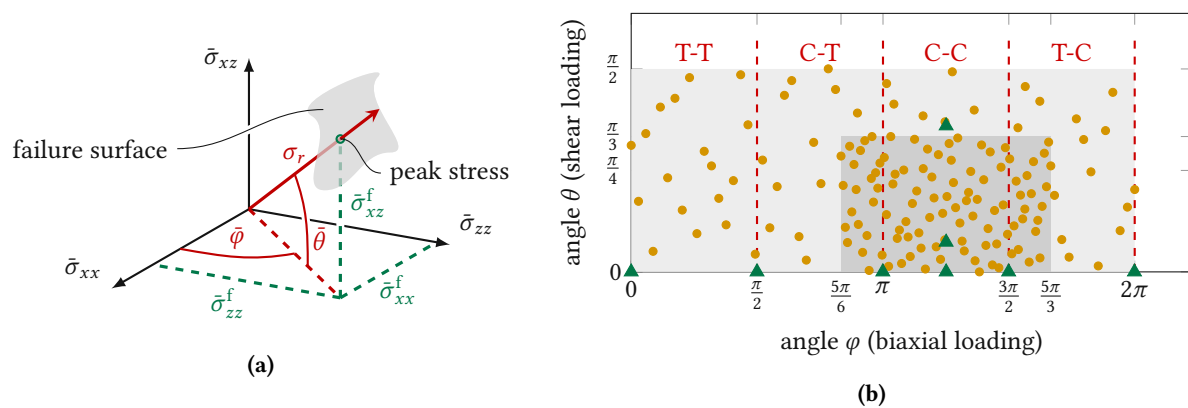


Fig. 4.7: (a) Spherical coordinates for the stress components and the intersection of the load path with the failure surface. (b) Example for loading combinations randomly sampled with LHS. The sample density in the darker area was chosen five times as large as in the lighter area. Red capital letters denote the loading regime (C ... Compression, T ... Tension).

Considering the failure surfaces found by Ganz [54] and Lourenço [86], the compressive strengths are expected to be significantly larger than the tensile strengths. This implies that the failure surface is further from the coordinate origin in the compressive loading regime. Since the LHS creates samples evenly distributed over the given domain, the distance between the calculated points on the surface is larger in the compressive than in the tensile loading regime. Therefore, the sample density in the compressive loading regime was chosen five times as large as in the tensile loading regime (see Figure 4.7b).

With a stress resultant of $r = 15$ MPa (large enough to cause material failure for any combination of $\bar{\varphi}$ and $\bar{\theta}$), we randomly generated 150 samples for each head joint type, resulting in 450 simulations (see also Fig. 4.8). Additionally, we added the seven loading states proposed by Lourenço [86], which are marked by green triangles in Fig. 4.7b.

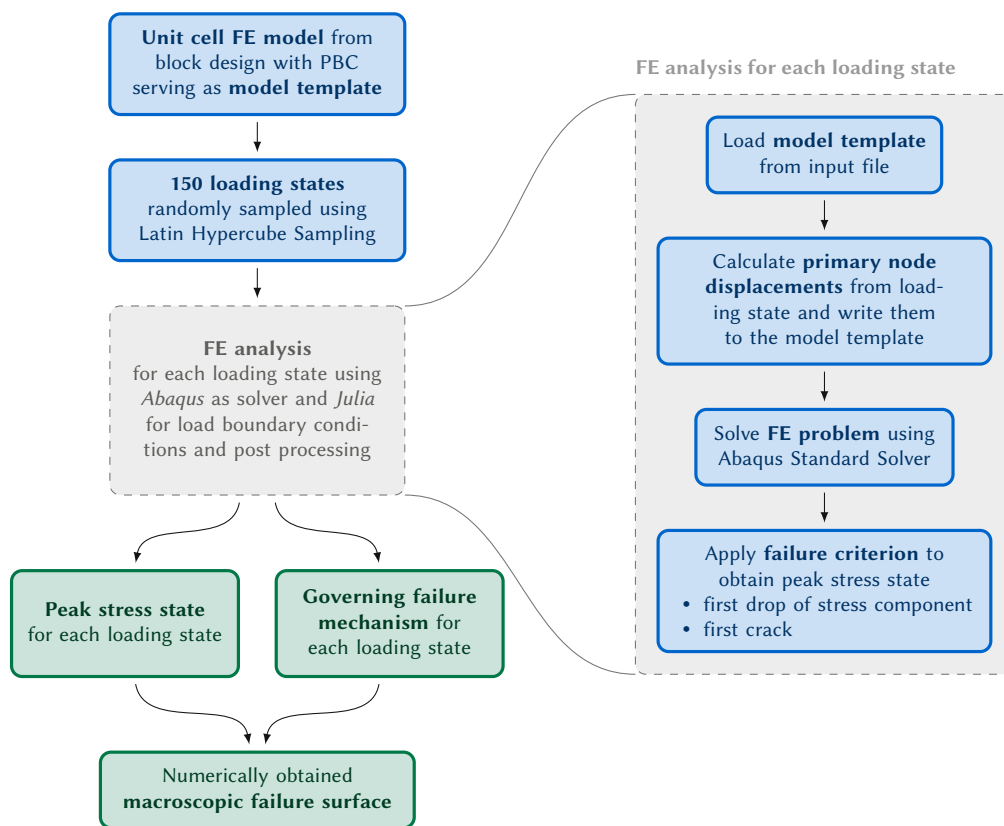


Fig. 4.8: Overview of the simulation procedure.

4.3.6 Computational Aspects

The simulations were performed on a high-performance computing cluster with 168 CPUs in total. Using eight CPU cores in parallel, one simulation took approximately 144 minutes on average to finish. For overcoming numerical instabilities related to the initiation of contact between two surfaces, an additional step was introduced at the beginning of the calculation. In this step, the displacements of each primary node were set to zero. Due to the chosen pressure-overclosure formulation with an insignificant compressive contact stress at zero distance between the surfaces, contact could be ensured in each relevant point, before the displacement-controlled loading was applied in the following step. To prevent

numerical instabilities when solving the interface damage conditions, damage stabilization was used for the cohesive interfaces.

4.3.7 Postprocessing

After the simulations were completed, we extracted the results by using the postprocessing procedure described in the following sections (see Fig. 4.8). Two different results were most interesting to us: the effective stresses and strains on the macroscopic level, which are essential for defining a macroscopic failure surface, and the failure mechanism on the microscale, which gives insights into the overall behavior and helps define the exact point of failure.

At first, we derived the macroscopic stresses and strains by homogenizing the stresses and strains on the microscale over the repeating unit cell. Afterward, we used the macroscopic stress-strain relation and indicators on the microscale to specify a failure point. These procedures are discussed next.

4.3.7.1 Obtaining macroscopic stresses and strains

For homogenizing the behavior from the micro to the macroscale, we assume that the behavior of the smallest possible repeating unit cell in the wall is representative for each point in the homogenized macroscopic wall. The unit cell concept is well suited for micro-to-macro homogenization since the displacements and reaction forces of the total structure are concentrated in the primary nodes of the unit cell. Thus, the stresses and strains can be easily calculated from the extracted reaction forces RF_i and displacements u_i by considering the dimensions l_i of the repeating unit cell as follows:

$$\bar{\sigma}_{xx} = \frac{RF_{xx}}{l_y \cdot l_z}, \quad \bar{\sigma}_{zz} = \frac{RF_{zz}}{l_x \cdot l_y}, \quad \text{and} \quad \bar{\sigma}_{xz} = \frac{1}{2} \cdot \left(\frac{RF_{xz}}{l_y \cdot l_z} + \frac{RF_{zx}}{l_y \cdot l_z} \right) \quad \text{as well as} \quad (4.5)$$

$$\bar{\varepsilon}_{xx} = \frac{u_{xx}}{l_x}, \quad \bar{\varepsilon}_{zz} = \frac{u_{zz}}{l_z}, \quad \text{and} \quad \bar{\varepsilon}_{xz} = \frac{1}{2} \cdot \left(\frac{u_{xz}}{l_x} + \frac{u_{zx}}{l_z} \right). \quad (4.6)$$

4.3.7.2 Detecting Failure

For defining the macroscopic failure stress state for each simulation we considered the same two-part failure criterion as we used in [128]. At the macroscopic scale, the largest stress before the first significant decrease of a stress component was considered the peak stress. This criterion was relevant, especially for joint failure, which occurs much more ductile than block failure. Furthermore, a second criterion considering the first crack within the blocks was defined to capture block failure. This was necessary, since some of the simulations, where block failure was relevant, did not produce a significant drop in stresses. Instead, these simulations aborted when the first crack opened. Considering the findings of Kiefer et al. [76] and Suda et al. [142], this is a good approximation, since there, the first crack also occurred just before the peak stress was reached.

4.4 Results and Discussion

In the following section, the simulation results are presented and discussed. First, failure mechanisms are identified from the results of the simulations with the simplified geometry. Then, the Rankine–Hill surface [86] and the failure surface of Ganz [54] are calibrated using the simulation results and compared to the numerically obtained failure surface. Next, the developed procedure for defining a failure surface is applied to two real block designs and the results are discussed. Finally, the obtained results are gathered, to propose a concept for calibrating the Rankine–Hill surface, taking the differences between the numerically-obtained failure surfaces and the Rankine–Hill surface into account. For the sake of brevity, only the model with mortared head joints is discussed in detail, while the results for the other two models are presented in the supplementary material¹.

4.4.1 Numerically obtained failure surface

Fig. 4.9 shows the numerically obtained failure surface for the model with mortared head joints. Each circle in Fig. 4.9a represents the peak stress state of one simulation. The filled areas in the background mark regions, where we observed similar failure mechanisms in the simulations. In the following, we will discuss the peak stresses starting with the tensile regime and then moving clockwise around the boundary of the failure surface.

In the tensile regime, the maximum vertical macroscopic peak stress was 1.303 MPa, while the maximum horizontal macroscopic peak stress was 0.818 MPa. On the right side of the failure surface, the horizontal macroscopic peak stress stayed constant with increasing vertical compression until the vertical stress reached -9.157 MPa, which was the maximum vertical compressive peak stress observed in the simulations. On the bottom side, this maximum vertical compressive peak stress stayed constant with increasing horizontal compression until the horizontal stress reached -9.023 MPa. On the left side, the failure surface showed a parabolic shape with a maximum horizontal compressive

¹The supplementary material can be found in the online version of the published article.

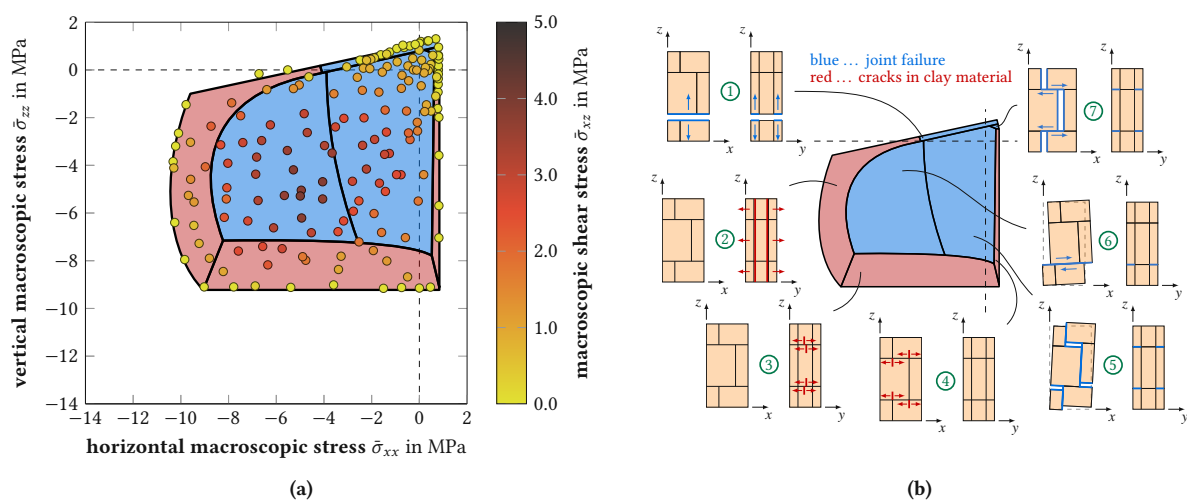


Fig. 4.9: Numerically obtained failure surface for the model with mortared head joints. Each point in (a) represents the peak stress state of one simulation. The filled areas in (b) mark regions with similar failure mechanisms.

peak stress of -10.325 MPa. The top side of the failure surface showed a linear relationship between the horizontal and the vertical macroscopic stress, with an increasing vertical macroscopic peak stress for decreasing horizontal compression. The macroscopic peak shear stress was 3.928 MPa occurring at $\bar{\sigma}_{xx} = -4.992$ MPa and $\bar{\sigma}_{zz} = -5.286$ MPa.

Vertically perforated clay block masonry is known to show significant strength anisotropies. Typically, the ratio of the macroscopic peak stress parallel to the bed joints to the macroscopic peak stress perpendicular to the bed joints is between 0.25 and 0.63 , depending on the block design [86]. However, the maximum horizontal macroscopic peak stress in the simulations was similar to the maximum vertical macroscopic peak stress, which most likely roots in the given block design. Comparable block designs, such as typical hollow concrete block masonry, tend to show a less pronounced strength anisotropy (see, e. g., Lourenço [86]). Nevertheless, the simulations did show a significant anisotropy considering the failure mechanisms, which we will discuss in the following.

The observed failure mechanisms, labeled 1–7, are assigned to the filled areas in Fig. 4.9b. Note, that the failure mechanisms are not necessarily unique to the corresponding area, but are the dominating ones. While surfaces, where block failure was observed, are filled red (2, 3, and 4), surfaces, where joint failure was observed, are filled blue (1, 5, 6, and 7).

Failure mechanism 1 was observed under governing vertical tensile stresses and is characterized by tensile failure of the bed joints since the vertical tensile stresses introduce tensile stresses in the bed joints. With increasing horizontal compression, shear stresses are additionally introduced in the bed joints, which leads to a decreasing vertical tensile strength of the bed joints (see Eq. (4.1)).

Failure mechanism 2 was observed under governing horizontal compression and is characterized by tensile cracks in the connection between transversal and longitudinal webs (see Fig. 4.10a). In a previous numerical study [128], we traced back these cracks to bending moments, introduced to the transversal webs by deformation differences in the mortar head joints.

Failure mechanism 3 was observed under governing vertical compression and is characterized by tensile cracks in the transversal webs (see Fig. 4.10b) since large vertical compressive stresses lead to tensile stresses in the transversal web (see Kiefer et al. [76], Suda et al. [142], and Reismüller et al. [128]).

Failure mechanism 4 was observed under horizontal tension in combination with vertical compression and is characterized by tensile cracks in the longitudinal webs (see Fig. 4.10c). With decreasing vertical compression, the shear strength of the bed joints decreases (see Eq. (4.1)), which leads to a change to

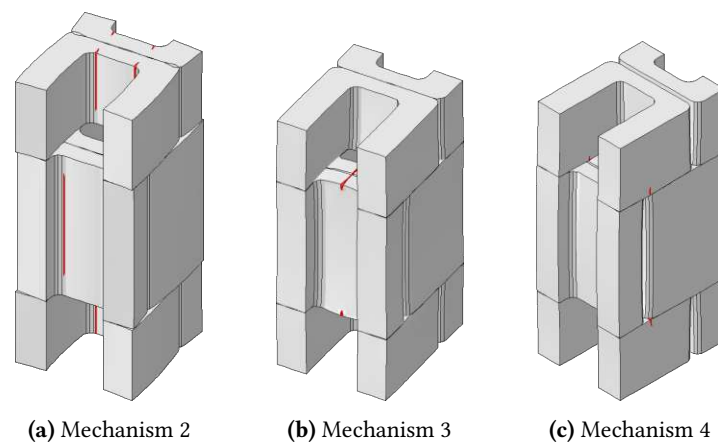


Fig. 4.10: Block failure mechanisms observed in the simulations.

failure mechanism 7. When the shear strength of the bed joints falls below a certain value, joint failure occurs before the failure of the longitudinal webs.

Failure mechanism 5 was observed under governing shear stresses in combination with low horizontal compression and is characterized by a stepped shear failure of the bed joints and head joints. The inhomogeneous nature of masonry leads to a rotation of the blocks under shear loading [101], introducing bending moments in the joints. In addition to the shear stresses parallel to the joints, these bending moments induce stresses perpendicular to the joints. Depending on the magnitude of the vertical and horizontal macroscopic stresses, tensile stresses perpendicular to the joints can occur. Thus, despite failure mechanism 5 being labeled as shear failure, especially with low vertical compression, a combination of shear and tensile failure was observed.

In contrast to the previous mechanism, failure mechanism 6, which was observed under governing shear stresses in combination with large horizontal compression, is characterized by a shear failure solely of the bed joints. This is because the larger horizontal compression leads to a larger shear strength of the head joints, which prevents joint failure there.

Failure mechanism 7 was observed in the tensile regime under governing horizontal tension and is characterized by tensile failure of the head joints and shear failure in the bed joints. This is because the horizontal tensile stresses introduce tensile stresses in the head joints and shear stresses in the bed joints. As discussed for failure mechanism 4, the shear strength of the bed joints increases with increasing vertical compression. Thus, increasing vertical compression leads to a change in failure mechanism from joint failure (7) to block failure (4).

Fig. 4.11 shows the peak stresses and failure mechanisms of the models with and without frictional contact in the head joints. Most of the previously described failure mechanisms were also observed in these models. However, some noteworthy differences compared to the model with mortar head joints occurred.

Despite showing similar maximum values for the tensile, compressive, and shear stresses, the failure surface of the model with frictional contact in the head joints (HJC) shows some differences in the

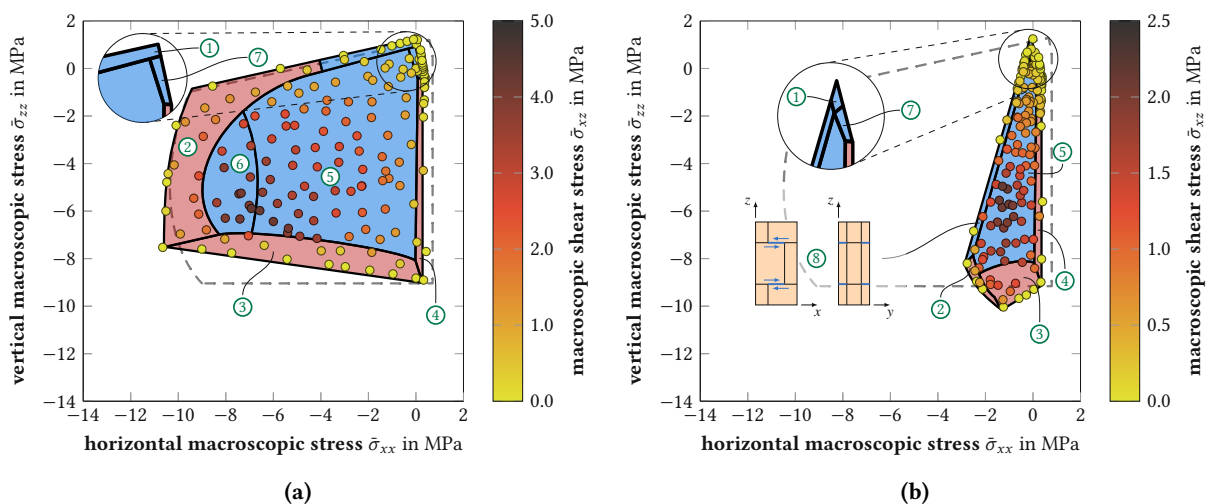


Fig. 4.11: Numerically obtained failure surface for (a) the model with frictional contact in the head joints and (b) the model without any contact in the head joints. Each point represents the peak stress state of one simulation. The filled areas mark regions with similar failure mechanisms. The numbers refer to the failure mechanisms in Fig. 4.9b.

overall shape, compared to the model with mortar head joints (Fig. 4.11a). Most notably, the maximum vertical compressive peak stress decreases with increasing horizontal compression (bottom side of the failure surface). Additionally, the maximum shear stress is reached at higher horizontal and vertical compressive stresses, although showing a similar magnitude. Thus, when moving along the hydrostatic axis in the compressive regime, the increase of the peak shear stress is less steep in the model with frictional contact in the head joints.

The failure surface of the model without contact in the head joints (HJG, Fig. 4.11b) shows a significantly different shape compared to both other models. Most notably, failure region 2, which is governed by block failure under horizontal compression, nearly vanished. Instead, under horizontal compression, failure is mainly governed by a shear failure of the bed joints, similar to failure mechanism 7 but in the opposite direction (region 8). This is because the horizontal compressive stresses are being transferred via shear stresses in the bed joints since no contact in the head joints is present. With the adapted interface condition in the joint interfaces, the horizontal compressive peak stress increases with increasing vertical compression in region 8. Hence, the maximum horizontal compressive peak stress is only 3.0 MPa, which is significantly lower than in the other models. Additionally, the maximum shear stress 2.5 MPa is 50 % lower. While the maximum tensile peak stresses and the maximum vertical peak stress are similar to the other models, another noteworthy difference is the increasing vertical compressive peak stress with increasing horizontal compression in region 3.

4.4.2 Comparison to available failure surfaces

In the following, the numerically obtained failure surface of the model with mortar head joints (HJM) is compared to the failure surfaces of Ganz [54] and Lourenço [86]. A similar comparison for the models with frictional contact in the head joints and without any contact in the head joints is given in the supplementary material².

4.4.2.1 Failure surface according to Ganz

The failure surface of Ganz [54] was calibrated to the simulations by adjusting the ten parameters of the failure criteria (see Appendix A) as follows: We obtained the uniaxial compressive masonry strengths $f_{m,x}$ and $f_{m,z}$, the vertical uniaxial tensile strength $f_{t,z}$, and the ratio of the horizontal tensile masonry strength to its compressive counterpart, ω_m , from the simulation results. The distance of the head joints, a_s , and the distance of the bed joints, a_L , are defined by the model's geometry. The remaining parameters, the cohesion shear stress c , the friction angle of the joints, φ , and the additional parameter μ , were calibrated to the simulations by minimizing the mean squared error between the numerically obtained peak stresses and the failure surface. The resulting failure surface and the chosen values for the parameters are shown in Fig. 4.12a. The mean absolute error (MAE) between the numerically obtained peak stresses and the calibrated failure surface is 0.708 MPa.

The most noticeable difference between the numerically obtained peak stresses and the calibrated failure surface can be found under horizontal tension in combination with vertical compression (right side of the failure surface). Here, the failure surface predicts a decreasing horizontal tensile peak stress with increasing vertical compression, while staying constant in the simulations. Regarding the shear behavior, the calibrated failure surface predicts a 23 % larger maximum shear stress than the simulations.

²The supplementary material can be found in the online version of the published article.

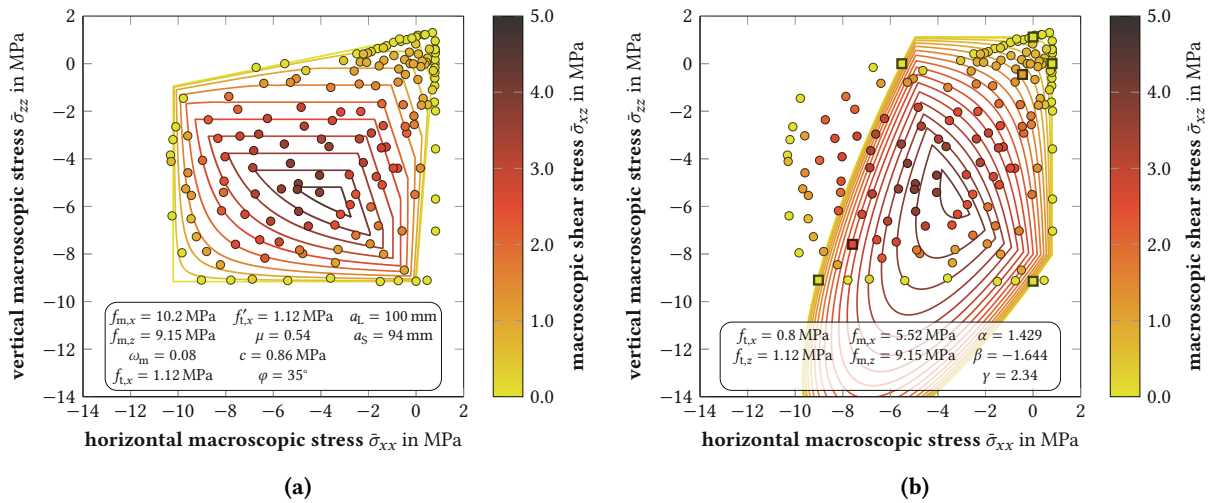


Fig. 4.12: Calibrated failure surfaces using the numerically-obtained peak stresses from the simplified model with mortared head joint: (a) failure surface after Ganz [54] and (b) Rankine–Hill surface after Lourenço [86]. The seven peak stress states used for calibrating the Rankine–Hill surface are marked with squares.

Additionally, this peak occurs at a lower horizontal compression than in the simulations, leading to significant shear stress deviations in this region compared to the simulations.

4.4.2.2 Rankine–Hill failure surface

Next, we will compare the numerically obtained results to the Rankine–Hill surface [86]. We calibrated the seven parameters of the Rankine–Hill surface in two different ways: (i) By determining the parameters from the seven simulations of ideal loading states and (ii) by minimizing the mean squared error between the numerically obtained peak stresses and the failure surface (“Opt”).

First, we derived the parameters by simulating the seven loading combinations proposed by Lourenço [86] (see Fig. 4.4). The resulting failure surface and the chosen values for the parameters are shown in Fig. 4.12b. Therein, the seven simulations used for the calibration are marked with squares.

Using the seven suggested loading combinations results in significant differences between the Rankine–Hill surface and the numerically obtained peak stresses, which is reflected by a large MAE of 2.395 MPa. The Rankine–Hill surface predicts a 49.8 % higher maximum vertical compressive stress and a 46.5 % lower maximum horizontal compressive stress than the simulations. Given that only seven loading states were considered, the Rankine-type criterion shows good agreement with the simulations, and the maximum shear stress has a similar magnitude, as the numerically obtained results.

In the second step, we optimized the parameters of the Rankine–Hill surface by minimizing the mean squared error between the numerically obtained peak stresses and the failure surface. While Lourenço suggests the seven loading combinations as a good option for minimizing the effort and maximizing the accuracy of the calibration, he also states that the mean error optimization is better, if enough data is available. The resulting failure surface and the chosen values for the parameters are shown in Fig. 4.13. The MAE between the numerically obtained peak stresses and the calibrated failure surface is 0.832 MPa. The mean error optimization delivers a significantly better fit than calibration with the seven loading combinations. However, the Rankine–Hill surface still shows differences compared to the numerically obtained peak stresses. The vertical uniaxial compressive strength is predicted to be 21.0 % lower than

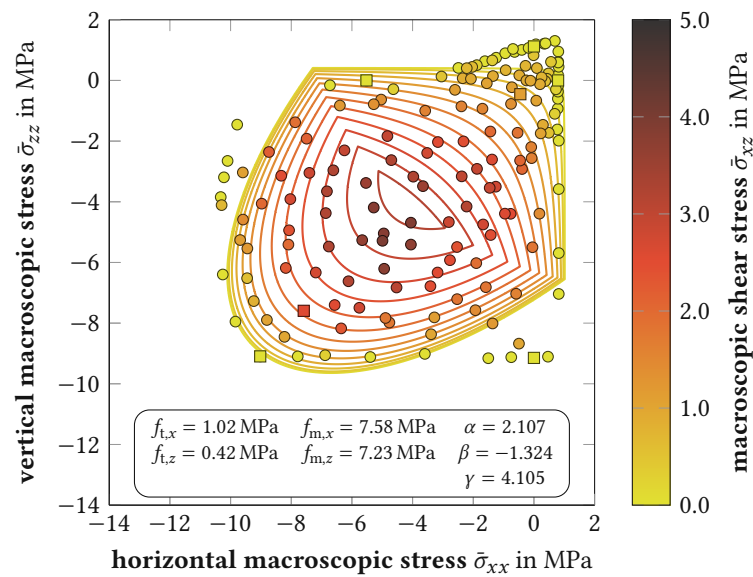


Fig. 4.13: Calibrated Rankine–Hill surface for the simplified model with mortared head joints using mean squared error optimization (Opt). The seven peak stress states used for calibrating the Rankine–Hill surface in Fig. 4.12b are marked with squares.

in the simulations and the vertical uniaxial tensile strength is predicted to be 62.5 % lower, whereas the horizontal uniaxial compressive strength is predicted to be 37.3 % higher. Additionally, some simulations with large horizontal compressive stresses are not captured by the failure surface. Furthermore, the peak shear stress is predicted to be 17.0 % lower than in the simulations.

The most noticeable differences can be found under vertical tension in combination with horizontal compression (top part of the failure surface) and under large vertical compression in combination with horizontal compression (bottom side of the failure surface), where the calibrated Rankine–Hill surface predicts significantly smaller peak stresses than the simulations. In general, the linearly decreasing vertical tensile peak stress with increasing horizontal compression (top part of the simulated peak stresses, Failure Mechanism 1) cannot be replicated by the Rankine–Hill surface, since it predicts a constant vertical tensile peak stress. Furthermore, the Rankine–Hill surface is smooth in the compressive regime, while the simulation results show a distinct edge, where the failure mechanism changes from horizontal compressive block failure (Region 2) to vertical compressive block failure (Region 3).

Removing the simulations where failure mechanisms 1 and 3 were governing from the set of peak stress states and applying the mean squared error optimization leads to the failure surface shown in Fig. 4.14. The obtained Rankine–Hill surface shows good agreement with the simulations and the vertical uniaxial compressive and tensile peak stresses are predicted similarly to the simulations, while the maximum shear stress is predicted to be 21 % lower than in the simulations. The MAE between the numerically obtained peak stresses and the calibrated Rankine–Hill surface is 0.867 MPa, which is only 4.2 % larger than the MAE using all the simulations. This shows that the Rankine–Hill surface can capture the majority of the simulations. However, we could identify some regions, where the simulations show a qualitatively different behavior than the Rankine–Hill surface, suggesting a more complex failure envelope of vertically perforated clay block masonry than the Rankine–Hill surface can provide. While the differences in failure region 1 can also be seen, when Lourenço [86] fitted the Rankine–Hill surface to the experimental data from Page [119], the differences under large vertical compression are most

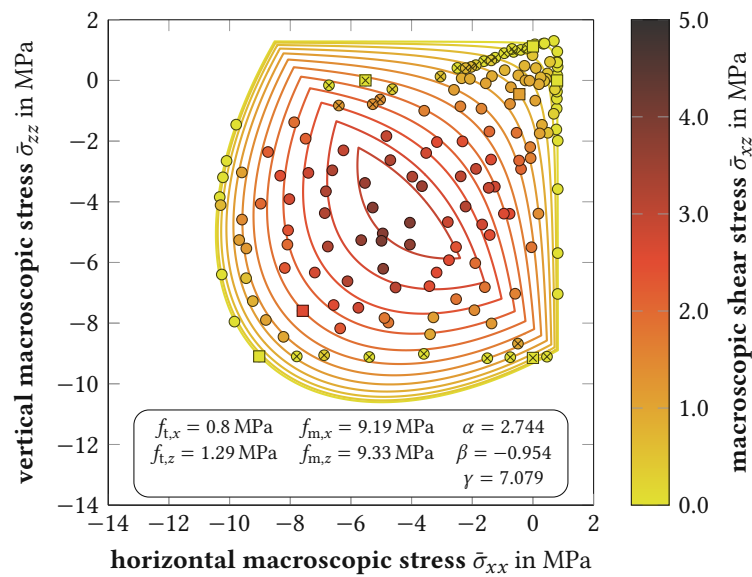


Fig. 4.14: Calibrated Rankine–Hill surface for the simplified model with mortared head joints using mean squared error optimization (Opt) without the simulations where Failure Mechanisms 1 and 3 were governing. The seven peak stress states used for calibrating the Rankine–Hill surface in Fig. 4.12b are marked with squares.

likely a phenomenon of vertically perforated clay block masonry, since the change in failure mechanism leading to this difference is caused by the perforations.

In conclusion, the mean squared error optimization on all peak stress states leads to a good representation of the results, assuming that the numerically obtained peak stresses resemble the real behavior of vertically perforated clay block masonry. However, the optimization procedure also leads to a significant underestimation of the vertical compressive peak stress and the vertical tensile peak stress. Adapting the set of peak stress state showed that the Rankine–Hill surface can capture the majority of the simulations, while still showing some discrepancies. Thus, a slightly more complex failure surface is needed to fully utilize the strength of the masonry.

4.4.3 Application to real block designs

To further verify our model, we used the developed procedure to calibrate the Rankine–Hill surface for two different real block designs, the SwissModul 15 [156] used in the experiments from Bitterli and Salmanpour [11, 133], and an insulation-filled block from Wienerberger [151].

The SwissModul 15 is a vertically perforated clay block with a height of 190 mm, a length of 290 mm, and a width of 150 mm. The blocks are used in conjunction with 10 mm thick mortar bed joints and mortar-filled head joints with similar thickness. For calibrating the failure surfaces, we used the 34 simulations from our previously published study [128]. In that study, we used the numerical unit cell model to simulate the experiments from Bitterli and Salmanpour [11, 133].

Simulating the loading states suggested by Lourenço [86], we obtained the failure surface shown in Fig. 4.15a with an MAE of 0.868 MPa. Using the mean squared error optimization procedure, we obtained the failure surface shown in Fig. 4.15b. The obtained Rankine–Hill surface is in good agreement with the simulations. However, a similar discrepancy between the surface and the numerically obtained peak stresses can be found under vertical compression, when failure mechanism 3 is relevant. In this

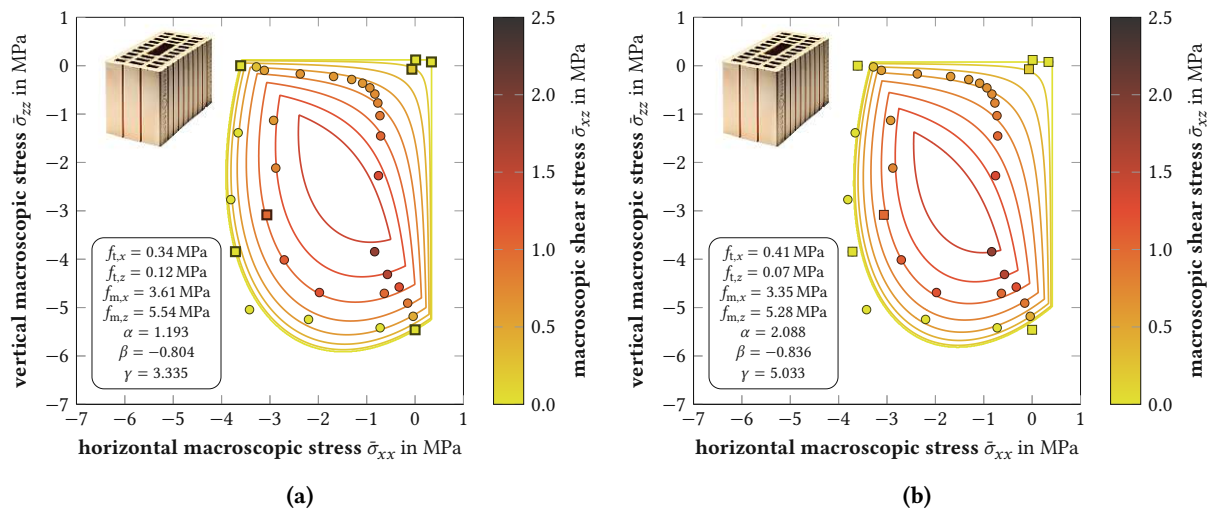


Fig. 4.15: Calibrated Rankine–Hill surfaces for SwissModul 15 with mortared head joints: (a) was calibrated using the loading states suggested by Lourenço [86] and (b) was calibrated using the mean squared error optimization procedure. The seven peak stress states used for calibrating the Rankine–Hill surface in (a) are marked with squares.

region, the calibrated Rankine–Hill surface predicts up to 9.2 % larger peak stresses than obtained in the simulations. Considering the second region with discrepancies identified with the simplified model (i. e., where Failure Mechanism 1 was governing), we cannot make a statement for this block design, since we did not simulate enough loading combinations in this region. The MAE of the Rankine–Hill surface calibrated for the SwissModul 15 is 0.417 MPa using all simulations. Thus, the optimization procedure leads to a better, yet more conservative fit of the Rankine–Hill surface with the numerically obtained peak stresses.

The second block design we used for calibrating the Rankine–Hill surface is an insulation-filled block from Wienerberger [151], which is 248 mm long, 249 mm high, and 365 mm wide. It is typically used in conjunction with 1 mm thin bed mortar joints and dry head joints. Thus, frictional contact was used in the head joints in the simulations. We calibrated the Rankine–Hill surface shown in Fig. 4.16 to 31 simulations. The model was created using the same modeling strategies as used for the previous simulations.

Notably, the results of the simulations predict a much more anisotropic behavior than with the SwissModul 15 and the simplified block design with a ratio of the horizontal compressive peak stress to the vertical compressive peak stress of 0.35. This is also reflected in the calibrated Rankine–Hill surface, which is in good agreement with the simulations. Using the loading states suggested by Lourenço [86], we obtained the failure surface shown in Fig. 4.16a with an MAE of 0.446 MPa. The failure surface obtained with the optimization procedure is presented in Fig. 4.16b. With this geometry, the optimized Rankine–Hill surface predicts up to 4.2 % smaller peak stresses than obtained in the simulations in the region, where failure mechanism 3 is relevant. Additionally, we observed a similar discrepancy under vertical tension combined with horizontal compression, as identified with the simplified model. The MAE of the calibrated Rankine–Hill surface is 0.372 MPa using all simulation. Similar to the SwissModul 15, the optimization procedure yielded a better, yet slightly more conservative fit of the Rankine–Hill surface.

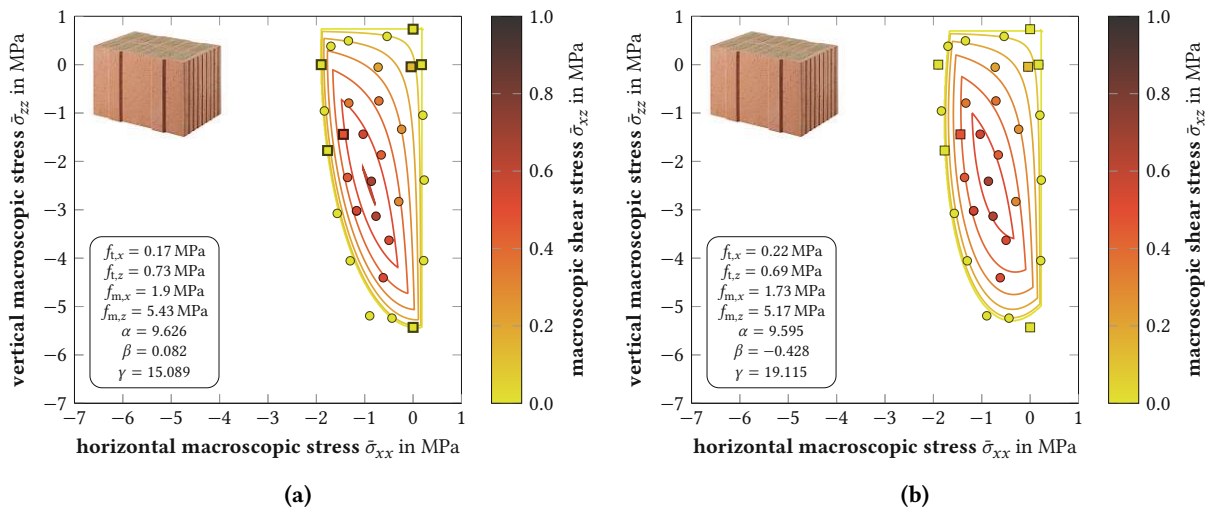


Fig. 4.16: Calibrated Rankine–Hill surfaces for the Wienerberger block with contact in the head joints: (a) was calibrated using the loading states suggested by Lourenço [86] and (b) was calibrated using the mean squared error optimization procedure. The seven peak stress states used for calibrating the Rankine–Hill surface in (a) are marked with squares.

4.4.4 Concept for deriving a numerically calibrated failure surface

Considering all the results presented in the previous sections, we propose the following concept for deriving a numerically calibrated failure surface for masonry. Since the Rankine–Hill surface depicts the numerically obtained peak stresses very well in most regions and can easily be implemented into FE software, we recommend using it for macroscopic simulations of vertically perforated clay block masonry. Simulating the loading states proposed by Lourenço [86] for the calibration of the Rankine type surface (i. e. parameters $f_{t,x}$, $f_{t,z}$, and f_α) led to a good agreement with the numerically obtained peak stresses in each case. Hence, we suggest using these three simulations for the calibration of this part of the surface (see Fig. 4.17). However, using the suggested loading states for the calibration of the Hill type surface (i. e. parameters $f_{m,x}$, $f_{m,z}$, f_β , and f_γ) did not always lead to a good agreement with the numerically obtained peak stresses. While we obtained good agreement for the real block geometries, we observed significant deviations for the simplified block design. Thus, we suggest simulating seven additional loading states for the calibration of the Hill-type surface (see Fig. 4.17b). We chose these such that the loading path is directed towards the regions, where we observed the largest discrepancies between the numerically obtained peak stresses and the calibrated Hill-type surface. Using these additional peak stresses, we can derive the parameters for the Hill-type surface using a mean error optimization procedure. Therefore, the resulting failure surface will underestimate some of the peak stresses in failure region 2, but also show fewer differences to the simulations in failure region 3.

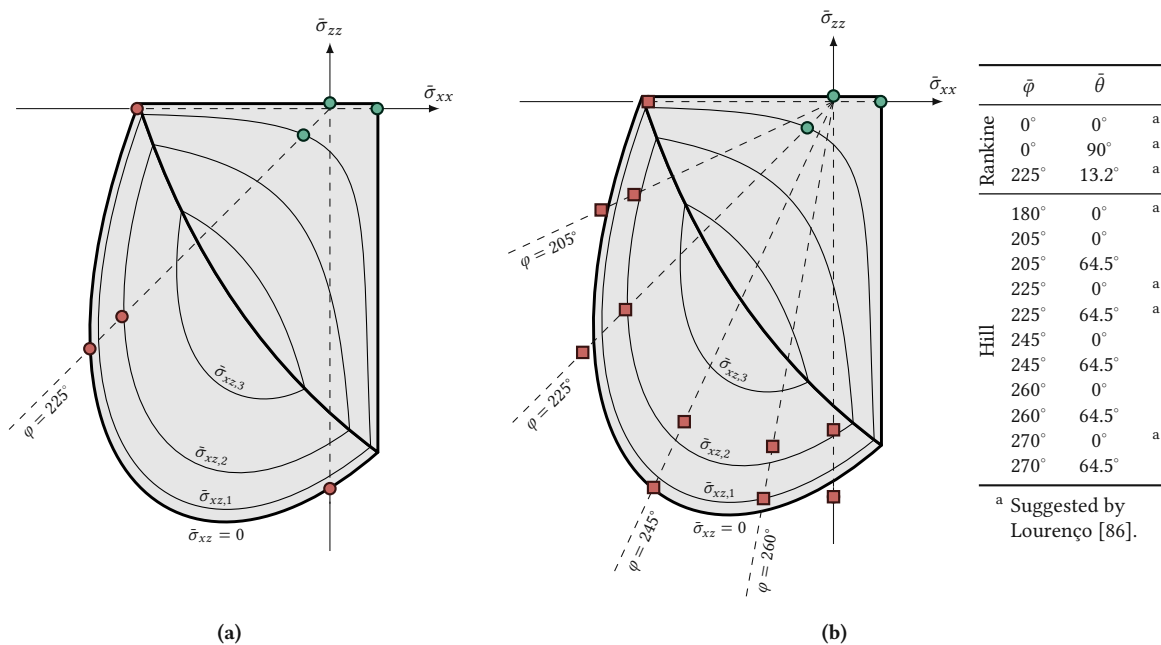


Fig. 4.17: Concept for deriving a numerically calibrated Rankine–Hill surface. (a) Calibration with the loading states suggested by Lourenço [86], and (b) mean error optimization of $f_{m,x}$, $f_{m,z}$, β , and γ using 11 simulations. Peak stresses used for calibration of the Rankine-type surface are filled green, and those used for calibration of the Hill-type surface are filled red. Simulations used for mean error optimization are marked with squares.

4.5 Conclusion and Outlook

Within this work, we presented a new approach to develop failure surfaces for vertically perforated clay block masonry under in-plane loading using numerical simulations. Using a previously published unit cell FE model [76, 128] and a simplified block design, we derived the peak stresses from 450 simulations in total, with 150 arbitrarily generated loading states. Additionally, we investigated the influence of the head joint, by considering three different types, i. e., a mortared head joint, frictional contact in the head joint, and no contact in the head joint. Hence, we were able to numerically derive failure surfaces for the three different head joint types. For each type, we also identified seven different realistic failure mechanisms and assigned these mechanisms to regions of the failure surface.

After the rigorous discussion of the numerically-obtained failure surfaces, we compared them to the failure surfaces proposed by Ganz [54] and Lourenço [86], by calibrating the necessary parameters to the simulation results. The failure surface of Ganz was found to be in good agreement with the numerically-obtained failure surfaces, with the most significant difference under horizontal tension. Additionally, the maximum shear stress was found to be 23 % higher than in the numerically-obtained failure surface. The quality of the fit of the failure surface after Lourenço depends on the chosen calibration procedure. While calibrating the failure surface by simulating the seven loading combinations suggested by Lourenço [86] resulted in a poor agreement with the numerically-obtained peak stresses, a mean squared error optimization procedure yielded a good agreement. Thereby, two regions with significant differences were identified, i. e., the region of vertical tension and the region of vertical compression.

To assess this difference in more detail, we used the developed procedure to calibrate the Rankine–Hill surface for two real block designs. The results showed, that the differences also occur for real block designs, although the differences are less significant. Nevertheless, the Rankine–Hill surface overestimated the peak stress of the numerical model up to 12.8 %, suggesting a more complex failure surface.

Finally, we proposed a concept to numerically calibrate the parameters of the Rankine–Hill surface, taking the differences between the numerically-obtained failure surfaces and the Rankine–Hill surface into account. Therefore, we suggested simulating the seven loading combinations proposed by Lourenço [86] for calibrating the surface, and to simulate two additional loading combinations with governing vertical compressive stresses to assess the quality of the fit and to adjust the parameters accordingly.

In future research, we could improve the proposed concept by considering the following aspects: Since the model is restricted to in-plane loading, the next step would be to extend the model to out-of-plane loading, like Mojsilović [101] did for the failure surface of Ganz [54]. Additionally, the model is not yet reasonably validated for horizontal and vertical tension, since no experimental data is available for vertically perforated clay block masonry. Thus, an experimental campaign would be necessary to validate the model for these loading states. Another interesting modification to consider is the use of the phase field method (see, e. g., Miehe et al. [97]), as a substitute for the XFEM approach. The phase field method is known to be very stable, even for complex crack topologies, as, e. g., Pech et al. [120, 121] showed for wood, and could therefore enable the investigation of the post-peak behavior of vertically perforated clay block masonry in more detail. Finally, the model could also be validated for masonry glued with polyurethane adhesive in the bed joints, since this is a rising technology in the field of masonry construction and could be considered in the presented model with only minor adaptations.

Acknowledgements

The authors gratefully acknowledge the financial support of the Austrian Research Promotion Agency (FFG, project number 865067) and the industry partner Wienerberger for funding the research work within the project “Innovative Brick 2”. Furthermore, the authors acknowledge TU Wien Bibliothek for financial support through its Open Access Funding Programme.

4.6 Appendix A: Failure Criteria according to Ganz

In the following, the 12 failure criteria developed by Ganz [54] are presented. Note, that the indices are different than in the original publication. While Ganz [54] refers to the vertical direction with x and to the horizontal direction with y , we use x for the horizontal direction and z for the vertical direction.

4.6.1 Block Failure

$$\Phi_{1a} = \tau_{xz}^2 - (\omega_m \cdot f_{m,x} - \sigma_{xx}) (2\omega_m \cdot f_{m,z} - \sigma_{zz}) \leq 0. \quad (4.7)$$

$$\Phi_{1b} = (1 + \omega_m)^2 \cdot \tau_{xz}^2 + [\omega_m \cdot (\sigma_{zz} + f_{m,z}) - \sigma_{xx}] [\sigma_{zz} + f_{m,z} - f_{m,x} - \omega_m \cdot (\sigma_{xx} + f_{m,x})] \leq 0. \quad (4.8)$$

$$\Phi_{1c} = (1 + \omega_m)^2 \cdot \bar{\sigma}_{xz}^2 + [\omega_m \cdot (\bar{\sigma}_{zz} - 2\omega_m \cdot f_{m,z} + f_{m,x} \cdot (1 + \omega_m)) - \bar{\sigma}_{xx}] \cdot [\bar{\sigma}_{zz} - 2\omega_m \cdot f_{m,z} - \omega_m \cdot f_{m,x}] \leq 0. \quad (4.9)$$

$$\Phi_2 = \tau_{xz}^2 - (\sigma_{xx} + f_{m,x}) \cdot (\sigma_{zz} + f_{m,z}) \leq 0. \quad (4.10)$$

$$\Phi_{3ab} = \tau_{xz}^2 + \sigma_{xx} \cdot (\sigma_{xx} + f_{m,x}) \leq 0. \quad (4.11)$$

$$\Phi_{3c} = \tau_{xz}^2 + (\sigma_{xx} - \omega_m \cdot f_{m,x} + R_a)^2 - R_a^2 \leq 0. \quad (4.12)$$

$$R_a = d \cdot \tan\left(\frac{\pi}{4} - \frac{\tan^{-1}(k)}{2}\right) - f_{m,x} \cdot \frac{1 - \omega_m}{2} \quad \text{where } d = \frac{\omega_m \cdot f_{m,x}}{2 \cdot \sqrt{\omega_m}} \text{ and } k = \frac{\omega_m - 1}{2 \cdot \sqrt{\omega_m}} \quad (4.13)$$

$$\Phi_{3d} = 4\omega_m \cdot \tau_{xz}^2 - [\omega_m \cdot f_{m,x} - \sigma_{xx} \cdot (1 - \omega_m)]^2 \leq 0. \quad (4.14)$$

4.6.2 Mortar Joint Failure

$$\Phi_{4a} = \tau_{xz}^2 - (c - \sigma_{zz} \cdot \tan(\varphi))^2 \leq 0. \quad (4.15)$$

$$\Phi_{4b} = \tau_{xz}^2 + (\sigma_{zz} - f_{t,z} + R_b)^2 - R_b^2 \leq 0. \quad (4.16)$$

$$\Phi_{4c} = \tau_{xz}^2 + \left[\sigma_{zz} - f'_{t,z} \cdot \left(\frac{\sigma_{xx}}{\mu \cdot f_{m,x}} + 1 \right) + R_c \right]^2 - R_c^2 \leq 0. \quad (4.17)$$

$$\Phi_{4d} = \tau_{xz}^2 \cdot \left(1 + \frac{2 \cdot a_L}{a_s} \cdot \tan(\varphi) \right)^2 - \left(\sigma_{zz} \cdot \tan(\varphi) + \sigma_{xx} \cdot \frac{2 \cdot a_L}{a_s} - c \right)^2 \leq 0. \quad (4.18)$$

$$\Phi_{4e} = \left(|\tau_{xz}| + \frac{2a_L}{a_s} \cdot \sigma_{xx} \right)^2 + \left(\sigma_{zz} + |\tau_{xz}| \cdot \frac{2a_L}{a_s} - f_{t,z} + R_b \right)^2 - R_b^2 \leq 0. \quad (4.19)$$

$$R_b = c \cdot \tan\left(\frac{\pi}{4} + \frac{\varphi}{2}\right) - f_{t,z} \cdot \frac{\sin(\varphi)}{1 - \sin(\varphi)} \quad (4.20)$$

$$R_c = c \cdot \tan\left(\frac{\pi}{4} + \frac{\varphi}{2}\right) - f'_{t,z} \cdot \left(\frac{\sigma_{xx}}{\mu \cdot f_{m,x}} + 1 \right) \cdot \frac{\sin(\varphi)}{1 - \sin(\varphi)} \quad (4.21)$$

Note, that the equation for failure criterion 3c in the original publication seems to be wrong, since it always indicates failure at $\sigma_{xx} \geq 0$, although horizontal tensile stresses should be possible. Using the verbal description of Ganz [54], a new criterion was defined, assuming the surface to describe a cylinder (see Eq. (4.12)). The original equation in the publication is the following:

$$\Phi_{3c,o} = \tau_{xz}^2 + \sigma_{xx} \cdot (\sigma_{xx} - \omega_m \cdot f_{m,x}) \leq 0. \quad (4.22)$$

4.7 Appendix B: Rankine–Hill Surface

The Rankine-type surface is defined in the following manner:

$$f_1 = \frac{(\sigma_x - f_{t,x}) + (\sigma_z - f_{t,z})}{2} + \sqrt{\left(\frac{(\sigma_x - f_{t,x}) - (\sigma_z - f_{t,z})}{2}\right)^2 + \alpha \tau_{xz}^2} = 0, \quad (4.23)$$

with the parameter α , which is derived from the uniaxial tensile strengths, $f_{t,x}$ and $f_{t,z}$, as well as the pure shear strength of the material, τ_u as follows:

$$\alpha = \frac{f_{t,x} \cdot f_{t,z}}{\tau_u}. \quad (4.24)$$

The Hill-type surface forms a rotated centered ellipsoid, which reads as

$$f_2 = A \cdot \sigma_x^2 + B \cdot \sigma_x \cdot \sigma_z + C \cdot \sigma_z^2 + D \cdot \tau_{xz}^2 - 1 = 0. \quad (4.25)$$

The four parameters A , B , C , and D can be derived from the material strengths and equivalent yield stresses in the following way:

$$A = \frac{1}{(f_{m,x})^2}, \quad B = \frac{\beta}{f_{m,x} \cdot f_{m,z}}, \quad C = \frac{1}{(f_{m,z})^2}, \quad \text{and} \quad D = \frac{\gamma}{f_{m,x} \cdot f_{m,z}}. \quad (4.26)$$

Conclusion and Perspectives

In the following, the main findings of Publications 1 to 4 are summarized, and future research is discussed.

Main Findings

Publication 1 deals with assessing the impact of bed joint reinforcement on the vertical compressive strength of vertically perforated clay block masonry. For this purpose, we enhanced the numerical unit cell model of Kiefer et al. [76] by a multi-scale homogenization approach to account for the bed joint reinforcement. Using the developed modeling strategies, we simulated 30 models with randomly allocated strength values and three different reinforcement ratios. In doing so, we were able to show that adding bed joint reinforcement could increase the 5%-quantile of the compressive strength of vertically perforated clay block masonry by up to 33 %. Furthermore, we could identify two mechanisms that were responsible for the increase in compressive strength: Firstly, the first crack occurred at a higher load level, due to the decrease of lateral tensile stresses in the transversal webs, and secondly, the onset of a crack arose at a higher load level, as the fiber mesh bridged the open crack. Additionally, the reinforcement prevented the outermost longitudinal web from spalling, after the first crack occurred, leading to a more ductile behavior of the masonry. Considering the results of the stochastic simulations without any reinforcement, we were able to evaluate the mean value and standard deviation of the numerically obtained compressive strength. These values were in good agreement with experimental results on five wall specimens. Furthermore, these simulations showed, that mostly weaker transversal webs affect the value of the vertical compressive strength, which is why the fixed-value approach of Kiefer et al. [76] tended to overestimate the compressive strength. Nevertheless, considering the large fluctuations of experiments on masonry walls and the effort of the stochastic simulations, the results of the fixed-value approach are still acceptable. Concludingly, bed joint reinforcement has a large potential to increase the vertical compressive strength of vertically perforated clay block masonry, especially since the potential in modifying the block geometry is already exhausted.

Publication 2 addresses the numerical simulation of a firing test on a vertically perforated clay block masonry wall. Thereby, we used a coupled temperature-displacement finite element model to assess the performance of the wall and compared the results to novel experimental data. By using a novel energy-based spalling criterion, the spalling of the outermost longitudinal webs could be decoupled from the vertical loading of the wall. Thus, two-dimensional simulations using unit cell models were sufficient, which reduced the computational effort significantly. Considering the temperatures gained from 2D thermal simulations and energy parameters gained from 2D mechanical simulations we were able to predict the performance of the wall with good agreement to the experimental results, without any empirical adjustments. Furthermore, the small but detailed model enabled unique insights into the thermal and mechanical behavior of the wall. In this way, we could observe the redistribution of heat flow from the transversal webs to the air-filled cavities at higher temperatures, due to increasing radiation and convection effects. Additionally, we could show, that the most critical effect on spalling is

the deformation difference of two adjacent longitudinal webs. This deformation difference is caused by the thermal expansion and introduces tensile stresses in the transversal webs, which lead to spalling. Designing block geometries which show less deformation difference without increasing the occurring tensile stresses in the transversal webs, e. g. by maximizing contact in the head joints, could be a promising approach to reduce the risk of spalling.

Publication 3 deals with developing a numerical unit cell model for evaluating the peak stress state of vertically perforated clay block masonry subjected to arbitrary in-plane loading states. For this purpose, we extended the unit cell model of Kiefer et al. [76], which was already used in Publication 1, by introducing a failure model for the mortar joints. Thereby, we modelled the joints as interfaces between the blocks and used cohesive behavior with a quadratic stress interaction criterion for considering joint failure. This extended model was then used to model seven uniaxial compressive experiments on wall specimens with inclined bed joints, conducted by Bitterli and Salmanpour [11, 133]. The obtained peak stresses were mostly in good agreement with the experimental results. Only under governing horizontal compression, the model tended to overestimate the peak stress. Additionally, the failure mechanisms obtained from the numerical simulations were similar to the experimental observations. Thereby, for the first time, failure under horizontal compression could be linked to deformation differences of the longitudinal webs. These deformations differences led to tensile stresses in the transversal webs, comparable to the observations in Publication 2. After validation of the model, simulating seven loading states recommended by Lourenço [86] allowed for calibrating the model parameters of a Rankine–Hill failure surface. The obtained surface showed good agreement with the numerically obtained peak stress states of 34 different loading states. Further comparison with the failure surface developed by Ganz [54] and various experimental studies strengthened the validity of the model. Thus, the developed model is a sound basis for further investigations on numerically generating macroscopic failure surfaces for vertically perforated clay block masonry.

Publication 4 contains investigations on numerically developing macroscopic failure surfaces for vertically perforated clay block masonry, using the unit cell model of Publication 3 as a basis. Using a simplified block design, we analyzed the peak stress states and failure mechanisms of 450 simulations, considering 150 arbitrary loading states and three different head joint types. In doing so, we obtained a dense data set of peak stress states, which were used to develop macroscopic failure surfaces. Additionally, we identified seven different failure mechanisms and associated them with regions of the failure surface. Next, we compared the peak stress states with two failure surfaces: the failure surface developed by Ganz [54] and the Rankine–Hill failure surface proposed by Lourenço [86]. While the failure surface from Ganz showed good agreement with the simulations, the fit of the Rankine–Hill failure surface depended on the calibration procedure. Simulating the seven loading states recommended by Lourenço led to an unacceptable fit. Nevertheless, using a mean squared error optimization procedure led to a good agreement with the numerically obtained peak stress states. Yet, we identified two areas with significant differences: (i) failure under governing vertical tension in combination with horizontal compression, and (ii) failure under governing vertical compression in combination with horizontal compression. Simulating various loading states for real block designs showed that these differences were less pronounced but still present. However, considering the large fluctuations of experiments on masonry walls and the overall good agreement of the Rankine–Hill surface, a more complex failure surface is probably not worth the effort. Thus, we proposed a concept for numerically calibrating the Rankine–Hill surface for vertically perforated clay block masonry using the unit cell model of Publication 3, taking the identified differences into account.

Perspectives and Future Research

For the presented unit cell model, there are several possibilities for further research in the fields of *validation*, *model improvements*, and *applications*. In the following, some of these possibilities are discussed.

Since the results of Publication 1 are solely based on numerical simulation, they would benefit from further experimental validation. Thus, conducting a series of vertical compressive tests on wall specimens with reinforced bed joints would strengthen the findings of Publication 1. Furthermore, conducting experiments on unreinforced wall specimens under vertical and horizontal tension, as well as biaxial compression would increase the significance of the model developed in Publication 3 and Publication 4. Glued masonry using polyurethane adhesives is a relatively new promising technology, which allows for a more efficient construction process. The developed numerical model could account for this technology by introducing only minor changes. Thus, the validation of the model for glued masonry would be interesting for further research.

In addition to the improved validation, the developed unit cell model could be further enhanced by considering the following aspects: Since the drying and firing process often introduces defects in the clay blocks, especially in regions where the ratio of raw material to surface area is large, the model could be improved by considering these defects. This could be incorporated by automatically reducing the strength of the blocks in these regions. Additionally, it would be interesting to use the phase field method (see e. g. Miehe et al. [97]) as an alternative to XFEM, since it is known to be very stable, even for complex crack topologies, as e. g. Pech et al. [120, 121] showed for wood. Thus, it could enable the simulation of the post-peak behavior of vertically perforated clay block masonry in more detail.

Last but not least, the developed model could be used for various new applications. For example, the model could be used to conduct parametric studies on the influence of the block geometry on the macroscopic material properties of vertically perforated clay block masonry. This could be used to investigate the impact of different parameters, like the web thickness or the block dimensions, on the thermal and mechanical properties of the masonry. Furthermore, the model could be used to consider out-of-plane bending, and combinations of bending with the in-plane loading states investigated in Publications 3 and 4. Since bending moments yield a linear distribution of normal stresses over the wall thickness, which can be captured by the already implemented failure criteria, this would only require minor changes to the boundary conditions of the model. To complete the circle, the influence of bed joint reinforcement on the peak stress state under arbitrary loading states could be investigated. Especially under shear loads, the reinforcement could have a significant impact on the peak stress state and the ductility, which would improve the use of masonry in earthquake regions.

Concludingly, utilizing the available computational methods for extending the knowledge on the thermal and mechanical behavior of the material could lead to a more efficient and sustainable use of vertically perforated clay block masonry.

Bibliography

- [1] AIT. *Thermophysical Characterisation of Fired Clay*. Tech. rep. Austrian Institute of Technology, 2011.
- [2] U. Andreaus. “Failure Criteria for Masonry Panels under In-Plane Loading”. In: *Journal of Structural Engineering* 122.1 (1996), pp. 37–46. ISSN: 0733-9445, 1943-541X. DOI: 10.1061/(ASCE)0733-9445(1996)122:1(37).
- [3] A. Anthoine. “Derivation of the In-Plane Elastic Characteristics of Masonry through Homogenization Theory”. In: *International Journal of Solids and Structures* 32.2 (1995), pp. 137–163. ISSN: 00207683. DOI: 10.1016/0020-7683(94)00140-R.
- [4] A. Anthoine and P. Pegon. “Numerical Analysis and Modelling of the Damage and Softening of Brick Masonry”. In: *Numerical Analysis and Modelling of Composite Materials*. Ed. by J. W. Bull. Dordrecht: Springer Netherlands, 1996, pp. 152–184. ISBN: 978-94-011-0603-0. DOI: 10.1007/978-94-011-0603-0_7.
- [5] A. G. Barbosa de Lima, J. B. da Silva, G. S. Almeida, J. J. S. Nascimento, F. V. S. Tavares, and V. S. Silva. “Clay Products Convective Drying: Foundations, Modeling and Applications”. In: *Drying and Energy Technologies*. Ed. by J. Delgado and A. G. Barbosa de Lima. Vol. 63. Cham: Springer International Publishing, 2016, pp. 43–70. ISBN: 978-3-319-19766-1 978-3-319-19767-8. DOI: 10.1007/978-3-319-19767-8_3.
- [6] L. Beddiar, F. Sahnoune, M. Heraiz, and D. Redaoui. “Thermal Transformation of Fired Clay Ceramics by Dilatometric Analysis”. In: *Acta Phys. Pol. A* 134.1 (2018), pp. 86–89. DOI: 10.12693/APhysPolA.134.86.
- [7] T. Belytschko and T. Black. “Elastic Crack Growth in Finite Elements with Minimal Remeshing”. In: *International Journal for Numerical Methods in Engineering* 45.5 (1999), pp. 601–620. ISSN: 0029-5981, 1097-0207. DOI: 10.1002/(SICI)1097-0207(19990620)45:5<601::AID-NME598>3.0.CO;2-S.
- [8] T. L. Bergman, A. S. Lavine, F. P. Incropera, and D. P. DeWitt. *Fundamentals of Heat and Mass Transfer*. 8th ed. New York: Wiley, 2017. ISBN: 978-1-119-33767-6.
- [9] E. Bertolesi, G. Milani, M. Fagone, T. Rotunno, and E. Grande. “Heterogeneous FE Model for Single Lap Shear Tests on FRP Reinforced Masonry Curved Pillars with Spike Anchors”. In: *Construction and Building Materials* 258 (2020), p. 119629. DOI: 10.1016/j.conbuildmat.2020.119629.
- [10] J. Bezanson, A. Edelman, S. Karpinski, and V. B. Shah. “Julia: A Fresh Approach to Numerical Computing”. In: *SIAM Review* 59.1 (2017), pp. 65–98. ISSN: 0036-1445, 1095-7200. DOI: 10.1137/141000671.

- [11] S. Bitterli. “Versuche an Mauerwerkselementen Mit Geneigten Lagerfugen”. MA thesis. Zürich: ETH Zürich, 2014. URL: https://ethz.ch/content/dam/ethz/special-interest/baug/ibk/structural-masonry-dam/education/MS_Thesis_Bitterli.pdf (visited on 02/24/2021).
- [12] P. Bocca, A. Carpinteri, and S. Valente. “Fracture Mechanics of Brick Masonry: Size Effects and Snap-Back Analysis”. In: *Materials and Structures* 22.5 (1989), pp. 364–373. ISSN: 0025-5432, 1871-6873. DOI: 10.1007/BF02472507.
- [13] H. J. Böhm. “A Short Introduction to Basic Aspects of Continuum Micromechanics”. In: *ILSB-Arbeitsbericht 2016* (2016). URL: <https://www.ilsb.tuwien.ac.at/%20links/downloads/ilsbrep206.pdf> (visited on 07/01/2018).
- [14] H. J. Böhm. “A Short Introduction to Basic Aspects of Continuum Micromechanics”. In: *ILSB Report* (2023). URL: <https://www.ilsb.tuwien.ac.at/links/downloads/ilsbrep206.pdf> (visited on 04/23/2023).
- [15] M. Bolhassani, A. A. Hamid, A. C. Lau, and F. Moon. “Simplified Micro Modeling of Partially Grouted Masonry Assemblages”. In: *Construction and Building Materials* 83 (2015), pp. 159–173. ISSN: 09500618. DOI: 10.1016/j.conbuildmat.2015.03.021.
- [16] J. Bošnjak, S. Gambarelli, A. Sharma, and A. Mešković. “Experimental and Numerical Studies on Masonry after Exposure to Elevated Temperatures”. In: *Construction and Building Materials* 230 (2020), p. 116926. DOI: 10.1016/j.conbuildmat.2019.116926.
- [17] J. Bourret, N. Tessier-Doyen, R. Guinebretiere, E. Joussein, and D. Smith. “Anisotropy of Thermal Conductivity and Elastic Properties of Extruded Clay-Based Materials: Evolution with Thermal Treatment”. In: *Applied Clay Science* 116–117 (2015), pp. 150–157. ISSN: 01691317. DOI: 10.1016/j.clay.2015.08.006.
- [18] M. Bruggi and A. Taliercio. “Design of Masonry Blocks with Enhanced Thermomechanical Performances by Topology Optimization”. In: *Construction and Building Materials* 48 (2013), pp. 424–433. DOI: 10.1016/j.conbuildmat.2013.07.023.
- [19] T. Buchner, T. Kiefer, W. Gaggl, L. Zelaya-Lainez, and J. Füssl. “Automated Morphometrical Characterization of Material Phases of Fired Clay Bricks Based on Scanning Electron Microscopy, Energy Dispersive X-ray Spectroscopy and Powder X-ray Diffraction”. In: *Construction and Building Materials* 288 (2021), p. 122909. ISSN: 09500618. DOI: 10.1016/j.conbuildmat.2021.122909.
- [20] T. Buchner, T. Kiefer, M. Königsberger, A. Jäger, and J. Füssl. “Continuum Micromechanics Model for Fired Clay Bricks: Upscaling of Experimentally Identified Microstructural Features to Macroscopic Elastic Stiffness and Thermal Conductivity”. In: *Materials & Design* 212 (2021), p. 110212. ISSN: 02641275. DOI: 10.1016/j.matdes.2021.110212.
- [21] T. Buchner, T. Kiefer, L. Zelaya-Lainez, W. Gaggl, T. Konegger, and J. Füssl. “A Multitechnique, Quantitative Characterization of the Pore Space of Fired Bricks Made of Five Clayey Raw Materials Used in European Brick Industry”. In: *Applied Clay Science* 200 (2021), p. 105884. ISSN: 01691317. DOI: 10.1016/j.clay.2020.105884.

- [22] T. Buchner, M. Königsberger, W. Gaggl, G. Früh, T. Kiefer, and J. Füssl. “A Continuum Micromechanics Model Challenged to Predict Thermo-Mechanical Properties of 18 Different Clay Bricks and Sensitivity Analysis Revealing Effects of Compositional and Microstructural Features”. In: *Construction and Building Materials* 403 (2023), p. 132601. ISSN: 09500618. DOI: 10.1016/j.conbuildmat.2023.132601.
- [23] T. Buchner, M. Königsberger, A. Jäger, and J. Füssl. “A Validated Multiscale Model Linking Microstructural Features of Fired Clay Brick to Its Macroscopic Multiaxial Strength”. In: *Mechanics of Materials* 170 (2022), p. 104334. ISSN: 01676636. DOI: 10.1016/j.mechmat.2022.104334.
- [24] L. Bujotzek, D. Müller, and C.-A. Graubner. “Monte Carlo Simulation of Masonry Walls in Compression Considering Spatially Variable Material Properties”. In: *Brick and Block Masonry—from Historical to Sustainable Masonry*. CRC Press, 2020, pp. 178–186.
- [25] T. Celano, L. U. Argiento, F. Ceroni, and C. Casapulla. “Literature Review of the In-Plane Behavior of Masonry Walls: Theoretical vs. Experimental Results”. In: *Materials* 14.11 (2021), p. 3063. ISSN: 1996-1944. DOI: 10.3390/ma14113063.
- [26] K. H. Conrad. “Beeinflussung von Technischen Eigenschaften Zementgebundener Mörtel Durch Geeignete Epoxidharzsysteme Unter Berücksichtigung Der Mehrachsialen Festigkeiten”. PhD thesis. Grenoble: Institut National Polytechnique de Grenoble, 1986.
- [27] J. del Coz Díaz, P. G. Nieto, F. Á. Rabanal, and A. L. Martínez-Luengas. “Design and Shape Optimization of a New Type of Hollow Concrete Masonry Block Using the Finite Element Method”. In: *Engineering Structures* 33.1 (2011), pp. 1–9. DOI: 10.1016/j.engstruct.2010.09.012.
- [28] F. Da Porto, G. Guidi, E. Garbin, and C. Modena. “In-Plane Behavior of Clay Masonry Walls: Experimental Testing and Finite-Element Modeling”. In: *Journal of Structural Engineering* 136.11 (2010), pp. 1379–1392. ISSN: 0733-9445, 1943-541X. DOI: 10.1061/(ASCE)ST.1943-541X.0000236.
- [29] Dassault Systèmes. *Abaqus Online Documentation*. 2022. URL: https://help.3ds.com/2022/English/DSSIMULIA_Established/SIMULIA_Established_FrontmatterMap/sim-r-DSDocAbaqus.htm?contextscope=all (visited on 11/05/2022).
- [30] Dassault Systèmes. *Abaqus Online Documentation*. 2022. URL: https://help.3ds.com/2022/English/DSSIMULIA_Established/SIMULIA_Established_FrontmatterMap/sim-r-DSDocAbaqus.htm?contextscope=all (visited on 11/05/2022).
- [31] A. Daware and M. Z. Naser. “Fire Performance of Masonry under Various Testing Methods”. In: *Construction and Building Materials* 289 (2021), p. 123183. ISSN: 0950-0618. DOI: 10.1016/j.conbuildmat.2021.123183.
- [32] J. del Coz Díaz, P. G. Nieto, A. M. Rodríguez, A. L. Martínez-Luengas, and C. B. Biempica. “Non-Linear Thermal Analysis of Light Concrete Hollow Brick Walls by the Finite Element Method and Experimental Validation”. In: *Applied Thermal Engineering* 26.8-9 (2006), pp. 777–786. ISSN: 13594311. DOI: 10.1016/j.applthermaleng.2005.10.012.
- [33] J. Dethier. *Down to Earth: Mud Architecture, an Old Idea, a New Future*. London: Thames and Hudson, 1982. ISBN: 978-0-500-27277-0.

- [34] C. Dialer. “Bruch- und Verformungsverhalten von schubbeanspruchten Mauerwerksscheiben, zweiachsige Versuche an verkleinertem Modellmauerwerk”. PhD thesis. München: TU München, 1990.
- [35] DIN 4108-7. *Wärmeschutz Und Energie-Einsparung in Gebäuden - Teil 7: Luftdichtheit von Gebäuden - Anforderungen, Planungs- Und Ausführungsempfehlungen Sowie -Beispiele*. Standard. Berlin, GER: DIN Deutsches Institut für Normung e. V., 2011.
- [36] J. Ding, T. Yu, Y. Yang, and T. Q. Bui. “An Efficient Variable-Node XFEM for Modeling Multiple Crack Growth: A Matlab Object-Oriented Implementation”. In: *Advances in Engineering Software* 140 (2020), p. 102750. DOI: 10.1016/j.advengsoft.2019.102750.
- [37] Dlubal Software GmbH. *Masonry Design Using the Rankine–Hill Failure Surface*. 2020. URL: <https://www.dlubal.com/en/products/add-ons-for-rfem-6-and-rstab-9/design/masonry-design> (visited on 08/14/2023).
- [38] D. H. Doan, T. Q. Bui, T. V. Do, and N. D. Duc. “A Rate-Dependent Hybrid Phase Field Model for Dynamic Crack Propagation”. In: *Journal of Applied Physics* 122.11 (2017), p. 115102. DOI: 10.1063/1.4990073.
- [39] P. L. J. Domone and J. Illston, eds. *Construction Materials: Their Nature and Behaviour*. 4. Edition. London: Spon Press/Taylor & Francis, 2010. ISBN: 978-0-415-46515-1 978-0-415-46516-8.
- [40] W. J. Drugan and J. R. Willis. “A Micromechanics-Based Nonlocal Constitutive Equation and Estimates of Representative Volume Element Size for Elastic Composites”. In: *Journal of the Mechanics and Physics of Solids* 44.4 (1996), pp. 497–524. DOI: 10.1016/0022-5096(96)00007-5.
- [41] A. Eis and T. Vassilev. “Übersicht über abgeschlossene und laufende Forschungsvorhaben im Mauerwerksbau”. In: *Mauerwerk-Kalender 2012*. Ed. by W. Jäger. Weinheim, Germany: Wiley, 2013, pp. 609–647. ISBN: 978-3-433-60161-7 978-3-433-02987-9. DOI: 10.1002/9783433601617.ch17. (Visited on 11/05/2021).
- [42] EN 1015-11. *Methods of Test for Mortar for Masonry - Part 11: Determination of Flexural and Compressive Strength of Hardened Mortar*. Standard. Brussels, BEL: CEN – European Committee for Standardization, 2019.
- [43] EN 1052-1. *Methods of Test for Masonry - Part 1: Determination of Compressive Strength*. Standard. Brussels, BEL: CEN – European Committee for Standardization, 1998.
- [44] EN 1052-3. *Methods of Test for Masonry - Part 3: Determination of Initial Shear Strength*. Standard. Brussels, BEL: CEN – European Committee for Standardization, 2002.
- [45] EN 13501-2. *Fire Classification of Construction Products and Building Elements - Part 2: Classification Using Data from Fire Resistance Tests, Excluding Ventilation Services*. Standard. CEN – European Committee for Standardization, 2016.
- [46] EN 1745. *Masonry and Masonry Products - Methods for Determining Thermal Properties*. Standard. CEN – European Committee for Standardization, 2020.
- [47] EN 1996-1-2. *Design of Masonry Structures –Part 1-2: General Rules –Structural Fire Design*. Standard. CEN – European Committee for Standardization, 2011.
- [48] EN 772-1. *Methods of Test for Masonry Units - Part 1: Determination of Compressive Strength*. Standard. Brussels, BEL: CEN – European Committee for Standardization, 2016.

- [49] J. D. Eshelby. “The Determination of the Elastic Field of an Ellipsoidal Inclusion, and Related Problems”. In: *Proceedings of the Royal Society A: Mathematical, Physical and Engineering Sciences* 241 (1957), pp. 376–396. DOI: 10.1098/rspa.1957.0133.
- [50] A. S. Essawy and R. G. Drysdale. “Macroscopic Failure Criterion for Masonry Assemblages”. In: *Proceedings of the 4th Canadian Masonry Symposium, Fredericton, NB, Canada*. 1986.
- [51] A. Fódi. “Effects Influencing the Compressive Strength of a Solid, Fired Clay Brick”. In: *Periodica Polytechnica Civil Engineering* 55.2 (2011), p. 117. ISSN: 0553-6626, 1587-3773. DOI: 10.3311/pp.ci.2011-2.04.
- [52] S.-Y. Fu, B. Lauke, E. Mäder, C.-Y. Yue, and X. Hu. “Tensile Properties of Short-Glass-Fiber- and Short-Carbon-Fiber-Reinforced Polypropylene Composites”. In: *Composites Part A: Applied Science and Manufacturing* 31.10 (2000), pp. 1117–1125. DOI: 10.1016/S1359-835X(00)00068-3.
- [53] D. Gaetano, F. Greco, L. Leonetti, P. Lonetti, A. Pascuzzo, and C. Ronchei. “An Interface-Based Detailed Micro-Model for the Failure Simulation of Masonry Structures”. In: *Engineering Failure Analysis* 142 (2022), p. 106753. ISSN: 13506307. DOI: 10.1016/j.engfailanal.2022.106753.
- [54] H. R. Ganz. “Mauerwerksscheiben unter Normalkraft und Schub”. PhD thesis. ETH Zurich, 1985, 133 S. DOI: 10.3929/ETHZ-A-000360363. URL: <http://hdl.handle.net/20.500.11850/138655> (visited on 02/01/2023).
- [55] H. R. Ganz and B. Thürlimann. “Versuche über die Festigkeit von zweiachsig beanspruchtem Mauerwerk”. In: (1982), 61 S. DOI: 10.3929/ETHZ-A-000248407. (Visited on 08/16/2023).
- [56] E. Grande, M. Imbimbo, and E. Sacco. “Finite Element Analysis of Masonry Panels Strengthened with FRPs”. In: *Composites Part B: Engineering* 45.1 (2013), pp. 1296–1309. ISSN: 13598368. DOI: 10.1016/j.compositesb.2012.09.002.
- [57] E. Grande, G. Milani, and E. Sacco. “Modelling and Analysis of FRP-strengthened Masonry Panels”. In: *Engineering Structures* 30.7 (2008), pp. 1842–1860. ISSN: 01410296. DOI: 10.1016/j.engstruct.2007.12.007.
- [58] C.-A. Graubner and L. Richter. “Diskrete FE-Modellierung von Mauerwerk Zur Bestimmung Der Druckfestigkeit”. In: *Mauerwerk* 11 (6) (2007), pp. 342–348. DOI: 10.1002/dama.200700354.
- [59] A. Gravouil, N. Moës, and T. Belytschko. “Non-Planar 3D Crack Growth by the Extended Finite Element and Level Sets–Part II: Level Set Update”. In: *International Journal for Numerical Methods in Engineering* 53 (11) (2002), pp. 2569–2586. DOI: 10.1002/nme.430.
- [60] A. A. Griffith. “The Phenomena of Rupture and Flow in Solids”. In: *Philosophical Transactions of the Royal Society A: Mathematical, Physical and Engineering Sciences* 221.582-593 (1921), pp. 163–198.
- [61] N. Grillanda, M. Valente, G. Milani, A. Chiozzi, and A. Tralli. “Advanced Numerical Strategies for Seismic Assessment of Historical Masonry Aggregates”. In: *Engineering Structures* 212 (2020), p. 110441. DOI: 10.1016/j.engstruct.2020.110441.
- [62] A. A. Hamid and R. G. Drysdale. “Proposed Failure Criteria for Concrete Block Masonry under Biaxial Stresses”. In: *Journal of the Structural Division* 107.8 (1981), pp. 1675–1687. ISSN: 0044-8001, 2690-3377. DOI: 10.1061/JSDEAG.0005772.

- [63] J. Hannawald. “Determining the Tensile Softening Diagram of Concrete-like Materials Using Hybrid Optimisation”. In: *Measuring, Monitoring and Modeling Concrete Properties*. Ed. by M. S. Konsta-Gdoutos. Dordrecht: Springer Netherlands, 2006, pp. 179–187. ISBN: 978-1-4020-5103-6. DOI: 10.1007/978-1-4020-5104-3_22.
- [64] J. Hannawald and W. Brameshuber. “Ermittlung effektiver elastischer Eigenschaften von Hochlochziegeln mittels numerischer Simulation”. In: *Mauerwerk* 11.6 (2007), pp. 330–334. ISSN: 14323427, 14371022. DOI: 10.1002/dama.200700352.
- [65] G. A. Hegemier, S. Arya, G. Krishnamoorthy, W. Nachbar, and R. Furgeson. “On the Behavior of Joints in Concrete Masonry”. In: *Proc. North American Conference, Masonry Society, USA*. 1978.
- [66] A. W. Hendry. “A Note on the Strength of Brickwork in Combined Racking Shear and Compression”. In: *Proceeding of the British Ceramic Society*. Vol. 27. 1978, pp. 47–52.
- [67] O. Hoffman. “The Brittle Strength of Orthotropic Materials”. In: *Journal of Composite Materials* 1.2 (1967), pp. 200–206. ISSN: 0021-9983, 1530-793X. DOI: 10.1177/002199836700100210.
- [68] J. Holbery and D. Houston. “Natural-Fiber-Reinforced Polymer Composites in Automotive Applications”. In: *JOM Journal of the Minerals Metals and Materials Society* 58.11 (2006), pp. 80–86. DOI: 10.1007/s11837-006-0234-2.
- [69] D. Hordijk and H. Reinhardt. “Fracture of Concrete in Uniaxial Tensile Experiments as Influenced by Curing Conditions”. In: *Engineering Fracture Mechanics* 35.4-5 (1990), pp. 819–826. ISSN: 00137944. DOI: 10.1016/0013-7944(90)90166-E.
- [70] ISO 834-1. *Fire Resistance Tests – Elements of Building Construction – Part 1: General Requirements*. Tech. rep. International Organization for Standardization, 1999.
- [71] O. Iuorio and J. A. Dauda. “Retrofitting Masonry Walls against Out-Of-Plane Loading with Timber Based Panels”. In: *Applied Sciences* 11.12 (2021), p. 5443. ISSN: 2076-3417. DOI: 10.3390/app11125443.
- [72] S. Jafari, J. G. Rots, and R. Esposito. “Core Testing Method to Assess Nonlinear Behavior of Brick Masonry under Compression: A Comparative Experimental Study”. In: *Construction and Building Materials* 218 (2019), pp. 193–205. ISSN: 09500618. DOI: 10.1016/j.conbuildmat.2019.04.188.
- [73] R. Jasiński and Ł. Drobiec. “Study of Autoclaved Aerated Concrete Masonry Walls with Horizontal Reinforcement under Compression and Shear”. In: *Procedia Engineering* 161 (2016), pp. 918–924. DOI: 10.1016/j.proeng.2016.08.758.
- [74] H. Kariem, C. Hellmich, T. Kiefer, A. Jäger, and J. Füssl. “Micro-CT-based Identification of Double Porosity in Fired Clay Ceramics”. In: *Journal of Materials Science* 53.13 (2018), pp. 9411–9428. ISSN: 0022-2461, 1573-4803. DOI: 10.1007/s10853-018-2281-9.
- [75] H. Kariem, T. Kiefer, C. Hellmich, W. Gaggli, A. Steiger-Thirsfeld, and J. Füssl. “EDX/XRD-based Identification of Micrometer-Sized Domains in Scanning Electron Micrographs of Fired Clay”. In: *Materials and Structures* 53.4 (2020), p. 109. ISSN: 1359-5997, 1871-6873. DOI: 10.1617/s11527-020-01531-7.

- [76] T. Kiefer, H. Kariem, M. Lukacevic, and J. Füssl. “The Compressive Strength of Vertically Perforated Clay Block Masonry Predicted by Means of a Unit-Cell Type Numerical Simulation Tool Taking Discrete Cracking into Account”. In: *Construction and Building Materials* 150 (2017), pp. 24–34. ISSN: 09500618. DOI: 10.1016/j.conbuildmat.2017.05.201.
- [77] C. Kohlhauser and C. Hellmich. “Ultrasonic Contact Pulse Transmission for Elastic Wave Velocity and Stiffness Determination: Influence of Specimen Geometry and Porosity”. In: *Engineering Structures* 47 (2013), pp. 115–133. DOI: 10.1016/j.engstruct.2012.10.027.
- [78] R. Krueger. “Virtual Crack Closure Technique: History, Approach, and Applications”. In: *Applied Mechanics Reviews* 57.2 (2004), pp. 109–143. ISSN: 0003-6900, 2379-0407. DOI: 10.1115/1.1595677.
- [79] P. Kumar and V. Kodur. “Modeling the Behavior of Load Bearing Concrete Walls under Fire Exposure”. In: *Construction and Building Materials* 154 (2017), pp. 993–1003. DOI: 10.1016/j.conbuildmat.2017.08.010.
- [80] P. Kumar and G. Srivastava. “Numerical Modeling of Structural Frames with Infills Subjected to Thermal Exposure: State-of-the-art Review”. In: *Journal of Structural Fire Engineering* 8.3 (2017), pp. 218–237. DOI: 10.1108/jsfe-05-2017-0031.
- [81] N. Laws. “The Determination of Stress and Strain Concentrations at an Ellipsoidal Inclusion in an Anisotropic Material”. In: *Journal of Elasticity* 7 (1) (1977), pp. 91–97. DOI: 10.1007/bf00041133.
- [82] H. S. Lee, W. S. Jeon, Y. K. Kim, B. D. Purusatama, A. R. Kim, J. I. Cho, W. J. Kim, H. C. Kim, and N. H. Kim. “Design of a Modified Charcoal Production Kiln for Thermal Therapy and Evaluation of the Charcoal Characteristics from This Kiln”. In: *BioResources* 14.3 (2019), pp. 7275–7284. ISSN: 19302126, 19302126. DOI: 10.15376/biores.14.3.7275-7284.
- [83] J. Lee and G. L. Fenves. “Plastic-Damage Model for Cyclic Loading of Concrete Structures”. In: *Journal of Engineering Mechanics* 124.8 (1998), pp. 892–900. ISSN: 0733-9399, 1943-7889. DOI: 10.1061/(ASCE)0733-9399(1998)124:8(892).
- [84] L. Leonetti, F. Greco, P. Trovalusci, R. Luciano, and R. Masiani. “A Multiscale Damage Analysis of Periodic Composites Using a Couple-Stress/Cauchy Multidomain Model: Application to Masonry Structures”. In: *Composites Part B: Engineering* 141 (2018), pp. 50–59. ISSN: 13598368. DOI: 10.1016/j.compositesb.2017.12.025.
- [85] P. Lourenço, G. Vasconcelos, P. Medeiros, and J. Gouveia. “Vertically Perforated Clay Brick Masonry for Loadbearing and Non-Loadbearing Masonry Walls”. In: *Construction and Building Materials* 24.11 (2010), pp. 2317–2330. ISSN: 09500618. DOI: 10.1016/j.conbuildmat.2010.04.010.
- [86] P. B. Lourenço. “Computational Strategies for Masonry Structures”. PhD thesis. Delft University of Technology, 1996. URL: <http://resolver.tudelft.nl/uuid:4f5a2c6c-d5b7-4043-9d06-8c0b7b9f1f6f> (visited on 02/27/2023).
- [87] J. Lubliner, J. Oliver, S. Oller, and E. Oñate. “A Plastic-Damage Model for Concrete”. In: *International Journal of Solids and Structures* 25.3 (1989), pp. 299–326. ISSN: 00207683. DOI: 10.1016/0020-7683(89)90050-4.

- [88] H. A. Mang and G. Hofstetter. *Festigkeitslehre*. 5., ergänzte Auflage. Berlin, Heidelberg: Springer Vieweg, 2018. ISBN: 978-3-662-57563-5.
- [89] W. Mann and H. Müller. “Failure of Shear-Stressed Masonry: An Enlarged Theory, Tests and Application to Shear Walls”. In: *Proceeding of the British Ceramic Society*. Vol. 30. 1982, pp. 223–235.
- [90] J.-J. Marigo, C. Maurini, and K. Pham. “An Overview of the Modelling of Fracture by Gradient Damage Models”. In: *Meccanica. International Journal of Theoretical and Applied Mechanics* 51.12 (2016), pp. 3107–3128. DOI: 10.1007/s11012-016-0538-4.
- [91] M. D. McKay, R. J. Beckman, and W. J. Conover. “Comparison of Three Methods for Selecting Values of Input Variables in the Analysis of Output from a Computer Code”. In: *Technometrics* 21.2 (1979), pp. 239–245. ISSN: 0040-1706, 1537-2723. DOI: 10.1080/00401706.1979.10489755.
- [92] J. M. Melenk and I. Babuška. “The Partition of Unity Finite Element Method: Basic Theory and Applications”. In: *Computer Methods in Applied Mechanics and Engineering* 139 (1-4) (1996), pp. 289–314. DOI: 10.1016/S0045-7825(96)01087-0.
- [93] N. Mendes, S. Zanotti, and J. V. Lemos. “Seismic Performance of Historical Buildings Based on Discrete Element Method: An Adobe Church”. In: *Journal of Earthquake Engineering* (2018), pp. 1–20. DOI: 10.1080/13632469.2018.1463879.
- [94] F. Messali, R. Esposito, G. J. P. Ravenshorst, and J. G. Rots. “Experimental Investigation of the In-Plane Cyclic Behaviour of Calcium Silicate Brick Masonry Walls”. In: *Bulletin of Earthquake Engineering* 18.8 (2020), pp. 3963–3994. DOI: 10.1007/s10518-020-00835-x.
- [95] *Methods of Test for Masonry - Part 1: Determination of Compressive Strength*. Standard. Brussels, BEL: CEN – European Committee for Standardization, 1998.
- [96] J. Michel, H. Moulinec, and P. Suquet. “Effective Properties of Composite Materials with Periodic Microstructure: A Computational Approach”. In: *Computer Methods in Applied Mechanics and Engineering* 172.1-4 (1999), pp. 109–143. ISSN: 00457825. DOI: 10.1016/S0045-7825(98)00227-8.
- [97] C. Miehe, M. Hofacker, and F. Welschinger. “A Phase Field Model for Rate-Independent Crack Propagation: Robust Algorithmic Implementation Based on Operator Splits”. In: *Computer Methods in Applied Mechanics and Engineering* 199.45 (2010), pp. 2765–2778. ISSN: 0045-7825. DOI: 10.1016/j.cma.2010.04.011.
- [98] G. Mininno, B. Ghiassi, and D. V. Oliveira. “Modelling of the In-Plane and Out-of-Plane Performance of TRM-Strengthened Masonry Walls”. In: *Key Engineering Materials* 747 (2017), pp. 60–68. ISSN: 1662-9795. DOI: 10.4028/www.scientific.net/KEM.747.60.
- [99] N. Moës, A. Gravouil, and T. Belytschko. “Non-Planar 3D Crack Growth by the Extended Finite Element and Level Sets – Part I: Mechanical Model”. In: *International Journal for Numerical Methods in Engineering* 53 (11) (2002), pp. 2549–2568. DOI: 10.1002/nme.429.
- [100] N. Mojsilović. “Strength of Masonry Subjected to In-Plane Loading: A Contribution”. In: *International Journal of Solids and Structures* 48.6 (2011), pp. 865–873. ISSN: 00207683. DOI: 10.1016/j.ijsolstr.2010.11.019.

- [101] N. Mojsilović. “Zum Tragverhalten von kombiniert beanspruchtem Mauerwerk”. PhD thesis. ETH Zurich, 1995, 130 S. DOI: 10.3929/ETHZ-A-001549685. URL: <http://hdl.handle.net/20.500.11850/142387> (visited on 02/20/2023).
- [102] E. Moradabadi, D. F. Laefer, J. A. Clarke, and P. B. Lourenço. “A Semi-Random Field Finite Element Method to Predict the Maximum Eccentric Compressive Load for Masonry Prisms”. In: *Construction and Building Materials* 77 (2015), pp. 489–500. DOI: 10.1016/j.conbuildmat.2014.12.027.
- [103] T. Mori and K. Tanaka. “Average Stress in Matrix and Average Elastic Energy of Materials with Misfitting Inclusions”. In: *Acta Metallurgica* 21.5 (1973), pp. 571–574. DOI: 10.1016/0001-6160(73)90064-3.
- [104] N. S. Müller, V. Kilikoglou, P. M. Day, and G. Vekinis. “The Influence of Temper Shape on the Mechanical Properties of Archaeological Ceramics”. In: *Journal of the European Ceramic Society* 30.12 (2010), pp. 2457–2465. ISSN: 09552219. DOI: 10.1016/j.jeurceramsoc.2010.04.039.
- [105] A. Nadjai, M. O’Garra, F. A. Ali, and D. Laverty. “A Numerical Model for the Behaviour of Masonry under Elevated Temperatures”. In: *Fire and Materials* 27.4 (2003), pp. 163–182. DOI: 10.1002/fam.824.
- [106] A. Nadjai, M. O’Garra, and F. Ali. “Finite Element Modelling of Compartment Masonry Walls in Fire”. In: *Computers & Structures* 81.18 (2003), pp. 1923–1930. DOI: 10.1016/s0045-7949(03)00212-8.
- [107] B. Nagy. “Numerical Geometry Optimization and Modelling of Insulation Filled Masonry Blocks”. In: *Proceedings of the 1st International Conference on Numerical Modelling in Engineering*. Springer Singapore, 2018, pp. 1–13. DOI: 10.1007/978-981-13-2405-5_1.
- [108] F. A. Nahhas, R. A. Saada, G. Bonnet, and P. Delmotte. “Resistance to Fire of Walls Constituted by Hollow Blocks: Experiments and Thermal Modeling”. In: *Applied Thermal Engineering* 27.1 (2007), pp. 258–267. DOI: 10.1016/j.applthermaleng.2006.04.017.
- [109] M. A. Najafgholipour, M. R. Maheri, and P. B. Lourenço. “Capacity Interaction in Brick Masonry under Simultaneous In-Plane and out-of-Plane Loads”. In: *Construction and Building Materials* 38 (2013), pp. 619–626. DOI: 10.1016/j.conbuildmat.2012.08.032.
- [110] H. Netzel and G. P. A. G. Van Zijl. “Nonlinear Numerical Simulation of Settlement-Induced Damage to Solid Masonry Walls”. In: *13th International Brick Masonry Conference, Amsterdam*. Citeseer, 2004.
- [111] T.-D. Nguyen and F. Meftah. “Behavior of Clay Hollow-Brick Masonry Walls during Fire. Part 1: Experimental Analysis”. In: *Fire Safety Journal* 52 (2012), pp. 55–64. ISSN: 03797112. DOI: 10.1016/j.firesaf.2012.06.001.
- [112] T.-D. Nguyen and F. Meftah. “Behavior of Hollow Clay Brick Masonry Walls during Fire. Part 2: 3D Finite Element Modeling and Spalling Assessment”. In: *Fire Safety Journal* 66 (2014), pp. 35–45. ISSN: 03797112. DOI: 10.1016/j.firesaf.2013.08.017.

- [113] T.-D. Nguyen, F. Meftah, R. Chammas, and A. Mebarki. “The Behaviour of Masonry Walls Subjected to Fire: Modelling and Parametrical Studies in the Case of Hollow Burnt-Clay Bricks”. In: *Fire Safety Journal* 44.4 (2009), pp. 629–641. ISSN: 03797112. DOI: 10.1016/j.firesaf.2008.12.006.
- [114] T. H. A. Nguyen, T. Q. Bui, and S. Hirose. “Smoothing Gradient Damage Model with Evolving Anisotropic Nonlocal Interactions Tailored to Low-Order Finite Elements”. In: *Computer Methods in Applied Mechanics and Engineering* 328 (2018), pp. 498–541. DOI: 10.1016/j.cma.2017.09.019.
- [115] S. Noor-E-Khuda. “An Explicit Finite-Element Modeling Method for Masonry Walls Using Continuum Shell Element”. In: *Journal of Architectural Engineering* 27.4 (2021), p. 04021040. ISSN: 1076-0431, 1943-5568. DOI: 10.1061/(ASCE)AE.1943-5568.0000518.
- [116] R. G. Oliveira, J. P. C. Rodrigues, J. Miguel Pereira, P. B. Lourenço, and R. F. R. Lopes. “Experimental and Numerical Analysis on the Structural Fire Behaviour of Three-Cell Hollowed Concrete Masonry Walls”. In: *Engineering Structures* 228 (2021), p. 111439. ISSN: 0141-0296. DOI: 10.1016/j.engstruct.2020.111439.
- [117] R. L. G. Oliveira, J. P. C. Rodrigues, J. M. Pereira, P. B. Lourenço, and H. U. Marschall. “Thermomechanical Behaviour of Refractory Dry-Stacked Masonry Walls under Uniaxial Compression”. In: *Engineering Structures* 240 (2021), p. 112361. DOI: 10.1016/j.engstruct.2021.112361.
- [118] A. W. Page. “The Biaxial Compressive Strength of Brick Masonry”. In: *Proceedings of the Institution of Civil Engineers* 71 (1981), pp. 893–906.
- [119] A. W. Page. “The Strength of Brick Masonry under Biaxial Tension-Compression”. In: *International journal of masonry construction* 3.1 (1983), pp. 26–31.
- [120] S. Pech, M. Lukacevic, and J. Füssl. “A Hybrid Multi-Phase Field Model to Describe Cohesive Failure in Orthotropic Materials, Assessed by Modeling Failure Mechanisms in Wood”. In: *Engineering Fracture Mechanics* 271 (2022), p. 108591. ISSN: 00137944. DOI: 10.1016/j.engfracmech.2022.108591.
- [121] S. Pech, M. Lukacevic, and J. Füssl. “Validation of a Hybrid Multi-Phase Field Model for Fracture of Wood”. In: *Engineering Fracture Mechanics* 275 (2022), p. 108819. ISSN: 00137944. DOI: 10.1016/j.engfracmech.2022.108819.
- [122] V. Pensée and Q.-C. He. “Generalized Self-Consistent Estimation of the Apparent Isotropic Elastic Moduli and Minimum Representative Volume Element Size of Heterogeneous Media”. In: *International Journal of Solids and Structures* 44.7-8 (2007), pp. 2225–2243. DOI: 10.1016/j.ijsolstr.2006.07.003.
- [123] S. Pohl. “Beitrag des Mauerwerksbaus zum nachhaltigen Bauen”. In: *Mauerwerk* 24.2 (2020), pp. 100–107. ISSN: 1432-3427, 1437-1022. DOI: 10.1002/dama.202000003.
- [124] P. R. Prakash, M. Azenha, J. M. Pereira, and P. B. Lourenço. “Finite Element Based Micro Modelling of Masonry Walls Subjected to Fire Exposure: Framework Validation and Structural Implications”. In: *Engineering Structures* 213 (2020), p. 110545. ISSN: 01410296. DOI: 10.1016/j.engstruct.2020.110545.

- [125] M. Rahiminejad and D. Khovalyg. “Thermal Resistance of Ventilated Air-Spaces behind External Claddings; Definitions and Challenges (ASHRAE 1759-RP)”. In: *Science and Technology for the Built Environment* 27.6 (2021), pp. 788–805. ISSN: 2374-4731, 2374-474X. DOI: 10.1080/23744731.2021.1898819.
- [126] R. Reismüller. *AbaqusUnitCell2D*. 2021. URL: <https://github.com/raphaelsuda/AbaqusUnitCell2D>.
- [127] R. Reismüller, M. Königsberger, A. Jäger, and J. Füssl. “The Performance of Vertically Perforated Clay Block Masonry in Fire Tests Predicted by a Finite-Element Model Including an Energy-Based Criterion to Identify Spalling”. In: *Fire Safety Journal* 135 (2023), p. 103729. ISSN: 03797112. DOI: 10.1016/j.firesaf.2022.103729.
- [128] R. Reismüller, M. Lukacevic, S. Pech, A. Jäger, and J. Füssl. “A Numerical Unit Cell Model for Predicting the Failure Stress State of Vertically Perforated Clay Block Masonry under Arbitrary In-Plane Loads”. In: *Engineering Structures* 293 (2023), p. 116557. ISSN: 01410296. DOI: 10.1016/j.engstruct.2023.116557.
- [129] J. G. Rots, F. Messali, R. Esposito, S. Jafari, and V. Mariani. “Thematic Keynote Computational Modelling of Masonry with a View to Groningen Induced Seismicity”. In: *Structural Analysis of Historical Constructions: Anamnesis, Diagnosis, Therapy, Controls*. CRC Press, 2016, pp. 227–238.
- [130] E. Rybicki and M. Kanninen. “A Finite Element Calculation of Stress Intensity Factors by a Modified Crack Closure Integral”. In: *Engineering Fracture Mechanics* 9.4 (1977), pp. 931–938. ISSN: 00137944. DOI: 10.1016/0013-7944(77)90013-3.
- [131] E. Rybicki, D. Schmueser, and J. Fox. “An Energy Release Rate Approach For Stable Crack Growth in the Free-Edge Delamination Problem”. In: *Journal of Composite Materials* 11.4 (1977), pp. 470–487. ISSN: 0021-9983, 1530-793X. DOI: 10.1177/002199837701100409.
- [132] H. Sadek and S. Lissel. “Seismic Performance of Masonry Walls with GFRP and Geogrid Bed Joint Reinforcement”. In: *Construction and Building Materials* 41 (2013), pp. 977–989. DOI: 10.1016/j.conbuildmat.2012.07.005.
- [133] A. H. Salmanpour. “Displacement Capacity of Structural Masonry”. PhD thesis. ETH Zurich, 2017, 148 p. DOI: 10.3929/ETHZ-B-000172566.
- [134] V. Sarhosis and Y. Sheng. “Identification of Material Parameters for Low Bond Strength Masonry”. In: *Engineering Structures* 60 (2014), pp. 100–110. ISSN: 01410296. DOI: 10.1016/j.engstruct.2013.12.013.
- [135] J. Scacco, B. Ghiassi, G. Milani, and P. B. Lourenço. “A Fast Modeling Approach for Numerical Analysis of Unreinforced and FRCM Reinforced Masonry Walls under Out-of-Plane Loading”. In: *Composites Part B: Engineering* 180 (2020), p. 107553. ISSN: 13598368. DOI: 10.1016/j.compositesb.2019.107553.
- [136] J. Scacco, N. Grillanda, G. Milani, and P. B. Lourenço. “Novel Non-Linear Static Numerical Model for Curved Masonry Structures Based on a Combined Adaptive Limit Analysis and Discrete FE Computations”. In: *International Journal of Solids and Structures* 236–237 (2022), p. 111265. ISSN: 00207683. DOI: 10.1016/j.ijsolstr.2021.111265.

- [137] R. Schlegel and K. Rautenstrauch. “Ein Elastoplastisches Berechnungsmodell Zur Räumlichen Untersuchung von Mauerwerkstrukturen”. In: *Bautechnik* 77.6 (2000), pp. 426–436. ISSN: 09328351. DOI: 10.1002/bate.200003100.
- [138] J. Segura, L. Pelà, S. Saloustros, and P. Roca. “Experimental and Numerical Insights on the Diagonal Compression Test for the Shear Characterisation of Masonry”. In: *Construction and Building Materials* 287 (2021), p. 122964. ISSN: 09500618. DOI: 10.1016/j.conbuildmat.2021.122964.
- [139] W. Seim. *Numerische Modellierung Des Anisotropen Versagens Zweiachsig Beanspruchter Mauerwerksscheiben*. 1995.
- [140] L. C. Silva, P. B. Lourenço, and G. Milani. “Numerical Homogenization-based Seismic Assessment of an English-bond Masonry Prototype: Structural Level Application”. In: *Earthquake Engineering & Structural Dynamics* 49.9 (2020), pp. 841–862. ISSN: 0098-8847, 1096-9845. DOI: 10.1002/eqe.3267.
- [141] L. C. Sousa, C. F. Castro, C. C. António, and H. Sousa. “Topology Optimisation of Masonry Units from the Thermal Point of View Using a Genetic Algorithm”. In: *Construction and Building Materials* 25.5 (2011), pp. 2254–2262. DOI: 10.1016/j.conbuildmat.2010.11.010.
- [142] R. Suda, T. Kiefer, C. Schranz, and J. Füssl. “A Finite-Element-Based Approach to Quantify the Impact of Bed Joint Reinforcement on the Compressive Strength of Vertically Perforated Clay Block Masonry”. In: *Engineering Structures* 239 (2021), p. 112277. ISSN: 01410296. DOI: 10.1016/j.engstruct.2021.112277.
- [143] J. Thamboo and M. Dhanasekar. “Nonlinear Finite Element Modelling of High Bond Thin-Layer Mortared Concrete Masonry”. In: *International Journal of Masonry Research and Innovation* 1.1 (2016), p. 5. ISSN: 2056-9459, 2056-9467. DOI: 10.1504/IJMRI.2016.074727.
- [144] A. Trinko, C. Schranz, and A. Pech. “Tragfähigkeitserhöhung Bei Mauerwerk Durch Textilglasgitterverstärkte Mörtelfugen (English: Increase of the Vertical Load Carrying Capacity of Masonry Due to Mortar Bed Joints with Textile Glass Mesh Reinforcement)”. In: *Mauerwerk* 24.2 (2020), pp. 72–80. DOI: 10.1002/dama.201900019.
- [145] R. Van der Pluijm. “Out-of-Plane Bending of Masonry : Behaviour and Strength”. PhD thesis. Technische Universiteit Eindhoven, 1999. URL: <https://research.tue.nl/en/publications/out-of-plane-bending-of-masonry-behaviour-and-strength> (visited on 11/05/2021).
- [146] VDI e. V., ed. *VDI Heat Atlas*. Berlin, Heidelberg: Springer Berlin Heidelberg, 2010. ISBN: 978-3-540-77876-9 978-3-540-77877-6. DOI: 10.1007/978-3-540-77877-6.
- [147] B. de Vekey. “Masonry: Brickwork, Blockwork and Stonework”. In: *Construction Materials: Their Nature and Behaviour*. Ed. by P. L. J. Domone and J. Illston. 4. ed., reprinted. London: Spon Press/Taylor & Francis, 2010, pp. 247–304. ISBN: 978-0-415-46515-1 978-0-415-46516-8.
- [148] V. Vratsanou. “Das Nichtlineare Verhalten Unbewehrter Mauerwerksscheiben Unter Erdbebenbeanspruchung”. In: *Hilfsmittel zur Bestimmung der q-Faktoren. Diss. Universität Karlsruhe* (1992).
- [149] Q. Wan and W. Yi. “The Shear Strength of Masonry Wall under Combined Stresses”. In: *Proceedings of the Fourth Canadian Masonry Symposium. University of New Brunswick, Canada*. 1986.

- [150] L. Wen and R. Tian. “Improved XFEM: Accurate and Robust Dynamic Crack Growth Simulation”. In: *Computer Methods in Applied Mechanics and Engineering* 308 (2016), pp. 256–285. DOI: 10.1016/j.cma.2016.05.013.
- [151] Wienerberger AG. *Porotherm S9 36,5 MW*. 2023. URL: <https://www.wienerberger.de/produkte/wand/ziegel/poroton-s9-36,5-miwo.html> (visited on 08/02/2023).
- [152] W. M. Willems, ed. *Lehrbuch der Bauphysik*. Wiesbaden: Springer Fachmedien Wiesbaden, 2017. ISBN: 978-3-658-16073-9 978-3-658-16074-6. DOI: 10.1007/978-3-658-16074-6.
- [153] T. Yu and T. Q. Bui. “Numerical Simulation of 2-D Weak and Strong Discontinuities by a Novel Approach Based on XFEM with Local Mesh Refinement”. In: *Computers & Structures* 196 (2018), pp. 112–133. DOI: 10.1016/j.compstruc.2017.11.007.
- [154] Y. Zhou, L. J. Sluys, and R. Esposito. “An Improved Mean-Field Homogenization Model for the Three-Dimensional Elastic Properties of Masonry”. In: *European Journal of Mechanics - A/Solids* 96 (2022), p. 104721. ISSN: 09977538. DOI: 10.1016/j.euromechsol.2022.104721.
- [155] K. Zilch and D. Schermer. “Untersuchungen Zum Verhalten von Mauerwerksgebäuden Unter Erdbebenbeanspruchung”. In: *Bauingenieur* 78.7 (2003), pp. 360–368.
- [156] Zürcher Ziegeleien AG. *SwissModul 15*. 2023. URL: <https://www.zz-ag.ch/produkte/wand/mauerwerk/swissmodul-15.html> (visited on 01/12/2023).

Publications

Books

Ch. Schranz, R. Suda¹, S. Pech:

LaTeX, Excel, Word – Werkzeuge für den ingenieurwissenschaftlichen Hochschul-Einsatz

TU Verlag, Wien, 2018, ISBN: 978-3-903024-66-3; 408 S.

Ch. Schranz, R. Suda¹, S. Pech:

LaTeX, Excel, Word – Werkzeuge für den ingenieurwissenschaftlichen Hochschul-Einsatz (2., korrigierte und erweiterte Auflage)

TU Verlag, Wien, 2019, ISBN: 978-3-903024-90-8; 432 S.

Ch. Schranz, R. Suda¹, S. Pech:

LaTeX, Excel, Word – Werkzeuge für den ingenieurwissenschaftlichen Hochschul-Einsatz (3., korrigierte und erweiterte Auflage)

TU Verlag, Wien, 2021, ISBN: 978-3-903311-22-0; 432 S.

Ch. Schranz, R. Reismüller, S. Pech:

LaTeX, Excel, Word – Werkzeuge für den ingenieurwissenschaftlichen Hochschul-Einsatz (4., korrigierte und erweiterte Auflage)

TU Verlag, Wien, 2022, ISBN: 978-3-903311-35-0; 438 S.

Journal Articles

R. Suda¹, Ch. Schranz, A. Jäger:

Development of a tool for the structural design of the vertical load-bearing capacity of unreinforced masonry
Mauerwerk, 21 (2017), 4; S. 223 - 234.

R. Suda¹, T. Kiefer, Ch. Schranz, J. Füssl:

A Finite-Element-Based Approach to Quantify the Impact of Bed Joint Reinforcement on the Compressive Strength of Vertically Perforated Clay Block Masonry
Engineering Structures, 239 (2021), 112277.

R. Reismüller, M. Königsberger, A. Jäger, J. Füssl

The performance of vertically perforated clay block masonry in fire tests predicted by a finite-element model including an energy-based criterion to identify spalling

Fire Safety Journal, 135 (2023), 103729.

¹In June 2021, my last name has changed from Suda to Reismüller due to marriage.

R. Reismüller, M. Lukacevic, S. Pech, A. Jäger, J. Füssl:

A numerical unit cell model for predicting the failure stress state of vertically perforated clay block masonry under arbitrary in-plane loads

Engineering Structures, 293 (2023), 116557.

Conference Proceedings

R. Suda, T. Kiefer, Ch. Schranz, J. Füssl:

Do Fibre Reinforced Bed Joints Affect the Compressive Strength of Brick Masonry? A Stochastic, Finite Element Based Approach to Quantify the Increase of the Load Carrying Capacity

in: *Programme & Proceedings of the China-Austria Forum for Postgraduates of Civil Engineering*, J. Zhang, B. Pichler (Hrg.); Vienna University of Technology, 2019, S. 91 - 93.

R. Reismüller, M. Lukacevic, T. Kiefer, J. Füssl:

A Finite-Element-Based Unit Cell Approach for Simulating Vertically Perforated Clay Block Masonry

in: *Proceedings of the 8th European Congress on Computational Methods in Applied Sciences and Engineering (ECCOMAS Congress 2022)*, International Center for Numerical Methods in Engineering (CIMNE), 2022, Paper-Nr. 846, 1 S.

Conference Presentations

R. Suda²:

Do Fibre Reinforced Bed Joints Affect the Compressive Strength of Brick Masonry? A Stochastic, Finite Element Based Approach to Quantify the Increase of the Load Carrying Capacity

Vortrag: China-Austria Forum for Postgraduates of Civil Engineering, Vienna, Austria; 07.10.2019 - 08.10.2019.

R. Suda², T. Kiefer, T. Buchner, C. Schranz, J. Füssl:

A Multiscale Model for Brick Masonry with Special Focus on Bed Joint Reinforcement

Vortrag: 14th World Congress in Computational Mechanics (WCCM) & ECCOMAS Congress 2020, Virtual Congress; 11.01.2021 - 15.01.2021.

R. Reismüller:

A Finite-Element-Based Unit Cell Approach for Simulating Vertically Perforated Clay Block Masonry

Vortrag: 8th European Congress on Computational Methods in Applied Sciences and Engineering (ECCOMAS2022), Oslo, Norway; 05.06.2022 - 09.06.2022.

Master's Thesis (own and supervised)

R. Suda²:

Finite Element Based Determination of the Vertical Load Carrying Capacity Increase of Brick Masonry Due to Fibre Reinforced Bed Joints

Betreuer/in(nen): J. Füssl, T. Kiefer, Ch. Schranz; Institut für Mechanik der Werkstoffe und Strukturen, 2019; Abschlussprüfung: 18.01.2019.

²In June 2021, my last name has changed from Suda to Reismüller due to marriage.

Curriculum Vitae

Personal Data

Name: Raphael Reismüller (formerly Suda)

Date of Birth: [REDACTED]

Place of Birth: [REDACTED]

Nationality: [REDACTED]

Current Address: [REDACTED]

Education

since 2019: Doctoral program in Civil Engineering at TU Wien, Austria

2017–2019: Master program in Civil Engineering at TU Wien, Austria

2013–2017: Bachelor program in Civil Engineering and Management Infrastructure at TU Wien, Austria

2007–2013: Höhere technische Bundeslehranstalt, HTBL Krems, Austria, Upper Secondary School, Civil Engineering

Work experience

since 2019: Project assistant/University assistant at the Institute for Mechanics of Materials and Structures, TU Wien, Austria

since 2018: Technical employee at BC Consulting GmbH, Melk, Austria

2014–2018: Student assistant at the Civil Engineering Computer Laboratory, TU Wien, Austria